UNIVERSIDADE FEDERAL DO RIO GRANDE DO SUL
PROGRAMA DE PÓS-GRADUAÇÃO EM FÍSICA
DEPARTAMENTO DE ASTRONOMIA

Tese de Doutorado

Estudo das populações estelares
em galáxias ativas
no infravermelho próximo:
o caso de NGC 4303*

Natacha Zanon Dametto

Tese de doutorado realizada sob orientação do Prof. Dr. Rogério Riffel e apresentada ao Programa de Pós-Graduação em Física da Universidade Federal do Rio Grande do Sul, como requisito parcial para a obtenção do título de Doutora em Ciências.

Porto Alegre, RS, Brasil

Setembro de 2018

Abstract

Aimed at studying the relation between circumnuclear star-formation and the active galactic nuclei, we present here a detailed study of a prototype object: NG 4303. We present a stellar population study of the inner $\sim$200 pc radius of this source using near-infrared ($\sim$ 1.1-2.4μm) integral field spectroscopy with the VLT instrument SINFONI at a spatial resolution of 40-80 pc. Our methodology consists of performing stellar population synthesis using the STARLIGHT code and new generations of stellar population models. As the first part of this thesis, we tested the reliability of the stellar population models in the near-infrared, after that, we applied our methodology to NGC 4303 in order to study spatially the star formation history of this source. We found the distribution of the stellar populations presents a spatial variation, suggesting an age stratification. Three main structures stand out. Two nuclear blobs, one composed by young stars (t $\leq$ 50 Myr) and one with intermediate-age stars (50 Myr $<$ t $\leq$ 2 Gyr) both shifted from the centre. The third one is an internal intermediate-age spiral arm-like structure, surrounding the blob of young stars. Our results indicate star formation has occurred through multiple bursts in this source. Furthermore, the younger stellar populations (t $\lesssim$ 2 Gyr) are distributed along a circumnuclear star-forming ring with r$\sim$250 pc. The ring displays star formation rates (SFRs) in the range of 0.002-0.14 $M_\odot yr^{-1}$, favoring the 'pearls-on-a-string' scenario. The old underlying bulge stellar population component (t $>$ 2 Gyr) is distributed outside the two blob structures. For the nuclear region (inner $\sim$60 pc radius) we derived a SFR of 0.43 $M_\odot yr^{-1}$ and found no signatures of non-thermal featureless continuum and hot dust emission, supporting the scenario in which a LLAGN/LINER-like source is hidden in the centre of NGC 4303. Thus, our results reveal a rather complex star formation history in NGC 4303, with different stellar population components coexisting with a low efficiency accreting black hole in its centre.

Resumo

Com o objetivo de estudar a relação entre a formação estelar circumnuclear e o núcleo ativo de galáxias, apresentamos aqui um estudo detalhado de uma galáxia protótipo: NG 4303. Assim, apresentamos o estudo das populações estelares na região central (r $\lesssim$ 200 pc) dessa fonte, através de espectroscopia de campo integral no infravermelho próximo ($\sim$ 1.1-2.4μm). Os dados foram obtidos com o instrumento SINFONI, anexado ao telescópio VLT e apresentam resolução espacial de 40-80 pc. A metodologia do trabalho consiste em realizar síntese de população estelar utilizando o código STARLIGHT e novas gerações de modelos de populações estelares. Como primeira parte do trabalho, testamos a confiabilidade dos modelos no intervalo espectral do infravermelho próximo. Depois disso, aplicamos a metodologia a NGC 4303, no intuito de estudar o histórico de formação estelar espacialmente resolvido nessa fonte. Encontramos que a distribuião das populações estelares apresenta uma variação espacial, sugerindo uma estratificação em idade. Três principais estruturas se destacam: Dois *blobs*, um composto por estrelas jovens ($t \leq 50\times10^6$anos) e outro composto por estrelas de idade intermediária (50×10^6anos $< t \leq 2\times10^9$anos), ambos deslocados do centro. A terceira é uma estrutura do tipo braço-espiral interno com estrelas de idade intermediária, circundando o *blob* de estrelas jovens. Nossos resultados indicam que a formação estelar ocorreu atrravés de múltiplos surtos de formação estelar nessa fonte. Além do mais, as populações estelares mais jovens (t $\lesssim$ 2 Gyr) estão distribuídas ao longo de um anel de formação estelar circumnuclear, com raio de r$\sim$250 pc. O anel apresenta taxas de formação estelar (SFRs) no intervalo de 0.002-0.14 $M_\odot$ano^{-1}, favorecendo o cenário de formação estelar chamado 'pearls-on-a-string'. A componente velha da população estelar ($t > 2\times10^9$anos), a qual atribuímos à população estelar do bojo, está distribuída fora dos dois *blobs* de idades mais jovens. Para a região nuclear (r$\sim$60 pc internos), derivamos um SFR de 0.43 $M_\odot$ano^{-1} e não encontramos nenhuma assinatura de contínuo não-térmico ou emissão de poeira quente, dando suporte ao cenário no qual um AGN de baixa luminosidade/LINER está obscurecido no centro de NGC 4303. Assim, nossos resultados revelam um cenário complexo de hstórico de formação estelar em NGC 4303, com diferentes componentes da população estelar coexistindo com um buraco negro de baixa eficiência de acreção no seu centro.

Conteúdo

Capítulo 1

Introdução

Um dos pontos fundamentais da astrofísica moderna é entender qual é a origem da fonte de energia responsável pelo contínuo e linhas de emissão observadas em galáxias com núcleo ativo (AGNs, do inglês *Active Galactic Nuclei*). O paradigma atual propõe que a acreção de material a um buraco negro super-massivo (SMBH, do inglês *Supermassive Black Hole*), localizado no centro da galáxia, é o mecanismo responsável pelos fenômenos observados nos AGNs. Além desta fonte central, estudos anteriores mostraram que regiões de intensa formação estelar são frequentemente detectadas nas regiões centrais de galáxias que hospedam um AGN (Mizutani et al., 1994, Imanishi & Dudley, 2000, Storchi-Bergmann et al., 2000, Imanishi, 2002, Rodríguez-Ardila & Viegas, 2003, Riffel et al., 2007, Dors et al., 2008). Neste cenário, buracos negros e intensa formação estelar coexistem na região nuclear das galáxias, o que vem motivando o estudo da conexão AGN-*starburst*.

1.1   Núcleos ativos de galáxias

O termo AGN se refere ao fenômeno energético que ocorre na região central de galáxias, o qual não pode ser explicado unicamente por processos físicos ocorridos no interior estelar. Considerados os objetos mais energéticos do Universo, os AGNs são encontrados em regiões compactas no centro de galáxias, apresentando luminosidades da ordem de L $\geq 10^{10}$L$\odot$ (Peterson, 1997, Beckmann & Shrader, 2012).

Carl Seyfert nos anos de 1940, foi um dos primeiros a encontrar evidências de que algumas galáxias apresentavam uma fonte adicional de energia na região central destes objetos. Ele obteve o espectro de seis galáxias, as quais apresentavam linhas de emissão de alta excitação sobrepostas a um espectro estelar típico (Seyfert, 1943), além de perceber a presença de linhas largas de emissão em algumas galáxias,

enquanto outras só apresentavam linhas estreitas. Por muitos anos se acreditou na hipótese de que essas linhas de emissão fossem produzidas por uma alta concentração de estrelas na região nuclear desses objetos. In 1959, Woltjer publicou que seria necessária uma massa de $10^8 M\odot$ para explicar a concentração da emissão nos 100 pc internos de galáxias (Woltjer, 1959).

Um notório avanço nesta área foi o surgimento da concepção de que no centro dessas galáxias se encontraria um objeto bastante massivo do tipo estelar, o qual emitiria radiação principalmente via processos de acreção de um disco de gás circundante (Hoyle & Fowler, 1963). Demoraria mais um ano para que a idéia de que um buraco negro seria a fonte responsável pela emissão nuclear nessas galáxias, ao invés de uma estrela supermassiva, fosse impulsionada (e.g. Salpeter, 1964). Na verdade, a concepção de que um SMBH estivesse presente no centro dos AGNs (Salpeter, 1964, Zel'dovich & Novikov, 1964, Lynden-Bell, 1969) e também no centro da nossa galáxia (Lynden-Bell & Rees, 1971) explicava não somente a grande quantidade de energia liberada através dos processos de acreção via liberação de energia gravitacional, como também solucionava o problema do pequeno tamanho da região emissora.

Ao longo dos anos, os avanços em instrumentação permitiram a observação de diversas classes de AGNs, cada uma apresentando suas particularidades. As principais características dos AGNs, em linhas gerais, são listadas abaixo (Peterson, 1997, Beckmann & Shrader, 2012):

- Uma das características mais notáveis, primeiramente observada nos AGNs foi a presença de linhas de emissão intensas e altamente alargadas, com larguras à meia altura (FWHM, do inglês *Full Width Half Maximum*) de até $1000 \, \mathrm{kms}^{-1}$;

- Os AGNs podem chegar a emitir até L $\sim 10^{15} \mathrm{L}\odot$, o que em alguns casos pode equivaler a cerca de 100 vezes a radiação de toda a galáxia hospedeira;

- Variabilidade no contínuo e nas linhas de emissão, observadas em todo o intervalo espectral da distribuição espectral de energia (SED, do inglês *Spectral Energy Distribution*). As escalas de tempo de variabilidade em geral são da ordem de meses ou anos, porém alguns AGNs mais luminosos podem apresentar variações de dias ou até mesmo minutos, em comprimentos de onda menores (raios-X e raios gama);

- Podem apresentar ejeção de material com altas velocidades na forma de jatos que se estendem desde 10^{-5} pc até $\sim$100 kpc.

Os AGNs podem ser classificados de diversas formas, uma delas esta relacionada com sua luminosidade e características espectrais: os quasares, classe dos AGNs mais luminosos, com luminosidade bolométrica entre 10^{44} e 10^{48} erg s^{-1}, as galáxias Seyfert, cuja luminosidade é da ordem de um fator de 100 menor que a dos quasares. Uma outra classe de galáxias são os LINERs (do inglês *Low-Ionization Nuclear Emission-Line Region*), cujo núcleo apresenta linhas de emissão de baixa ionização e são consideravelmente menos luminosos. Diferentemente dos demais AGNs, estes objetos ainda não tem sua fonte de energia bem entendida. O gás pode ser ionizado por um AGN luminoso, choques, formação estelar ou estrelas evoluídas e na fase de pós-AGBs (e.g. Cid Fernandes et al., 2005a, Ho et al., 1997, 2001, Heckman et al., 1997).

Um ponto fundamental no estudo dos AGNs consiste justamente na tentativa de unificar essas diferentes classes em um modelo comum (cuja fonte de energia fosse intrinsicamente a mesma), uma vez que estas compartilham características em comum. Antonucci & Miller (1985) propuseram um Modelo Unificado, no qual a radiação da fonte central seria proveniente do processo de acreção de matéria por um SMBH de massa M $\gtrsim 10^8$M$\odot$. Além disso os autores sugerem que tanto o SMBH como a região no entorno do disco de acreção, conhecida como região de linhas largas (BLR, do inglês *Broad Line Region*), estão envoltos por um toróide de poeira e que as diferentes classes de AGNs podem ser explicadas variando o ângulo de visada do observador.

Em resumo, o modelo unificado descrito por Antonucci (1993) previa que as linhas de emissão alargadas seriam produzidas na BLR por nuvens de gás de alta densidade ($n_e \sim 10^{11}$ cm^{-3}) com temperaturas de até 20000 K. Essas nuvens extremamente quentes e densas seriam responsáveis por dispersões de velocidade da ordem de 1-10$\times 10^3$kms^{-1}, estando distribuídas em uma região não resolvida (r < 1 pc) em volta do disco de acreção. Já as linhas de emissão estreitas seriam produzidas na chamada região de linhas estreitas (NLR, do inglês *Narrow Line Region*), a qual se estende até um raio de 1 kpc (diferentemente da compacta BLR) e apresenta densidades de $n_e \sim 10^3$ cm^{-3}. As linhas de emissão estreitas são originadas tanto por transições proibidas quanto permitidas e apresentam larguras de 200-1000 kms^{-1}. A classificação dos AGNs pelo Modelo Unificado pode se resumir em duas amplas classes de objetos:

- AGNs de tipo 1: ângulo de visada próximo ao eixo polar (*face-on*), visualizando diretamente a região central (BLR) e também a NLR.

- AGNs do tipo 2: se observa a estrutura toroidal em ângulos de visada próximos

ao plano equatorial do toróide (*edge-on*). Observa-se somente a NLR, uma vez que a BLR estaria obscurecida pelo toróide.

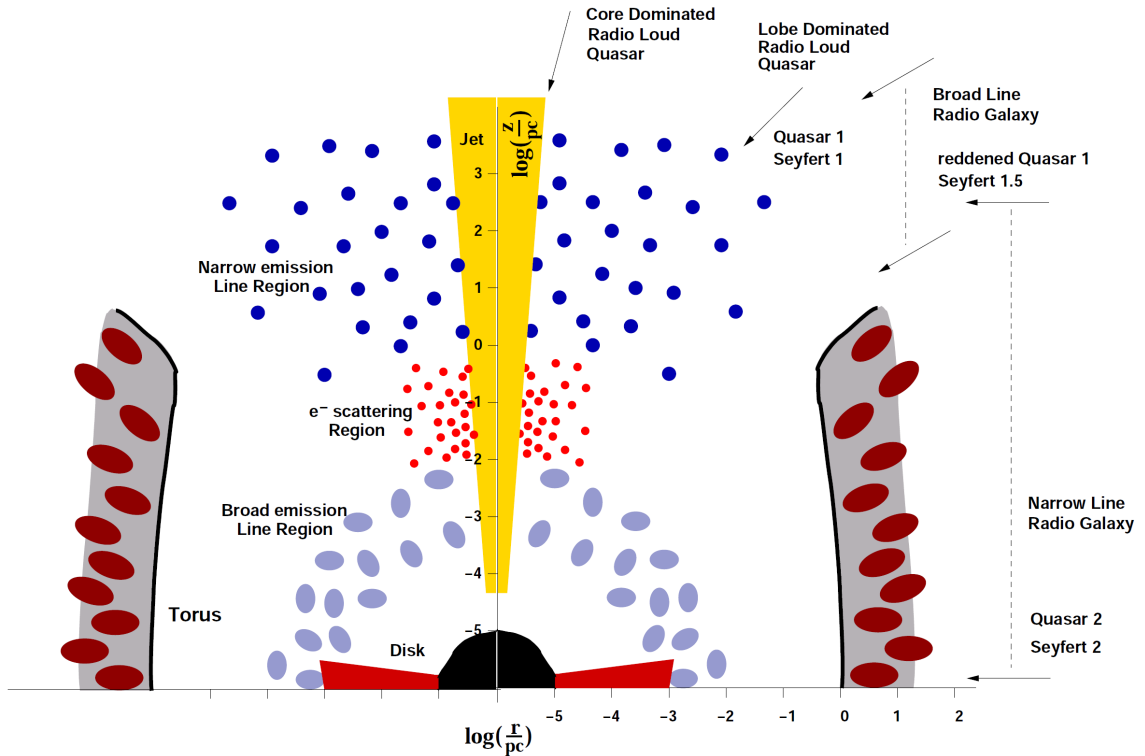Na Fig. 1.1, apresenta-se um esquema ilustrando as estruturas consideradas no modelo Unificado de AGNs.

Figura 1.1: Ilustração do modelo unificado de AGNs. As principais estruturas estruturas estão representadas com sua respectiva escala. Da região central à parte mais externa temos: o SMBH, o disco de acreção, a BLR, o toróide de poeira, a NLR e os jatos relativísticos. Figura retirada de Zier & Biermann (2002).

1.2 O AGN e a galáxia hospedeira

O AGN, como o nome já diz, não é uma estrutura isolada no espaço e se encontra no centro de galáxias. Este interage de muitas formas com o meio que o circunda: primeiramente através de acreção de matéria do disco ao SMBH, mas também através da emissão de radiação e partículas, as quais se propagam pelo meio em seu entorno. Na verdade, sabemos que algumas propriedades físicas do bojo das galáxias possuem relação com os núcleos ativos que abrigam, como por exemplo a conhecida relação $M_\bullet - \sigma$ (Ferrarese & Merritt, 2000), na qual é obser-

vada uma correspondência entre a massa do SMBH ($M_\bullet$) e a dispersão de velocidades das estrelas do bojo (σ).

A existência dessas correlações sugere que possa existir uma ligação causal entre a formação do bojo e do buraco negro central, ou até mesmo, que a evolução de ambos seja regulada por uma causa comum. A formação estelar circumnuclear, por exemplo, é um forte candidato a explicar a ligação entre esses dois fenômenos, uma vez que ambos dependem do escoamento de gás para as regiões mais internas da galáxia. Ainda que não seja uma propriedade comum a todos os AGNs, diversos estudos encontram formação estelar recente e/ou a presença de estrelas jovens em galáxias do tipo Seyfert (e.g. Cid Fernandes et al., 2001, Storchi-Bergmann et al., 2000, 2005, Davies et al., 2007, Mallmann et al., 2018).

Recentemente, Mallmann et al. (2018) estudaram as populações estelares espacialmente resolvidas de 62 AGNs observados com o MaNGA *survey* (Mapping Nearby Galaxies at Apache Point Observatory Bundy et al., 2015). Eles encontram uma maior fração de estrelas jovens (t $\lesssim 40 \times 10^6$ anos) nas regiões mais centrais (R $\leq$ 0.5Re) de AGNs luminosos (L[OIII] $\gtrsim 10^{41.25}$ ergs/s), quando comparado com a amostra de controle e frações similares de estrelas jovens dentro de 1 Re para AGNs de baixa luminosidade. Esses resultados sugerem que o gás que está escoando para as regiões mais centrais para alimentar o AGN, também está sendo usado para formar novas estrelas. Ainda, os autores encontram que a fração de estrelas de idade intermediária aumenta para maiores raios na galáxia e é maior em galáxias ativas, enquanto que as estrelas velhas dominam as regiões mais internas de ambas amostras de galáxias, ativas e não-ativas.

Kauffmann et al. (2003), analisaram a dependência entre a massa da galáxia hospedeira e o AGN em uma amostra de mais de 22 mil galáxias do *Sloan Sky Digital Survey*. Utilizando a linha de emissão de [OIII] como traçador de atividade nuclear, estes autores encontraram que todo AGN reside em galáxias massivas, porém não encontraram um indicativo de correlação entre a intensidade do AGN e a massa da galáxia hospedeira. Além do mais, concluíram que os AGNs de mais alta luminosidade são comumente encontrados em bojos com SPs jovens. Estudos sobre a luminosidade do AGN e a formação estelar em escalas de tempo cosmológicas sugerem que ambos experimentaram um pico em torno de $z \sim 2$ (e.g. Silverman et al., 2008). Ainda, Diamond-Stanic & Rieke (2012) e LaMassa et al. (2013) encontram correlações positivas entre a taxa de acreção do buraco negro (i,e., luminosidade do AGN) e as taxas de formação estelar (SFRs). No campo teórico, simulações hidrodinâmicas apresentam resultados similares (Hopkins & Quataert, 2010, Volonteri

et al., 2015), com uma correlação mais fraca para o SFR global.

No tocante á relação entre a taxa de acreção do buraco negro e a SFR, o ponto central está na perda de momento angular do gás. O mecanismo mais lógico seria o processo de fusão de galáxias ricas em gás, porém o número de galáxias com AGNs luminosos que não são perturbadas é grande em demasiado para esse processo ser considerado dominante. Outro processo que possibilita a transferência de momento angular, propiciando o escoamento de gás para as regiões mais internas é a presença de barras (Lynden-Bell & Kalnajs, 1972, Hernquist & Mihos, 1995). Independentemente do processo, temos que sempre ter em mente o fato de que os AGNs são objetos que apresentam variabilidade, desde escalas de dias (e.g. Schimoia et al., 2015) até 10^7 anos (e.g. Schawinski et al., 2015). Desta maneira, podemos acabar concluindo que os fenômenos (atividade nuclear e *starburst*) são independentes, caso estejamos limitados a um instante de inatividade do AGN.

O melhor entendimento da relação AGN-*starburst* é de suma importância também no ramo da cosmologia, uma vez que estes estudos podem fornecer subsídios para a compreensão da existência de SMBH a altos *redshifts*. Sabemos que buracos negros de até 10^{10} M$\odot$ são encontrados em z$\sim$6-7 (i.e., quando o Universo tinha menos de 1 bilhão de anos, Wu et al., 2015, Dors et al., 2018), justamente por meio da detecção de quasares. Estes objetos são considerados a versão mais energética de atividade nuclear (AGN) e a física que rege estas fontes seria correspondente a das galáxias Seyfert do Universo Local (z $\lesssim$ 0.03).

1.3 Populações Estelares

Como podemos ver acima, existem fortes indícios para uma possível relação entre a atividade nuclear e a formação estelar em galáxias. Deste modo, estudos de populações estelares espacialmente resolvidos da região nuclear destes objetos pode introduzir informações importantes acerca destes fenômenos.

Como o bojo das galáxias é composto principalmente por estrelas, gás (atômico, molecular e ionizado), poeira e uma fonte não-térmica no caso dos AGNs, a soma de todas estas componentes contribui para o espectro integrado da galáxia. Desta maneira, para determinar se a formação estelar circumnuclear e o AGN são fenômenos correlacionados, ou apenas acidentais, é de fundamental importância a correta caracterização do primeiro, uma vez que uma fração substancial da energia emitida por uma galáxia, desde o óptico até o infravermelho próximo (NIR, do inglês *Near-infrared*) é devido a estrelas.

A população estelar (SP) que domina a luz das galáxias na região ultravioleta e óptica vem sendo intensamente estudada nas últimas décadas. Estes estudos mostraram que a SP das galáxias apresenta grandes variações na idade e metalicidade (e.g. Bica & Alloin, 1986, Alloin et al., 1998, Bonatto et al., 1999, Schmitt et al., 1996, Raimann et al., 2000b,a, Rickes et al., 2004, Cid Fernandes et al., 2005a, Rembold & Pastoriza, 2007, Cid Fernandes et al., 2013, Sánchez-Blázquez et al., 2014, López Fernández et al., 2016, Goddard et al., 2016, Zheng et al., 2017, Goddard et al., 2017). Recentemente, avanços na compreensão das SPs que dominam a luz no NIR vem sendo feitas (e.g. Davies et al., 2007, Riffel et al., 2008a, 2010, 2011b, Storchi-Bergmann et al., 2012, Dametto et al., 2014, Schönell et al., 2016). Contudo, a detecção de características espectrais intrínsecas da região do NIR, no bojo de galáxias, que permitem a identificação e datação de SPs jovens é difícil.

Essa dificuldade está associada, principalmente, ao fato de que ainda não existem modelos de população estelar simples (SSP, do inglês *Simple Stellar Population*) completamente satisfatórios nesta região espectral. Um dos principais problemas está no fato de que a física por trás de alguns estágios evolutivos, como o dos pulsos térmicos do ramo assintótico das gigantes (TP-AGB, do inglês *Thermally Pulsing Asymptotic Giant Branch*) por exemplo, é pouco conhecida. Outro ponto importante está no fato de que alguns processos físicos envolvidos no estudo da evolução estelar (perda de massa, opacidades, *dredge-up*, entre outros) não são completamente entendidos, e além disso, os diferentes modelos de SSPs (Bruzual & Charlot, 2003, Maraston, 2005, Conroy et al., 2009) utilizam diferentes receitas para o tratamento desses processos. Dito isso, a escolha do modelo a ser utilizado para síntese de SP deve ser feita sempre levando em conta os problemas intrínsecos dos modelos.

Resultados pioneiros de síntese de SP no NIR (0.8 - $2.4\mu m$) sugerem que as SPs que dominam a luz no NIR e no óptico são diferentes (Riffel et al., 2008a, 2009a). Nesses trabalhos, foi utilizado o código STARLIGHT (Cid Fernandes et al., 2004, 2005b), no intervalo espectral entre $0.8\mu m$ e $2.4\mu m$, introduzindo uma nova componente – a poeira quente – como um elemento adicional da base de elementos. Componente, essa, que revelou-se necessária para o correto ajuste da SED de galáxias ativas no NIR (veja Figura 1.2 e Riffel et al., 2009a, 2010, Martins et al., 2010) e que foi associada à poeira próxima à temperatura de sublimação, localizada no toróide de poeira requerido pelo modelo unificado de AGNs (Antonucci & Miller, 1985, Antonucci, 1993).

Utilizando dados de espectroscopia de campo integral (IFS, do inglês *Integral Field Spectroscopy*), nosso grupo começou a caracterizar as SPs nos kiloparsecs centrais
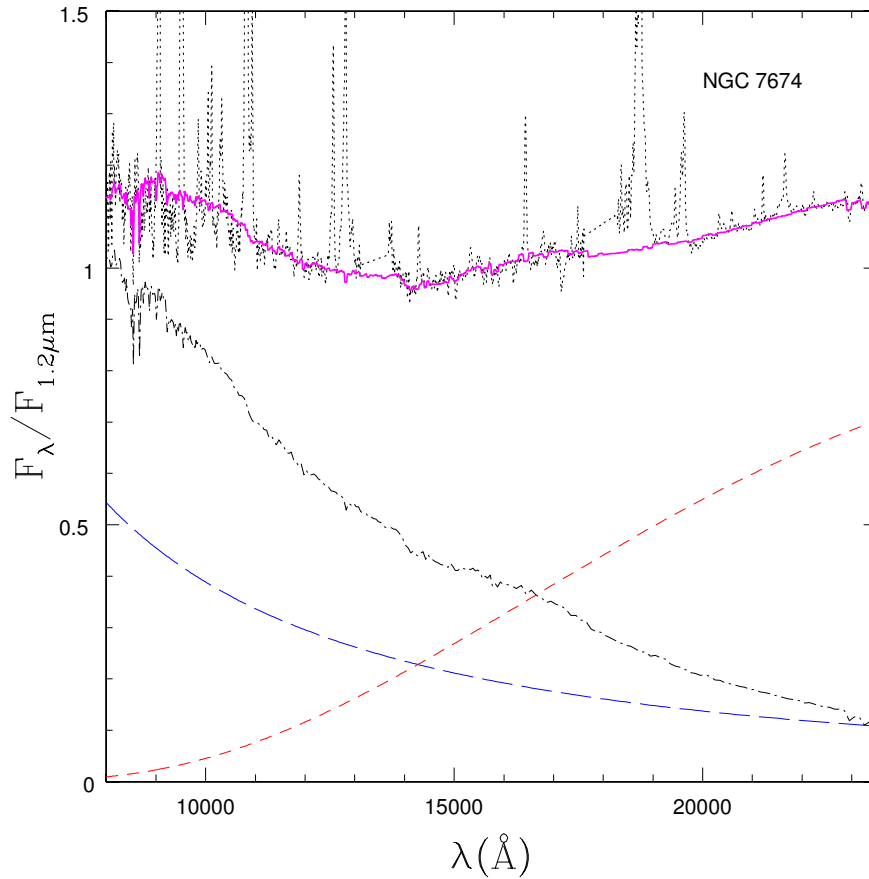
Figura 1.2: Três componentes do contínuo de NGC 7674 (Sy 2). A linha com ponto-tracejado representa a SP. A contribuição não térmica e a contribuição da poeira quente são representadas pelas linhas com tracejado longo e curto, respectivamente. A linha sólida é a soma das três componentes e a linha pontilhada representa o espectro observado (figura adaptada de Riffel et al., 2009a).

de uma amostra de Seyferts do Universo Local (Mrk 1066, Mrk 1157, NGC 1068 and NGC 5548). Para os $\sim$160 pc centrais de Mrk 1066 e Mrk 1157, Riffel et al. (2010) e Riffel et al. (2011b), respectivamente, encontraram um predomínio de estrelas velhas ($t \geq 5 \times 10^9$ anos), enquanto estrelas de idade intermediária ($0.3 \leq t \leq 0.7 \times 10^9$ anos) dominam a região circumnuclear nesses objetos. Os autores também encontram que estes anéis de SP de idade intermediária estão correlacionados com baixos valores de dispersão de velocidades ($\sigma_\star \sim 50\,\mathrm{km s^{-1}}$). Eles discutem que tal idade é consistente com um cenário de formação desses anéis de baixa dispersão ($\sigma_\star$), no qual um evento passado causou um escoamento de gás para as regiões mais internas, formando estrelas, as quais ainda mantém a cinemática fria, característica do gás do qual se formaram.

Storchi-Bergmann et al. (2012) encontrou dois episódios de formação estelar recente em NGC 1068: o primeiro que teria ocorrido a 300×10^6 anos, estendendo-se pelos 300 pc centrais da galáxia, e um segundo que teria ocorrido a somente 30×10^6 anos em um estrutura do tipo anel à ~100 pc do núcleo (veja a Fig. 1.3), coincidindo com um anel de emissão de H_2 quente em expansão. Ainda, em concordância com os resultados encontrados para Mrk 1066 and Mrk 1157, Schönell et al. (2016) encontraram que a componente de idade intermediária da SP domina nos 160 pc internos de NGC 5548, enquanto a componente de idade mais velha ($> 2 \times 10^9$ anos) é predominante na região entre 160-300 pc. Poeira em emissão foi detectada em três objetos (Mrk 1066, NGC 1068 e NGC 5548), representando de 30 a 90% do fluxo na banda K (para a região nuclear), enquanto uma componente do contínuo sem características (FC, do inglês *featureless continuum*), associada à emissão do AGN, foi detectada em duas fontes, contribuindo com ~25% do fluxo da região nuclear na banda K em NGC 1068 e ~60% em NGC 5548.
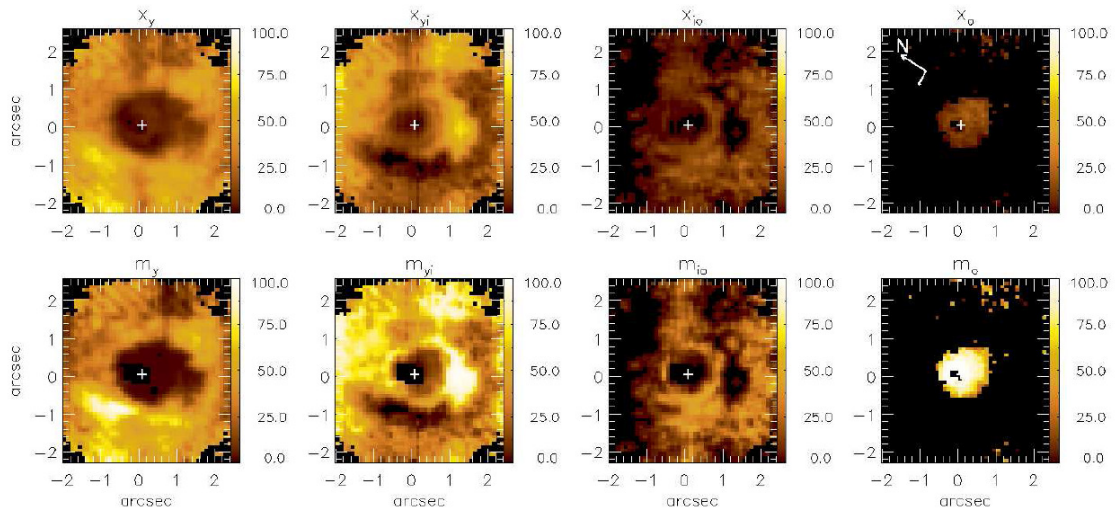

Figura 1.3: *Topo:* distribuições espaciais da contribuição percentual (pesada em fluxo) de cada componente da SP ao fluxo em λ=2.1μm para NGC 1068. Da *esquerda* para *direita*: jovem ($\leq 100 \times 10^6$ anos), jovem-à-intermediária (0.3 - 0.7 $\times 10^9$ anos), intermediária-à-velha (1 - 2 $\times 10^9$ anos) e velha (5 - 13 $\times 10^9$ anos). *Base:* distribuição espacial das contribuições pesadas em massa para cada componente da SP. Figura retirada de Storchi-Bergmann et al. (2012).

Existem inúmeras razões para estudar a SP que domina a luz das galáxias na região do NIR. Esta faixa espectral, por exemplo, é certamente a mais apropriada para estudar a SP de fontes muito obscurecidas como as regiões circumnucleares de AGNs e as galáxias infravermelhas ultraluminosas. Vale a pena ressaltar que o *James Webb Space Telescope* (JWST) vai ser otimizado para observações no in-

fravermelho. Deste modo, é importante testar o potencial da síntese de SPs neste intervalo espectral. Apesar dos recentes esforços para entender as SPs no NIR, questões fundamentais ainda permanecem em aberto:

1. Como é a variação espacial da SP nas galáxias ativas do tipo Seyfert?

2. Qual o efeito do AGN sobre a formação estelar?

3. Existe alguma conexão AGN-*starburst* que possa ser detectada no NIR?

1.4   Galáxias Starburst

Como o objetivo da presente tese é estudar o efeito da formação estelar em galáxias que hospedam um AGN, faz-se necessário comparar as taxas de formação estelar derivadas em galáxias que tenham intensa formação estelar, porém não hospedem um AGN. Essa mesma amostra pode ser utilizada para testar o método, pois o espectro não sofre com os efeitos do AGN, permitindo assim um estudo de conteúdo estelar 'puro'. Nesse sentido, escolhemos um conjunto de galáxias *Starburst*. Objetos estes que foram descobertos por Morgan (1958), que identificou estruturas peculiares (*Hot Spots*) na região nuclear de algumas galáxias.

Posteriormente, Sérsic & Pastoriza (1965) mostraram que existe uma relação entre o núcleo dessas galáxias e seu respectivo tipo morfológico. Em estudos subsequentes, Pastoriza (1967, 1975) demonstrou que essas galáxias, as quais vieram a ser chamadas de galáxias Sérsic-Pastoriza (Osmer et al., 1974), tinham características bastante similares às de regiões H ii (ou seja, regiões compostas por gás ionizado por estrelas quentes do tipo O e B, associadas com regiões de formação estelar recente). A partir destes resultados pioneiros, seguiram-se inúmeros estudos na tentativa de compreender melhor a natureza desses objetos.
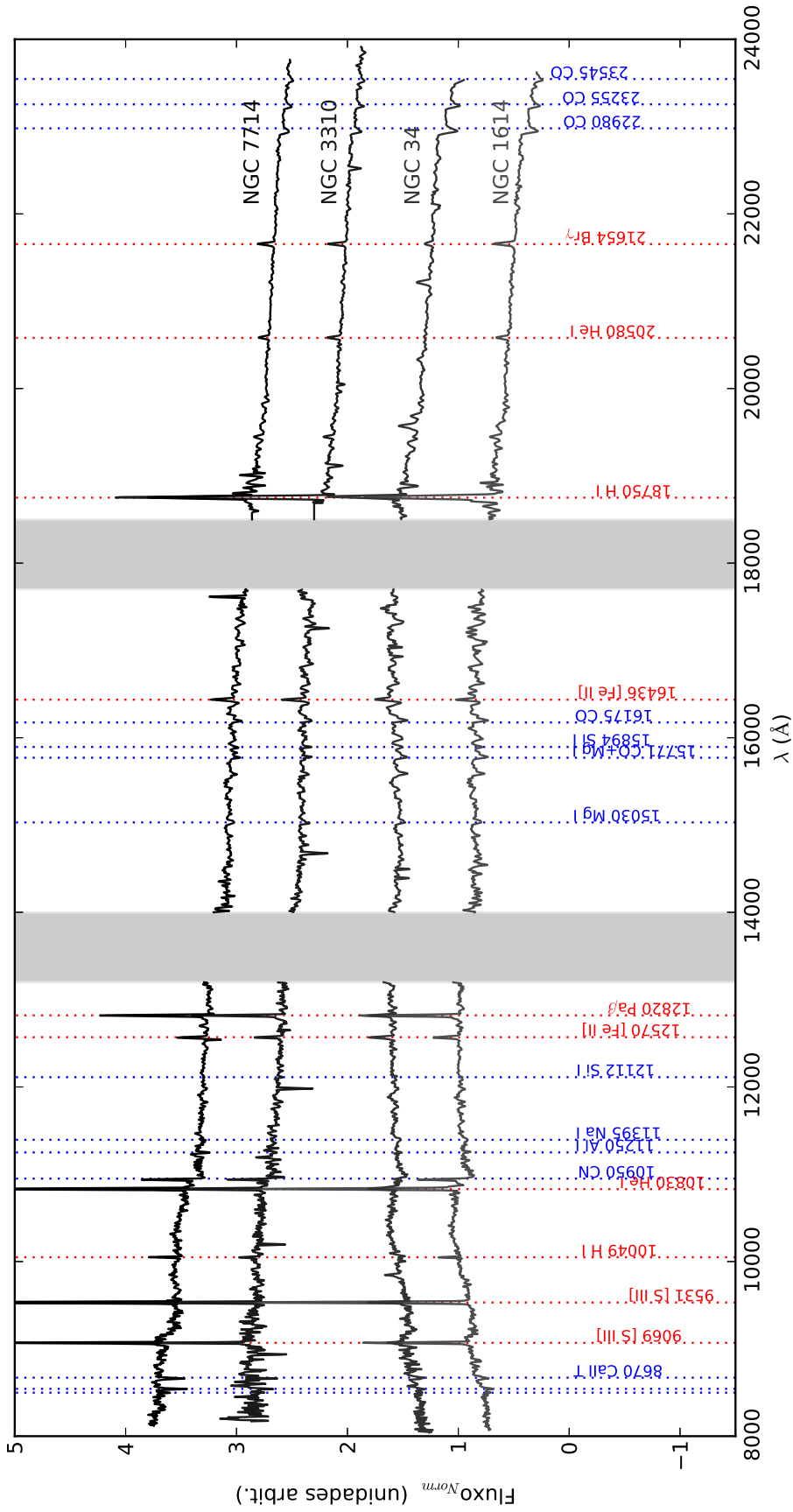
Figura 1.4: Espectros normalizados ($\lambda = 12280$Å) do núcleo das galáxias, ordenados de acordo com os seus formatos, do mais inclinado (*topo*) ao mais plano (*base*). Algumas linhas de absorção (*azul*) e emissão (*vermelho*) estão identificadas. As regiões de absorção telúrica estão marcadas na área sombreada.arrumar legenda explicando as galáxias

Definem-se como galáxias *Starburst* os objetos cuja energia emitida é dominada pela emissão de estrelas jovens e massivas (tipo O e B, Weedman, 1983). Essas fontes apresentam intensa formação estelar, geralmente na região central (r $\lesssim 1\,$kpc). Suas taxas de formação estelar (SFRs, do inglês *Star Formation Rates*) variam de 5 a $50\mathrm{M}_\odot\mathrm{yr}^{-1}$, dentro de uma região que se estende de 0.1 a 1 kpc do núcleo. Esses valores excedem em $\sim 10^3$ vezes os encontrados para uma região similar em galáxias normais (Heckman, 2000). Por exemplo, Güsten (1989) encontra um SFR de $0.5\mathrm{M}_\odot\mathrm{yr}^{-1}$ dentro de $\sim$100 pc no centro Galáctico. Além disso, o espectro desses objetos é caracterizado por linhas de emissão bastante intensas, como as linhas de recombinação do hidrogênio e hélio e linhas de transições proibidas do enxofre, oxigênio e nitrogênio (ver Fig. 1.4). Essas linhas são características de galáxias espirais, principalmente por estas apresentarem grandes quantidades de gás.

As galáxias do tipo *Starburst* estão entre os melhores laboratórios para se estudar a formação e evolução de estrelas massivas, o efeito destas no meio interestelar, assim como os processos físicos envolvidos na formação de galáxias e no enriquecimento do meio intergaláctico, o que as torna objetos ideais para serem usados como comparativos das taxas de formação estelar encontradas nas regiões circumnucleares de AGNs.

1.5 Motivação e Objetivos

Atualmente, existem muitas evidências observacionais indicando que, tanto o núcleo ativo, quanto a formação estelar, podem estar associados com escoamento de gás em direção ao centro da galáxia (Shlosman et al., 1989, 1990, Maiolino et al., 1997, Knapen et al., 2000, Fathi et al., 2006, Riffel et al., 2008b), dando suporte a conexão AGN-*starburst* (e.g. Norman & Scoville, 1988, Terlevich et al., 1990, Heckman et al., 1997, González Delgado et al., 1998, Ferrarese & Merritt, 2000, Heckman, 2004, Riffel et al., 2008b). Por outro lado, há os que defendem a hipótese de que a conexão AGN-*starburst* possa ser casual, pois muitas Seyfert não mostram evidência de atividade *starburst* (e.g. Filippenko et al., 1993), e estudos espectroscópicos na região óptica de grandes amostras de objetos não indicam que a formação estelar é mais comum em galáxias Seyfert do que em galáxias normais (Pogge, 1989).

Do ponto de vista teórico, ambos os cenários são suportados (Kawakatu & Wada, 2008, Vollmer et al., 2008). Davies et al. (2007), por exemplo, argumentou que somente após as fases turbulentas iniciais do *feedback* estelar é que o gás consegue ser acretado de forma eficiente a escalas menores. Mesmo que observações de alguns

AGNs do Universo local sejam consistentes com esse cenário, os resultados ainda são controversos, como relatado em Riffel et al. (2010, veja na Sec. 1.3) a formação estelar recente está ocorrendo em um anel com raio de $\sim 200\,pc$ na galáxia Mrk 1066 (resultados similares são encontrados por estes autores também para Mrk 1157 e NGC 1068), ao invés de estar ocorrendo diretamente no núcleo. Por outro lado, o cenário de acreção de material estelar ejetado a escalas menores foi proposto em diferentes situações, como por exemplo o caso do Centro Galático (Cuadra et al., 2006), em aglomerados estelares (Cuadra et al., 2006) e também do centro de M 31 (Chang et al., 2007). Neste contexto, o estudo detalhado das SPs espacialmente resolvidas na região central de galáxias é de extrema importância para testar se ventos estelares pós-*starburst* tem um papel decisivo na alimentação do AGN.

Pelo exposto acima fica claro que ainda não existe um consenso sobre se a alimentação do AGN (ao SMBH) ocorre concomitantemente com a formação estelar ou se seria posterior a ela, ocorrendo durante uma fase pós-*starburst*. Contudo, um avanço importante no entendimento do papel do conteúdo estelar no entorno de AGNs pode ser feito por um teste simples: testar se SPs jovens ou intermediárias são encontradas na região circumnuclear de AGNs de diferentes classes e comparar os resultados com os obtidos para galáxias de controle, como por exemplo uma galáxia *Starburst*. Neste contexto, se a região central for dominada por SP jovens, a alimentação do AGN é concomitante à formação estelar. Se encontrarmos um predomínio de populações intermediárias, por exemplo, a alimentação se dará por meio de material ejetado (ventos) por estrelas pós-*starburst*, ou seja, a fase de atividade do AGN é posterior a formação estelar. Por final, encontrando-se um predomínio de SPs velhas implicaria no fato de que o escoamento de gás para a região central é eficiente e a formação estelar não ocorre neste processo.

Felizmente, com o advento das unidades de campo integral (IFUs, do inglês *Integral Field Unit*) associadas à óptica adaptativa, tornou-se possível o estudo detalhado da região central de AGNs, especialmente na região do NIR. Isso, associado ao fato do NIR permitir o estudo de regiões altamente obscurecidas e de ser o intervalo espectral propício para a detecção de assinaturas de estrelas massivas e evoluídas (em fases como o *Red Giant Branch* e o TP-AGB), torna esse intervalo espectral o mais atraente para esse tipo de estudo (Oliva et al., 1995, Maraston, 2005, Riffel et al., 2007, 2008a, 2015).

Com o que foi dito acima em mente, combinado ao fato de não termos uma amostra completa, propomos aqui um estudo de caso. Neste trabalho, realizaremos

um estudo das SPs espacialmente resolvidas em uma galáxia protótipo: NGC 4303[1], cujas principais características seguem abaixo:

- Essa fonte tem uma classificação ambígua de LINER/Seyfert 2, se encontra à 16.1 Mpc e apresenta um AGN de baixa luminosidade (LLAGN, do inglês *Low Luminosity AGN*).

- A atividade central de NGC 4303 é singular:

  - Apresenta uma barra secundária;

  - Intensa emissão UV;

  - Super aglomerado estelar (SSC, do inglês *super-star cluster*) coexistindo com um AGN de baixa eficiência de acreção;

- Essa galáxia já foi amplamente estudada em diferentes intervalos espectrais (e.g. Colina et al., 1997, Colina & Wada, 2000, Colina et al., 2002, Jiménez-Bailón et al., 2003). Apresentamos os resultados da SP espacialmente resolvida no capítulo 3;

---

[1]Essa galáxias faz parte de uma amostra de 30 AGNs (a amostra ainda não foi completamente observada), a qual nosso grupo pretende realizar estudos sobre as SPs, a cinemática e dinâmica do gás e das estrelas.

Capítulo 2

Método de Síntese de População Estelar

Tendo em vista que grandezas físicas globais, como idade e metalicidade, não podem ser extraídas diretamente do espectro integrado de SPs de galáxias, desenvolveram-se ao longo do tempo métodos comparativos, também conhecidos como método de síntese de SP. Tal processo consiste na combinação de diversos espectros de SSPs, cujas propriedades são bem conhecidas, para formar o espectro da população de interesse e, com isso, inferir suas propriedades físicas. Uma SSP é um grupo de estrelas de mesma idade e composição química (Renzini, 1981).

Existem, basicamente, dois métodos utilizados para fazer síntese de SPs em espectros de galáxias a partir da combinação de SSPs. A diferença entre esses dois métodos está, essencialmente, no modo como as SSPs são obtidas e/ou calculadas. O primeiro método consiste na construção de uma biblioteca de SSPs empíricas, através da obtenção do espectro integrado de aglomerados, com idade e metalicidade conhecidas. Bica & Alloin (1986) implementaram esse método na região do óptico, observando 63 aglomerados de estrelas da Via Láctea e das Nuvens de Magalhães, com idades entre $10^6 \leq t \leq 1.65 \times 10^{10}$ anos e metalicidades entre $-2.1 \leq [Z/Z_\odot] \leq 0.1$. A principal vantagem desse método é ser livre de limitações da teoria de evolução estelar, assim como suposições sobre a função inicial de massa (IMF, do inglês *Initial Mass Function*). Um problema, entretanto, é que as bibliotecas empíricas são limitadas às propriedades dos aglomerados próximos.

O segundo método é conhecido como síntese evolutiva de população estelar (EPS, do inglês *Evolutionar Population Synthesis* - e.g., Bruzual & Charlot, 2003, Maraston, 2005, Conroy et al., 2009, daqui em diante: BC03, M05 e C09). Nesse método, o conteúdo estelar dos aglomerados para as diferentes idades e metalicidades é mo-

delado de forma teórica através do conhecimento de evolução estelar, posteriormente combinando-se os espectros estelares teóricos e/ou empíricos para produzir o espectro integrado da SSP. Os trabalhos pioneiros nessa abordagem foram Tinsley (1972) e Tinsley & Gunn (1976). Existem duas técnicas para o cálculo do modelo da SSP, as quais diferem-se pela variável de integração adotada no cálculo da evolução: aqueles que utilizam uma grade de isócronas e integram observáveis em função da massa em cada estágio evolutivo (e.g. Charlot & Bruzual, 1991, Kotulla et al., 2009); e aqueles que utilizam o teorema do consumo de combustível, cuja variável de integração seria esse combustível, i.e. a quantidade de hidrogênio e/ou hélio que é consumida através da queima nuclear para as fases além da sequência principal (e.g. M05, Maraston & Strömbäck, 2011).

Dito isso, passemos para os dois principais ingredientes da síntese de SP: a base de elementos (um conjunto de modelos de SSPs) e o código utilizado para fazer a mistura das SSPs.

2.1 A Base de Populações Estelares Simples

O objetivo da síntese de SP é quantificar a contribuição de cada SP ao espectro integrado da galáxia. Para isso, o código mistura as SSPs que compõem a base de elementos até ajustar o espectro da fonte. Assim, um conjunto ideal de elementos para compor a base deveria cobrir o intervalo de propriedades espectrais observadas na amostra de galáxias, propiciando resolução suficiente em idade e metalicidade para ajustar, da melhor forma possível, o espectro observado (Cid Fernandes et al., 2005a). Em outras palavras, um conjunto confiável seria uma biblioteca de espectros integrados de aglomerados de estrelas (i.e., eles dependem somente das idades e metalicidades das estrelas e são livres de qualquer suposição com relação à evolução estelar e IMF, Bica & Alloin, 1986, Riffel et al., 2011c). Entretanto, até agora, não existe nenhuma biblioteca desse tipo disponível para o intervalo espectral do NIR. Assim, o uso de uma base de elementos composta por SSPs teóricas, cobrindo esse intervalo espectral, tem se tornado uma abordagem bastante comum (Riffel et al., 2009a, 2010, 2011b, Storchi-Bergmann et al., 2012, Martins et al., 2010, 2013b, Dametto et al., 2014).

Tendo em vista que o NIR carrega assinaturas de estrelas evoluídas (e.g. Riffel et al., 2007, Ramos Almeida et al., 2009, Martins et al., 2013b) e que isso é crucial para modelar o espectro em absorção de galáxias nesse intervalo espectral, nós utilizamos os modelos EPS de M05. Estes modelos incluem espectros empíricos de

estrelas ricas em carbono e oxigênio (Lançon & Wood, 2000) e com isso, são capazes de prever essas assinaturas, tal como a banda de CN em 1.1μm (Riffel et al., 2007, 2008a, 2009a, Martins et al., 2013b). A detecção dessa banda no espectro da galáxia é considerada como uma forte evidência da presença de estrelas de idade jovem à intermediária. Esses modelos vêm sendo utilizados pelo nosso grupo ao longo dos anos para o estudo das SPs em AGNs (Riffel et al., 2007, 2009a, 2010, Martins et al., 2010, Riffel et al., 2011b, Storchi-Bergmann et al., 2012) e em SBs/*star-forming* (Riffel et al., 2008a, Martins et al., 2013b, Dametto et al., 2014). Neste trabalho também testamos outros dois modelos de SSPs bastante utilizados na literatura: BC03 e C09. As principais características dos diferentes modelos são apresentadas abaixo.

2.1.1 M05

A versão original dos modelos EPS de Maraston é Maraston (1998), a qual é baseada no teorema do consumo de combustível (Renzini, 1981), conforme mencionado acima. O código foi atualizado em M05 [1], no qual o teorema do consumo de combustível é estendido para calcular modelos de idades jovens e intermediárias ($>30 \times 10^6$anos). Além disso, na versão de 2005 foi incluído de forma semi-empírica e bem calibrada a fase evolutiva das TP-AGBs, assim como foram calculadas cores realísticas para as SPs de idade intermediária ($\lesssim 2 \times 10^9$anos).

Os modelos de M05 (espectros em *cinza* na Figura 2.1) cobrem um intervalo de idades de 0.001 M a 15×10^9 anos, de acordo com uma grade de 67 modelos para 6 metalicidades diferentes ($0.005 \leq$ Z/Z$\odot \leq 3.5$)[2], 2 IMFs (do inglês *initial Mass Function*): Salpeter e Kroupa (Salpeter, 1955, Kroupa, 2001, respectivamente) e 3 morfologias para o ramo horizontal (HB, do inglês *Horizontal Branch* - vermelha, intermediária e azul - para mais detalhes, veja M05). Vale ressaltar que os modelos com Z=0.005Z$_\odot$ e Z=3.5Z$_\odot$, são disponibilizados somente para idades maiores do que 1×10^9 anos (em uma grade de 16 modelos), portanto, eles não foram incluídos na base. Esse subconjunto de modelos foi produzido com as isócronas de Cassisi (Cassisi et al., 1997a,b) e Padova 2000 (Girardi et al., 2000). As 4 metalicidades restantes (calculadas com a grade de 67 idades) são associadas aos caminhos evolutivos de Cassisi + Geneva (Schaller et al., 1992). Os espectros estelares utilizados são os da

---

[1]Disponível em http://www-astro.physics.ox.ac.uk/~maraston/Claudia's_ Stellar_ Population_ Models.html

[2]Note que estamos usando as metalicidades relativas à metalicidade do Sol, cujo valor é $Z_\odot = 0.02$ nesses modelos.

biblioteca estelar BaSeL 2.2 (Lejeune et al., 1997, 1998), a qual cobre o intervalo espectral de 91Å-160μm, com uma resolução espectral de 5-10 Å até a região do óptico e de 20-100 Å no NIR e infravermelho distante.

BaSeL 2.2 é uma biblioteca estelar de baixa resolução espectral, cujos espectros estelares foram compilados de forma teórica por Lejeune et al. (1997, 1998). Essa biblioteca é amplamente usada em estudos de síntese de SP e foi construída a partir da junção de espectros de modelos de atmosferas de (Kurucz (1995) - *comunicação privada*, Bessell et al., 1989, 1991), com modelos de atmosferas para estrelas frias (Fluks et al., 1994). Como essa biblioteca não contém estrelas ricas em carbono e oxigênio (fase das TP-AGBs), Maraston incluiu os espectros empíricos de Lançon & Mouhcine (2002).

2.1.2 BC03

GALAXEV[3] é um modelo EPS amplamente utilizado, o qual foi calculado com o código de síntese de isócronas de Bruzual & Charlot (2003,, também conhecido como BC03). Esses modelos estão divididos em 221 espectros irregularmente espaçados em espaços temporais de 0-20 $\times 10^9$anos, para uma grade ampla de metalicidades (0.005 $\leq$ Z/Z$\odot$ $\leq$ 2.5). Ainda, os modelos utilizam basicamente as bibliotecas estelares de BaSeL 3.1 + (Lejeune et al., 1997, 1998, Westera et al., 2002) STELIB (Le Borgne et al., 2003), cobrindo o intervalo espectral de 91Å-160μm, com resolução espectral de 3 Å (STELIB) no óptico (entre 3200-9500 Å), e 20-100 Å (BaSeL 3.1) para os comprimentos de onda restantes. Os autores também disponibilizam modelos calculados a partir das bibliotecas STELIB/Pickles (Pickles, 1998).

São oferecidas duas opções de IMF: Salpeter e Chabrier (Chabrier, 2003). e 3 opções devido caminhos evolutivos: Geneva, Padova 1994 (Alongi et al., 1993, Bressan et al., 1993, Fagotto et al., 1994a,b, Girardi et al., 1996) e Padova 2000. Estes modelos não incluem a fase das TP-AGBs.

2.1.3 C09

O código FSPS[4] (do inglês *'Flexible' Stellar Population Synthesis*) combina cálculos de evolução estelar com bibliotecas espectrais estelares no intuito de produzir modelos de SSPs. A característica singular desse código é que ele integra de forma flexível os ingredientes de síntese de SP, permitindo que o usuário escolha o con-

---

[3]Disponível em http://www2.iap.fr/users/charlot/bc2003/
[4]http://scholar.harvard.edu/cconroy/sps-models

junto de isócronas e biblioteca estelar, por exemplo. Ainda, o código contém um número de parâmetros, os quais controlam o peso de certas fases evolutivas estelares, como a fase das TP-AGBs, a morfologia do HB e estrelas *blue stragglers*. Assim como M05, esse modelo inclui espectros empíricos de estrelas na fase das TP-AGBs de Lançon & Mouhcine (2002).

As SSPs geradas abrangem o intervalo de idades de 0.3×10^6 a 14×10^9 anos, divididos em 188 modelos para 22 metalicidades diferentes ($0.01 \leq$ Z/Z$\odot \leq 1.5$). Os modelos são baseados nos caminhos evolutivos de Padova (Marigo & Girardi, 2007, Marigo et al., 2008), com 3 opções de IMF (Salpeter, Kroupa and Chabrier) e utilizam a biblioteca estelar de BaSeL 3.1, a qual cobre um intervalo espectral de 91Å-160μm, com resolução espectral de 20 Å no óptico e 20-100 Å no NIR.

2.1.4 Montando a base de SSPs

Como pequenas diferenças na SP são insignificantes em dados reais (i.e. elas são diluídas pelo ruído em dados observados, Cid Fernandes et al., 2004), seguindo Dametto et al. (2014), nós decidimos incluir somente os espectros de SSPs representativos (i.e. somente aqueles que apresentam diferenças significativas com relação ao espectro subsequente) na base de elementos, no intuito de evitar informações redundantes e degenerescências (veja, por exemplo, Schmidt et al., 1991). Para escolhermos quais espectros iriam compor a base, calculamos o módulo da diferença entre duas SSPs consecutivas (normalizadas em fluxo em 1.2225μm) em idade (t), dividido pelo número de pixeis (N), ou seja, resolvendo a equação:

$$Idades_{dif} = \frac{1}{N} \sum_{\lambda} |F_\lambda(t_i) - F_\lambda(t_{i+1})|. \tag{2.1}$$

Os mesmos procedimentos forma aplicados para as 3 bases de SSPs. Um exemplo do resultado desse processo, para metalicidade solar, é mostrado na Figura 2.1. As SSPs representativas (que constituem a base de elementos) estão marcadas com uma estrela e são traçadas em *azul*, conforme mostra a Figura 2.1. Note que esse procedimento foi feito somente para o intervalo espectral de 8000Å a 2.45μm, para quatro metalicidades, com todas as idades disponíveis. O conjunto final compreende 31 idades (t=0.0010, 0.0030, 0.0035, 0.0040, 0.0050, 0.0055, 0.0060, 0.0065, 0.0070, 0.0075, 0.0080, 0.0085, 0.0090, 0.010, 0.015, 0.020, 0.025, 0.030, 0.050, 0.080, 0.2, 0.3, 0.4, 0.5, 0.7, 0.8, 1.0, 1.5, 2.0, 3.0, 13.0 $\times 10^9$ anos) e quatro metalicidades (Z= 0.02, 0.5, 1 e 2 $Z_\odot$), resultando em uma base de elementos composta por 124 SSPs.
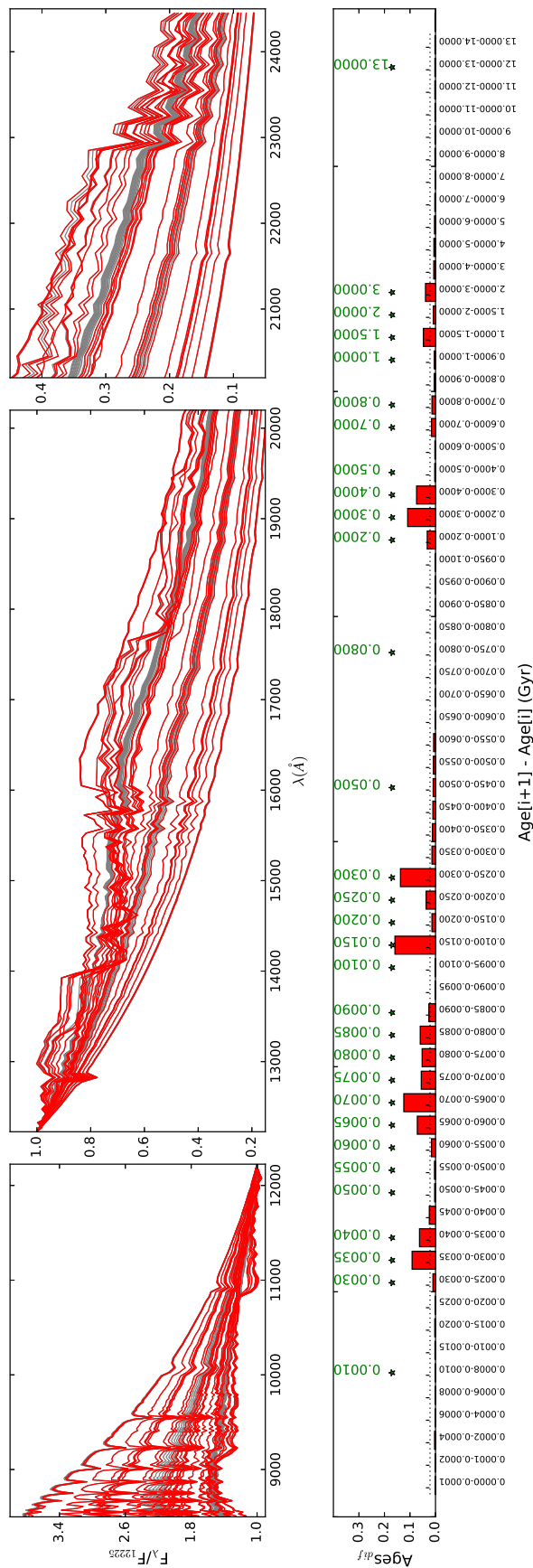
Figura 2.1: Todas as 67 SSPs de M05 para Z=$Z_\odot$ são mostradas em (*cinza*) no painel superior, juntamente com as 31 SSPs selecionadas (*vermelho*) para compor a base de elementos para essa metalicidade (normalizadas em fluxo em 1.2225μm). No painel inferior, mostramos a diferença quadrática de duas SSPs com idades consecutivas. Os modelos representativos escolhidos para compor a base de elementos estão marcados com uma estrela e desenhados em *vermelho* no painel superior. O painel superior está dividido em 3 intervalos de comprimento de onda para melhor visualização.

É importante chamar a atenção para o fato de que a resolução espectral dos modelos de M05, no NIR (R $\leq$ 250), é significativamente mais baixa que a dos espectros observados da amostra (R $\sim$2000) e varia com o comprimento de onda ($\Delta\lambda$=20Å na banda J, $\Delta\lambda$=50Å na banda H e $\Delta\lambda$=100Å na banda K). Por essa razão, degradamos os espectros observados à resolução dos modelos, convoluíndo-os com uma gaussiana.

2.2 O Código: STARLIGHT

Uma vez que a base de elementos foi definida, o outro ingrediente chave para síntese de SP é o código, o qual vai misturar as componentes individuais da base (as SSPs) para ajustar o espectro observado. Neste trabalho, utilizamos o código STARLIGHT (Cid Fernandes et al., 2004, 2005b, Mateus et al., 2006, Asari et al., 2007), o qual combina técnicas computacionais originalmente desenvolvidas para síntese empírica de SP com ingredientes dos modelos EPS. Resumidamente, o código ajusta o espectro observado O_λ com uma combinação, em diferentes proporções, das SSPs que compõem a base de elementos ($b_{j,\lambda}$), tiradas dos modelos EPS. Uma característica importante desse código é que ele ajusta o espectro inteiro, de 8000Å a 2.4μm, excluindo as linhas de emissão e dados espúrios (e.g. raios cósmicos, ruído e regiões das bandas telúricas), que são mascarados ou removidos do ajuste (veja mais detalhes a seguir).

A extinção do fluxo devido à poeira é modelada pelo STARLIGHT assumindo uma distribuição uniforme da poeira na linha de visada. O código nos permite escolher a lei de extinção a ser utilizada no ajuste. Optamos pela Lei de Calzetti et al. (2000), pois essa é a mais adequada para o cálculo do avermelhamento em galáxias com formação estelar recente. Como a nossa cobertura espectral vai até $\sim$ 2.4μm, optamos pela Lei de Calzetti implementada pelo código *hyperz*[5] (Bolzonella et al., 2000), o qual calcula a Lei de Calzetti para comprimentos de onda maiores ($\lambda >$ 2.2μm) do que em Calzetti et al. (2000).

A dispersão de velocidades é um parâmetro livre para o STARLIGHT, o qual alarga cinematicamente as SSPs, a fim de melhor ajustar as linhas de absorção do espectro observado. Os resultados desse passo, contudo, não são relevantes no nosso caso, uma vez que a resolução dos modelos é muito baixa.

Essencialmente, o código resolve a seguinte equação para um espectro modelo

---

[5]O *hyperz* é um código público que calcula *redshifts* fotométricos, via ajuste da distribuição espectral de energia (SED, do inglês *Spectral Energy Distribution*) da fonte.

M_λ (Cid Fernandes et al., 2005a):

$$M_\lambda = M_{\lambda_0} \left[\sum_{j=1}^{N_\star} x_j \, b_{j,\lambda} r_\lambda \right] \otimes G(v_\star, \sigma_\star), \tag{2.2}$$

na qual M_{λ_0} é o fluxo sintético no comprimento de onda de normalização ($\lambda_0 = 2.067\mu m$); x_j é a contribuição da j-ésima componente do vetor de SP da base de elementos; $b_{j,\lambda} r_\lambda$ é o espectro avermelhado da j-ésima SSP normalizada em λ_0, sendo $r_\lambda = 10^{-0.4(A_\lambda - A_{\lambda_0})}$ o termo de extinção; $\otimes$ denota o operador convolução e $G(v_\star, \sigma_\star)$ é a distribuição gaussiana usada para modelar os movimentos estelares na linha de visada, centrados em uma velocidade $v_\star$, com dispersão $\sigma_\star$. Nós escolhemos $\lambda_0 = 2.067\mu$m como comprimento de onda de normalização, uma vez que esta região é livre de linhas de emissão e absorção (Riffel et al., 2008a). O STARLIGHT normaliza todos os espectros da base por F_{λ_0}. Já o espectro observado é normalizado pelo fluxo mediano medido em uma janela de 80Å, no caso deste trabalho, centrada em λ_0, definida de maneira a evitar os efeitos de um pixel ruim (ruído, raios cósmicos etc.) em λ_0 no espectro observado. Finalmente, o código investiga o espaço de combinações lineares entre os espectros da base, procurando por uma solução que minimize o χ^2 (melhor ajuste), dado pela equação abaixo:

$$\chi^2 = \sum_\lambda [(O_\lambda - M_\lambda) w_\lambda]^2$$

Tanto o χ^2, quanto o Adev, podem ser usados para medir a qualidade e robustez do ajuste da SP. O Adev é o desvio percentual médio $|O_\lambda - M_\lambda|/O_\lambda$, sendo O_λ o espectro observado e M_λ o modelo ajustado. O código utiliza uma combinação de métodos estatísticos para a realização dos ajustes, tais quais o algoritmo de *simulated annealing*[6] (Kirkpatrick et al., 1983) e o algoritmo de *Metropolis-Hastings*[7] (Metropolis et al., 1953, Hastings, 1970), que gradualmente focam na região mais provável do espaço de parâmetros, evitando que o código fique preso em um mínimo local.

As linhas de emissão e os dados espúrios (ruído, regiões de bandas telúricas, raios cósmicos etc.) são mascarados utilizando $w_\lambda = 0$ para as regiões onde essas características são encontradas. Em suma, após excluir os pontos mascarados no es-

---

[6]*Simulated annealing* é um método probabilístico para se encontrar um mínimo global de uma função, a qual pode ter vários mínimos locais.

[7]O algoritmo de *Metropolis-Hastings* é um método de MCMC (do inglês *Markov Chain Monte Carlo*), geralmente utilizado para a obtenção de uma sequência de amostragens aleatórias, a partir de uma distribuição de probabilidade, para a qual uma amostragem direta é de difícil realização.

pectro, o processo de minimização do STARLIGHT consiste nos seguintes estágios: (i) o código faz uma ampla varredura do espaço de parâmetros, começando de uma alta 'temperatura' (em termos estatísticos) para permitir que o sistema explore todos os tipos de configurações e, então, implementando um cronograma de resfriamento, que gradualmente reduz a 'temperatura', deixando, assim, que o sistema se estabeleça em estados de mais baixa energia, (ii) exclusão de pixeis que não puderam ser ajustados no primeiro estágio, por desviarem muito do melhor ajuste (M_λ) encontrado nessa primeira etapa, (iii) ajuste detalhado utilizando toda as SSPs da base de elementos e (iv) o ajuste é aperfeiçoado repetindo toda sequência de etapas, excluindo as componentes irrelevantes (x_j=0) ao ajuste. Uma discussão detalhada dos procedimentos de ajuste do STARLIGHT pode ser encontrada em Cid Fernandes et al. (2004, 2005a) e no manual do código, disponível em http://astro.ufsc.br/starlight/.

Capítulo 3

Resultados e Discussão

Os resultados e discussões deste trabalho estão descritos em dois artigos científicos. Um publicado e intitulado *Probing the circumnuclear stellar populations of starburst galaxies in the near-infrared* (Dametto et al., 2014) e outro cujas correções já foram enviadas ao referee, intitulado *A SINFONI view of the nuclear activity and circumnuclear star formation in NGC 4303 - II: Spatially resolved stellar populations*. Esse artigo faz parte de uma série de quatro artigos dos quais a estudante faz parte, o primeiro apresentando o estudo da dinâmica e cinemática do gás em emissão e das estrelas na região central de NGC 4303, já publicado e intitulado *A SINFONI view of the nuclear activity and circumnuclear star formation in NGC 4303* (vide anexo I Riffel et al., 2016).

3.1 Populações estelares em galáxias *Starburst* no NIR

Os resultados do artigo listado abaixo foram desenvolvidos parcialmente ao longo do trabalho de mestrado, e refinados e publicados como parte do presente trabalho de doutorado.

1. **Probing the Circumnuclear Stellar Populations of Starburst Galaxies in the Near-infrared**,
   N.Z. Dametto, R. Riffel, M. G. Pastoriza, A. Rodríguez-Ardila, J. A. Hernandez-Jimenez & E. A. Carvalho, Monthly Notices of the Royal Astronomical Society, v.443, p.1754-1778, September 2014.

Probing the circumnuclear stellar populations of starburst galaxies in the near-infrared

N. Z. Dametto,[1]⋆ R. Riffel,[1] M. G. Pastoriza,[1] A. Rodríguez-Ardila,[2]†
J. A. Hernandez-Jimenez[1] and E. A. Carvalho[3,4]

[1]*Departamento de Astronomia, Universidade Federal do Rio Grande do Sul. Av. Bento Gonçalves 9500, Porto Alegre, RS, 91501-970, Brasil*
[2]*Laboratório Nacional de Astrofísica/MCTI – Rua dos Estados Unidos 154, Itajubá, MG, 37504-564, Brasil*
[3]*Universidade Federal de Itajubá. Rua Doutor Pereira Cabral, 1303, Pinheirinho, Itajubá, MG, 37500-903, Brasil*
[4]*Instituto Federal do Sudeste de Minas, Campus São João Del Rei, Rua Américo Davim Filho, S/No, São João Del Rei, MG, 36301-358, Brasil*

ABSTRACT

We employ the NASA Infrared Telescope Facility's near-infrared spectrograph SpeX at 0.8–2.4 μm to investigate the spatial distribution of the stellar populations (SPs) in the four well-known starburst galaxies: NGC 34, NGC 1614, NGC 3310 and NGC 7714. We use the STARLIGHT code updated with the synthetic simple SPs models computed by Maraston. Our main results are that the near-infrared light in the nuclear surroundings of the galaxies is dominated by young-/intermediate-age SPs ($t \leq 2 \times 10^9$ yr), summing from ∼40 up to 100 per cent of the light contribution. In the nuclear aperture of two sources (NGC 1614 and NGC 3310), we detected a predominant old SP component ($t > 2 \times 10^9$ yr), while for NGC 34 and NGC 7714 the younger component prevails. Furthermore, we found evidence of a circumnuclear star formation ring-like structure and a secondary nucleus in NGC 1614, in agreement with previous studies. We also suggest that the merger/interaction experienced by three of the galaxies studied, NGC 1614, NGC 3310 and NGC 7714, can explain the lower metallicity values derived for the young SP component of these sources. In this scenario, the fresh unprocessed metal poorer gas from the destroyed/interacting companion galaxy is driven to the centre of the galaxies and mixed with the central region gas, before star formation takes place. In order to deepen our analysis, we performed the same procedure of SP synthesis using the Maraston & Strömbäck evolutionary population synthesis models. Our results show that the newer and higher resolution M11 models tend to enhance the old-/intermediate-age SP contribution over the younger ages.

Key words: galaxies: bulges – galaxies: ISM – galaxies: starburst – galaxies: stellar content – infrared: galaxies – infrared: stars.

1 INTRODUCTION

A galaxy that is undergoing an intense star formation, usually in the central region ($r \lesssim 1$ kpc) is called a starburst galaxy (SB). These objects present star formation rates (SFRs) of 5–50 $M_\odot$ yr^{-1} within a region of 0.1–1 kpc extent, exceeding the values found within a similar region in the Galactic centre (0.5 $M_\odot$ yr^{-1}; Gusten 1989) or in normal galaxies (e.g. Heckman 2000). Also, its spectrum is char-

acterized by unusually bright emission lines, especially hydrogen and helium recombination lines.

It is widely known that what powers the starburst are massive stars that emit their primary radiation in the ultraviolet (UV) part of the spectrum (Heckman 2000), while the interstellar medium absorbs these radiation and re-radiates it at longer wavelengths. Massive stars evolve rapidly to red supergiants (RSGs) that emit most of their radiation in the near-infrared (NIR). These RSGs, therefore, are indicators of young stellar populations (SPs), providing means to identify recent starbursts in the NIR (Oliva et al. 1995). Thus, SBs are key sources to study the formation and evolution of massive stars in galaxies.

Moreover, the thermally pulsing asymptotic giant branch (TP-AGB) stellar phase has an important contribution in the NIR (Maraston 1998, 2005; Riffel et al. 2008), being enhanced in young-to intermediate-age SPs ($t < 2$ Gyr). With the new generation of the

evolutionary population synthesis (EPS) models that include the empirical spectra of stars in the TP-AGB phase (Maraston 2005, hereafter M05), it became possible to study in more detail the SP of galaxies in the NIR. A further benefit with the inclusion of these empirical spectra of C- and O-rich stars to the models (Lançon & Wood 2000) was the detection of NIR characteristic absorption features from the CN band. Riffel et al. (2007) for instance, detected the 1.1 μm CN band in the spectra of SBs and Seyfert galaxies. In addition, Martins et al. (2013) detected the band at 1.1 μm and that at 1.4 μm of the same molecule.

Even though tracing star formation in the NIR is a difficult task, this spectral range is the most suitable one to unveil the SPs in highly obscured sources (Origlia & Oliva 2000). With the improvement of infrared (IR) arrays, it became possible to obtain spectra at moderate resolution on faint and extended sources (Riffel et al. 2008, hereafter R08) allowing a more detailed study of SPs in the NIR spectral region. Also, the simultaneous wavelength coverage provided by these instruments via cross-dispersed spectroscopy brings an improvement to the SP synthesis once it avoids the aperture and seeing effects while the study in the *J*, *H* and *K* spectroscopy done in long-slit and single-band modes. It is worth mentioning that the *James Webb Space Telescope* will be optimized for observations in the IR. Thus, it is important to test the SP synthesis method in this spectral region.

In spite of the large amount of results about SPs gathered by means of NIR in active galactic nuclei (AGNs) or individual objects, few studies have concentrated on the analysis of the SPs along the spatial directions at distances larger than a few hundred of parsecs. It is thus necessary to develop proxies for the analysis of SPs along the radial direction and compare these results with those found at other wavelengths. This allows us to find out complementary information that the SP synthesis in the NIR is able to provide. To this purpose, we selected a sample composed by the four well-known SBs in the local Universe (NGC 34, NGC 1614, NGC 3310, NGC 7714), which were widely studied in the optical and NIR (see Section 2.1) and whose spatial extension and proximity allow the study of SPs at distances as large as several hundreds of parsecs.

An important aspect regarding our sample is the fact that all four galaxies are merging systems. It is known that mergers can trigger star formation (Mihos & Hernquist 1999), as well as create peculiar structures as tidal tails, bridges(e.g. Toomre & Toomre 1972) and rings (e.g. Lynds & Toomre 1976). An evidence of that is the presence of luminous HII regions in collisional rings (e.g. Fosbury & Hawarden 1977; Marston & Appleton 1995) and in extended tidal tails (e.g. Duc & Renaud 2013). In fact, interacting galaxies usually have strong IR emission (luminous infrared galaxies - LIRGs and ultraluminous infrared galaxies - ULIRGs;[1] e.g. Rieke et al. 1980) and present different types of nuclear activity like nuclear starbursts, AGN as well as post-starburst activity. With this in mind, we also would like to emphasize the importance of the detailed study of star-forming interacting systems in the local universe using NIR spectral range. These results can provide further support to studies of high-*z* sources (e.g. Pope et al. 2013), once almost all systems displayed intense bursts of star formation and were strongly interacting at the early universe (*z* ∼ 1–5; Carilli & Walter 2013).

Thus, aimed at studying the nuclear and off-nuclear SP in SBs and building a scenario of the star formation history (SFH) of these sources, we will analyse the spacial distribution of the SPs, in

---

the NIR spectral range of NGC 34, NGC 1614, NGC 3310 and NGC 7714, by means of SP fitting.

This paper is structured as follows. In Section 2.1, we present a summary of previous SP studies of our sample and in Section 2.2 the observations and data reduction. In Section 3, we describe the method used to perform the SP synthesis. The results are presented and discussed in Section 4 and the conclusions are left to Section 5. We assume $H_0 = 75$ km s^{-1} Mpc^{-1}.

2 THE DATA

2.1 Sample and previous SP studies

In this section, we summarize the properties of the galaxies as well as the results of the previous SP studies of our sample.

NGC 34: at a distance of 78.4 Mpc, this LIRG was classified as a merger system by Vorontsov-Velyaminov (1959). The nuclear activity classification of this galaxy is controversial. For example, Mazzarella, Bothun & Boroson (1991) and Riffel, Rodríguez-Ardila & Pastoriza (2006) classified this source as an SB. Yet, according to Gonçalves, Véron-Cetty & Véron (1999), its optical nuclear spectrum is not only starburst dominated, but also hosts a Seyfert 2 (Sy 2) nuclei. In fact, many studies have classified this source as an Sy 2 (e.g. Véron-Cetty & Véron 1986; Goldader et al. 1997a), while others have emphasized the apparent weakness of the [OIII] λ5007 emission line relative to either Hα or Hβ and classified NGC 34 as narrow-emission-line galaxy (e.g. Osterbrock & Dahari 1983; Goldader et al. 1997b).

Using optical images and spectroscopic observations, Schweizer & Seitzer (2007) proposed a scenario about the merging history of NGC 34. They suggested that two disc gas-rich galaxies of unequal mass (with an estimated mass ratio of $1/3 \leq m/M \leq 2/3$) merged, yielding a galaxy-wide starburst. This starburst occurred first ∼600 Myr (showing a peak over 100 Myr ago) and, according to the authors, seems to have formed an extensive system of young globular clusters with ages in the range of 0.1–1.0 Gyr. This work also reveals a young, blue stellar exponential disc that formed ∼400 Myr ago. At present, the two merging galaxies' nuclei appear to have coalesced, the starburst has shrunk to its current central (≤1 kpc) state and there is a strong gaseous outflow.

In addition, R08 analysed the inner 230 pc of this source in the NIR and detected a young-/intermediate-age SP with solar metallicity. Their results are in agreement with the fact that this galaxy has a strong 1.1 μm CN absorption band in its spectrum (Riffel et al. 2007) characteristic of SPs with that age (∼1 Gyr; M05).

NGC 1614: at a distance of 63.7 Mpc, NGC 1614 is considered a suitable laboratory to study starbursts since it has a modest extinction and fairly face-on viewing geometry (Alonso-Herrero et al. 2001). This source is catalogued as LIRG and shows a spectacular outer structure with tidal tails or plumes, suggesting that this morphology and its extreme IR luminosity result from the interaction/merger with at least other two galaxies (e.g. Neff et al. 1990; Alonso-Herrero et al. 2001). Also, the highly asymmetric extended emission present around this source favours that this interaction scenario is still occurring (e.g. Kotilainen et al. 2001). *Hubble Space Telescope*/NIR camera and multi-object spectrometer (NICMOS) observations reported by Alonso-Herrero et al. (2001) show deep CO stellar absorption, interpreted by them as tracers of a starburst nucleus of ∼45 pc in diameter surrounded by an ∼600 pc diameter ring of supergiant HII regions revealed in Paα line emission. This ring is coincident with a ring of radio continuum emission detected by Olsson et al. (2010), who conclude that the LINER-like activity

---

[1] LIRGs are defined as $10^{11} \leq L/L_{\odot} < 10^{12}$ and ULIRGs as $L/L_{\odot} \geq 10^{12}$.

1756   *N. Z. Dametto et al.*

Table 1. Log of observations.

Galaxy	Type	RA ($^{h\ m\ s}$)	Dec. ($^{\circ\ \prime\prime\prime}$)	z	Date of observation	T_{exp} (s)	Airmass	PA$_{obs}$ (deg)	$E(B-V)_G$ (mag)	Nuclear aperture (arcsec)	Scale (pc arcsec^{-1})
(1)	(2)	(3)	(4)	(5)	(6)	(7)	(8)	(9)	(10)	(11)	(12)
NGC 34	SB/Sy2	00:11:06	−12:06:26	0.019 774	24/10/03	1680	1.19	4	0.027	1.0	383
NGC 1614	SB	04:33:59	−08:34:46	0.016 070	24/10/03	1800	1.14	0	0.154	1.0	324
NGC 3310	SB	10:38:45	00:33:06	0.003 641	21/04/02	840	1.21	158	0.022	1.4	71
NGC 7714	H II	23:36:14	02:09:18	0.009 931	24/10/03	2400	1.05	348	0.052	1.0	192

Notes: (1) galaxy name; (2) galaxy classification; (3) right ascension; (4) declination; (5) average redshift, determined from the position of the emission lines of [S III] 0.9531 μm, He I 1.083 μm, Paβ and Brγ; (6) date of observation; (7) total exposure time for each galaxy; (8) airmass; (9) position angle of the slit; (10) galactic extinction from NED; (11) aperture diameter for the nuclear extraction; off-nuclear apertures were extracted with a diameter of 0.4 arcsec until the extended emission drop to 1 per cent of the peak value; (12) plate scale.

observed in NGC 1614 can be attributed to starburst activity, and not to an AGN. Alonso-Herrero et al. (2001) also states that the presence of a secondary nucleus can be interpreted as being a fragment of the companion galaxy, smaller than NGC 1614, which had long been destroyed. Thus, this source was classified as an advanced merger system by Doyon, Joseph & Wright (1989) and Neff et al. (1990). Moreover, R08 detected a dominant 1 Gyr old SP in the inner 154 pc in agreement to the fact that the integrated spectra of both NGC 34 and NGC 1614 are very similar.

NGC 3310: it is a well-known nearby SB ($d = 13.2$ Mpc) which presents a disturbed morphology (Elmegreen et al. 2002), suggesting that it recently underwent at least one significant merger. Balick & Heckman (1981) were the first to propose this merging scenario, suggesting that star formation occurring in the past 10^8 yr has been triggered by a collision with a dwarf galaxy. These authors also state that the well-known 'arrow' morphology (Walker & Chincarini 1967) on the western side comprises the remnant of this dwarf galaxy. NGC 3310 harbours a circumnuclear ring of about 8 to 12 arcsec in diameter (720–1080 pc; Elmegreen et al. 2002) that has been studied over a wide range of wavelengths, such as X-rays (e.g. Zezas, Georgantopoulos & Ward 1998), far-UV (e.g. Smith et al. 1996), UV (e.g. Meurer et al. 1995), optical (e.g. Balick & Heckman 1981; Grothues & Schmidt-Kaler 1991; Pastoriza et al. 1993), NIR (e.g. Telesco & Gatley 1984; Pastoriza et al. 1993; Elmegreen et al. 2002), IR (e.g. Telesco & Gatley 1984) and radio (e.g. Balick & Heckman 1981). This ring is filled with giant H II regions (Pastoriza et al. 1993). Studying the inner 56 pc of this source in the NIR spectral range, R08 detected an intense starburst activity, with four starbursts, one dominant at 1 Gyr, which contributes with up to ∼30 per cent of the light in this spectral range.

NGC 7714: an SB galaxy at 37.3 Mpc classified as a prototypical SB by Weedman et al. (1981). This galaxy is in interaction/merger with its companion NGC 7715, and such interaction could be responsible for the star formation bursts (Kinney, Bohlin & Calzetti 1993). In fact, Lançon et al. (2001) show the bridge between NGC 7714 and its companion NGC 7715 (see their fig. 2). This source is very well studied with large amount of data in the optical and NIR part of the spectrum (e.g. González-Delgado et al. 1995, 1999; Lançon et al. 2001; Brandl et al. 2004). For example, analysing narrow-band Hα imaging, González-Delgado et al. (1995) conclude that the star formation burst in the inner 5 arcsec (945 pc) of the galaxy is a collection of smaller H II regions with ages between 4 and 5 Myr. With very little silicate absorption and temperature of the hottest dust component of 340 K, NGC 7714 is defined by Brandl et al. (2004) as the perfect template for young, unobscured starburst. Moreover, analysing the optical continuum and far-infrared (FIR) colours, Bernlöhr (1993) found that the star formation in this source is consistent with a continuous SFR dur-

ing the past 20 Myr. R08 detected three star formation bursts, one dominant at 1 Gyr which contributes with up to ∼34 per cent of the light and two minor bursts with ages 30 (∼10 per cent) and 50 Myr (∼13 per cent).

2.2 Observations and data reduction

Spectra of NGC 1614, NGC 34, NGC 3310, NGC 7714 were obtained at the NASA 3 m Infrared Telescope Facility (IRTF) in two observing runs. The first one in 2002 April 21, and the second one on the night of 2003 October 24. Table 1 shows the log of observations for all galaxies. The SpeX spectrograph[2] (Rayner et al. 2003) was used in the short cross-dispersed mode (0.8–2.4 μm). The detector consists of a 1024×1024 ALADDIN 3 InSb array with a spatial scale of 0.15 arcsec pixel^{-1}. A 0.8 arcsec × 15 arcsec slit oriented along the parallactic angle (see column 9 of Table 1) was used, providing a spectral resolution, on average, of 320 km s^{-1}. This value was determined both from the arc lamp and the sky line spectra and was found to vary very little with wavelength along the observed spectra. The seeing, on average, was 0.8 arcsec. As SpeX does not provide the position of the slit centre, we derived them by matching the slit and the image profile using χ^2 statistics. The results are shown in Fig. 1 where we present the slit position overlapping the NICMOS images of the galaxies. For NGC 7714, we present the Wide Field and Planetary Camera 2 (WFPC2) *F814W* filter ($\lambda = 7940$ Å) image, as there is no NICMOS image available for this galaxy.

Observations were done nodding in an object–sky–sky–object pattern, with the sky position usually several arcminutes from the galaxy nucleus, free of extended emission or background stars. Immediately after each galaxy, an A0V telluric star, close in airmass to the former, was observed to remove telluric features and to perform the flux calibration, see Riffel et al. (2006) where a complete description of the reduction procedure is provided. In summary, the spectral reduction, extraction and wavelength calibration procedures were performed using SPEXTOOL,[3] the in-house software developed and provided by the SpeX team for the IRTF community (Cushing, Rayner & Vacca 2004). In addition to the nuclear spectrum, a different number of off-nuclear apertures were extracted for each galaxy, depending on the size of the extended emission across the slit. Table 1 (column 11) lists the diameter of the nuclear apertures. Off-nuclear spectra were extracted with a diameter of 0.4 arcsec along the spatial direction at both sides of the nuclear

[2] http://irtfweb.ifa.hawaii.edu/~spex/
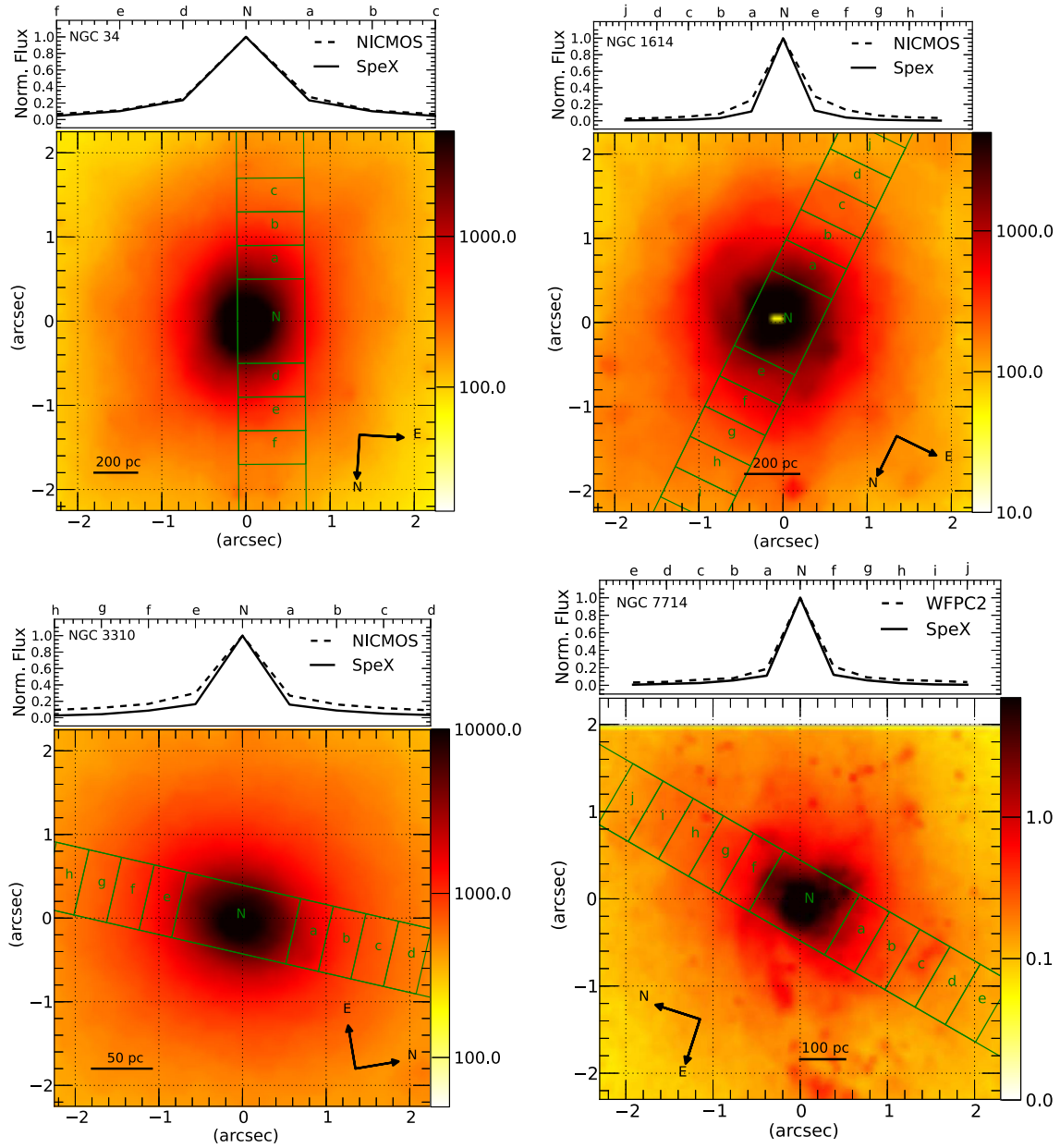
[3] http://irtfweb.ifa.hawaii.edu/~cushing/Spextool.html

Figure 1. Top: NICMOS and SpeX profile (continuum profile at $\lambda_{cent} = 12\,230\,\text{Å}$). Bottom: slit position overlapping the NICMOS image of the galaxies. For NGC 7714, we present WFPC2/*F*814*W* image.

aperture until the signal drops to 1 per cent of the peak nuclear value.

Telluric features removal and flux calibration were done using XTELLCOR (Vacca, Cushing & Rayner 2003), another software available by the SpeX team, which was designed specifically to perform telluric corrections on spectra obtained with Spex. Thereafter, the different orders were merged into a single 1D spectrum from 0.8 to 2.4 µm using the *xmergeorders* routine. The agreement between the

overlapping region of two consecutive orders was excellent and usually with errors of less than 1 per cent. Finally, the merged spectra were corrected for Galactic extinction using the Cardelli, Clayton & Mathis (1989) law and the extinction maps of Schlegel, Finkbeiner & Davis (1998).

Figs 2–5 show the nuclear and off-nuclear spectra for each source, already corrected by redshift. The most prominent absorption and emission lines are marked, as well as the telluric absorption
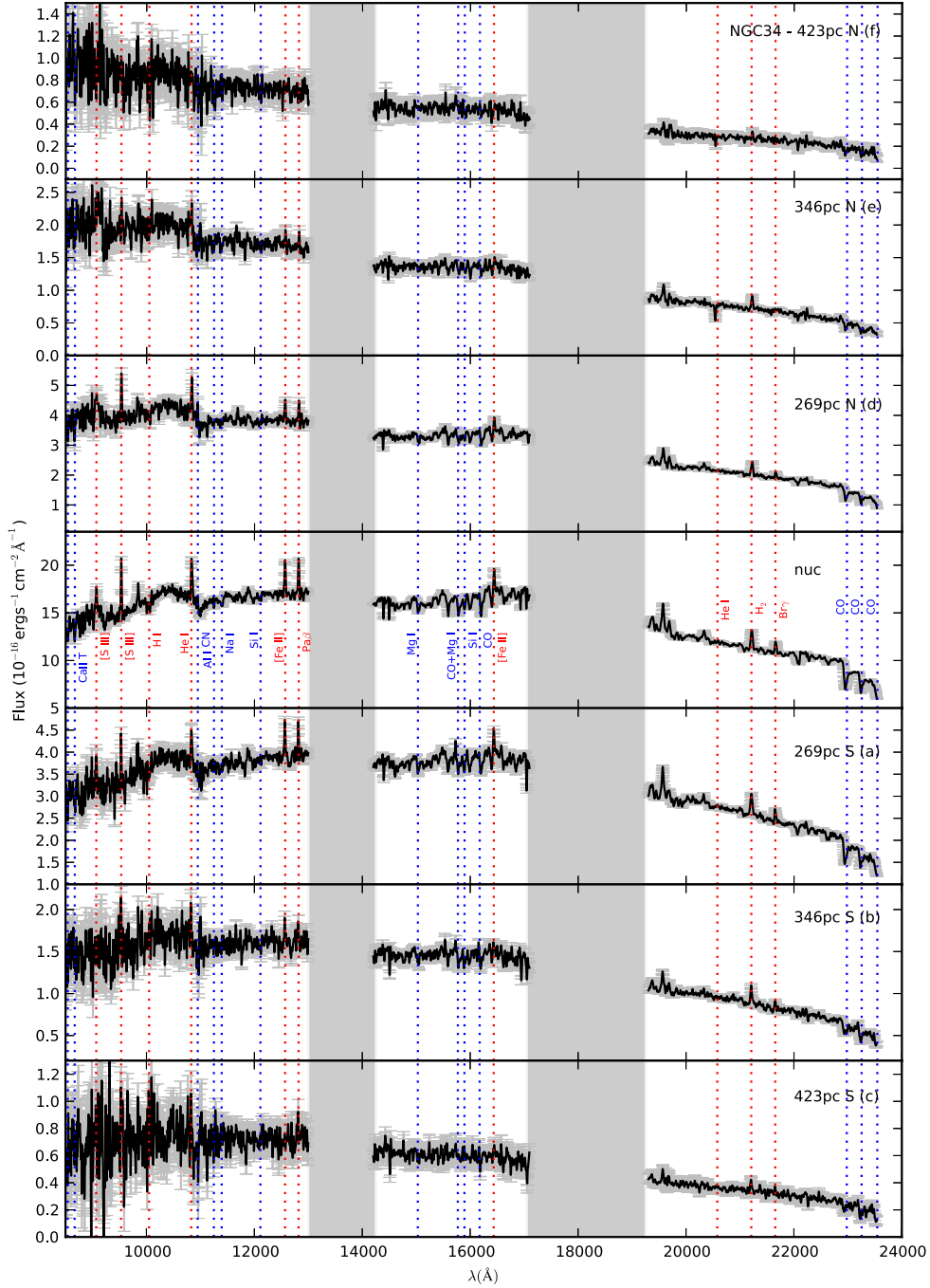
Figure 2. NGC 34 nuclear and extended region spectra. North (N) and south (S) are on the labels. The letters representing the apertures are used along the other figures (see Fig. 1). Error bars are in grey. Absorption (blue) and emission (red) lines are marked. Telluric absorption regions are displayed in the shaded area (grey).
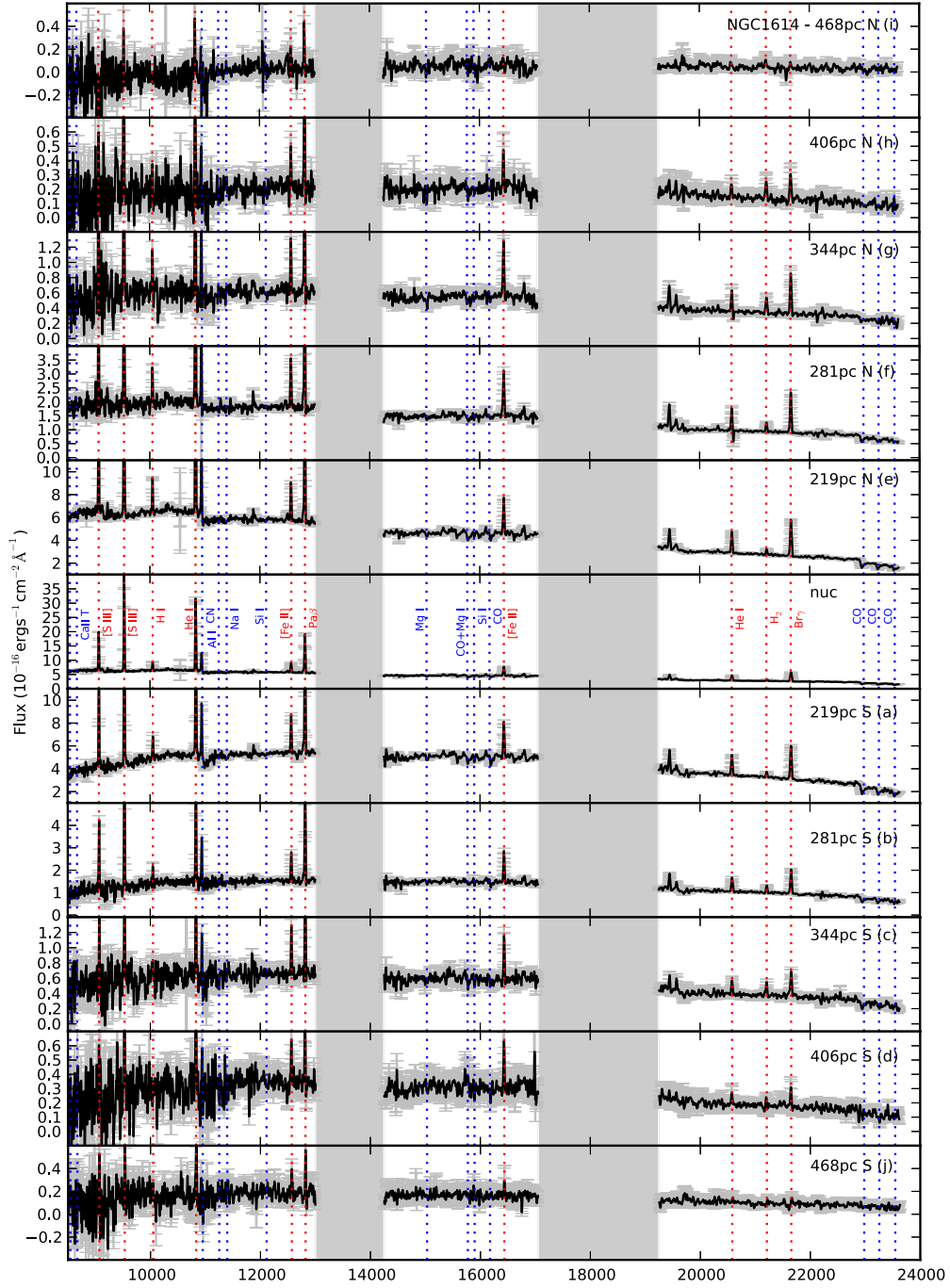
Figure 3. Same as Fig. 2, but for NGC 1614.

regions. The redshift, listed in Table 1 (column 5), was determined from the position of the emission lines of [S III] 0.9531 µm, He I 1.083 µm, Paβ and Brγ measured in the nuclear spectrum of each galaxy.

3 THE SP SYNTHESIS METHOD

There are two key ingredients when performing SP synthesis in galaxies: the base set (a set of simple SPs templates – SSPs) and
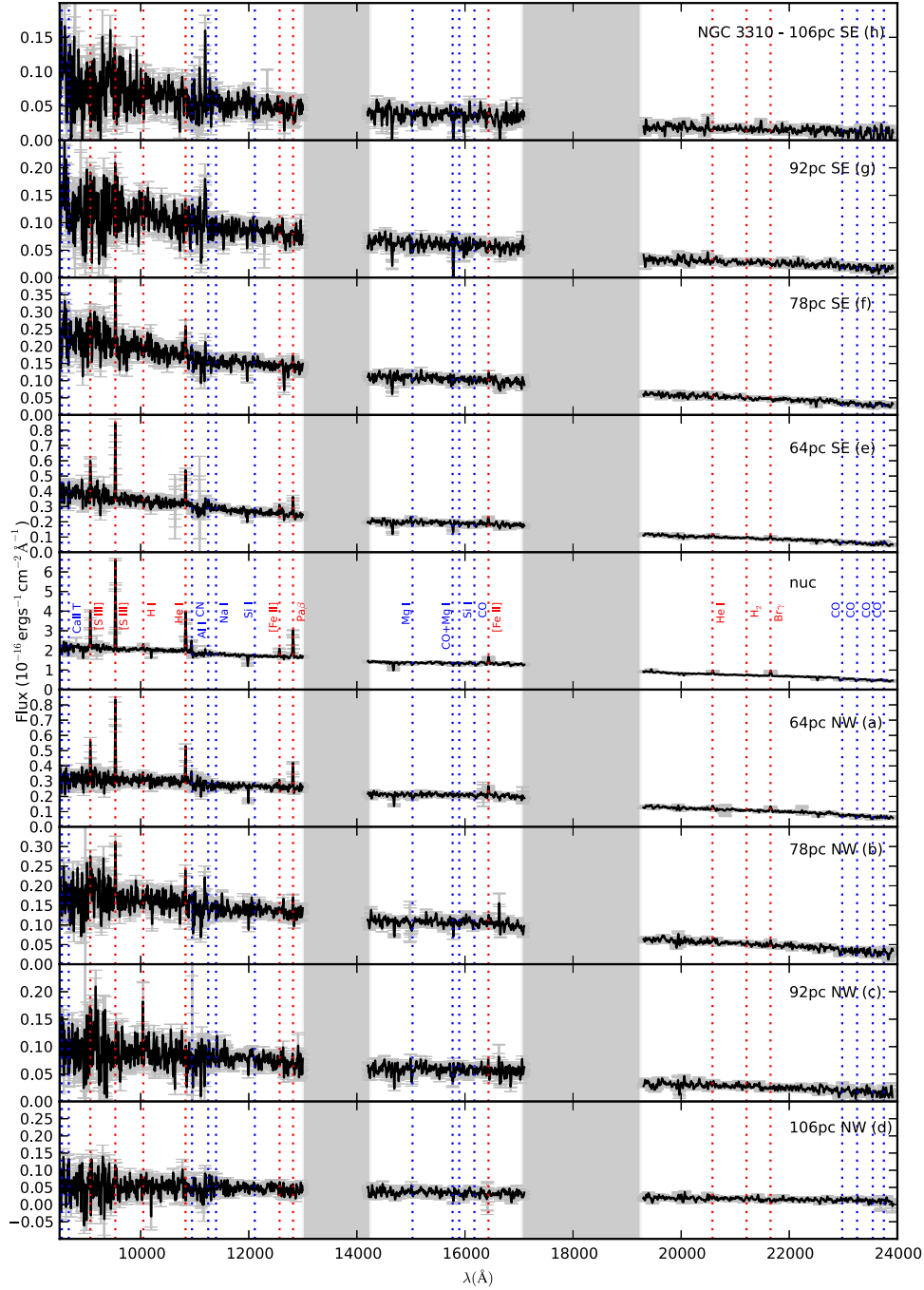
Figure 4. Same as Fig. 2, but for NGC 3310. North-west (NW) and south-east (SE) are on the labels.

the code. The purpose is to disentangle the SP components from the spectral energy distribution of a galaxy into the different SPs contributions. For that, the code will mix the SSPs until it fits the galaxy's absorption spectra. Thus, an ideal base set should cover

the range of spectral properties observed in the galaxy sample (Cid Fernandes et al. 2005) and should provide enough resolution in age and metallicity, in order to best fit the observed spectrum. In other words, a reliable base set would be a library of integrated spectra
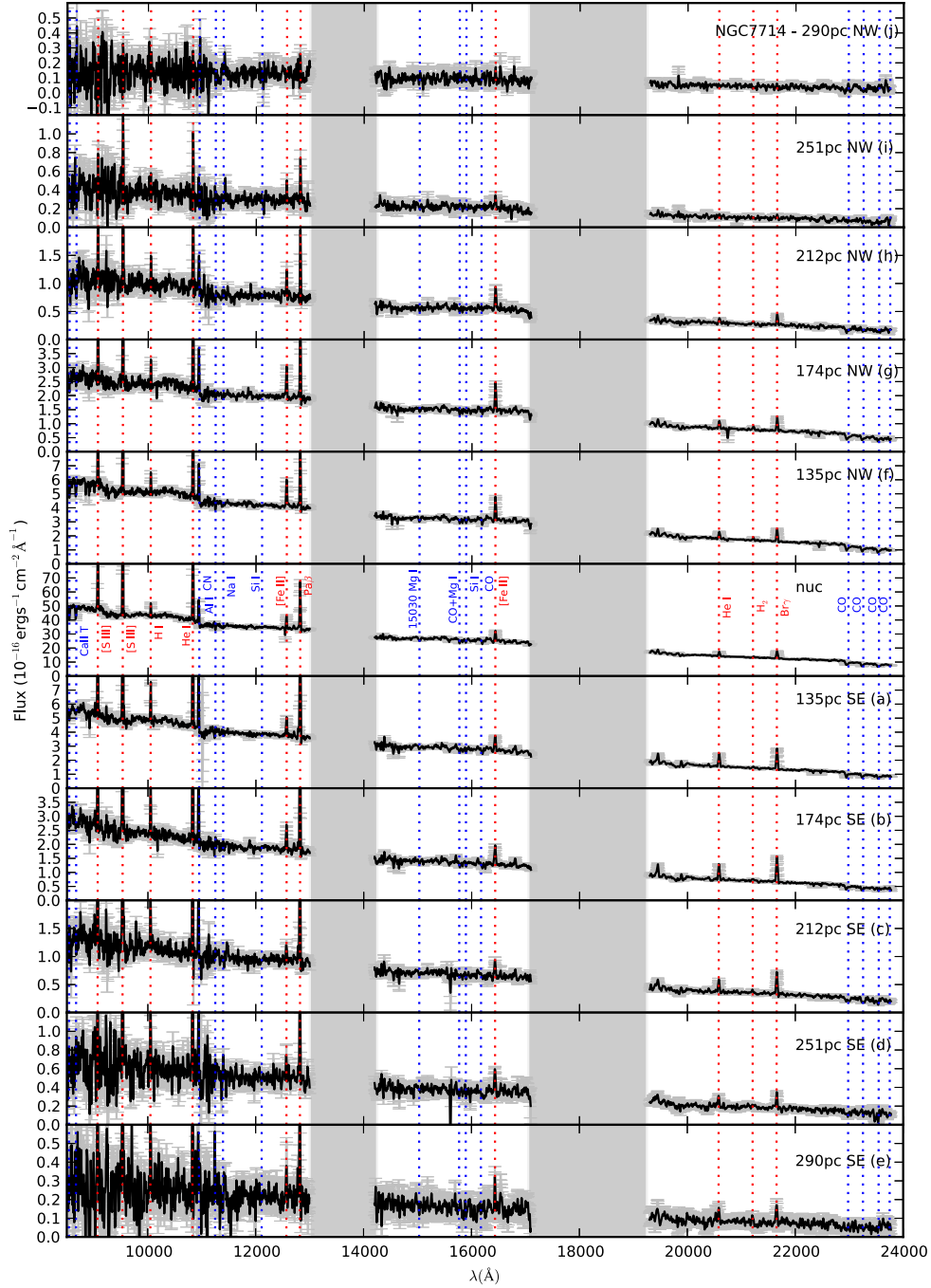
Figure 5. Same as Fig. 2, but for NGC 7714. North-west (NW) and south-east (SE) are on the labels.

of star clusters (i.e. they only depend on ages and metallicities of the stars and are free from any assumptions on stellar evolution and the initial mass function; Bica & Alloin 1986; Riffel et al. 2011a). However, up to now there is no such library available in the

literature for the NIR spectral region. In this way, the use of a base set composed of theoretical SSPs, covering this spectral region, is becoming a common approach (e.g. Riffel et al. 2009; Martins et al. 2010, 2013; Storchi-Bergmann et al. 2012).
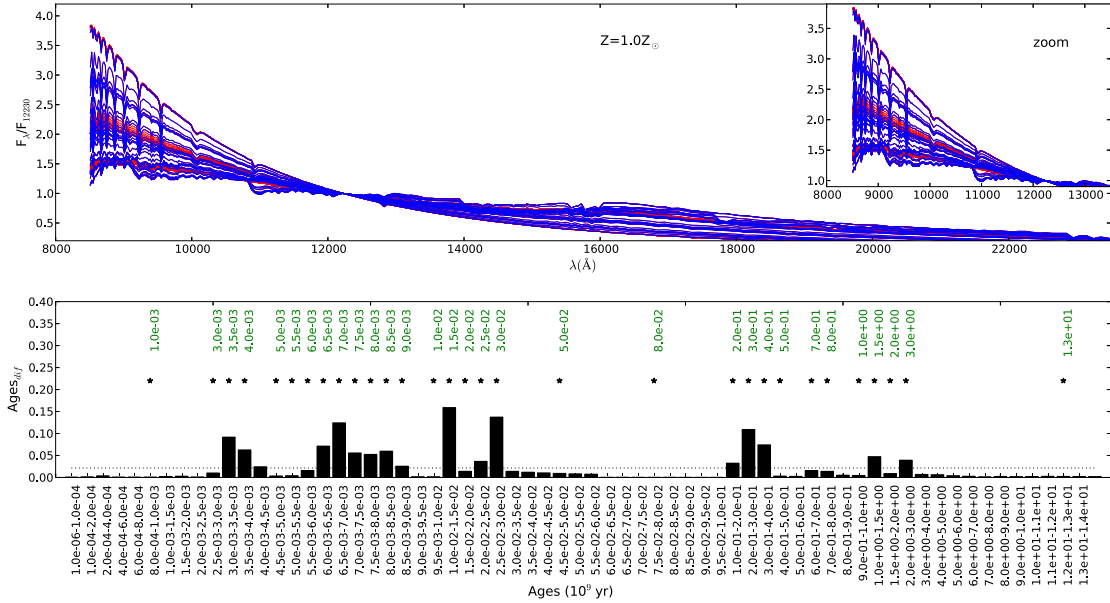
Figure 6. All the 67 M05 SSPs for $Z = Z_\odot$ are plotted (red) in the upper panel together with the 31 SSPs selected (blue) to compose the base set for this metallicity. In the bottom panel, the quadratic difference between two consecutive SSPs with consecutive ages is shown. The representative templates chosen to compose the base of elements are marked with a star and the correspondent ages are plotted in red in the top panel. A zoom of the blue end (where the main differences are observed) is also shown.

Since the NIR carries fingerprints from evolved stars (e.g. Riffel et al. 2007; Ramos Almeida, Pérez García & Acosta-Pulido 2009; Martins et al. 2013) and these are crucial to model the absorption line spectra of the galaxies, we used the M05 EPS models. They include empirical spectra of C- and O-rich stars (Lançon & Wood 2000) and thus, are able to predict these features. These models (grey lines in Fig. 6) span over an age range from 1 to 15 Gyr according to a grid of 67 models with four different metallicities.[4] Since, small differences in the SP are washed away in real data (i.e. they are diluted by the noise in real data; Cid Fernandes et al. 2004), we decided only to include in the base the representative SSPs (i.e. where significant differences between them are observed) to avoid redundant information and degeneracies in the base set. In order to choose the elements to compose the base, we compute the square root of the quadratic difference between two consecutive SSPs with consecutive ages (t) normalized to the unit at 12 230 Å and divided by the number of pixels (N), i.e. solving the equation

$$\text{Ages}_{\text{dif}} = \frac{1}{N} \sum_\lambda |F_\lambda(t_i) - F_\lambda(t_{i+1})|. \quad (1)$$

An example of the results of this procedure, for the solar metallicity, is shown in Fig. 6. The representative SSPs (which constitute the base set) are marked with a star and are overplotted in red on Fig. 6, top panel. Note that this procedure was done only in the wavelength interval between 8000 and 24 500 Å and for the four metallicities with all ages available. The final base set results in 31 ages, $t =$

[4] It is worth calling attention to the reader that Maraston do provide models with $Z = 0.005$ and $3.5 Z_\odot$, but only for ages older than 1 Gyr; therefore, we left them out of the base set.

0.0010, 0.0030, 0.0035, 0.0040, 0.0050, 0.0055, 0.0060, 0.0065, 0.0070, 0.0075, 0.0080, 0.0085, 0.0090, 0.010, 0.015, 0.020, 0.025, 0.030, 0.050, 0.080, 0.2, 0.3, 0.4, 0.5, 0.7, 0.8, 1,1.5, 2, 3, and 13 Gyr, and 4 metallicities, $Z = 0.02, 0.5, 1$ and $2 Z_\odot$. Thus, the final base set is composed of 124 SSPs.

It is important to call the attention to the fact that the spectral resolution of the M05 models in the NIR is significantly lower ($R \leq 250$) than that of the observed data ($R \sim 750$; Rayner et al. 2003) and varies with wavelength. For this reason, the observations were degraded to the model's resolution, by convolving them with a Gaussian. One example of a final smoothed spectrum is shown in Fig. 7.

Once the base set is defined, the other fundamental ingredient in SP fitting is the code, which will mix the individual components of the base set to get the best fit to the observed spectrum. Here, we used the STARLIGHT code (Cid Fernandes et al. 2004, 2005, 2009, 2010, 2011; Mateus et al. 2006; Asari et al. 2007, 2009) which mixes computational techniques originally developed for empirical population synthesis with ingredients from EPS models. Briefly, the code fits the observed spectrum O_λ with a combination in different proportions of $N_\star$ SSPs in the base set, $b_{j,\lambda}$ taken from the EPS models. Another important aspect is that the code fits the entire spectrum, from 0.8 to 2.4 µm, excluding emission lines and spurious features (e.g. cosmic rays, noise and telluric regions), which are masked out or clipped (see below for details).

The extinction law used in this work was the Calzetti law (Calzetti et al. 2000) implemented by HYPERZ (Bolzonella, Miralles & Pelló 2000), a public photometric redshift code which computed the Calzetti law for $\lambda > 2.2$ µm.

Velocity dispersion is a free parameter for STARLIGHT, which broadens the SSPs in order to better fit the absorption lines in
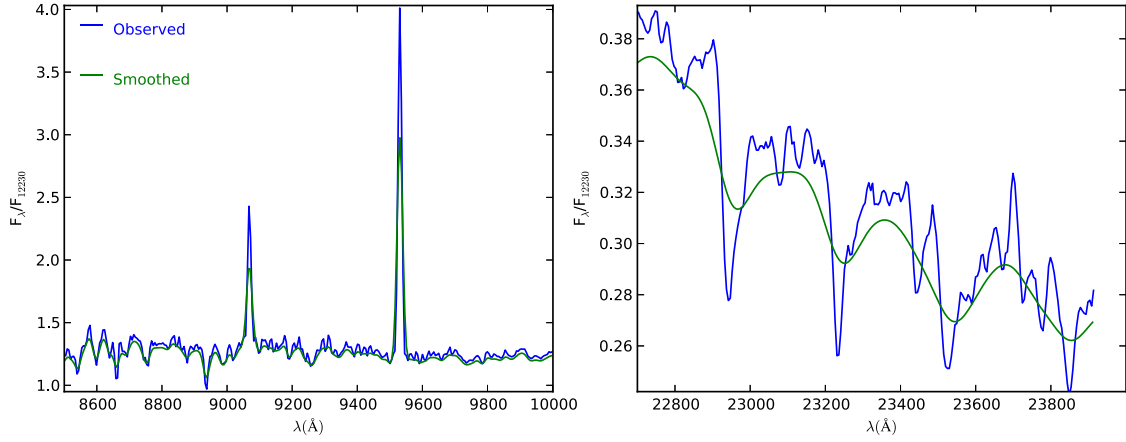
Figure 7. Comparison between the observed nuclear spectrum of NGC 3310 (blue) and the result of the Gaussian smoothing (green). We split the spectrum in two parts, the left-hand panel presents the effect of the Gaussian smoothing on the emission lines and the right-hand panel shows the effect on the CO absorption band.

the observed spectra. However, this step is not relevant in our case, because of the low-resolution models.

Basically, STARLIGHT solves the following equation for a model spectrum M_λ (Cid Fernandes et al. 2005):

$$M_\lambda = M_{\lambda 0} \left[\sum_{j=1}^{N_\star} x_j b_{j,\lambda} r_\lambda \right] \otimes G(v_\star, \sigma_\star), \qquad (2)$$

where $M_{\lambda 0}$ is the synthetic flux at the normalization wavelength ($\lambda_0 = 12\,240$ Å); x_j is the jth population vector component of the base set; $b_{j,\lambda} r_\lambda$ is the reddened spectrum of the jth SSP normalized at λ_0 in which $r_\lambda = 10^{-0.4(A_\lambda - A_{\lambda 0})}$ is the extinction term; $\otimes$ denotes the convolution operator and $G(v_\star, \sigma_\star)$ is the Gaussian distribution used to model the line-of-sight stellar motions, centred at velocity $v_\star$ with dispersion $\sigma_\star$. We choose as normalization wavelength $\lambda_0 = 12\,240$ Å, since this region is free from emission and absorption lines. STARLIGHT normalizes all the base spectra by $F_{\lambda 0}$ and the observed spectrum is normalized by the mean flux measured in a window (we used 80 Å), a region centred at λ_0 defined in order to avoid the effect of a bad pixel (noise spike, cosmic ray, etc.) at λ_0 in the observed spectrum. Finally, the best fit is achieved by STARLIGHT as the code searches for the minimum of the equation

$$\chi^2 = \sum_\lambda [(O_\lambda - M_\lambda) w_\lambda]^2. \qquad (3)$$

The STARLIGHT output parameters χ^2 and Adev can be used to measure the robustness of the SP fit. Adev is the percent mean deviation $|O_\lambda - M_\lambda|/O_\lambda$, where O_λ is the observed spectrum and M_λ is the fitted model. The fits are carried out with a mixture of simulated annealing (Kirkpatrick, Gelatt & Vecchi 1983) plus Metropolis scheme, which gradually focuses on the most likely region in parameter space, avoiding (through the logic of the cooling schedule) trapping on to local minimum.

The emission lines and spurious features (noise, telluric regions, cosmic rays) are masked out by using $w_\lambda = 0$ in the regions where they are located. In our case, the emission lines masked were [S III] 9069 Å, [S III] 9531 Å, He I 10 830 Å, Paγ 10 938 Å, [Fe II] 12 570 Å, Paβ 12 810 Å, [Fe II] 16 444 Å, Paα 19 570 Å, Brγ 21 650 Å

and H$_2$ 21 213 Å. Spurious data were also masked out. Examples of masked regions are indicated in Figs 8–11.

In summary, after excluding the masked points, the minimization process consists of the following stages: (i) make a broad sweep of the parameter space, starting from a high 'temperature' (in statistical mechanics terms) to allow the system to explore all sorts of configuration and then implementing a cooling schedule to gradually reduce the 'temperature', therefore letting the system to settle into the lowest energy states, (ii) exclude pixels which could not be fitted by the first stage, once they deviate strongly from the best M_λ found in this first stage, (iii) detailed fit with the full base and (iv) the whole fit is fine-tuned repeating the full loop excluding all irrelevant components ($x_j = 0$) to the fit. A well-detailed discussion of the STARLIGHT procedures can be found in Cid Fernandes et al. (2004, 2005) and in STARLIGHT manual, available at http://astro.ufsc.br/starlight/.

3.1 Uncertainties on the fits

The use of statistics in order to interpret spectral synthesis results is widespread (e.g. Panter et al. 2007), once averaging results tends to reduce the uncertainties (Cid Fernandes et al. 2013). Another good reason to use the statistical interpretation is to produce an estimation of the uncertainties, which STARLIGHT does not provide as a standard output. The most straightforward way to achieve this is to perturb the input spectra according to some realistic prescription of the errors involved (Cid Fernandes et al. 2013). In order to estimate these uncertainties, we simulate 100 spectra for each aperture of each galaxy in our sample. The simulated flux for each wavelength (λ_i) is computed assuming a Gaussian distribution of the uncertainties. Therefore, the mean flux in each λ_i corresponds to the measured flux value and the standard deviation is given by the errors provided by SPEXTOOL. Thus, we simulate the flux at λ_i according to its normal probability.

STARLIGHT provides a single best-fitting set of parameters among typically many millions trials during its likelihood-guided sampling of the parameter space. These single solutions, however, are not necessarily mathematically unique. In this scenario, we performed
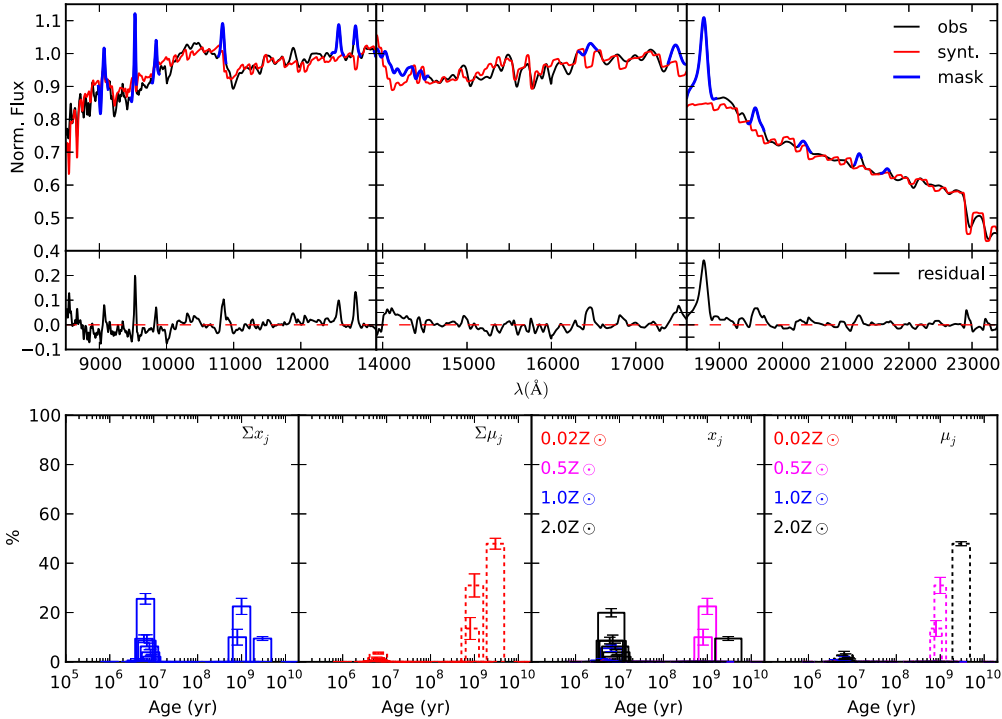
Figure 8. Results for NGC 34. Upper panels: we present the synthesis result (red) and the masked points (blue) overlapping the observed spectra (black), below the residual spectrum is shown (the dashed line in red marks the zero-point in flux). Bottom panels: we display four histograms, the two on the left present the flux-weighted (x_j) and mass-weighted (μ_j) SPs vectors contributions sorted only by age (metallicities summed) and the two on the right show the flux-weighted (x_j) and mass-weighted (μ_j) SPs vectors contributions sorted by age and metallicity. Telluric regions were omitted.

SP synthesis in all the simulated spectra in order to obtain an average result together with the standard deviation associated with each aperture of each galaxy. As a result, we have an estimate of the uncertainties associated with the SP fitting (see Figs 8–11).

4 RESULTS AND DISCUSSION

By making a systematic study over the SP variance along the galaxy, we built a scenario for the star formation in the four SBs studied here. An example of the individual results for the nuclear extraction of each galaxy is shown in Figs 8–11. These plots include (i) in the top panel are the synthesis result (red) and the masked points (blue) overlapping the observed spectra (black); (ii) the residual spectrum (the dashed line in red marks the zero-point in flux) and (iii) the bottom panel shows four histograms, the two on the left present the flux-weighted (x_j) and mass-weighted (μ_j) SP vectors contributions sorted only by age (metallicities summed) and the two on the right show x_j and μ_j sorted by age and metallicity. In these figures, we can analyse the results individually for each aperture of each galaxy, controlling the quality of the fits and improving the mask files when necessary.

On the other hand, grouping the population vector in age bins should thus provide a coarser but more powerful description of the SFH of the galaxies (Cid Fernandes et al. 2001; Cid Fernandes, Leão & Lacerda 2003; Riffel et al. 2010, 2011b, among others.).

Actually, Cid Fernandes et al. (2001) show that measurement errors as well as the use of reduced sets of observables are responsible for spreading a strong contribution in one component preferentially among base elements of same age. In this sense, we used their definition of binned population vectors as follows: young: x_y ($t \leq 50 \times 10^6$ yr), intermediate-age: x_i ($50 \times 10^6 < t \leq 2 \times 10^9$ yr) and old: x_o ($t > 2 \times 10^9$ yr).

In addition to this, in order to describe the metallicity behaviour of the SP mixture along the galaxy, we have used the flux- and mass-weighted mean metallicity defined by Cid Fernandes et al. (2005) as

$$\langle Z_\star \rangle_F = \sum_{j=1}^{N_\star} x_j Z_j, \tag{4}$$

for the flux-weighted mean metallicity and

$$\langle Z_\star \rangle_M = \sum_{j=1}^{N_\star} m_j Z_j \tag{5}$$

for the mass-weighted mean metallicity. Both definitions are bounded by the $\frac{1}{50}$–2 $Z_\odot$ range.

Therefore, to best analyse our results, we create a series of histograms for each galaxy shown in Figs 12–15. Each figure includes seven plots: (i) panels (a) and (b) present a global analysis of each source by plotting the average contribution in flux and mass,
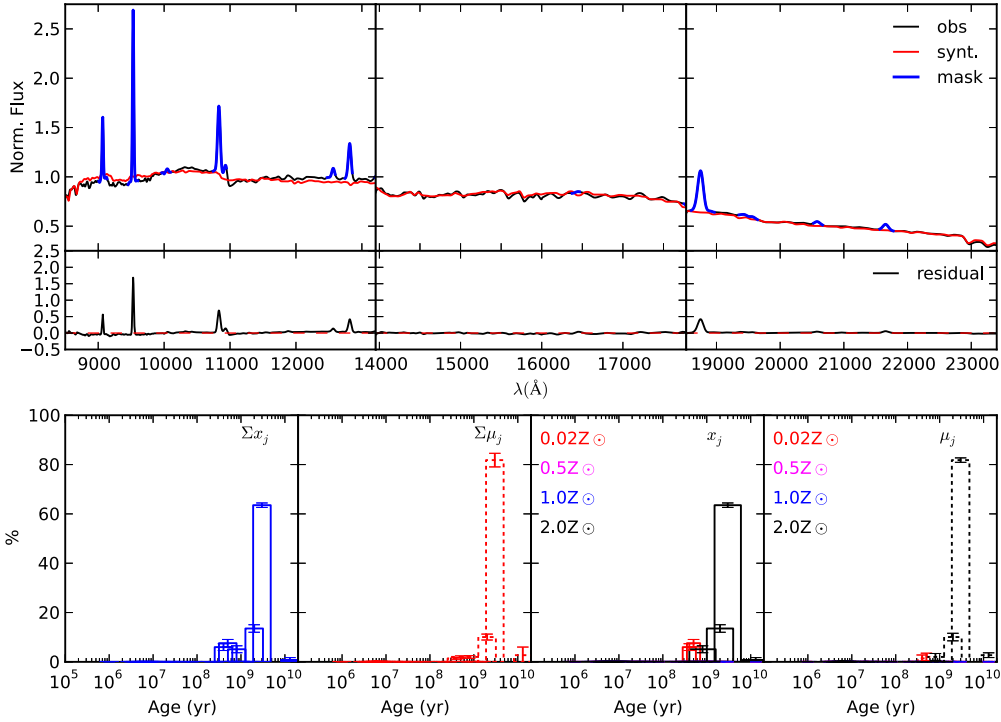
Figure 9. The same as Fig. 8 but for NGC 1614.

respectively, of the binned vectors along the apertures; (ii) panel (c) shows the mean-metallicity-weighted by flux (Z_F) and by mass (Z_M); (iii) the extinction (A_v) is plotted along the apertures in panel (d); (iv) the average χ^2 and Adev are plotted in panel (e); (v) the continuum profile at $\lambda_{cent} = 12\,230$ Å is shown in panel (f); (vi) the signal-to-noise ratio (SNR) in panel (g), which was estimated as being the ratio between the mean values of the F_λ points (in a window of 60 Å) and their standard deviation. These histograms will enable us to construct the star formation scenario for each galaxy, revealing the predominant ages of the population as well as indicating the possible presence of nuclear structures.

It is important to mention that the uncertainties increase with decreasing SNR (higher error bars in the outer apertures – see Figs 12–15). Nevertheless, we decided to include these results (for SNR ≤ 10) in the analysis, as they follow the same tendency of the SP distribution along the galaxy. The average results from the SP synthesis are in Table 2.

Below we describe the results obtained through our SP analysis for each galaxy and compare them with the results found in the literature.

4.1 NGC 34

Panels (a) and (b) of Fig. 12 show a predominance of younger ages in the nuclear region shifted towards the south direction, while the intermediate-age SP is more pronounced towards north of the nucleus. The contribution of the old SP is enhanced in the mass fraction histogram as expected, once the older the SP is, less light

it will radiate, decreasing the flux contribution and increasing the mass contribution of this age in the SP components. These results are in agreement with the literature. For example, studying the optical properties of NGC 34 (on a larger field of view), Schweizer & Seitzer (2007) conclude that this source supports a rich system of young massive star clusters, a blue exponential disc and a strong gaseous outflow, all signatures of a recent gas-rich merger accompanied by a strong starburst. This source was also studied by R08 in the NIR part of the spectrum. Analysing the 230 central parsecs of this galaxy, they found a dominating intermediate-age SP ($\sim$1 Gyr).

In Fig. 12(c), we show the mass- and flux-weighted mean metallicities along the apertures of NGC 34. Our results point to above-solar mean metallicity values along the galaxy. Moreover, the apertures displaying higher mass-weighted mean metallicity values than the flux-weighted ones are those in which the contribution of the old SP increases. Such discrepancy can be associated with the well-known age–metallicity degeneracy, i.e. for a fixed mass, a high-metallicity SP looks cooler – and older – than a low-metallicity SP, thus resulting in a higher M/L ratio. In this context, one can interpret that the flux-weighted metallicity is more sensitive to the young component, while the mass-weighted metallicity is more sensitive to the old one.

The north side of the galaxy displays lower visual extinction ($A_v < 2.0$ mag) than the nuclear ($A_v \sim 3.0$ mag) and southern region ($A_v \sim 2.0$ mag), suggesting a differential reddening. To better compare our results with those found in the literature, we estimated a weighted average of the visual extinction values derived by
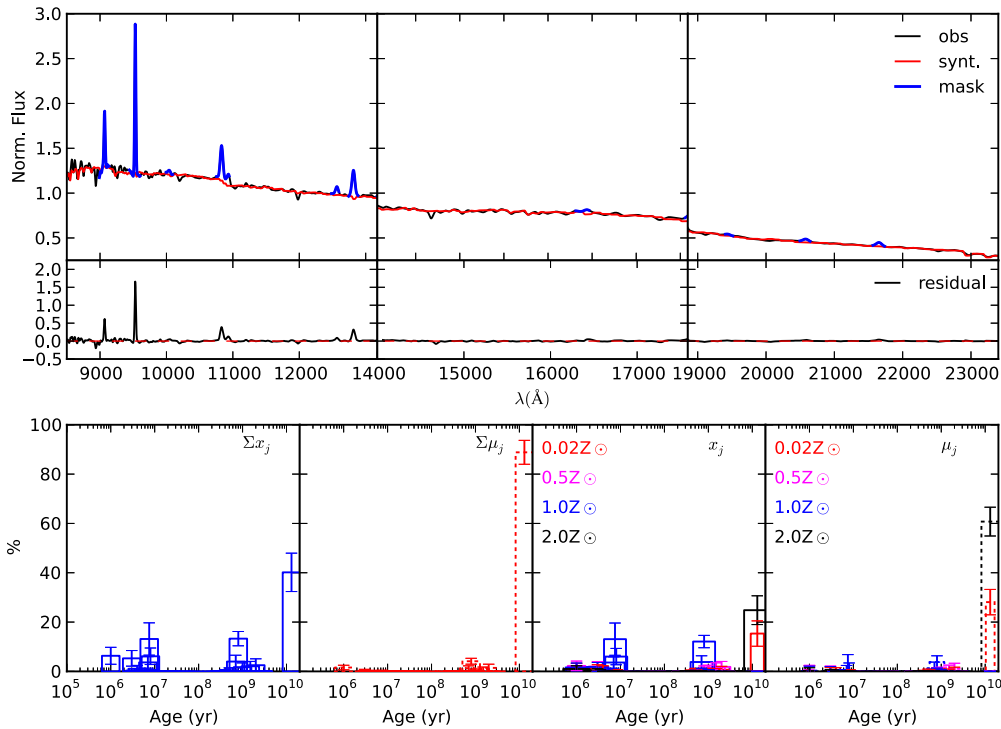
Figure 10. The same as Fig. 8 but for NGC 3310.

STARLIGHT, resulting in $\bar{A}_v = 2.49 \pm 0.10$ mag for NGC 34. Using the values of $E(B - V)$ quoted by Veilleux et al. (1995), Goldader et al. (1997a) derived $A_K = 0.67$ mag (in a 1.5 arcsec × 4.5 arcsec beam), which results in $A_v = 6.2$ mag when using the relation $A_K = 0.108A_v$ (Mathis 1990).

In order to assess the robustness of the fit, we display the χ^2 and Adev (per cent mean deviation) along the apertures in Fig. 12(e), the continuum profile at $\lambda_{cent} = 12\,230$ Å in Fig. 12(f) and the SNR along the galaxy in Fig. 12(g). As the SNR drops to values below 10, the per cent mean deviation (Adev) reaches higher values (see Figs 13 e–g).

4.2 NGC 1614

From Fig. 13(a), we can see a peak of old SP in nucleus at 219 pc south, while the off-nuclear northern apertures present a dominant young-/intermediate-age SP component. The fact that we are not detecting a contribution of the young SP ($t \leq 50 \times 10^6$ yr) in the nuclear aperture can be explained in two different scenarios: (i) the presence of an AGN, which would quench star formation in the nuclear region (Nesvadba et al. 2006), or (ii) that the NIR still cannot reveal the young stars embedded in dustier nuclear regions (Imanishi & Nakanishi 2013). By modelling the starburst of this galaxy, Alonso-Herrero et al. (2001) associated the strong CO concentrations found in the nucleus with an older part of the starburst (10^9 yr old or older stars), which is similar to the dominant SP age we found in the nuclear aperture.

Moreover, we found evidence of a circumnuclear ring-like structure[5] of young-/intermediate-age SP with a diameter of about 600 pc. In fact, Olsson et al. (2010) detected a ring-like structure traced out by 1.4 and 5 GHz MERLIN contours with a radius of around 310 pc, which is consistent with our results. This also has been reported by Alonso-Herrero et al. (2001), which have stated that the relation between the strong stellar CO bands to surrounding ionized gas rings to molecular gas suggests that the luminous starburst started in the nucleus and is propagating outwards into a molecular ring. Väisänen et al. (2012), through the analysis of *L*-band IFU observations of the inner kpc of NGC 1614, detected a ring that extends from 200 to 500 pc from the nucleus, from the equivalent width map of 3.3 μm polycyclic aromatic hydrocarbon emission. It is worth mentioning that such kind of nuclear rings are quite common in AGNs, but rarely found in these systems (e.g. Riffel et al. 2011b, 2010; Storchi-Bergmann et al. 2012).

The increase in the young-/intermediate-age SP component at ∼300 pc north from the nucleus can also be interpreted as being an evidence of the secondary nucleus (see Fig. 13 a), also reported by Alonso-Herrero et al. (2001) as the remnant of the merger with a smaller galaxy, which has by now largely been destroyed. In a

---

[5] As we used an unidimensional slit, we can only see an increase in the young-/ intermediate-age SP in both sides of the nucleus, in this sense we cannot assert if this pattern surrounds the nuclear region. Although, from Alonso-Herrero et al. (2001, Fig. 4) we can see that the Paα emission image reveals a nuclear ring-like structure with approximate diameter of 650 pc, possibly formed by H II regions. A deeper analysis will be made using integral field unit (IFU) data of this source.
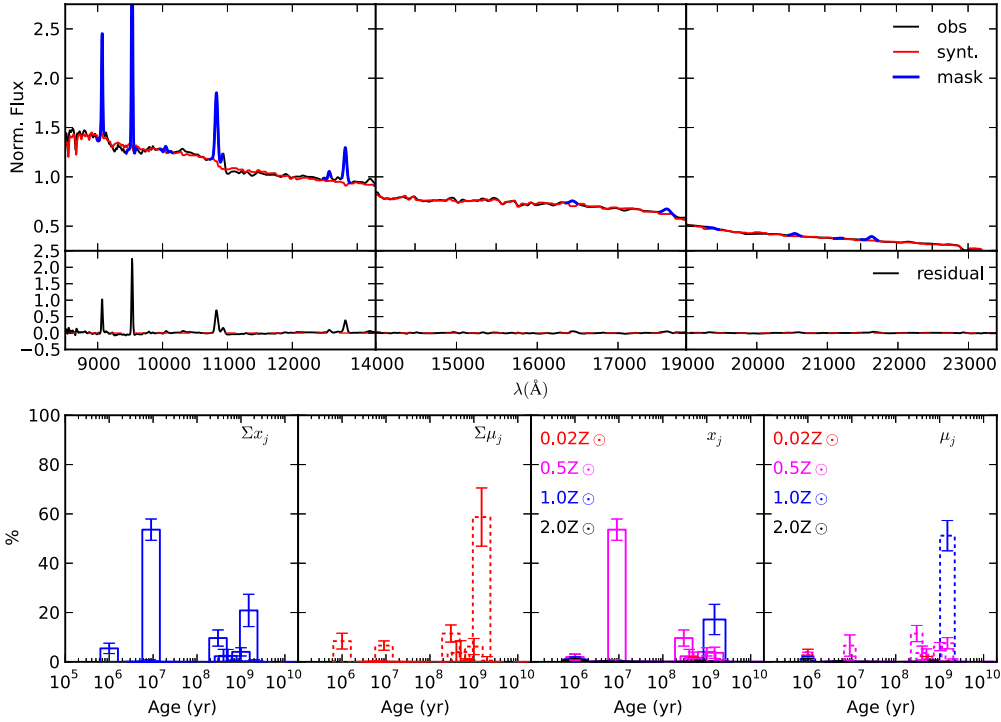
Figure 11. The same as Fig. 8 but for NGC 7714.

previous work, R08 found a 1 Gyr old SP dominating the light in the inner 154 pc of this source.

We found above solar values for the flux- and mass-weighted mean metallicity along the galaxy (see Fig. 13 c). As the contribution of the young SP component grows north, the metallicity tends to decrease, suggesting a metal-poor young SP at this side of the galaxy. In this scenario, the modest-sized galaxy which merged with NGC 1614 in the past (Alonso-Herrero et al. 2001) would have diluted the gas in the remnant, thus giving rise to a metal-poor SP, poorer than the old SP component already present in NGC 1614.

The values derived by us for the extinction (A_v) range from 1.7 to 3.9 mag ($\bar{A}_v = 2.66 \pm 0.08$). Results found in the literature are in agreement with ours, for example Neff et al. (1990) derived $A_v = 3$–5 mag assuming a foreground dust screen model, from optical and IR colours (in an ~20 arcsec$\times$ 20 arcsec beam), as well as IR emission lines (in a 2.7 arcsec $\times$ 4.3 arcsec beam). Using NIR colours, Shier, Rieke & Rieke (1996) found $A_v = 4.9$ mag (in a 2.4 arcsec $\times$ 4.8 arcsec beam), while Kotilainen et al. (2001) (in a 2 arcsec$\times$ 2 arcsec beam) derived $A_v = 1.8$ mag south-east of the nucleus and $A_v = 3.5$ mag north-west. Assuming an intrinsic stellar colour $H - K = 0.2$, Oliva et al. (1995) derived $A_v \sim 4$ mag (in a 2.2 arcsec $\times$ 4.4 arcsec beam). Moreover, Alonso-Herrero et al. (2001), using the flux of two [Fe II] emission lines at 1.257 and 1.644 μm as well as the hydrogen recombination lines Paβ and Brγ and a foreground dust screen model, derived the extinction to the gas in the K band as $A_K = 0.40$–0.49 mag (in a 19.5 arcsec $\times$ 19.5 arcsec beam), corresponding to $A_v \sim 4$ mag, using the Mathis (1990) relation of A_v and A_K. Also using recombination lines, Kotilainen et al. (2001) found

$A_v = 3.8$ mag (in a 3.5 arcsec $\times$ 3.5 arcsec beam), a similar value than the one Bushouse (1986) derived ($A_v \sim 3$ mag) for a similar beam. Likewise, Goldader et al. (1995, see section 1614) derived $A_v = 2.96$ mag (in 3 arcsec$\times$ 12 arcsec beam), using the values of $E(B - V)$ quoted by Veilleux et al. (1995).

On the other hand, Puxley & Brand (1994) present discrepant values when compared to those we derived and those found in the literature. Using hydrogen recombination line fluxes, they inferred a total visual extinction of $A_v = 15 \pm 2.5$ mag (in 9 arcsec $\times$ 3 arcsec beam) assuming a composite model (a mixture of dust, gas and foreground screen) and claimed that the extinction on NGC 1614 could not be modelled with a simple foreground dust screen model, for which they found visual extinction values ranging from 4.7 to 9.5 mag.

4.3 NGC 3310

Our results point out to a predominant young-/intermediate-age SP southwards (see Fig. 14a). An increase in the older component can be seen in both flux and mass contribution towards the opposite direction. Similar to our study, several previous works in the optical region (Balick & Heckman 1981; Telesco & Gatley 1984; Schweizer & Seitzer 1988) estimated the starburst age on this source in the range of 10^7–10^8 yr.

The nucleus and six surrounding H II regions, four of which are located at less than 400 pc from the galaxy nucleus (a wider range than the one analysed in this work, which comprehend only the
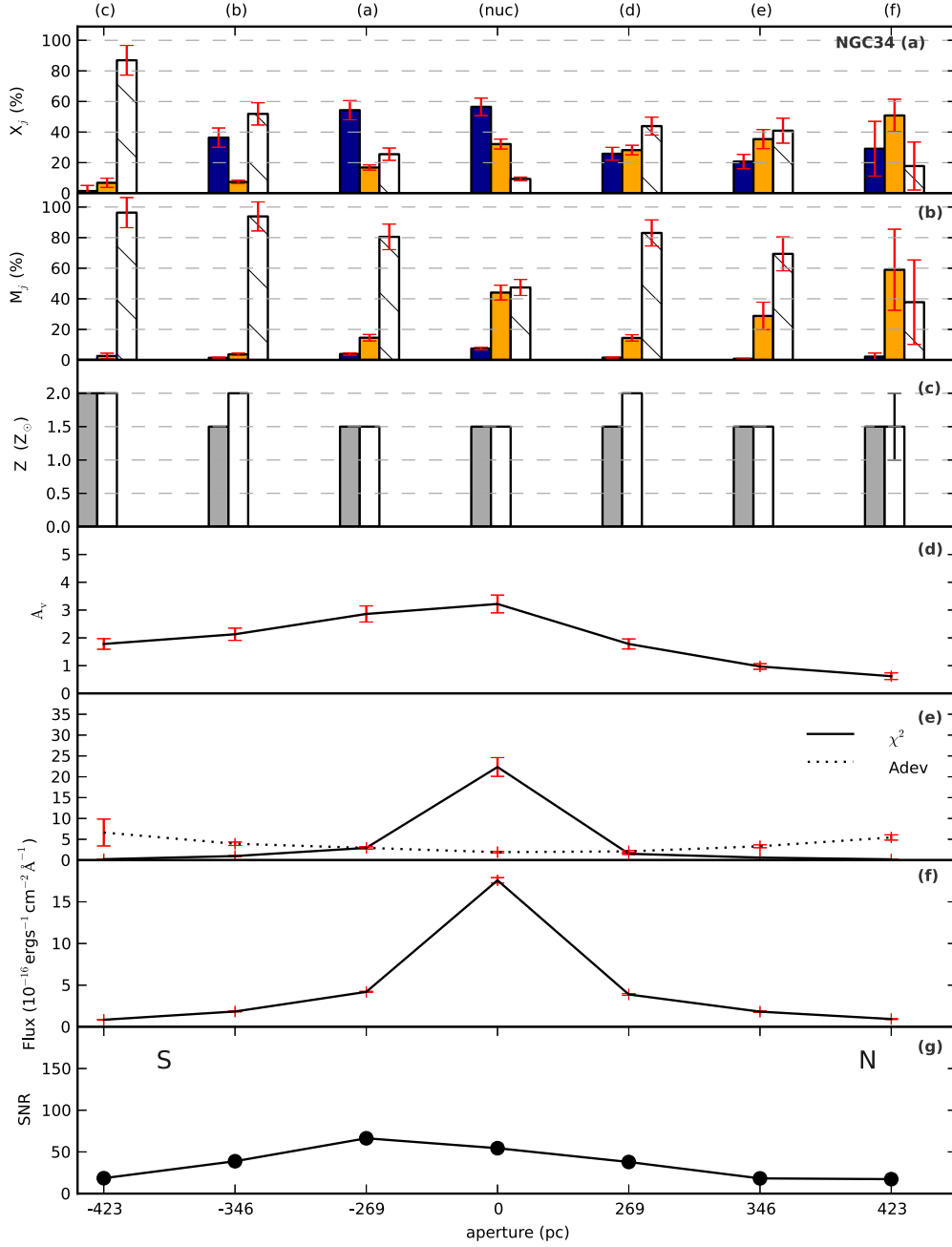
Figure 12. Global analysis for NGC 34. Panels (a) and (b) present the average contribution in flux and mass, respectively, of the population vectors along the apertures. Blue, yellow and red represent young (x_y), intermediate (x_i) and old (x_o) SP contributions, respectively; panel (c) shows the average metallicity weighted by flux (Z_F – filled) and by mass (Z_M – empty); the extinction (A_v) is plotted along the apertures in panel (d); the average χ^2 and Adev are plotted in panel (e); the continuum profile at $\lambda_{cent} = 12\,230$ Å in panel (f) and for last, the SNR along the galaxy in panel (g). The letters on the top of the figure correspond to those of Fig. 1. North (N) and south (S) direction are indicated in the bottom panel.
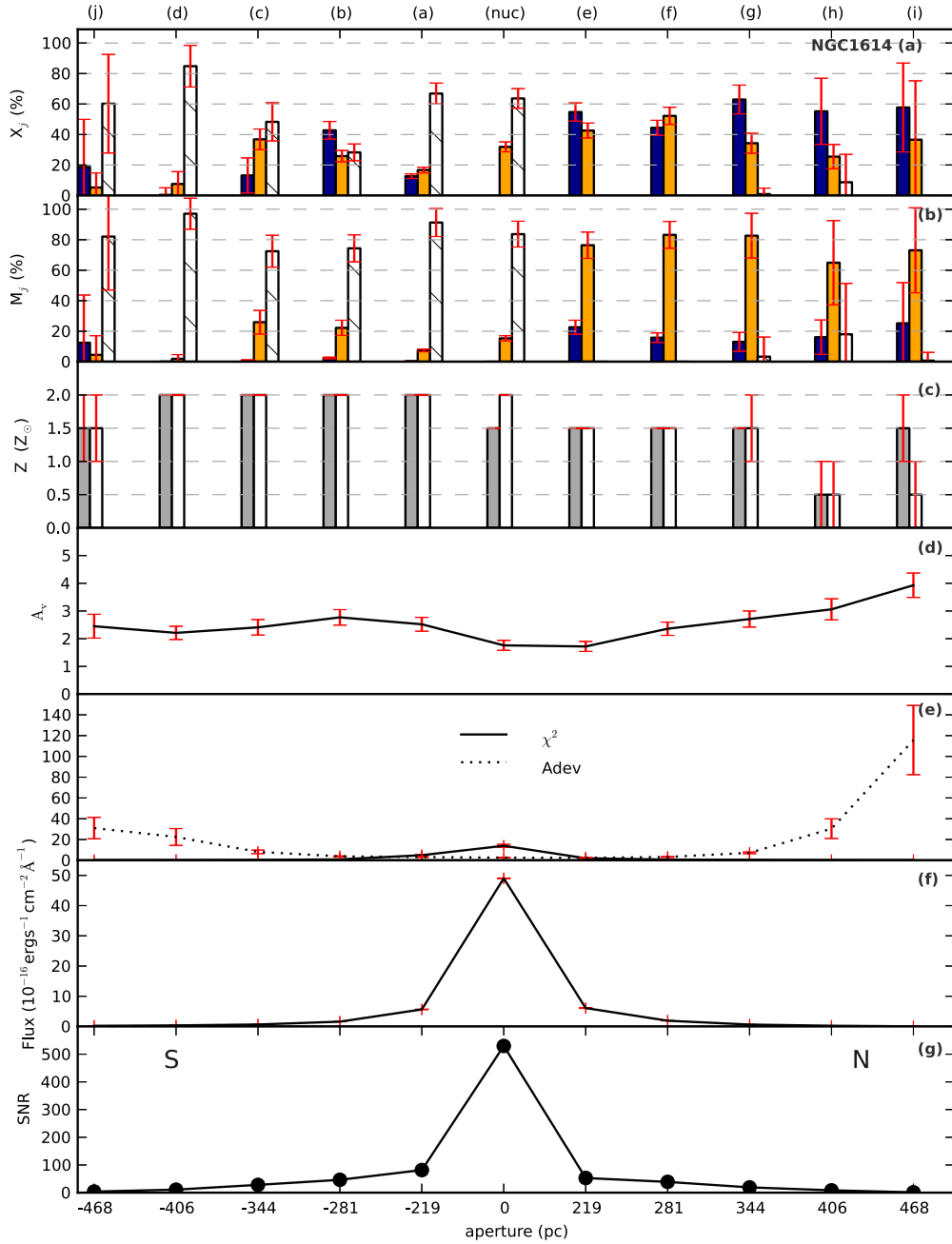
Figure 13. The same as Fig. 12, but for NGC 1614. North (N) and south (S) direction are indicated in the bottom panel.

nuclear region studied by these authors[6]), were investigated by Pastoriza et al. (1993) between 3600 and 9600 Å. In this study, they propose a two-age model (5 and 15 Myr) for the starburst

[6] It is worth mentioning that the apertures used in this source are the most inner ones in the sample, ranging only up to 106 pc from the nucleus.

activity and low-metallicity values (0.2–0.4 $Z_{\odot}$) for the circum-nuclear (400 pc from the centre) and disc H II regions, while the nucleus presented solar abundances, in agreement with our results ($Z \sim Z_{\odot}$ along the galaxy – see Fig. 14c). R08 also studied the inner 56 pc of NGC 3310 in the NIR part of the spectrum, detecting a dominant 1 Gyr old SP. Similar to the scenario we propose for NGC 1614, the low-metallicity SP derived for this source

Figure 14. The same as Fig. 12, but for NGC 3310. North-west (NW) and southeast (SE) direction are indicated in the bottom panel.

suggests that the gas present in the galaxy interacting with NGC 3310 (Balick & Heckman 1981) should be metal poor, giving rise to a metal poorer SP.

We found a extinction of $A_v \sim 1.7$ mag in the nucleus, ranging from 0.27 mag southwards to 1.5 mag towards the north direction

($\bar{A}_v = 1.43 \pm 0.06$). As for NGC 1614, Goldader et al. (1995) derived the extinction for this source and found $A_v = 2.69$ mag (in 3 arcsec × 9 arcsec beam), a slightly larger value than those we found. It is worth mentioning that this is the less interacting galaxy of the sample.
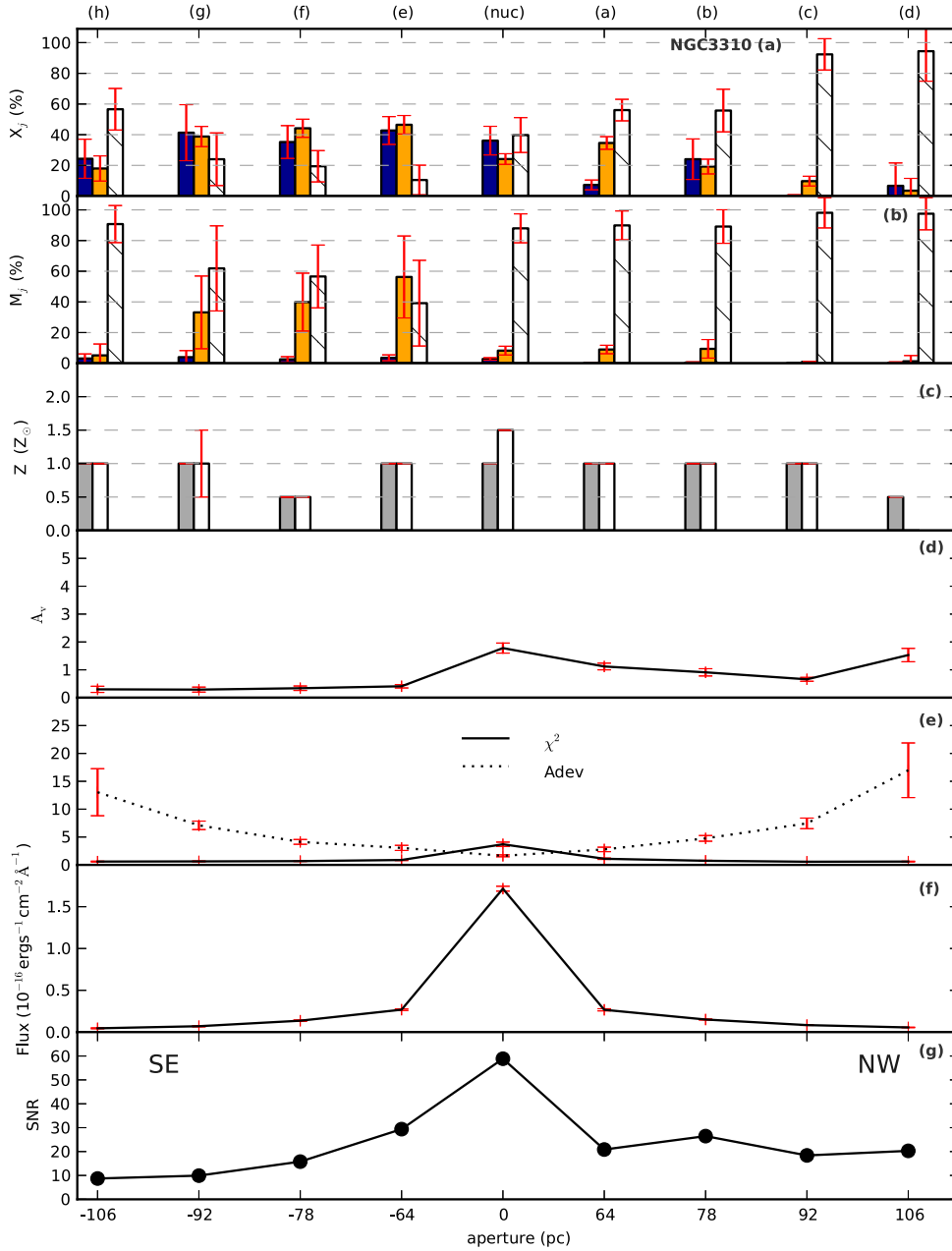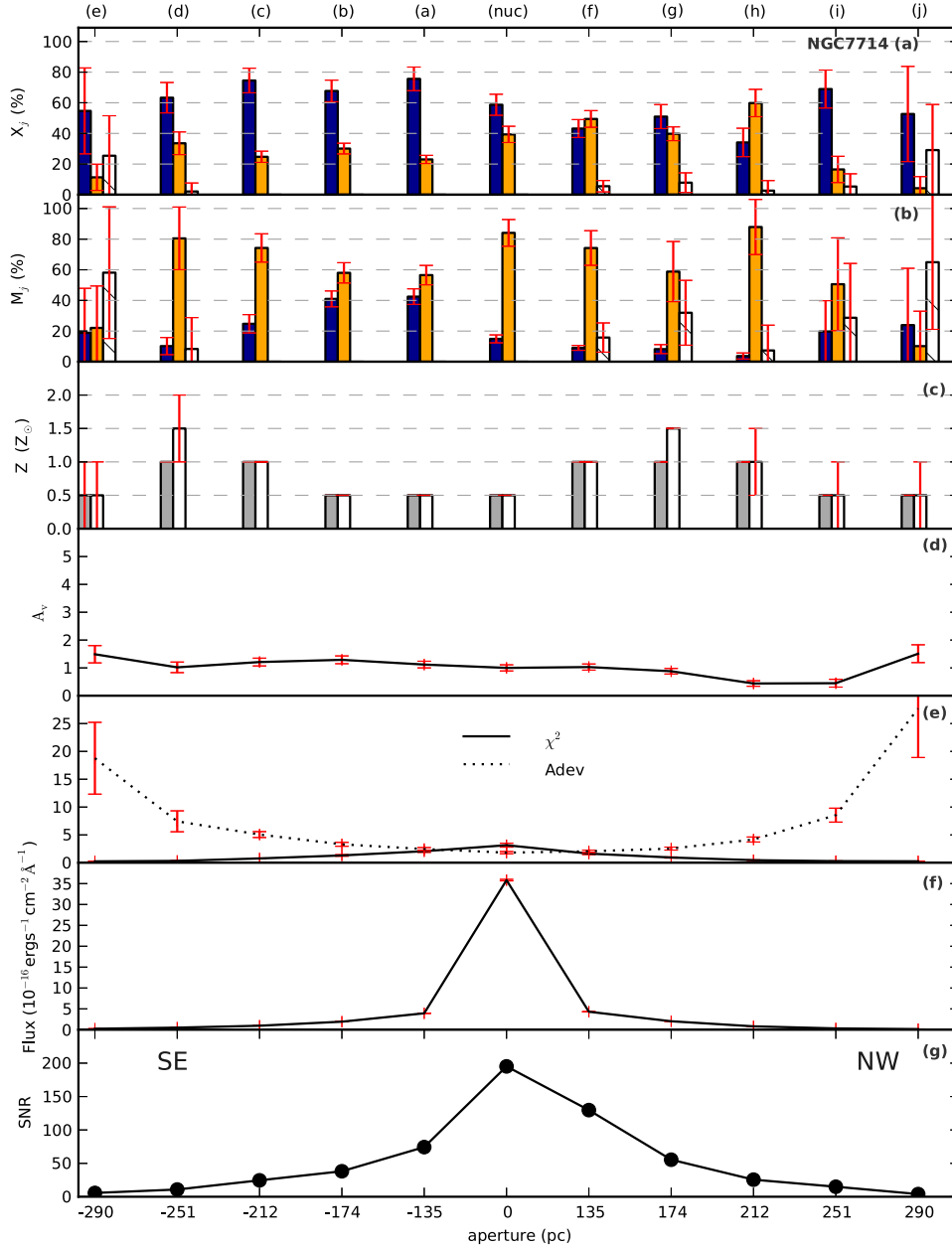
Figure 15. The same as Fig. 12, but for NGC 7714. North-west (NW) and southeast (SE) direction are indicated in the bottom panel.

4.4 NGC 7714

The analysis of the flux contribution of the SP vectors from Fig. 15(a) clearly shows the predominance of the young SP component along the galaxy. While the contribution of this young SP component increases towards south-east, the intermediate-age SP

component increases in the opposite direction. Bernlöhr (1993) has presented an evolutionary model for the pair NGC 7714 and NGC 7715 and stated that NGC 7715 is in the post-burst phase, starting its star formation around 10^8 yr ago, similar to our results. A tidal tail between these two galaxies can bee seen in Smith

1772   *N. Z. Dametto et al.*

Table 2. Average synthesis results.

Galaxy	Aperture (pc)	X_y (per cent) (1)	X_i (per cent) (2)	X_o (per cent) (3)	M_y (per cent) (4)	M_i (per cent) (5)	M_o (per cent) (6)	Z_F ($Z_\odot$) (7)	Z_M ($Z_\odot$) (8)	A_v (mag) (9)	Adev (per cent) (10)	χ^2 (11)
NGC 34	(c)423 S	2 ± 5	7 ± 3	87 ± 11	–	3 ± 2	96 ± 10	2.0	2.0	1.79 ± 0.19	6.3 ± 1.6	0.2
	(b)346 S	36 ± 6	7 ± 1	52 ± 7	1	4 ± 1	94 ± 9	1.5	2.0	2.13 ± 0.22	3.9 ± 0.4	1.0 ± 0.1
	(a)269 S	54 ± 6	17 ± 2	26 ± 4	4 ± 1	15 ± 2	81 ± 8	1.5	1.5	2.86 ± 0.29	2.9 ± 0.3	2.9 ± 0.3
	Nuc	49 ± 5	31 ± 3	18 ± 2	5 ± 1	30 ± 3	64 ± 7	1.5	1.5	3.23 ± 0.32	2.2 ± 0.2	30.4 ± 3.1
	(d)269 N	26 ± 4	28 ± 3	44 ± 6	2	14 ± 2	83 ± 9	1.5	2.0	1.78 ± 0.18	2.1 ± 0.2	1.5 ± 0.2
	(e)346 N	21 ± 5	35 ± 6	41 ± 8	1	29 ± 9	69 ± 11	1.5	1.5	0.97 ± 0.10	3.3 ± 0.4	0.6 ± 0.1
	(f)423 N	29 ± 18	51 ± 11	18 ± 16	2 ± 2	59 ± 27	38 ± 28	1.5	1.5 ± 0.5	0.62 ± 0.12	5.4 ± 0.6	0.2
NGC 1614	(j)468 S	19 ± 31	5 ± 10	60 ± 32	12 ± 31	5 ± 13	82 ± 35	1.5 ± 0.5	1.5 ± 0.5	2.45 ± 0.43	31 ± 10	0.2
	(d)406 S	1 ± 5	8 ± 8	85 ± 14	–	2 ± 3	97 ± 10	2.0	2.0	2.21 ± 0.24	22 ± 8	0.2
	(c)344 S	13 ± 11	37 ± 7	48 ± 13	1 ± 1	26 ± 8	72 ± 10	2.0	2.0	2.41 ± 0.28	8 ± 2	0.3
	(b)281 S	43 ± 6	26 ± 4	28 ± 5	2 ± 1	22 ± 5	74 ± 9	2.0	2.0	2.77 ± 0.28	4	0.9 ± 0.1
	(a)219 S	13 ± 2	17 ± 2	67 ± 7	–	7 ± 1	91 ± 9	2.0	2.0	2.52 ± 0.25	3	4.9 ± 0.5
	Nuc	–	32 ± 3	64 ± 6	–	15 ± 2	84 ± 8	1.5	2.0	1.76 ± 0.18	3	14.0 ± 1.4
	(e)219 N	54 ± 6	43 ± 5	–	22 ± 4	77 ± 9	–	1.5	1.5	1.73 ± 0.18	2	2.0 ± 0.2
	(f)281 N	44 ± 5	52 ± 6	–	16 ± 3	83 ± 9	–	1.5	1.5	2.36 ± 0.24	3	1.0 ± 0.1
	(g)344 N	63 ± 9	34 ± 7	9 ± 4	13 ± 6	83 ± 15	3 ± 13	1.5	1.5 ± 0.5	2.71 ± 0.29	7 ± 1	0.4 ± 0.1
	(h)406 N	55 ± 22	26 ± 8	8 ± 18	16 ± 11	65 ± 28	18 ± 33	0.5 ± 0.5	0.5 ± 0.5	3.06 ± 0.38	30 ± 9	0.3
	(i)468 N	49 ± 29	48 ± 40	–	18 ± 21	81 ± 23	1 ± 3	1.0 ± 0.5	0.5 ± 0.5	3.93 ± 0.41	116 ± 30	0.2 ± 0.1
NGC 3310	(d)106 N	7 ± 15	4 ± 8	94 ± 20	0 ± 1	1 ± 4	97 ± 11	0.5	–	1.53 ± 0.24	17 ± 5	0.6 ± 0.1
	(c)92 N	0 ± 1	10 ± 3	92 ± 10	–	1	98 ± 10	1.0	1.0	0.66 ± 0.07	7 ± 1	0.6 ± 0.1
	(b)78 N	24 ± 13	19 ± 5	56 ± 14	–	9 ± 6	89 ± 11	1.0	1.0	0.91 ± 0.13	5 ± 1	0.7 ± 0.1
	(a)64 N	6 ± 3	39 ± 5	53 ± 7	–	13 ± 3	86 ± 9	1.5	1.0	1.09 ± 0.11	3	1.2 ± 0.1
	Nuc	22 ± 4	22 ± 3	56 ± 7	2	5 ± 2	92 ± 9	1.0	1.0	1.73 ± 0.17	2	5.0 ± 0.5
	(e)64 S	39 ± 9	47 ± 6	14 ± 11	3 ± 2	48 ± 26	48 ± 27	1.0	1.0 ± 0.5	0.39 ± 0.07	3 ± 1	1.0 ± 0.1
	(f)78 S	35 ± 11	44 ± 6	19 ± 10	3 ± 2	40 ± 19	57 ± 20	0.5	0.5	0.34 ± 0.08	4	0.7 ± 0.1
	(g)92 S	34 ± 19	43 ± 8	28 ± 17	3 ± 3	39 ± 21	57 ± 23	1.0	1.0 ± 0.5	0.27 ± 0.08	7 ± 1	0.6 ± 0.1
	(h)106 S	24 ± 13	18 ± 8	57 ± 14	3 ± 3	5 ± 7	91 ± 12	1.0	1.0	0.30 ± 0.11	13 ± 4	0.6 ± 0.1
NGC 7714	(e)290 S	55 ± 28	11 ± 9	25 ± 26	19 ± 29	22 ± 27	58 ± 43	0.5 ± 0.5	0.5 ± 0.5	1.49 ± 0.31	19 ± 6	0.3
	(d)251 S	63 ± 10	34 ± 7	2 ± 6	10 ± 6	81 ± 20	8 ± 20	1.0	1.5 ± 0.5	1.02 ± 0.19	7 ± 2	0.3
	(c)212 S	75 ± 8	25 ± 4	–	25 ± 6	74 ± 9	–	1.0	1.0	1.21 ± 0.14	5 ± 1	0.8 ± 0.1
	(b)174 S	68 ± 7	30 ± 3	–	41 ± 5	58 ± 7	–	0.5	0.5	1.29 ± 0.14	3	1.3 ± 0.1
	(a)135 S	76 ± 8	23 ± 3	–	42 ± 5	56 ± 6	–	0.5	0.5	1.12 ± 0.12	2	2.1 ± 0.2
	Nuc	59 ± 7	39 ± 5	–	15 ± 3	84 ± 9	–	0.5	0.5	1.00 ± 0.11	2	3.2 ± 0.4
	(f)135 N	43 ± 6	49 ± 5	6 ± 4	9 ± 2	74 ± 11	16 ± 10	1.0	1.0	1.03 ± 0.11	2	1.6 ± 0.2
	(g)174 N	51 ± 8	40 ± 5	8 ± 6	8 ± 3	59 ± 20	32 ± 21	1.0	1.5	0.88 ± 0.10	3	0.9 ± 0.1
	(h)212 N	34 ± 9	60 ± 9	3 ± 7	3 ± 2	88 ± 18	7 ± 17	1.0	1.0 ± 0.5	0.44 ± 0.10	4	0.4 ± 0.1
	(i)251 N	69 ± 12	16 ± 9	5 ± 8	20 ± 20	51 ± 30	29 ± 35	0.5	0.5 ± 0.5	0.45 ± 0.14	9 ± 1	0.3
	(j)290 N	53 ± 31	4 ± 8	29 ± 30	24 ± 37	10 ± 23	65 ± 44	0.5	0.5 ± 0.5	1.51 ± 0.32	28 ± 9	0.3

Notes: (1), (2), (3): average contribution in flux of the young ($t \leq 50 \times 10^6$ yr), intermediate-age ($50 \times 10^6 < t \leq 2 \times 10^9$ yr) and old ($t > 2 \times 10^9$ yr) SP component, respectively; (4), (5), (6): average contribution of the SP components in mass; (7), (8): flux- and mass-weighted mean metallicities; (9) visual extinction; (10) percent mean deviation $|O_\lambda - M_\lambda|/O_\lambda$, where O_λ is the observed spectrum and M_λ is the fitted model and (11) reduced chi square. Whenever there are no error values, the uncertainties are zero.

& Wallin (1992), and we suggest that the SP distribution northwards (increasing intermediate-age SP component) can be related to this post-starburst population in NGC 7715. In fact, such an age is consistent with the scenario proposed by González-Delgado et al. (1999), where the presence of RSGs is associated with the Ca II triplet, present in the galaxy spectrum. Besides, this result is further supported by the fact that this is the side in which NGC 7714 interacted with NGC 7715 in the past (Smith, Struck & Pogge 1997; Struck & Smith 2003). Several previous studies in the UV and optical part of the spectrum (González-Delgado et al. 1995, 1999; Lançon et al. 2001; Cid Fernandes et al. 2003) detected young-age SP from the inner hundreds to thousands of parsecs, in agreement with our work. R08 also found a dominant star formation burst with 1 Gyr old studying the inner 115 pc of this source.

The metallicity, as can be seen from Fig. 15(c), increases with the increase of the intermediate SP, as expected. The lower mean

metallicity values derived for this source can be explained in the scenario proposed by González-Delgado et al. (1995), in which the unprocessed gas from the companion NGC 7715 could be the source of fuel to the starburst in NGC 7714.

As we can see from Fig. 15(d), the visual extinction is nearly constant along the galaxy with $\bar{A}_v = 1.13 \pm 0.04$, similar to the results found in the literature. For example, Kotilainen et al. (2001) derived $A_v = 1.2$ mag (in a 6 arcsec × 7 arcsec beam) from NIR colours and $A_v = 1.7$ mag from recombination line fluxes, while Oliva et al. (1995) found $A_v = 1$–2 mag (in a 2.2 arcsec × 4.4 arcsec beam) assuming an intrinsic stellar colour $H - K = 0.2$. Moreover, Puxley & Brand (1994) found $A_v = 1.8 \pm 0.7$ mag for a point-source model or $A_v = 3.9 \pm 1.7$ mag if sources and dust are homogeneously distributed. They claim, however, that different from NGC 1614, NGC 7714 presents low-extinction values and can indeed be modelled with a simple foreground dust screen model.

4.5 Emission gas

The sample of galaxies analysed in this work display strong emission lines in their spectra, as we can see from Figs 2–5. Apart from the absorption features that shape the continuum emission, these sources have been classified as star-forming/H ɪɪ galaxies by several previous works, particularly in the optical region (e.g. González-Delgado et al. 1999; Alonso-Herrero et al. 2001; Wehner et al. 2006; Schweizer & Seitzer 2007). Thus, we measured these nebular atomic emission lines ([S ɪɪɪ] λ9530, He ɪ λ10 830, [Fe ɪɪ] λ12 570, Paβ λ12 810, [Fe ɪɪ] λ16 440 and Brγ λ21 650) and the H₂ λ21 210 line. It is important to mention that the standard procedure to properly measure emission lines consist of subtracting the stellar continuum fitted by SP synthesis methods. However, we did not subtract the stellar continuum, because the emission lines were severely diluted as a result of the smoothing done in the observed spectra to match the resolution of M05 models ($R \leq 250$ – see Section 3).

The emission-line fluxes can be used, for example, to estimate the reddening effects on the emission gas. Therefore, we derived the interstellar extinction c, the colour excess $E(B - V)$ and the visual extinction A_v (equation 6) for each aperture of the galaxies by means of the emission lines. To this purpose, we assume the ratio of total to selective extinction as $R_V = 4.05 \pm 0.80$, from Calzetti et al. (2000), which is the most suitable one when dealing with SBs (Calzetti et al. 2000; Fischera, Dopita & Sutherland 2003). Moreover, we adopt the intrinsic value of 5.86 for the emission-line ratio Paβ/Brγ, following the case B ($T = 10\,000$ K, $N = 10^2$ cm^{-3}; Osterbrock & Ferland 2006). Using the above values, one can determine A_v following the equation:

$$A_v = -15.24 \log \left(\frac{1}{5.88} \frac{Pa\beta}{Br\gamma} \right). \tag{6}$$

The measured fluxes are listed in Table 3 and the reddening parameters in Table 4. In a previous work, as we have already mentioned, R08 performed SP synthesis in the nuclear region of the four galaxies studied here. They derived lower values for the colour excess $E(B - V)$ than those present in Table 4. We suggest that this difference can be related to the use of Cardelli et al. (1989) extinction law by R08 when fitting the SP, which is not the most suitable one for SBs (Calzetti, Kinney & Storchi-Bergmann 1994; Fischera et al. 2003).

In fact, when comparing the results for A_v obtained with the emission-line ratio Paβ/Brγ (Table 4 – column 2) and those derived by STARLIGHT code (Table 4 – column 3), we can see that the mean values derived from the emission lines are larger than those obtained from the spectral fitting. A possible explanation for this discrepancy is to consider that the hot ionizing stars could be associated with a dustier region with respect to the cold SP (Calzetti et al. 1994). Another important aspect is that as the merger experienced by the galaxies progresses, tidally induced gas motions and outflows from galactic winds become more frequent (e.g. Heckman, Armus & Miley 1990). In this scenario, shocks induced by large-scale gas flows have an influence on the emission-line gas (e.g. Colina & Montreal-Ibero 2005) and can contaminate the line ratios.

The emission lines can also be used to estimate the SFR of the sources. Adopting SFR $= L(H\alpha) \times 7.9 \times 10^{-42}$ and $L(H\alpha) = 103 L(Br\gamma)$ (Kennicutt 1998), we derived the SFR for each aperture of our galaxy sample using their reddening-corrected Brγ luminosities. The SFRs are listed in Table 4. Since STARLIGHT outputs the mass that have been processed into stars over the last t years ($M_\star^t$), this can be used to estimate the mean SFR over a period of time t.

We have estimated the mean SFR⋆ over the last $t \leq 10$ Myr as being the ratio of $M_\star^t/t$. The obtained values are also listed in Table 4.

As we can see from Table 4, the nuclear SFRs derived through Brγ (column 5) are those that exhibit the major discrepancies when compared to those calculated through STARLIGHT output. In fact, since our sample comprises only SBs, it is likely that a significant fraction of the star formation occurs in dusty regions (Imanishi & Nakanishi 2013). In this sense, our results of the SFR may suggest that the NIR spectral range would probe weaker obscured star-forming regions. Thus, we may miss dustier starburst regions, once our values tend to be smaller than those calculated in larger wavelengths.

For NGC 34, Fernández et al. (2010) calculated the SFR from radio luminosity and found a value of 64 M⊙ yr^{-1} (in a 3 arcmin× 2 arcmin beam), in agreement with SFR ~ 50 M⊙ yr^{-1} derived by Prouton et al. (2004) from the FIR luminosity for similar beam. For NGC 1614, Alonso-Herrero et al. (2001) found SFR $= 52$ M⊙ yr^{-1} from integrated FIR luminosity (in a 45 arcsec× 250 arcsec beam) and assuming that 70 per cent of this star formation occurs in the nucleus, they predict a nuclear SFR of 36 M⊙ yr^{-1}. For NGC 1614 and NGC 7714, assuming a constant star formation model, Kotilainen et al. (2001) derived SFRs ranging from 2.1 to 4.8 M⊙ yr^{-1} (in a 3.9 arcsec aperture) and 0.1 to 3.9 M⊙ yr^{-1} (in a 11.2 arcsec aperture), respectively, while assuming a model of an instantaneous burst of star formation (ISF) they derived SFRs ranging from 11 to 25 M⊙ yr^{-1} and 0.4 to 16 M⊙ yr^{-1}, respectively. The results derived assuming an ISF are closer to the values derived by us for NGC 1614 and NGC 7714 and we believe that the reason for that is the resembling spacial scale used in their work in relation to this study. Moreover, we suggest that the negligible value derived for the nuclear SFR of NGC 1614 by STARLIGHT can be explained if we consider the LINER classification of this source. In this scenario, the strong emission lines present in the nuclear spectra of this source can be associated with an AGN activity, which would quench the star formation (Nesvadba et al. 2006) in the nucleus and limit it to the outer regions.[7] It is important to reinforce the scenario in which shocks induced by large-scale gas flows in merging systems affect the emission-line gas and may contaminate the line ratios used to determine the SFRs and A_v for example.

4.6 Comparison between M05 and M11 models

In order to deepen our analysis, we performed SP synthesis for the four galaxies using the new models computed by Maraston & Strömbäck (2011, hereafter M11). These higher resolution models have been constructed in the same way as M05 (e.g. stellar energetics, the atmospheric parameters, the treatment of the TP-AGB phase and horizontal branch morphology), but are based on different stellar spectral libraries (empirical libraries). The set of templates that extend to the NIR are those based on the Pickles (1998) library. Rather than including spectra of individual stars, it practically averages out spectra from several sources. However, since there are not enough spectra to cover all evolutionary phases to a tolerable degree for other than solar metallicities, models were computed with $Z = Z_\odot$. Moreover, above ~ 1 μm about half of the spectra lack spectroscopic observations leading the authors to construct a smooth energy distribution from broad-band photometry, resulting in a featureless region on the M11 spectra. This may imply that some NIR absorption features are not well resolved, even for these

---

[7] A proper analysis of this evidence would require an IFU study of the nuclear region of this galaxy.

Table 3. Measured fluxes in units of 10^{-15} erg cm^{-2} s^{-1}.

Galaxy	Aperture	[S III] 0.953 μm (1)	He I 1.083 μm (2)	[Fe II] 1.257 μm (3)	Paβ 1.281 μm (4)	[Fe II] 1.644 μm (5)	H$_2$ 2.121 μm (6)	Brγ 2.165 μm (7)
NGC 34	(c)423 S	0.54 ± 0.21	0.46 ± 0.17	–	0.23 ± 0.08	0.25 ± 0.14	0.25 ± 0.03	0.09 ± 0.03
	(b)346 S	1.15 ± 0.31	0.65 ± 0.26	0.38 ± 0.12	0.37 ± 0.13	0.00 ± 0.00	0.73 ± 0.11	0.22 ± 0.06
	(a)269 S	1.46 ± 0.30	2.24 ± 0.52	1.63 ± 0.15	1.23 ± 0.11	1.78 ± 0.45	2.08 ± 0.22	0.81 ± 0.12
	Nuc	10.60 ± 0.84	12.00 ± 1.66	8.41 ± 0.82	7.58 ± 0.71	9.32 ± 2.34	8.21 ± 0.75	4.45 ± 0.54
	(d)269 N	2.77 ± 0.32	2.92 ± 0.59	1.74 ± 0.17	1.06 ± 0.11	1.65 ± 0.48	1.48 ± 0.12	0.68 ± 0.08
	(e)346 N	0.70 ± 0.21	–	0.48 ± 0.14	0.38 ± 0.11	–	0.63 ± 0.07	–
	(f)423 N	–	–	–	–	–	–	–
NGC 1614	(j)468 S	0.80 ± 0.19	1.13 ± 0.20	0.41 ± 0.15	0.57 ± 0.09	0.28 ± 0.06	0.08 ± 0.03	0.15 ± 0.04
	(d)406 S	1.55 ± 0.28	1.89 ± 0.26	0.50 ± 0.08	0.92 ± 0.08	0.74 ± 0.08	0.14 ± 0.03	0.36 ± 0.03
	(c)344 S	4.14 ± 0.36	3.20 ± 0.23	1.12 ± 0.09	2.68 ± 0.10	1.28 ± 0.11	0.53 ± 0.06	1.12 ± 0.07
	(b)281 S	14.40 ± 0.36	11.00 ± 0.32	2.78 ± 0.18	9.46 ± 0.17	3.33 ± 0.24	0.83 ± 0.09	3.47 ± 0.11
	(a)219 S	46.20 ± 0.44	33.90 ± 0.64	7.11 ± 0.27	25.80 ± 0.27	8.17 ± 0.84	1.36 ± 0.17	9.67 ± 0.20
	Nuc	227.00 ± 1.79	187.00 ± 3.60	28.20 ± 1.49	97.30 ± 1.32	17.80 ± 4.40	–	32.00 ± 1.68
	(e)219 N	64.40 ± 0.33	51.00 ± 0.59	7.79 ± 0.34	29.80 ± 0.32	8.84 ± 0.85	1.35 ± 0.15	10.40 ± 0.17
	(f)281 N	27.90 ± 0.35	21.30 ± 0.23	4.12 ± 0.17	13.90 ± 0.16	4.61 ± 0.24	0.98 ± 0.08	4.63 ± 0.08
	(g)344 N	9.61 ± 0.31	7.01 ± 0.22	1.48 ± 0.14	5.21 ± 0.14	1.93 ± 0.11	0.65 ± 0.07	1.71 ± 0.07
	(h)406 N	3.37 ± 0.31	2.24 ± 0.25	0.57 ± 0.10	1.87 ± 0.10	0.57 ± 0.09	0.43 ± 0.07	0.65 ± 0.07
	(i)468 N	0.65 ± 0.17	0.91 ± 0.21	0.36 ± 0.09	0.73 ± 0.10	–	0.24 ± 0.07	0.13 ± 0.05
NGC 3310	(d)106 N	–	–	–	–	–	–	–
	(c)92 N	0.09 ± 0.03	–	–	0.03 ± 0.02	–	–	–
	(b)78 N	0.26 ± 0.06	0.13 ± 0.04	–	–	–	–	0.03 ± 0.01
	(a)64 N	0.73 ± 0.04	0.40 ± 0.03	0.07 ± 0.02	0.28 ± 0.02	0.13 ± 0.03	–	0.10 ± 0.01
	Nuc	6.58 ± 0.10	3.57 ± 0.11	0.75 ± 0.07	2.44 ± 0.07	0.86 ± 0.13	–	0.77 ± 0.05
	(e)64 S	0.74 ± 0.05	0.38 ± 0.05	0.09 ± 0.02	0.19 ± 0.02	0.11 ± 0.03	0.06 ± 0.02	0.06 ± 0.01
	(f)78 S	0.31 ± 0.06	0.25 ± 0.08	–	0.07 ± 0.03	0.05 ± 0.02	–	–
	(g)92 S	0.15 ± 0.06	–	–	–	–	–	–
	(h)106 S	–	–	–	–	–	–	–
NGC 7714	(e)290 S	3.61 ± 0.25	1.82 ± 0.19	0.36 ± 0.08	1.21 ± 0.07	0.33 ± 0.08	0.10 ± 0.04	0.30 ± 0.05
	(d)251 S	7.17 ± 0.37	4.27 ± 0.18	0.48 ± 0.14	2.58 ± 0.14	0.69 ± 0.13	–	0.47 ± 0.05
	(c)212 S	15.90 ± 0.27	10.10 ± 0.17	0.66 ± 0.16	5.24 ± 0.12	0.71 ± 0.13	0.17 ± 0.05	1.14 ± 0.05
	(b)174 S	37.30 ± 0.33	23.50 ± 0.25	1.98 ± 0.16	11.20 ± 0.13	1.96 ± 0.21	–	2.78 ± 0.08
	(a)135 S	59.90 ± 0.40	41.10 ± 0.41	2.98 ± 0.20	18.50 ± 0.17	2.59 ± 0.27	–	4.55 ± 0.11
	Nuc	195.00 ± 1.89	132.00 ± 2.40	17.00 ± 0.91	63.30 ± 0.97	17.10 ± 2.83	2.56 ± 0.63	15.90 ± 0.66
	(f)135 N	24.40 ± 0.28	14.90 ± 0.33	4.06 ± 0.17	9.12 ± 0.15	3.76 ± 0.34	0.55 ± 0.08	2.51 ± 0.09
	(g)174 N	14.60 ± 0.20	8.67 ± 0.20	2.43 ± 0.16	5.69 ± 0.13	2.24 ± 0.17	0.39 ± 0.07	1.44 ± 0.06
	(h)212 N	5.40 ± 0.21	3.21 ± 0.14	0.85 ± 0.08	2.14 ± 0.08	1.00 ± 0.08	0.19 ± 0.06	0.57 ± 0.04
	(i)251 N	1.27 ± 0.18	0.98 ± 0.14	0.29 ± 0.07	0.74 ± 0.08	0.29 ± 0.07	–	0.09 ± 0.03
	(j)290 N	0.25 ± 0.10	0.14 ± 0.07	–	0.14 ± 0.04	0.14 ± 0.06	–	–

higher resolution models. The authors also call attention for the youngest ages (below ∼100 Myr), which should be used somewhat more cautiously, once their spectra are significantly attenuated by dust absorption in the UV.

To allow a proper comparison between both models sets, avoiding the discrepancies due to different metallicity ranges, we used a reduced base including only the solar metallicity SSPs from M05 models with the same age range used in Section 4. Figs 16 and 17 present the differences in STARLIGHT output parameters X_y, X_i, X_o, A_v, Adev and χ^2 between M05 and M11 models.

In general, M11 models enhance the old-/intermediate-age SP component in favour of younger ages when compared to M05, leading to small contributions of X_y (the young component would not cross the limit of 40 per cent along the galaxies with the exception of the nucleus of NGC 34 in which the young component reaches ∼48 per cent). This could be related with M11 models issue regarding younger ages, as mentioned before. The intermediate-age

SP component is the less affected by the choice of the model; however, this SP component tends to get higher values with M11 models, mainly in two galaxies, NGC 34 and NGC 7714. These two sources are the ones that display higher young SP contribution when using M05 models with the full range in metallicities of our base set.

The extinction A_v results are in good agreement (see Figs 16 and 17 – middle panels). NGC 3310 and NGC 7714 though, tend to be less reddened when using M11 models, as well as they present higher Adev and χ^2 values (indicators of the quality of the fit – see Section 3), as we can see by analysing the middle and left-hand panels in Figs 16 and 17.

Due to the limitations of M11 models as discussed above, it is not clear whether the use of these higher resolution models would bring an improvement capable of compensating the fact that they are only available for solar metallicities. Thus, we conclude that the use of low-resolution M05 models are still the best option in this wavelength range.

Table 4. Emission-line ratio and Paβ/Brγ derived quantities: c, A_v, $E(B - V)$ and SFR.

Galaxy	Aperture	c (1)	A_v (mag) (2)	$A_v^\star$ (mag) (3)	$E(B - V)$ (mag) (4)	SFR ($M_\odot$ yr^{-1}) (5)	SFR* ($M_\odot$ yr^{-1}) (6)
NGC 34	(c)423 S	2.21 ± 1.28	5.52 ± 0.32	2.86 ± 0.29	1.36 ± 0.22	0.13 ± 0.08	3.65 ± 0.60
	(b)346 S	3.32 ± 1.18	8.28 ± 0.29	2.13 ± 0.22	2.05 ± 0.33	0.48 ± 0.26	0.65 ± 0.21
	(a)269 S	3.59 ± 0.46	8.96 ± 0.11	1.79 ± 0.19	2.21 ± 0.35	1.97 ± 0.46	0.02 ± 0.06
	Nuc	3.28 ± 0.41	8.20 ± 0.10	3.23 ± 0.32	2.02 ± 0.32	9.63 ± 1.93	34.64 ± 3.68
	(d)269 N	3.52 ± 0.42	8.79 ± 0.10	1.78 ± 0.18	2.17 ± 0.34	1.62 ± 0.32	2.43 ± 0.65
	(e)346 N	–	–	0.97 ± 0.10	–	–	0.28 ± 0.10
	(f)423 N	–	–	0.62 ± 0.12	–	–	0.20 ± 0.18
	Mean	2.99 ± 0.24	7.45 ± 0.06	2.49 ± 0.10	2.01 ± 0.13		
NGC 1614	(j)468 S	1.16 ± 0.82	2.89 ± 0.20	2.52 ± 0.25	0.71 ± 0.12	0.09 ± 0.04	1.11 ± 0.14
	(d)406 S	2.21 ± 0.32	5.52 ± 0.08	2.77 ± 0.28	1.36 ± 0.22	0.34 ± 0.05	1.28 ± 0.20
	(c)344 S	2.38 ± 0.19	5.95 ± 0.05	2.41 ± 0.28	1.47 ± 0.23	1.13 ± 0.11	0.18 ± 0.16
	(b)281 S	2.04 ± 0.10	5.09 ± 0.02	2.21 ± 0.24	1.26 ± 0.20	3.04 ± 0.15	0.00 ± 0.03
	(a)219 S	2.09 ± 0.06	5.23 ± 0.02	2.45 ± 0.43	1.29 ± 0.20	8.67 ± 0.37	0.08 ± 0.14
	Nuc	1.75 ± 0.14	4.36 ± 0.04	1.76 ± 0.18	1.08 ± 0.17	25.06 ± 1.93	–
	(e)219 N	1.91 ± 0.05	4.76 ± 0.01	1.73 ± 0.18	1.17 ± 0.19	8.66 ± 0.23	12.44 ± 1.9
	(f)281 N	1.78 ± 0.06	4.45 ± 0.01	2.36 ± 0.24	1.10 ± 0.17	3.67 ± 0.10	6.60 ± 1.43
	(g)344 N	1.74 ± 0.13	4.35 ± 0.03	2.71 ± 0.29	1.07 ± 0.17	1.34 ± 0.09	0.89 ± 0.15
	(h)406 N	1.89 ± 0.32	4.73 ± 0.08	3.06 ± 0.38	1.17 ± 0.18	0.54 ± 0.09	0.24 ± 0.14
	(i)468 N	0.12 ± 1.08	0.30 ± 0.27	3.93 ± 0.41	0.08 ± 0.02	0.06 ± 0.03	0.04 ± 0.03
	Mean	1.17 ± 0.03	2.94 ± 0.01	2.66 ± 0.08	1.19 ± 0.02		
NGC 3310	(d)106 N	–	–	1.09 ± 0.11	–	–	–
	(c)92 N	–	–	0.91 ± 0.13	–	–	–
	(b)78 N	–	–	0.66 ± 0.07	–	–	–
	(a)64 N	1.97 ± 0.33	4.91 ± 0.08	1.53 ± 0.24	1.21 ± 0.19	–	–
	Nuc	1.64 ± 0.19	4.09 ± 0.05	1.73 ± 0.17	1.01 ± 0.16	0.02	0.12 ± 0.02
	(e)64 S	1.64 ± 0.52	4.10 ± 0.13	0.39 ± 0.07	1.01 ± 0.16	–	–
	(f)78 S	–	–	0.34 ± 0.08	–	–	–
	(g)92 S	–	–	0.27 ± 0.08	–	–	–
	(h)106 S	–	–	0.30 ± 0.11	–	–	–
	Mean	1.74 ± 0.16	4.35 ± 0.04	1.43 ± 0.06	1.08 ± 0.01		
NGC 7714	(e)290 S	1.00 ± 0.47	2.49 ± 0.12	1.12 ± 0.12	0.62 ± 0.10	0.06 ± 0.01	2.58 ± 0.31
	(d)251 S	0.18 ± 0.32	0.45 ± 0.08	1.29 ± 0.14	0.11 ± 0.02	0.07 ± 0.01	1.63 ± 0.24
	(c)212 S	0.65 ± 0.13	1.63 ± 0.03	1.21 ± 0.14	0.40 ± 0.06	0.20 ± 0.01	0.36 ± 0.09
	(b)174 S	1.00 ± 0.08	2.50 ± 0.02	1.02 ± 0.19	0.62 ± 0.10	0.56 ± 0.02	0.15 ± 0.05
	(a)135 S	0.98 ± 0.07	2.44 ± 0.02	1.49 ± 0.31	0.60 ± 0.10	0.90 ± 0.03	0.07 ± 0.05
	Nuc	1.03 ± 0.12	2.58 ± 0.03	1.00 ± 0.11	0.64 ± 0.10	3.23 ± 0.20	15.48 ± 2.35
	(f)135 N	1.28 ± 0.10	3.19 ± 0.03	1.03 ± 0.11	0.79 ± 0.12	0.56 ± 0.03	1.70 ± 0.26
	(g)174 N	1.05 ± 0.13	2.63 ± 0.03	0.88 ± 0.10	0.65 ± 0.10	0.30 ± 0.02	0.48 ± 0.11
	(h)212 N	1.19 ± 0.21	2.97 ± 0.05	0.44 ± 0.10	0.73 ± 0.12	0.12 ± 0.01	0.07 ± 0.03
	(i)251 N	–	–	0.45 ± 0.14	–	0.01 ± 0.00	0.01 ± 0.01
	(j)290 N	–	–	1.51 ± 0.32	–	–	0.03 ± 0.02
	Mean	0.86 ± 0.04	2.15 ± 0.01	1.13 ± 0.04	0.64 ± 0.02		

Notes: (1) interstellar extinction; (2) visual extinction derived by the emission-lines ratio; (3) visual extinction derived by STARLIGHT; (4) colour excess; (5) SFR derived by the emission-lines ratio; (6) SFR derived from STARLIGHT output parameters. Whenever there are no error values, the uncertainties are zero.

5 CONCLUSIONS

We have studied, by means of NIR spectroscopy (from 0.8 to 2.4 μm), the spatial variation of the SPs in the central region of the local universe SBs NGC 34, NGC 1614, NGC 3310 and NGC 7714. Therefore, we employed the STARLIGHT code updated with M05 EPS models, which are the most suitable ones, once they include a proper treatment of the TP-AGB phase crucial to model the SPs in the NIR (M05; Riffel et al. 2011a). Our main conclusions are as follows.

(i) The NIR light dominating the off-nuclear apertures of the galaxies is due to young-/intermediate-age stars ($t \leq 2 \times 10^9$ yr), summing from ∼40 per cent up to 100 per cent of the light contribution.

(ii) A predominance of young-/intermediate-age SP ($t \leq 2 \times 10^9$ yr) is observed also in the central region of the galaxies, except for NGC 1614 in which the old SP ($t \geq 2 \times 10^9$ yr) prevails in the nucleus, but the younger ages predominate the nuclear surroundings of this source.

(iii) Evidence of a ring-like structure of about 600 pc and a secondary nucleus at ∼300 pc north from the nucleus was detected in NGC 1614.

(iv) The increase in the intermediate-age SP component north from the nucleus in NGC 7714 could be related to the SP present in its companion, NGC 7715.

(v) The merger experienced by NGC 1614, NGC 3310 and NGC 7714 can explain the discrepancy in its metallicity values, once the fresh unprocessed metal poorer gas from the
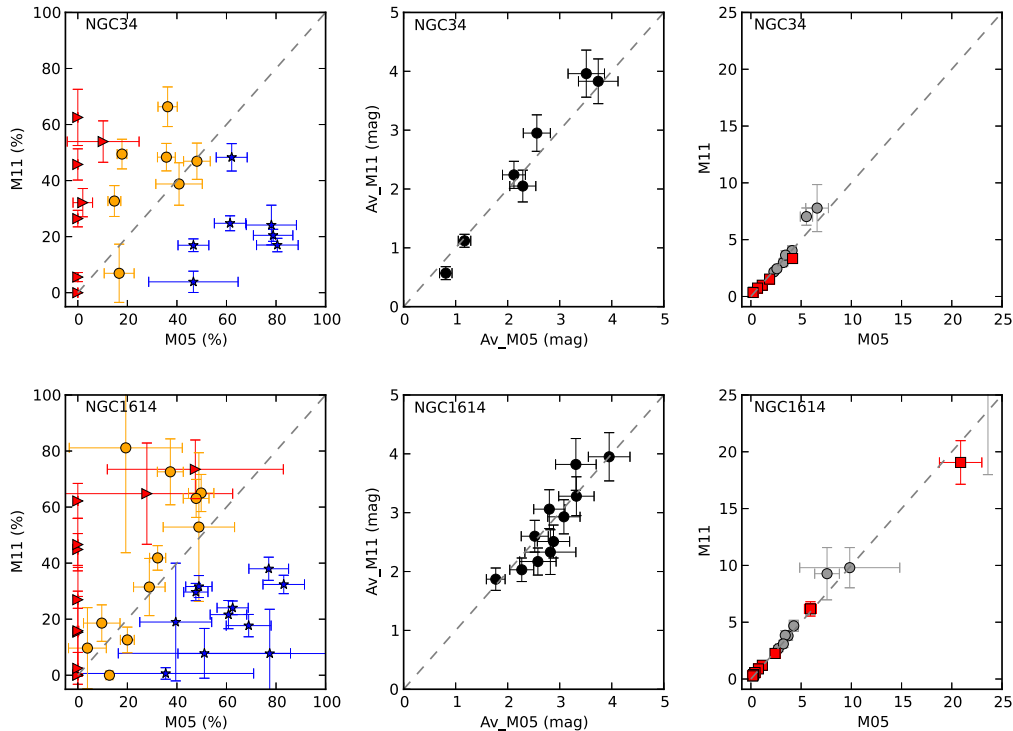
Figure 16. Comparison between the results obtained using M05 and M11 models for galaxies NGC 34 (upper panels) and NGC 1614 (bottom panels). Left-hand panels: SP distribution. The different markers indicate the SP age component: X_y (star), X_i (filled circle), X_o (triangle). Middle panels: optical extinction (A_v). Right-hand panels: quality of the fit. The square markers represent the χ^2 and the filled circles the Adev.

destroyed/interacting companion galaxy is driven to the centre of the galaxies and mixed with the central region gas, before star formation takes place. In this context, the lower metallicity values derived for the young SP component ($t \leq 5 \times 10^6$ yr) can be understood as the diluted gas of the remnant.

(vi) As our sample present strong emission lines in their spectra, we measure these nebular lines ([S III] $\lambda 9530$, He I $\lambda 10\,830$, [Fe II] $\lambda 12\,570$, Paβ $\lambda 12\,810$, [Fe II] $\lambda 16\,440$, H$_2$(1.0)S(1)$_o$ $\lambda 21\,210$ and Brγ $\lambda 21\,650$) and derived values for the visual extinction (A_v) and SFR along the galaxies. Our results on the interstellar extinction tend to agree with those found in the literature. We derived $\bar{A}_v = 7.45 \pm 0.06$, 2.94 ± 0.01, 4.35 ± 0.04 and 2.15 ± 0.01 for NGC 34, NGC 1614, NGC 3310 and NGC 7714, respectively. Our values for the SFRs tend to be smaller than those calculated in other wavelengths.

(vii) The comparison between M05 and M11 models indicates that M11 models tend to enhance the old-/intermediate-age SP contribution in favour of younger ages. This could be related to the fact that the templates representing the youngest ages (below ~ 100 Myr) are significantly attenuated by dust absorption in the UV (M11). Moreover, above ~ 1 μm about half of the spectra lack spectroscopic observations leading the authors to construct a smooth energy distribution from broad-band photometry. This may imply that some NIR absorption features are not well resolved, even for these higher resolution models. Due to these limitations of M11 models, it is not clear whether the use of these higher resolution models would

bring an improvement capable of compensating the fact that they are only available for solar metallicities. Thus, we conclude that the use of low-resolution M05 models is still the best option in the NIR wavelength range.

Therefore, the study of the distribution of the SP using the NIR spectral range is a useful tool in order to build a scenario for the star formation along the sources. Moreover, the results for these star-forming interacting systems in the local universe can provide further support to the study of high-z sources, which are of great importance for understanding the history of star formation in the early universe.
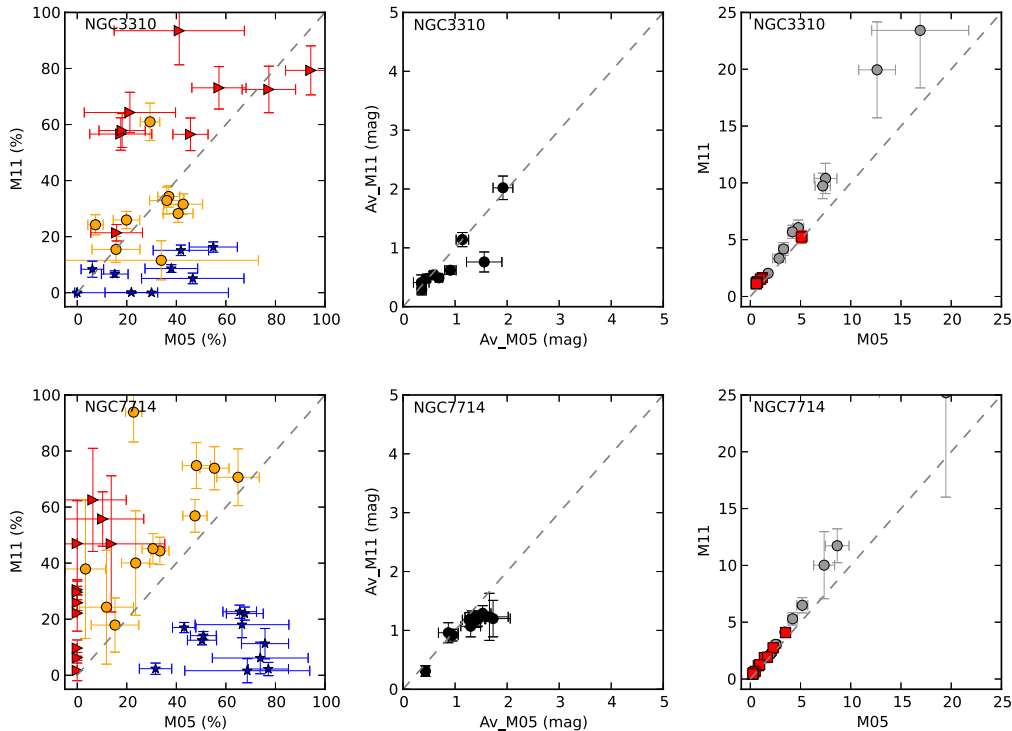
Figure 17. Same as Fig. 16 but for galaxies NGC 3310 (upper panels) and NGC 7714 (bottom panels).

REFERENCES

Alonso-Herrero A., Engelbracht C. W., Rieke M. J., Rieke G. H., Quillen A. C., 2001, ApJ, 546, 952

Asari N. V., Cid Fernandes R., Stasińska G., Torres-Papaqui J. P., Mateus A., Sodré L., Schoenell W., Gomes J. M., 2007, MNRAS, 381, 263

Asari N. V., Stasińska G., Cid Fernandes R., Goems J. M., Schlickmann M., Mateus A., Schoenell W., 2009, MNRAS, 396, L71

Balick B., Heckman T., 1981, A&A, 96, 271

Bernlöhr K., 1993, A&A, 268, 25

Bica E., Alloin D., 1986, A&A, 162, 21

Bolzonella M., Miralles J. M., Pelló R., 2000, A&A, 363, 476

Brandl B. R. et al., 2004, ApJS, 154, 188

Bushouse H. A., 1986, AJ, 91, 255

Calzetti D., Kinney A. L., Storchi-Bergmann T., 1994, ApJ, 429, 582

Calzetti D., Armus L., Bohlin R. C., Kinney A. L., Koornneef J., Storchi-Bergmann T., 2000, ApJ, 533, 682

Cardelli J. A., Clayton G. C., Mathis J. S., 1989, ApJ, 345, 245

Carilli C. L., Walter F., 2013, ARA&A, 51, 105

Cid Fernandes R., Sodré L., Schmitt H. R., Leão J. R. S., 2001, MNRAS, 325, 60

Cid Fernandes R., Leão J. R. S., Lacerda R. R., 2003, MNRAS, 340, 29

Cid Fernandes R., Gu Q., Melnick J., Terlevich E., Terlevich R., Kunth D., Rodrigues Lacerda R., Joguet B., 2004, MNRAS, 355, 273

Cid Fernandes R., González Delgado R. M., Storchi-Bergmann T., Martins L. P., Schmitt H., 2005, MNRAS, 356, 270

Cid Fernandes R. et al., 2009, Rev. Mex. Astron. Astrofis. Conf. Ser., 35, 127

Cid Fernandes R., Stasińska G., Schlickmann M., Mateus A., Asari N. V., Schoenell W., Sodré L., 2010, MNRAS, 403, 1036

Cid Fernandes R., Stasińska G., Mateus A., Asari N. V., 2011, MNRAS, 413, 1687

Cid Fernandes R. et al., 2013, A&A, 557, 86

Colina L., Montreal-Ibero A., 2005, ApJ, 261, 725

Cushing M. C., Vacca W. D., Rayner J. T., 2004, PASP, 116, 362

Doyon R., Joseph R. D., Wright G. S., 1989, in Kaldeich B. H., ed., ESA SP-290: Infrared Spectroscopy in Astronomy. ESA, Noordwijk, p. 477

Duc P. A., Renaud F., 2013, in Souchay J., Mathis S., Tokieda T., eds, Lecture Notes in Physics, Vol. 861, Tides in Astronomy and Astrophysics. Springer-Verlag, Berlin, p. 327

Elmegreen D. M., Chromey F. R., McGrath E. J., Ostenson J. M., 2002, AJ, 123, 1381

Fernández M. X., van Gorkom J. H., Schweizer F., Barnes J. E., 2010, ApJ, 140, 1974

Fischera J., Dopita M. A., Sutherland R. S., 2003, ApJ, 599, L21

Fosbury R. A. E., Hawarden T. G., 1977, MNRAS, 178, 473

Goldader J. D., Joseph R. D., Doyon R., Sanders D. B., 1995, ApJ, 444, 97

Goldader J. D., Joseph R. D., Doyon R., Sanders D. B., 1997a, ApJS, 108, 449

Goldader J. D., Joseph R. D., Doyon R., Sanders D. B., 1997b, ApJ, 474, 104

Gonçalves A. C., Véron-Cetty M.-P., Véron P., 1999, A&AS, 135, 437

González Delgado R. M., Pèrez E., Díaz A. I., García-Vargas M. L., Terlevich E., Vlchez J. M., 1995, ApJ, 439, 604

González Delgado R. M., García-Vargas M. L., Goldader J., Leitherer C., Pasquali A., 1999, ApJ, 513, 707

Grothues H. G., Schmidt-Kaler T., 1991, A&A, 242, 357

Gusten R., 1989, in Morris M., ed., Proc. IAU Symp. 136, The Center of the Galaxy. Kluwer, Dordrecht, p. 89

Heckman T., 2000, Encyclopedia of Astronomy & Astrophysics, Starburst Galaxies. IoP Publishing, Bristol

Heckman T., Armus L., Miley G. K., 1990, ApJS, 74, 833

Imanishi M., Nakanishi K., 2013, AJ, 146, 471

Kennicutt R. C., 1998, ARA&A, 36, 189

Kinney A. L., Bohlin R. C., Calzetti D., 1993, ApJ, 86, 5

Kirkpatrick S., Gelatt C. D., Vecchi M. P., 1983, Science, 220, 671

Kotilainen J. K., Reunanen J., Laine S., Ryder S. D., 2001, A&A, 366, 439

Lançon A., Wood P. R., 2000, A&AS, 146, 217

Lançon A., Goldader J. D., Leitherer C., González Delgado R. M., 2001, ApJ, 552, 150

Lynds R., Toomre A., 1976, ApJ, 209, 382

Maraston C., 1998, MNRAS, 300, 872

Maraston C., 2005, MNRAS, 362, 799 (M05)

Maraston C., Strömbäck G., 2011, MNRAS, 418, 2785 (M011)

Marston A. P., Appleton P. N., 1995, AJ, 109, 1002

Martins L. P., Riffel R., Rodríguez-Ardila A., Gruenwald R., de Souza R., 2010, MNRAS, 406, 2185

Martins L. P., Rodríguez-Ardila A., Diniz S., Riffel R., de Souza R., 2013, MNRAS, 435, 2861

Mateus A., Sodré L., Cid Fernandes R., Stasińska G., Schoenell W., Gomes J. M., 2006, MNRAS, 370, 721

Mathis J. S., 1990, AR&A, 28, 37

Mazzarella J. M., Bothun G. D., Boroson T. A., 1991, AJ, 101, 2034

Meurer G. R., Heckman T. M., Leitherer C., Kinney A., Robert C., Garnett D. R., 1995, AJ, 110, 2665

Mihos J. C., Hernquist L., 1996, ApJ, 464, 641

Neff S. G., Hutchings J. B., Standford S. A., Unger S. W., 1990, AJ, 99, 1088

Nesvadba N. P. H., Lehnert M. D., Eisenhauer F., Gilbert A., Tecza M., Abuter R., 2006, ApJ, 650, 693

Oliva E., Origlia L., Kotilainen J. K., Moorwood A. F. M., 1995, A&A, 301, 55

Olsson E., Aalto S., Thomasson M., Beswick R., 2010, A&A, 513, A11

Origlia L., Oliva E., 2000, New Astron. Rev., 44, 257

Osterbrock D. E., Dahari O., 1983, ApJ, 273, 478

Osterbrock D. E., Ferland G. J., 2006, Astrophysics of Gaseous Nebulae and Galactic Nuclei, 2nd edn. University Science Books, Sausalito, CA

Panter B., Jimenez R., Heavens A. F., Charlot S., 2007, MNRAS, 378, 1550

Pastoriza M. G., Dottori H. A., Terlevich E., Terlevich R., Diaz A. I., 1993, MNRAS, 260, 177

Pickles A. J., 1998, PASP, 110, 863

Pope A. et al., 2013, ApJ, 772, 92

Prouton O. R., Bressan A., Clemens M., Franceschini A., Granato G. L., Silva L., 2004, A&A, 421, 115

Puxley P. J., Brand P. W. J. L., 1994, MNRAS, 266, 431

Ramos Almeida C., Pérez García A. M., Acosta-Pulido J. A., 2009, ApJ, 694, 1379

Rayner J. T., Toomey D. W., Onaka P. M., Denault A. J., Stahlberger W. E., Vacca W. D., Cushing M. C., Wang S., 2003, PASP, 155, 362

Rieke G. H., Lebofsky M. J., Thompson R. I., Low F. J., Tokunaga A. T., 1980, ApJ, 238, 24

Riffel R., Rodríguez-Ardila A., Pastoriza M. G., 2006, A&A 457, 61

Riffel R., Pastoriza M. G., Rodríguez-Ardila A., Maraston C., 2007, ApJ, 659, L103

Riffel R., Pastoriza M. G., Rodríguez-Ardila A., Maraston C., 2008, MN-RAS, 388, 803 (R08)

Riffel R., Pastoriza M. G., Rodríguez-Ardila A., Bonatto C., 2009, MNRAS, 400, 273

Riffel R. A., Storchi-Bergmann T., Riffel R., Pastoriza M. G., 2010, ApJ, 713, 469

Riffel R., Ruschel-Dutra D., Pastoriza M. G., Rodríguez-Ardila A., Santos J. F. C., Jr, Bonatto C. J., Ducati J. R., 2011a, MNRAS, 410, 2714

Riffel R., Riffel R. A., Ferrari F., Storchi-Bergmann T., 2011b, MNRAS, 416, 493

Schlegel D. J., Finkbeiner D. P., Davis M., 1998, ApJ, 500, 525

Schweizer F., Seitzer P., 1988, ApJ, 328, 888

Schweizer F., Seitzer P., 2007, ApJ, 133, 2132

Shier L. M., Rieke M. J., Rieke G. H., 1996, ApJ, 470, 222

Smith B. J., Wallin J. F., 1992, ApJ, 393, 544

Smith D. A. et al., 1996, ApJ, 473, L21

Smith B. J., Struck C., Pogge R. M., 1997, ApJ, 483, 754

Storchi-Bergmann T., Riffel R. A., Riffel R., Diniz M. R., Borges Vale T., McGregor P. J., 2012, ApJ, 755, 87S

Struck C., Smith B. J., 2003, ApJ, 589, 157

Telesco C. M., Gatley I., 1984, ApJ, 284, 557

Toomre A., Toomre J., 1972, ApJ, 178, 623

Vacca W. D., Cushing M. C., Rayner J. T., 2003, PASP, 115, 389

Väisänen P., Rajpaul V., Zijlstra A. A., Reunanen J., Kotilainen J., 2012, MNRAS, 420, 2209

Veilleux S., Kim D. C., Sanders D. B., Mazzarella J. M., Soifer B. T., 1995, ApJS, 98, 171

Véron-Cetty M. P., Véron P., 1986, A&AS, 65, 241

Vorontsov-Velyaminov B. A., 1959, Atlas and Catalogue of Interacting Galaxies, Vol. 1. Sternberg Institute, Moscow

Walker M. F., Chincarini G., 1967, ApJ, 147, 416

Weedman D. W., Feldman F. R., Balzano V. A., Ramsey L. W., Sramek R. A., Wuu C.-C., 1981, ApJ, 248, 105

Wehner E. H., Gallagher J. S., Papaderos P., Frietze-von Alvensleben U., Westfall K. B., 2006, MNRAS, 371, 1047

Zezas A. L., Georgantopoulos I., Ward M. J., 1998, MNRAS, 301, 915

This paper has been typeset from a TEX/LATEX file prepared by the author.

3.2 Populações estelares espacialmente resolvidas: o caso de NGC 4303

Este artigo já foi submetido e tivemos uma primeira interação e tivemos uma resposta positiva do revisor. As sugestões do revisor já foram implementadas e o artigo reenviado para a revista.

2. **A SINFONI view of the nuclear activity and circumnuclear star formation in NGC 4303 - II: Spatially resolved stellar populations**, **N.Z. Dametto**, R. Riffel, L. Colina, R. A. Riffel, J. Piqueras López, R. I. Davies, L. Burtscher, R. B. Menezes, S. Arribas, M. G. Pastoriza, A. Labiano, T. Storchi-Bergmann, L. G. Dahmer-Hahn, D. A. Sales, Monthly Notices of the Royal Astronomical Society, *revised version submitted*, 2018.

A SINFONI view of the nuclear activity and circumnuclear star formation in NGC 4303 - II: Spatially resolved stellar populations

Natacha Z. Dametto,[1][*] R. Riffel,[1] L. Colina,[2] R. A. Riffel,[3] J. Piqueras López,[2]
R. I. Davies,[4] L. Burtscher,[5] R. B. Menezes,[6] S. Arribas,[2] M. G. Pastoriza,[1] A. Labiano,[7]
T. Storchi-Bergmann,[1] L. G. Dahmer-Hahn,[1] D. A. Sales[8]

[1] *Departamento de Astronomia, Instituto de Física, Universidade Federal do Rio Grande do Sul, CP 15051, Porto Alegre, RS 91501-970, Brazil*
[2] *Centro de Astrobiología (CAB, CSIC-INTA), Carretera de Ajalvir, E-28850 Torrejón de Ardoz, Madrid, Spain*
[3] *Departamento de Física, Centro de Ciências Naturais e Exatas, Universidade Federal de Santa Maria, Santa Maria, RS 97105900, Brazil*
[4] *Max Planck Institut für extraterrestrische Physik, Postfach 1312, D-85741, Garching, Germany*
[5] *Leiden Observatory, Leiden University, PO Box 9513, NL2300 RA Leiden, the Netherlands*
[6] *Instituto de Astronomia Geofísica e Ciências Atmosféricas, Universidade de São Paulo, Rua do Matão 1226, São Paulo, SP Brazil*
[7] *Institute for Astronomy, Department of Physics, ETH Zurich, CH-8093 Zurich, Switzerland*
[8] *Instituto de Matemática, Estatística e Física, Universidade Federal do Rio Grande, Rio Grande 96203-900, Brazil.*

ABSTRACT

We present a spatially resolved stellar population study of the inner ∼200 pc radius of NGC 4303 based on near-infrared integral field spectroscopy with SINFONI/VLT at a spatial resolution of 40-80 pc and using the STARLIGHT code. We found the distribution of the stellar populations presents a spatial variation, suggesting an age stratification. Three main structures stand out. Two nuclear blobs, one composed by young stars (t ≤ 50 Myr) and one with intermediate-age stars (50 Myr < t ≤ 2 Gyr) both shifted from the centre. The third one is an internal intermediate-age spiral arm-like structure, surrounding the blob of young stars. Our results indicate star formation has occurred through multiple bursts in this source. Furthermore, the younger stellar populations (t ≲ 2 Gyr) are distributed along a circumnuclear star-forming ring with r∼250 pc. The ring displays star formation rates (SFRs) in the range of 0.002-0.14 M$_\odot$yr^{-1}, favoring the 'pearls-on-a-string' scenario. The old underlying bulge stellar population component (t > 2 Gyr) is distributed outside the two blob structures. For the nuclear region (inner ∼60 pc radius) we derived a SFR of 0.43 M$_\odot$yr^{-1} and found no signatures of non-thermal featureless continuum and hot dust emission, supporting the scenario in which a LLAGN/LINER-like source is hidden in the centre of NGC 4303. Thus, our results reveal a rather complex star formation history in NGC 4303, with different stellar population components coexisting with a low efficiency accreting black hole in its centre.

Key words: stellar content – active – infrared: stars.

1 INTRODUCTION

The stellar population synthesis technique is a powerful tool to derive the galaxy star formation history (SFH). Disentangling the intrinsic properties of the galaxy, such as mass, age, metallicity and dust is a key step for the understanding of a galaxy formation and evolution. For example, there are physical properties of the galaxy bulges that correlate with properties of the active galactic nuclei (AGN) they harbor,

e.g. the $M_\bullet - \sigma_\star$ relation (Ferrarese & Merritt 2000; Gebhardt et al. 2000; Kormendy & Ho 2013), in which the mass of the supermassive black hole (SMBH, $M_\bullet$) correlates with the velocity dispersion of the bulge stars ($\sigma_\star$). The existence of such correlations suggests a possible causal link between the bulge formation and the central black hole or even that the evolution of both might be regulated by a common effect. A strong candidate to explain the relation between these two phenomena is the circumnuclear star formation, since they both depend on the inflow of gas towards the most inner re-

* E-mail: natacha.zanon@ufrgs.br

gions of the galaxy (e.g. Shlosman et al. 1990; Combes et al. 1994; Rosario et al. 2018).

Star formation tracers in the optical spectral range, for example, are considerably well known and have been used to identify star formation in galaxies over the years (e.g., Kennicutt 1988; Bica 1988; Worthey & Ottaviani 1997; Gu et al. 2006). Over the past two decades, optical studies on scales of hundreds of parsecs around the nucleus of Seyfert galaxies have shown that in ∼40% of them, young stars (t ≲ 50 Myr) coexist with the AGN (e.g. Storchi-Bergmann et al. 2000, 2001; González Delgado et al. 2001; Cid Fernandes et al. 2004; Asari et al. 2007; Dors et al. 2008), supporting the so-called AGN-starburst connection (Shlosman et al. 1989, 1990; Heckman et al. 1997). Moreover, these studies suggest the main difference between the stellar population of active and non-active galaxies is an excess of intermediate-age stars (t ∼0.05−2 Gyr) in the former.

Similar results were found in stellar population studies using near-infrared (NIR) long-slit spectroscopy (Riffel et al. 2007, 2009b; Martins et al. 2010), suggesting the continuum of Seyfert nuclei are dominated by the contribution of intermediate-age stellar populations. Moreover, contribution of hot dust emission to the nuclear NIR spectra was found in 50% of Seyfert 1 and in 20% of Seyfert 2 sources (Rodríguez-Ardila et al. 2005; Rodríguez-Ardila & Mazzalay 2006; Riffel et al. 2009a,c,b). The fact that the NIR is less affected by dust than the optical bands makes this spectral range the most suitable one to unveil the nuclear stellar populations in highly obscured sources (Origlia & Oliva 2000), such as the case of Seyfert 2 galaxies. The observed properties of this subclass of AGN suggest the SMBH powering the AGN is obscured to the line of sight by the torus surrounding the central engine. In addition, as has already been shown by e.g. Davies et al. (2006), star formation can take place within the torus, on scales of tens of parsecs from the nucleus.

The advent of *James Webb Space Telescope* (JWST) and the near-and mid-infrared integral field spectroscopic capabilities it will provide, opens the study of spatially resolved obscured stellar populations and hot dust using the entire 0.6 to 28μm range. Thus, to test the stellar population synthesis method in this particular spectral range is of fundamental importance for forthcoming studies with JWST.

The AGNIFS (AGN Integral Field Spectroscopy) team has started to characterize the stellar population in the inner kiloparsecs of a sample of nearby Seyfert galaxies (Mrk 1066, Mrk 1157, NGC 1068, NGC 5548 and Mrk 573) using *Gemini Near-Infrared Integral Field Spectrograph* (NIFS). For Mrk 1066, Mrk 1157 and Mrk 573 the inner ∼200 pc are dominated by old stars ($t \geq 2$ Gyr), while intermediate-age stars ($0.3 \leq t \leq 0.7$ Gyr) are the dominant contributors to the circumnuclear rings found in these sources (Riffel et al. 2010, 2011c; Diniz et al. 2017). These circumnuclear rings of intermediate-age stars are correlated with low stellar velocity dispersion values ($\sigma_\star \sim 50$ km s^{-1}), being consistent with a scenario in which the origin of the low-$\sigma_\star$ rings is a past event which triggered an inflow of gas and formed stars which still keep the colder kinematics of the gas from which they formed. Storchi-Bergmann et al. (2012) found two recent episodes of star formation in NGC 1068: a first one that took place 300 Myr ago extending over the inner 300 pc of the galaxy and a second one that occurred just

30 Myr ago in a ring-like structure at ∼100 pc from the nucleus, where it is coincident with an expanding ring of warm H$_2$ emission. Schönell et al. (2017), on the other hand, detected a dominant intermediate-age stellar population component (SPC) in the inner 160 pc of NGC 5548, while an old (> 2 Gyr) SPC dominates the region between 160 and 300 pc. Dust emission has been detected in all sources (with exception of NGC 1068) accounting for 30 to 90% of the K-band nuclear flux, while a featureless continuum component associated with the AGN emission was detected in three sources, contributing with ∼20−60% of the K-band nuclear flux (NGC 1068, Mrk 573 and NGC 5548).

Modeling the Brγ equivalent width (EW), supernovae rate and mass-to-light ratio, Davies et al. (2007) have quantified the SFH in the centre of nine nearby Seyfert galaxies using their STARS code. Their results indicate the age of the stars which contributes most to the NIR continuum lie in the range 10-30 Myr, pointing out these ages should be considered only as 'characteristic', as they have not performed a proper spectral synthesis, suggesting there may be simultaneously two or more stellar populations that are not coeval.

All these previous studies have focused on either nearby luminous Seyfert galaxies, in which the output energy is dominated by the AGN, or on galaxies with luminous circumnuclear star-forming rings. Low-luminosity AGNs (LLAGNs), on the other hand, including low-luminosity Seyfert galaxies, classical LINERs, weak-[OI] LINERs and LINER/HII transition-like objects are the most common type of galaxies that display nuclear activity (for a review on LINERs, see Filippenko 2003; Singh et al. 2013; Belfiore et al. 2016; Hsieh et al. 2017). LINERs alone comprise 50% to 70% of AGNs and 20% to 30% of all galaxies in surveys of nearby bright galaxies (Ho et al. 1997). Therefore, to identify the nature of the energy source in LLAGNs, as well as to disentangle the contribution of both SPCs and accreting black holes to the energy output of these sources is of utmost importance. In this context, a key object to move forward on the understanding of the role played by star formation in LLAGNs is NGC 4303, a nearby LINER/Seyfert 2 (Filippenko & Sargent 1986; Kennicutt et al. 1989; Ho et al. 1997; Colina & Arribas 1999) galaxy with a LLAGN coexisting with a young massive star cluster in the nucleus and a star-forming circumnuclear ring (see Sec. 1.1).

1.1 Previous stellar population studies of NGC 4303

NGC 4303 is a barred spiral classified as SB(rs)bc (de Vaucouleurs et al. 1991), located in the Virgo Cluster, at a distance of 16.1 Mpc (Ferrarese et al. 1996). A nuclear UV-bright spiral arm with an outer radius of 225 pc and spiraling all the way down to the unresolved (size < 8 pc) UV-bright core was detected in the HST/WFPC2 F218W images (Colina et al. 1997). This spiral structure was traced by several distinct regions, identified as young massive stellar clusters. These authors concluded the unresolved LINER-like core contributes with 16% of the UV luminosity of NGC 4303, which is dominated by the massive star-forming regions. Another important result is the presence of spiral star-forming structure in the nuclear region of a barred spiral supports the bar-induced AGN-starburst scenario. In this sense, the gas in the bar-driven nuclear spiral can flow inward towards

the core and fuel a preexisting black hole, producing an AGN (Shlosman et al. 1990; Combes 2003).

In a later work, Colina & Arribas (1999) used optical integral field spectroscopy to study the inner 9" × 8" (i.e. $700 \times 620 \, \mathrm{pc}^2$) and found, from optical emission-line ratios, that the circumnuclear star-forming regions (CNSFRs) of this source have ages of $2-3 \, \mathrm{Myr}$ (extremely young clusters of massive stars). Also, they concluded the presence of a massive ($8 \times 10^4 \mathrm{M_\odot}$) and young ($3.5-4 \, \mathrm{Myr}$) stellar cluster in the nucleus is consistent with the observed properties of the core of NGC 4303 (e.g. optical emission-line ratios, UV and Hα luminosities). Nevertheless, the presence of a non-thermal power-law AGN-like ionizing source cannot be ruled out. Thus, the authors classified the core of this galaxy as a [OI]-weak LINER or low-excitation Seyfert 2.

Studying the radial distributions of the Mg$_2$ and Fe5270 Lick spectral indices in the disk of NGC 4303, Mollá et al. (1999) found while in NGC 4303 both indices steeply rise towards the central region ($\lesssim 2 \, \mathrm{kpc}$), in the other objects studied by them (NGC 4321 and NGC 4535) a central deep is observed. In their study, by using SSP models, these authors inferred that NGC 4303 is still forming stars.

Using WFPC2 (F218W,F606W) and NICMOS (F160W) *Hubble Space Telescope* (HST) images, Colina & Wada (2000, hereafter C00) studied the inner 300 pc of NGC 4303 and identified a nuclear elongated bar-like structure of 250 pc in size. The images revealed a complex gas/dust distribution with a two-arm spiral structure of about 225 pc in radius. Also, they estimated the age of the UV-bright knots located along the star-forming spiral structure as $5-25 \, \mathrm{Myr}$ and masses of $0.5-1 \times 10^5 \mathrm{M_\odot}$.

From UV imaging and spectroscopy (HST/STIS), Colina et al. (2002, hereafter C02) concluded the UV emission from the nucleus of NGC 4303 comes from a region of 3.1 pc and it is identified as a young (4 Myr), massive ($10^5 \, \mathrm{M_\odot}$) nuclear cluster. The authors found this compact super-star cluster (SSC), commonly detected in the (circum)nuclear regions of spirals and starburst galaxies, is the dominant ionizing source in the nucleus. According to this study, an additional non-thermal ionizing source due to an AGN is not required. They also discuss the possibility of having an intermediate/old ($1-5 \, \mathrm{Gyr}$) star cluster coexisting with the low efficiency accreting black hole and the young and luminous SSC. Jiménez-Bailón et al. (2003) analyzed $2-10 \, \mathrm{keV}$ observations from the Chandra X-ray satellite and indicated an additional compact source was required to explain the $1.5-5 \, \mathrm{keV}$ emission, possibly a low-luminosity AGN.

In Riffel et al. (2016, hereafter R16) we presented the results concerning the kinematics and excitation properties of the different phases of the interstellar medium in the circumnuclear region of NGC 4303 using the same SIN-FONI datacubes presented in this work. A circumnuclear ring of star-forming regions (r$\sim$200$-$250 pc) was detected, displaying young ages in the range $2.5-15 \, \mathrm{Myr}$. Star formation in the ring appears to be episodic, with stars forming quasi-simultaneously. Moreover, NIR emission-line ratios ([FeII]/Brγ and H$_2$/Brγ) are consistent with the presence of an AGN and/or a SN-dominated star-forming region in the core (inner 60 pc radius) of NGC 4303.

Here we perform, for the first time, a spatially resolved full spectral fitting stellar population study of the nuclear region ($\sim$200 pc radius) of NGC 4303, using both STARLIGHT

code and VLT/SINFONI data. This paper is structured as follows: Sec. 2 presents the observations and data reduction procedures, while in Sec. 3 we introduce the stellar population synthesis method used in this work. The results are presented in Sec. 4 and discussed in Sec. 5. Finally we present our conclusions in Sec. 6. North is up and east is to the left throughout the images and maps presented in this paper.

2   OBSERVATIONS AND DATA REDUCTION

The data used are the same as the datacubes presented in R16. Here we summarize the information on observations and data reduction process, as follows. The observations were done during the period 82B (February 2009) at the ESO *Very Large Telescope* (VLT) with SINFONI, a NIR integral field spectrograph (Eisenhauer et al. 2003; Bonnet et al. 2004). The pointings were centered on the nucleus of the galaxy, covering a field of view (FoV) of $\sim$8″×8″ per exposure, enlarged by dithering up to $\sim$9.″25 × 9.″25, with a plate scale of 0.″125×0.″250 pixel^{-1}. The final data cube was re-sampled to a scale of 0.″125×0.″125 pixel^{-1}, corresponding to a spatial sampling of $\sim$10 pc per spaxel.

The data were taken in the J ($1.10-1.35 \, \mu m$), H ($1.45-1.80 \, \mu m$), and K ($1.97-2.44 \, \mu m$) bands with a total integration time of 2400 s per band. In the same way, a set of photometric standard stars was observed to perform the telluric and flux calibration. We estimated the spatial resolution of our seeing-limited observations by fitting a 2D Gaussian profile to a collapsed image of the standard stars. The spatial resolution (FWHM) measured for each band is $\sim$1″, $\sim$0.″6, and $\sim$0.″5 for J-, H-, and K-band, respectively, that correspond to 78 pc, 47 pc, and 39 pc at the adopted distance of 16.1 Mpc for NGC 4303. The reduction and calibration processes were performed using the standard ESO pipeline ESOREX (version 3.8.3), and our own IDL routines (see R16, where a complete description of the reduction and calibration procedures is provided).

2.1   Relative flux calibration

The accurate determination of the continuum shape plays an important role on the stellar population determinations (Baldwin et al. 2018). The stellar population synthesis technique used in this work is strongly dependent on a reliable continuum fit, meaning that any problem in the relative flux calibration between spectral bands would compromise the results. When dealing with emission-line measurements, on the other hand, this issue is much less important. The continuum estimation needed to fit an emission line is done within the range of only one spectral band, being nearly independent of relative flux calibrations. With this in mind, we decided to add an extra step concerning the relative flux calibration of our data set, in order to get a reliable relative calibration, adequate for the purpose of spectral energy distribution fitting.

Our target was observed in three different nights and only a limited number of standard stars were available to perform the flux calibration. Although the efficiency curves appear to be consistent, the flux calibration of the J-band data might be inaccurate outside the $1.15-1.30 \mu m$ range, since the slope of the curves is very uncertain beyond this

limit and the spectra is completely dominated by the noise from the atmospheric absorption bands. This fact is translated to uncertainties on the slope of the spectra in the data cubes (DCs) which, thus, cannot be used to perform a reliable stellar population synthesis using full spectral fitting (see Cid Fernandes et al. 2005b; Baldwin et al. 2018).

To address that, we used NIR cross-dispersed data of NGC 4303 from Martins et al. (2013a), obtained at the NASA 3m Infrared Telescope Facility (IRTF) using the SpeX spectrograph. As the observations at the J-, H- and K-band are done simultaneously in the cross-dispersed mode, the data do not suffer from relative flux calibration problems. Therefore, assuming the shape of the SpeX data was correct, we used it to scale our SINFONI observations. It is worth mentioning we have used SINFONI integrated spectra extracted with the same aperture size and position angle as the SpeX data.

2.2 Instrumental fingerprint removal

The instrumental fingerprint removal was performed using the Principal Component Analysis (PCA) Tomography technique, which consists of applying PCA to data cubes. First, the spectral lines of the data cube were removed. Then, PCA was applied and the obtained eigenvectors related to the fingerprint were used to construct a data cube containing only the fingerprint. Such a data cube was subtracted from the original one, completing the removal of the instrumental artifact. This entire procedure was applied separately to the J, H and K bands of the data cube. For more details, see (Menezes et al. 2014, 2015).

3 STELLAR POPULATION SYNTHESIS METHOD

A common way to disentangle the spectral energy distribution components of a galaxy spectrum is by performing stellar population synthesis. This method consists in fitting the galaxy absorption and continuum spectrum with a combination of simple stellar population (SSP) components. Therefore, the two main ingredients are: i) the SSP templates (hereafter, base set) and ii) the fitting code.

3.1 Base Set

An ideal set of templates should be able to foresee all the features expected to be found in spectra of galaxies (Schmidt et al. 1991; Cid Fernandes et al. 2005a). In other words, a reliable base set would be an empirical library of integrated spectra of star clusters (i.e. they only depend on ages and metallicities of the stars and are free from any assumptions on stellar evolution and the initial mass function - Bica & Alloin 1986; Riffel et al. 2011a). However, up to now there is no such library available in the literature for the NIR spectral region. Thus, the use of a base set composed of theoretical SSPs, covering this spectral region, has become a common approach (e.g. Riffel et al. 2009b; Martins et al. 2010; Dametto et al. 2014).

Since the NIR carries fingerprints from evolved stars (e.g. Riffel et al. 2007; Ramos Almeida et al. 2009; Martins et al. 2013b; Riffel et al. 2015) and these are crucial to model

the absorption line spectra of the galaxies, it is important to make use of SSPs models that can predict these features. Following Dametto et al. (2014), we decided to used the Maraston (2005, hereafter M05)[1] Evolutionary Population Synthesis (EPS) models, which include empirical spectra of C- and O-rich stars (Lançon & Wood 2000) and thus, are able to predict these features. We also tested other SSPs models from Bruzual & Charlot (2003, hereafter BC03) and Conroy et al. (2009, hereafter C09), see Sec. 4.1 for this discussion.

The M05 models span an age range from 0.001 Myr to 15 Gyr according to a grid of 67 models with six different metallicities ($0.005 \leq Z/Z_\odot \leq 3.5$), 2 Initial Mass Functions (IMFs) (Salpeter and Kroupa) and 3 horizontal branch (HB) morphologies (red, intermediate or blue - for more details, see M05). It is worth noting the models with Z=0.005Z$\odot$ and Z=3.5Z$\odot$ are provided only for ages older than 1 Gyr (in a grid of 16 ages) and are based on Cassisi (Cassisi et al. 1997b,a) and Padova 2000 (Girardi et al. 2000) isochrones, respectively. The remaining 4 metallicities, (computed for the full grid of 67 ages) are associated with Cassisi + Geneva (Schaller et al. 1992) tracks. The stellar spectra were taken from the BaSeL 2.2 library (Lejeune et al. 1997, 1998), covering the spectral range of 91Å to 160μm, with a spectral resolution of 5−10 Å up to the optical region, and 20−100 Å in the near- and far-infrared.

The BaSeL 2.2 is a library of low-resolution stellar spectra based on the theoretical templates compiled by Lejeune et al. (1997, 1998). This library is widely used in stellar population synthesis studies and was constructed by combining the model atmosphere spectra of Bessell et al. (1989, 1991) with the models for cool stars by Fluks et al. (1994). As synthetic spectral libraries do not contain TP-AGB carbon- and oxygen-rich stars, empirical and time-averaged spectra of C- and O-type stars from Lançon & Mouhcine (2002) were included in the M05 models.

In order to avoid redundant information and degeneracies in the base set, we used only the representative SSPs (see Dametto et al. 2014, for further details) and ended up with a final base set composed as follows: 31 ages (1.0 Myr $\leq$ t $\leq$ 13.0 Gyr) for each of the 4 metallicities (Z= 0.02, 0.5, 1 and 2 $Z_\odot$) totaling 124 SSPs. We also included blackbody functions for temperatures in the range 700−1400 K in steps of 100 K and a power law ($F_\nu \propto \nu^{-1.5}$) in order to account for possible contributions from dust emission and from a featureless continuum, respectively, at the nucleus (Cid Fernandes et al. 2004; Riffel et al. 2009b).

Spectral resolution of M05 models in the NIR is significantly lower (R $\leq$ 250) than that of the observed data (R$\sim$ 2000) and varies with wavelength. For this reason, observations were degraded to the models' resolution by convolving them with a Gaussian.

3.2 Fitting Code

Other fundamental ingredient in stellar population fitting is the code. Following Dametto et al. (2014), we used STARLIGHT code (Cid Fernandes et al. 2005b; Mateus et al.

---

[1] Available at http://www.icg.port.ac.uk/~maraston/Claudia's_Stellar_Population_Model.html

2006), which fits the observed spectrum O_λ with a combination in different proportions of $N_\star$ SSPs in the base set – $b_{j,\lambda}$ – taken from the EPS models. One of the key features of STARLIGHT is that the code fits the entire spectrum (from 0.8 to 2.4 μm in this case), excluding emission lines and spurious features (e.g. cosmic rays, noise and telluric regions), which are masked out.

Basically, STARLIGHT solves the following equation for a model spectrum M_λ (Cid Fernandes et al. 2005a):

$$M_\lambda = M_{\lambda_0} \left[\sum_{j=1}^{N_\star} x_j b_{j,\lambda} r_\lambda \right] \otimes G(v_\star, \sigma_\star), \qquad (1)$$

where M_{λ_0} is the synthetic flux at the normalization wavelength (λ_0=2.067μm); x_j is the jth population vector component of the base set; $b_{j,\lambda} r_\lambda$ is the reddened spectrum of the jth SSP normalized at λ_0 in which $r_\lambda = 10^{-0.4(A_\lambda - A_{\lambda_0})}$ is the extinction term; $\otimes$ denotes the convolution operator and $G(v_\star, \sigma_\star)$ is the gaussian distribution used to model the line-of-sight stellar motions, centered at velocity $v_\star$ with dispersion $\sigma_\star$. We choose as normalization wavelength λ_0=2.067μm, since K-band spectra present a higher SNR than those in the J- and H-band, and the spectral region near 2.067μm is free from emission/absorption lines.

Velocity dispersion is a free parameter for STARLIGHT which broadens the SSPs in order to better fit the absorption lines in the observed spectra, however this step is not relevant in our case. Assuming M05 (BaSeL based models) spectral resolution in velocity units as $\sim$1500 km s^{-1}, the velocity dispersion is $\sim$640 km s^{-1}, which are both much higher values than those calculated in R16 ($v_\star$:-80/+80 km s^{-1} and $\sigma_\star$: 20/100 km s^{-1}) for the stellar kinematics. Thus, because of the models' low resolution, we kept the kinematic parameters fixed ($v_\star$=0.0 and $\sigma_\star$=640 km s^{-1}) during the fits. It is important to highlight that for the low resolution models, the age information is incoded in the continuum shape (Riffel et al. 2009b; Baldwin et al. 2018; Dahmer-Hahn et al. 2018).

The extinction law used in this work was that of Calzetti law (Calzetti et al. 2000) implemented by Hyperz (Bolzonella et al. 2000), a public photometric redshift code which computed the Calzetti extinction law for $\lambda > 2.2\mu$m.

Lastly, the code searches for the minimum of the equation:

$$\chi^2 = \sum_\lambda [(O_\lambda - M_\lambda) w_\lambda]^2, \qquad (2)$$

and the best fit is achieved. In order to measure the robustness of the stellar population fit, we can use STARLIGHT output parameters χ^2 and Adev. The later is the percent mean deviation $|O_\lambda - M_\lambda|/O_\lambda$, where O_λ is the observed spectrum and M_λ is the fitted model. Emission lines and spurious features (noise, telluric regions, cosmic rays) are masked out by using $w_\lambda = 0$ in the regions where they are located. This procedure is done by first constructing a general mask, based on the emission-lines position. Next, we inspect spaxel-by-spaxel to remove any additional spurious data. For more details see Dametto et al. (2014) and STARLIGHT manual available at http://www.starlight.ufsc.br.

4   RESULTS

Following Dametto et al. (2014, and references therein), the stellar population vectors have been binned in three main components: *young* (blue): x_y ($t \leq 50 \times 10^6$ yr), *intermediate-age* (orange): x_i ($50 \times 10^6 < t \leq 2 \times 10^9$ yr) and *old* (red): x_o ($t > 2 \times 10^9$ yr). An example of the final fit for the nuclear region (r=0.″75$\sim$60 pc, central green circle in Fig. 1) of NGC 4303 is presented in Fig. 2. The nuclear spectrum is well described by a series of star formation bursts, the first one occurring $\sim$13 Gyr ago[2], contributing with $\sim$50% of the flux at 2.067μm. The fit reproduces individual minor bursts with ages ranging from 0.3 Gyr to 0.7 Gyr, corresponding to a 15% contribution of the intermediate-age SPC, while the young SPC accounts for 35% of the flux, with a major burst at 7.5 Myr ago. No contribution of the featureless continuum and/or hot dust components were necessary in order to reproduce the nuclear continuum of this source. Green lines represent the percentage contribution in mass of each SSP. The old SPC (m_o) dominates the mass contribution with 98%, while the contribution of the other two components are negligible. Moreover, the code fits a dust free (A_V=0.0) spectrum for the inner 60 pc of NGC 4303, agreeing with previous results from C02, which found low extinction values (A_V=0.3 mag) for the inner 0.″9 of this source.

Spatial distribution of the percent flux (top panels) and mass (bottom panels) contribution of each SPC bin is shown in Fig. 3[3]. As for Fig. 1, green circles represent the CNSFRs analyzed in R16. The physical sizes[4] of these regions are: Regions N/A/B (r=0.″75$\sim$60 pc); others (r=0.″5$\sim$39 pc). We point out the FoV used in this work is smaller than that used to study the emission lines in R16, mainly due to problems with the relative flux calibration and due to low SNR close to the borders, which represents a limitation when performing stellar population synthesis (Cid Fernandes et al. 2005b).

Analyzing the SPC contributions in Fig. 3, we can see the age of the dominant stellar population presents a spatial variation, suggesting an age stratification along the inner $\sim$200 pc radius of this source. Three main features are evident from the maps: A blob dominated by young stars in the nuclear region, shifted towards east from the centre (here defined as the peak of the Brγ emission line) and the UV emission peak; a second blob dominated by intermediate-age stars located southwest from the centre, clearly seen in the middle panels; and a more internal arm-like structure very close to the blob of young stars, mainly seen in the m_i map.

Younger SPCs (x_y and x_i) are distributed along the circumnuclear region (200−250 inner parsecs), similar to the results predicted from the emission line gas presented in R16. It is important to highlight that our FoV does not

---

[2] Note that the base is not a continuous distribution of ages, with the old ages being represented by 13 Gyr SSPs in this case, for details see (Dametto et al. 2014).

[3] We smoothed all maps to the H-band spatial resolution (0.″6). Note that the K-band has a higher (0.″5) spatial resolution, while the J-band has a lower one (1.″). We decided to smooth the maps using the H-band resolution since we are using a small spectral region in the J-band to perform the fits.

[4] The apertures were chosen by the authors in R16 to be larger than the seeing ($\sim$0.″5) and to include most of the Brγ flux of each region.
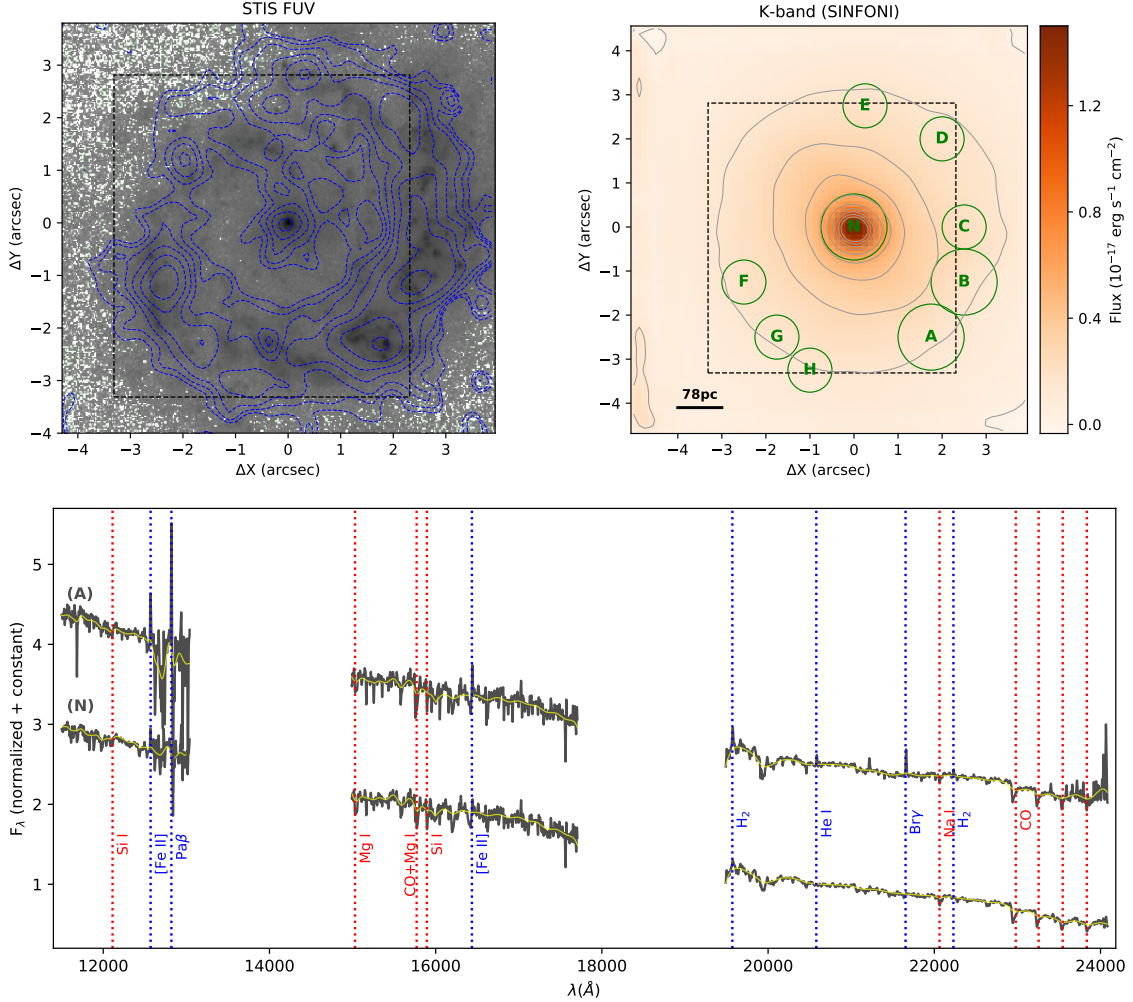
Figure 1. STIS (Space Telescope Imaging Spectrograph) F25QTZ far ultraviolet image of NGC 4303 previously presented by C02 in gray scale with Brγ emission line (SINFONI) contours in blue (top left). K-band continuum (grey contours represent some continuum intensities to help visualization), reconstructed from the SINFONI data cube as an average of the fluxes between 2.22 and 2.27 μm (top right). Green circles mark the position of the CNSFRs previously reported by R16 and the black box in both images denotes the FoV used in this work. The bottom panel shows the near-IR spectra for the nucleus (bottom) and for position A (top), extracted with a circular aperture with radius 0.″75 and normalized at 2.067μm. The smoothed spectra are over-plotted in yellow. A constant (1.5) was added to the spectrum of Region (A)

for visualization purpose. Absorption (red) and emission (blue) lines are marked.

cover the whole western part of the circumnuclear ring (we miss most of regions B and C). In fact, a major contribution of the young SPC is seen in the northeastern area, which is co-spatial with dustier regions reported by (C00, see their figure 3) using V-H color. As we are using NIR data, we were able to penetrate deeper into the dust layers, accessing these young stars missed in the UV and optical ranges, which are more sensitive to dust obscuration. This could explain why the young SPC map is not tracing the spiral-arm structure clearly seen in the UV emission (Fig. 1, darker knots repre-

sent less obscured regions), but the circumnuclear ring. The old SPC is distributed outside the two blob structures, being more prominent northwest from the centre.

Flux-weighted results have a dependence on the choice of the normalization wavelength (Riffel et al. 2011b). Thus, one should take this into consideration when comparing results from different spectral regions. By using the knowledge of stellar evolution, one can use the mass-to-light ratio (M/L) for each SSP and determine the percentage contribution in stellar mass, a physical parameter which does not
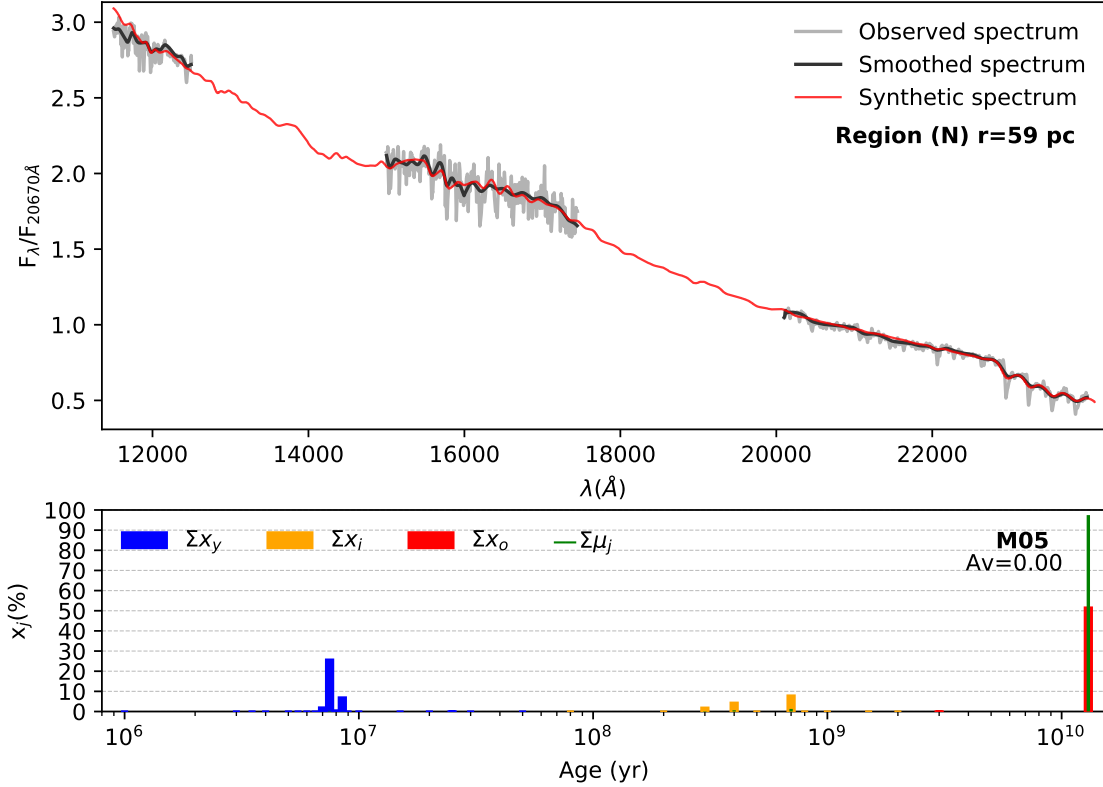
Figure 2. Example of the stellar population synthesis results for the nuclear region (r=0″75, corresponding to 60 pc) of NGC 4303 (central green circle in the maps). *Top panel*: observed (gray), smoothed (black) and synthetic (red) spectrum, normalized to unit at 2.067µm. *Bottom panel*: Histogram displaying the flux (x_j, colored bars) and mass-weighted (μ_j, green lines) stellar population vectors contributions sorted only by age (metallicities summed) and color coded by the three SPC age bins: young (blue: $\leq 50\,$Myr), intermediate-age (orange: $0.05-2\,$Gyr) and old (red: $> 2\,$Gyr). The reddening value (in magnitude units) is also shown. Telluric absorption regions are omitted.

depend on the normalization wavelength used in the fit. The bottom panels of Fig. 3 present the mass-weighted contribution of the SPCs. As we can see, the major contribution in mass comes from old (t > 2 *Gyr*) stars. In addition, the three internal structures mentioned above (the two blobs and the inner spiral arm) are highlighted in these maps.

Besides the SPC distributions, STARLIGHT full spectral fitting provides a measure of the internal extinction (A_V), which is shown in the left panel of Fig. 4. The nuclear spaxels clearly display the highest values (A_V=2.3 mag), within scales of tens of parsecs, while the average value over the FoV is ∼0.3 mag. The southern region of the reddening map displays a stripe-like pattern with reddening values around 1.5 mag. This stripe-like pattern may be partially related with a residual 'instrumental fingerprint', which we were not able to remove completely (see Sec. 2.2). Thus, possibly affecting the reddening values in these locations.

STARLIGHT code also outputs the mass that have been processed into stars over the last t years ($M_\star^t$). This can be used to estimate the mean SFR over a period of time t. We

have estimated the mean SFR$_\star$ over the last 10 Myr as being the ratio of $M_\star^t/t$ (for t≤10 Myr), and it is presented in the middle panel of Fig. 4. The nucleus clearly stands up with a SFR of ∼0.2 M$_\odot$yr^{-1} in the region co-spatial with the A$_V$ peak (∼40 pc radius). The mean SFR over the whole FoV is $2.1^{+9.7}_{-2.1}\times10^{-3}M_\odot$yr^{-1}.

As mentioned in Sec. 3, the quality of the fit can be measured by the STARLIGHT output parameter called *per-cent mean deviation*: Adev ($|O_\lambda - M_\lambda|/O_\lambda$), in which O_λ is the observed spectrum and M_λ is the fitted model (Cid Fernandes et al. 2004, 2005a). For our fits, Adev is below 4.5% at most locations (see Fig. 4, right panel), indicating the model reproduces well the observed spectra.

4.1 Robustness of the stellar population results: Comparison with BC03 and C09 SSP models

In order to deepen our analysis, we decided to perform stellar population synthesis using other EPS models available in the literature: Bruzual & Charlot (2003, hereafter BC03) and
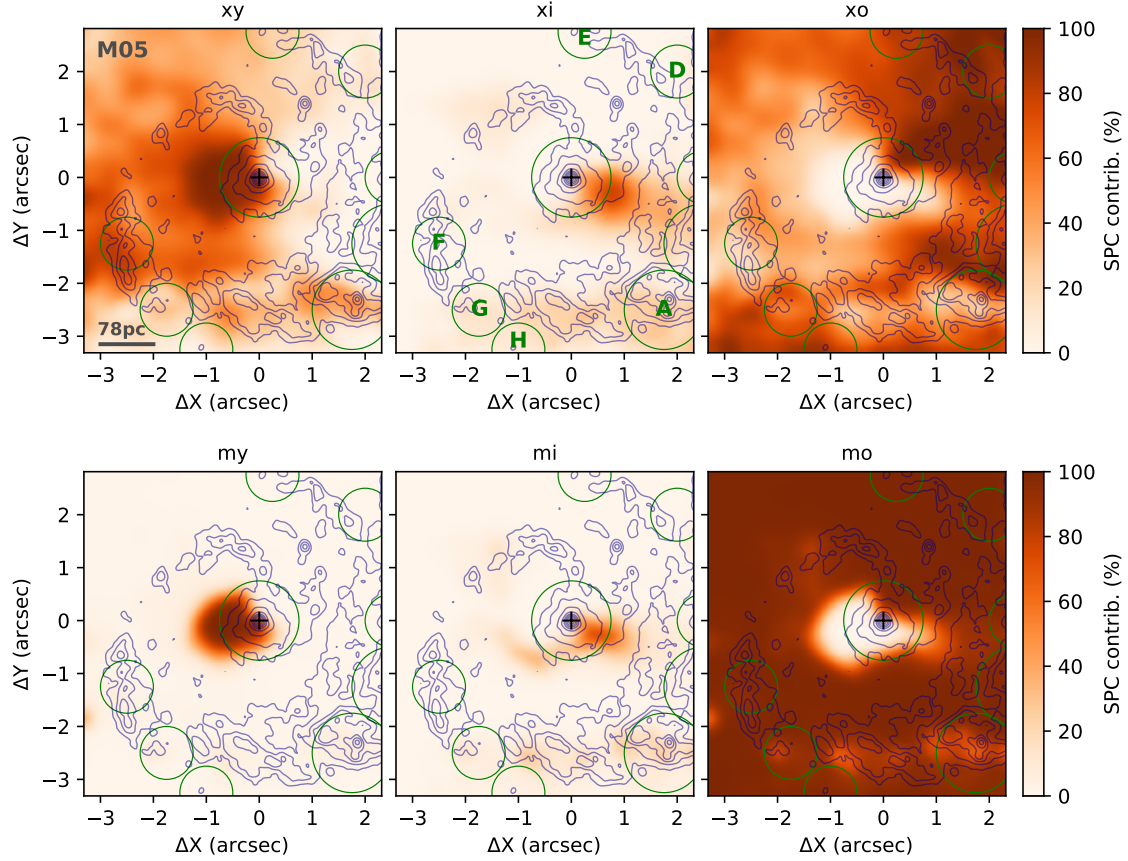
8   *N. Z. Dametto et al.*

Figure 3. Results using M05 models. Spatial distribution of the percent contribution of each SPC to the flux (x_j, top panels) and mass (m_j, bottom panels), where j represents the age of the SPC: young (y: $\leq 50\,\mathrm{Myr}$), intermediate-age (i: $0.05-2\,\mathrm{Gyr}$) and old (o: $> 2\,\mathrm{Gyr}$). Green circles mark the CNSFRs, clearly seen in the EW Brγ previously reported by R16. The black cross represents the peak of the Brγ emission line. STIS far-ultraviolet broad-band image is shown in blue contours, tracing the spiral structure reported in C02.
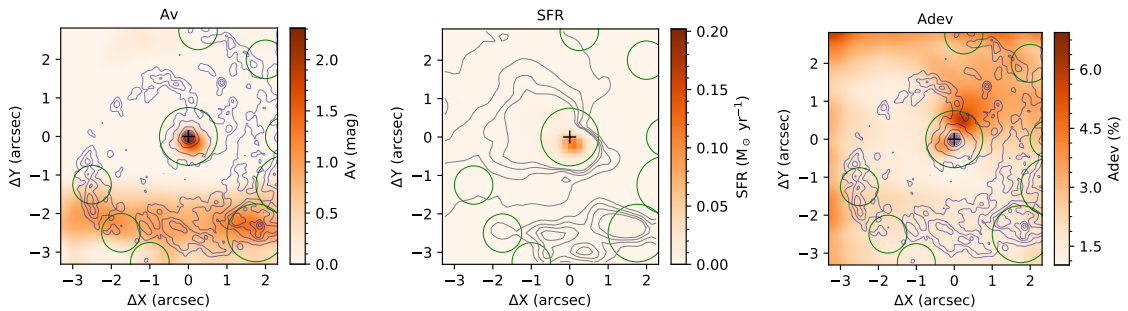
Figure 4. *Left:* Reddening (A_V); *Middle:* Star Formation Rate (SFR) over the last $10\,\mathrm{Myr}$; *Right:* Adev (percent mean deviation from the spectral fit). Grey contours in the middle panel represent SFRs up to $2.5\times10^{-3}\,\mathrm{M_\odot yr^{-1}}$, were included for display purposes.

Conroy et al. (2009, hereafter C09). We do not include the models from Maraston & Strömbäck (2011, hereafter M11) in this analysis, as the use of the lower resolution M05 models is a better option to deal with stellar population synthesis in the NIR when compared to the M11 ones (Dametto et al. 2014). Addressing to the limitations on the M11 models, an example is the fact that above ∼1μm about half of the spectra (from Pickles stellar spectral library, used to construct the M11 models that extent to the NIR, Pickles 1998) lack spectroscopic observations leading the authors to construct a smooth energy distribution from broad-band photometry, which may imply that some NIR absorption features are not well resolved, even for these higher resolution models. New sets of models presented by Meneses-Goytia et al. (2015), Röck et al. (2016) and Conroy et al. (2018) are available, which make use of the IRTF and E-IRTF stellar libraries. However, the age range of these models (t ≥ 1 Gyr) is not adequate to fit the spectrum of galaxies with active star formation, therefore these models were not employed here.

Firstly, the three models used in this work are constructed using different prescriptions (see Conroy 2013, for a review). Both BC03 and C09 models are constructed using the isochrone synthesis approach, while M05 uses the fuel consumption theory technique. In the former, the SSPs are constructed by integrating the contributions of all mass bins (along one isochrone) to the flux in the various passbands, after assuming a initial mass function (IMF). Yet, in the later, energetics of the post-main-sequence phases (i.e. the amount of fuel available for nuclear burning) are calculated using the evolutionary track of the turnoff mass.

The treatment of the TP-AGB phase - crucial to models the stellar populations in the NIR - is also a topic of discussion when comparing the results obtained with different EPS models. While BC03 constructed period-averaged spectra for C-type stars using broad-band photometry to calibrate the low-resolution stellar templates of Höfner et al. (2000), both M05 and C09 include empirical spectra of carbon- and oxygen-rich stars from Lançon & Mouhcine (2002). The inclusion of these empirical spectra of stars in the TP-AGB phase has enabled the detection of NIR characteristic absorption features, such as TiO (0.843 and 0.886μm), VO (1.048μm), CN (1.1 and 1.4μm) and CO (1.6 and 2.3 mum) bands (Riffel et al. 2015).

In recent studies, there has been an attempt to address for discrepancies in stellar population synthesis results using different EPS models. Baldwin et al. (2018) studying a sample of 12 nearby early-type galaxies recently concluded the variation in the derived SFHs using NIR is largely driven by the choice of stellar spectral library rather than the models' prescription. In order to better compare the results, our base sets are composed by SSPs constructed using basically the same stellar library (BaSeL[5]) in the NIR spectral range.

Performing stellar population synthesis with STARLIGHT code for 7 spectra from early-type galaxies, Dahmer-Hahn et al. (2018) found systematic differences in the results using M05, BC03 and C09 models. While BC03 presented a higher contribution of young stellar populations, C09 displayed a major contribution of the

older ages and M05 preferred solutions including a higher contribution (when compared to the other two models) of the intermediate-age components. One way to diminish such systematic effects is to fix the kinematic fit while running the code. As we degrade the resolution of the data to match the low resolution of these models in the NIR, the stellar features are considerably broadened, thus one cannot rely on the kinematic information obtained with STARLIGHT.

We have tested the results keeping the kinematics parameters fixed for NGC 4303 (see Sec. 3.2) and we were able to smooth the systematic effects found by Dahmer-Hahn et al. (2018), concluding the inclusion of a kinematic fit while running STARLIGHT with low resolution models (R∼300) do not yield reliable results, since the stellar features in the data are considerably broadened.

Base sets for BC03 and C09 were constructed in the same way as that of M05 and the same fitting procedure was applied (see Figs 5 to 7). C09 models do not provide the fraction of the initial stellar mass which is still present in form of stars at the age j for each base set component.Therefore we were not able to calculate the percentage mass contribution using these models and we only present the flux-weighted results.

In Fig. 5 we present an example of the fits for *Region A* (see Fig. 1) using the three EPS models for comparison. From the top panel we can see the overall good quality of the fits, primarily in the K-band. Analyzing the histograms in the bottom panels, it is clear the results assuming the binned stellar population vectors are in agreement between the models, presenting a ∼40% contribution for both young (8−9 Gyr) and old (9/13 Gyr) SPC, while the remaining ∼20% comes from intermediate-age stars (0.5−1 Gyr), with exception of BC03 results which do not display any contribution of the x_i component and present an increase in x_y (∼60%).

The reddening solutions are similar, deviating at most in 0.17 mag, which can be explained by the fact that the NIR spectral range is less sensitive to reddening variations when using full spectrum fitting (Baldwin et al. 2018; Dahmer-Hahn et al. 2018).

In Figs 6 and 7 we present the spatial distribution of the SPCs using BC03 and C09 models. The same trend of age stratification found using M05 models is reproduced in these figures: The young SPC is distributed along the circumnuclear region with clear knots shifted eastwards from the photometric center and the spiral-arm structure found in the UV (blue contours); the old SPC is distributed outside these knots, with a clear increase in the contribution towards northwest; the intermediate-age contribution is almost negligible using these sets of models, with small knots in the south region for BC03 and next to the centre (co-spatial with the intermediate-age blob found using M05 models) for C09.

In order to better compare the results, we present maps with the spatially resolved differences in the SPC vectors (flux-weighted) between the three models in Fig. 8. From the two first columns, we can see BC03 and C09 display higher contribution of the x_y SPC (redder colors in the left panels), while M05 favors the x_i and x_o SPCs (bluer colors in the middle and right panels). Major differences are found in the southern region, co-spatial with the residual 'instrumental fingerprint' from SINFONI data (see Sec. 2.2), which may

---

[5] M05: BaSeL 2.2 (Lejeune et al. 1997, 1998) and BC03/C09: BaSeL 3.1 (Lejeune et al. 1997, 1998; Westera et al. 2002)
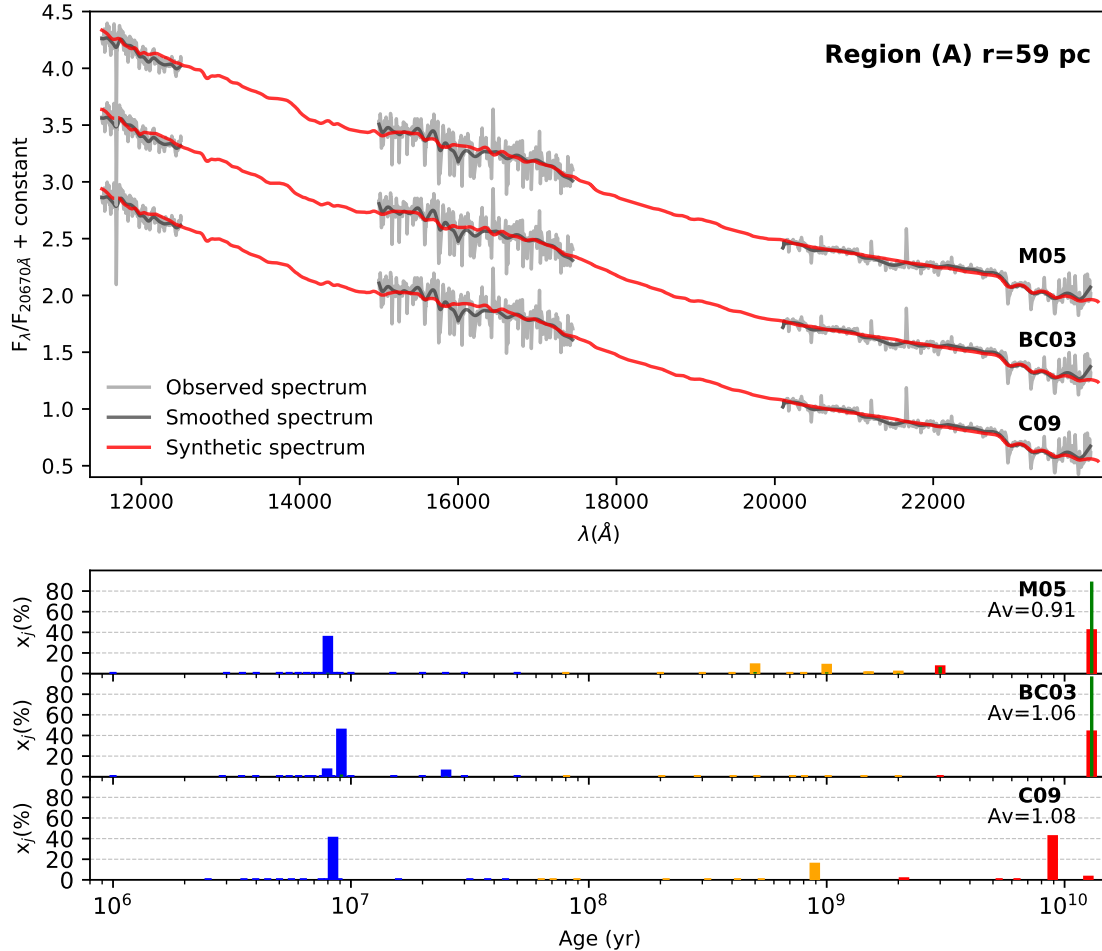
Figure 5. Same as Fig. 2, but for *Region A* (see Fig. 1). Results using different EPS models are presented.

be the cause of these discrepancies in this region. Moreover, the intermediate-age blob found using M05 models appears to be spread in the older ages using BC03 and C09 models, while the inner spiral-arm clearly seen in the mass-weighted M05 maps (Fig. 3) and traced by bluer regions in the middle panels of Fig. 8 is missed using BC03 and C09 models.

The smallest differences are displayed between BC03 and C09 models, as can be seen from the bottom column in Fig. 8. These two models also present nearly negligible contribution of the x_i SPC, in contrast to results produced using M05 models. This could be related to the different prescription plus treatment of the TP-AGB phase for the different models. For example, Baldwin et al. (2018) argue their results favor Maraston & Strömbäck (2011) treatment of the TP-AGB phase (same used in M05), in agreement with Riffel et al. (2015). Baldwin et al. (2018) also claim that the discrepancies found by Zibetti et al. (2013), which states M05 models overestimate the TP-AGB contribution,

are probably related to the technique used in Zibetti et al. (2013), consisting in measuring line indices rather than full-spectrum fitting.

We decided to discuss only the results for M05 in Sec.5, since these models present a proper treatment of the TP-AGB phase as discussed above, as well as the informations needed to calculate the percentage mass contributions of the stellar populations. Moreover, this will allow us to compare the results presented here with those previously published by our group using M05 models (e.g. Riffel et al. 2010, 2011c; Storchi-Bergmann et al. 2012; Dametto et al. 2014; Schönell et al. 2017; Diniz et al. 2017).
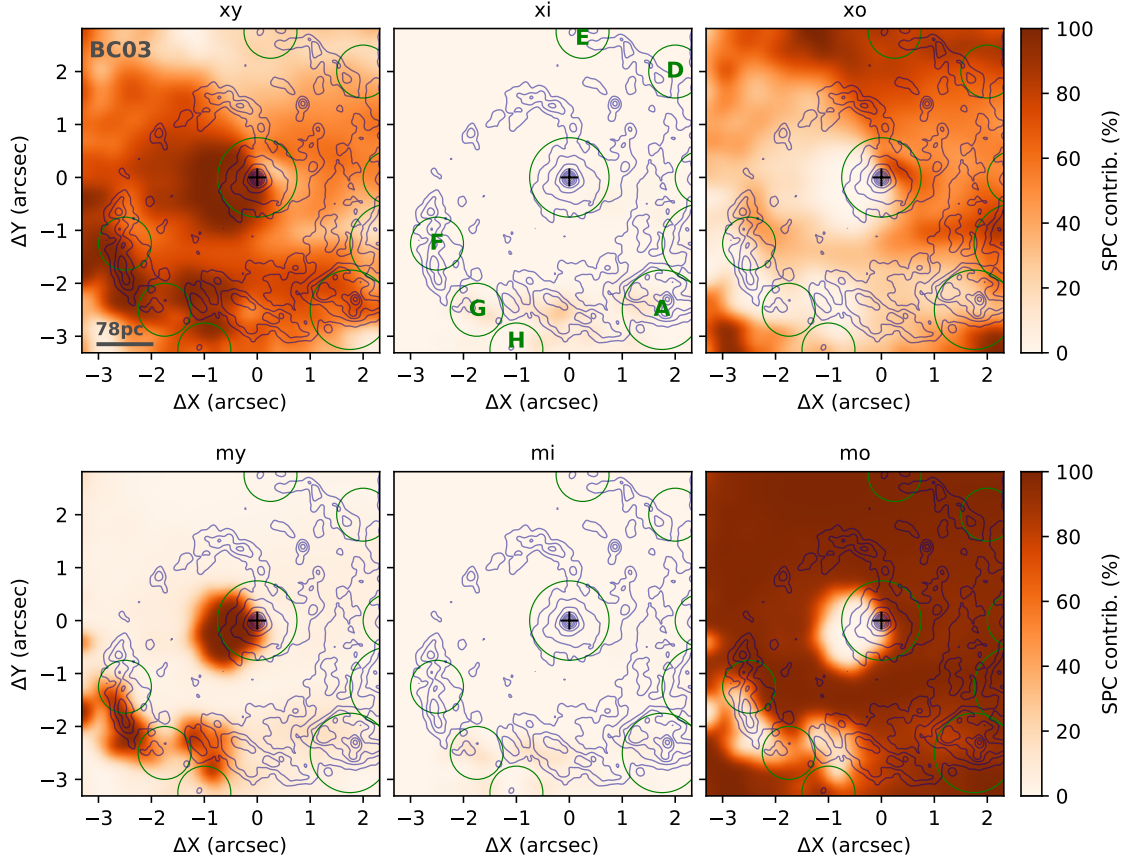
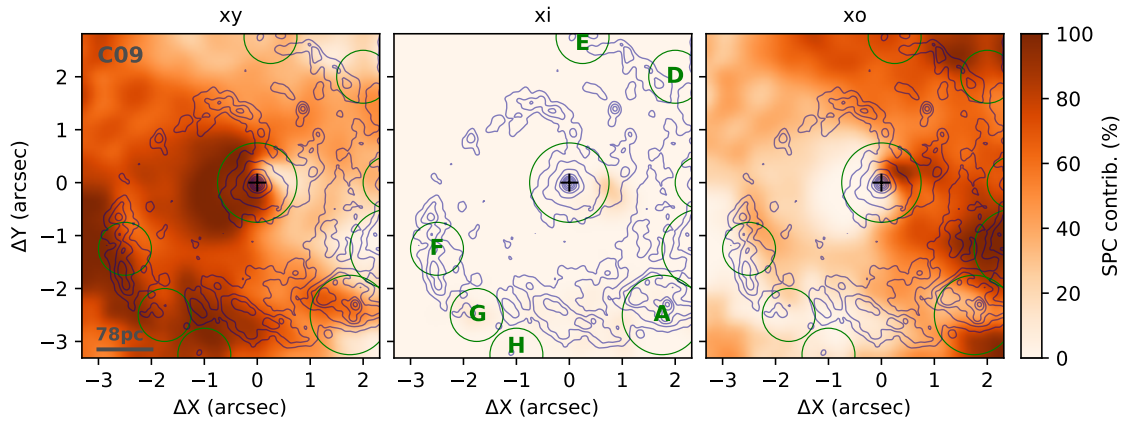**Figure 6.** Same as Fig. 3, but using **BC03** models.

Figure 7. Same as Fig. 3, but using C09 models. As these models do not provide the mass-to-light ratio needed to calculate the mass-weighted contributions, we only present the maps for the flux-weighted contribution of each SPC.
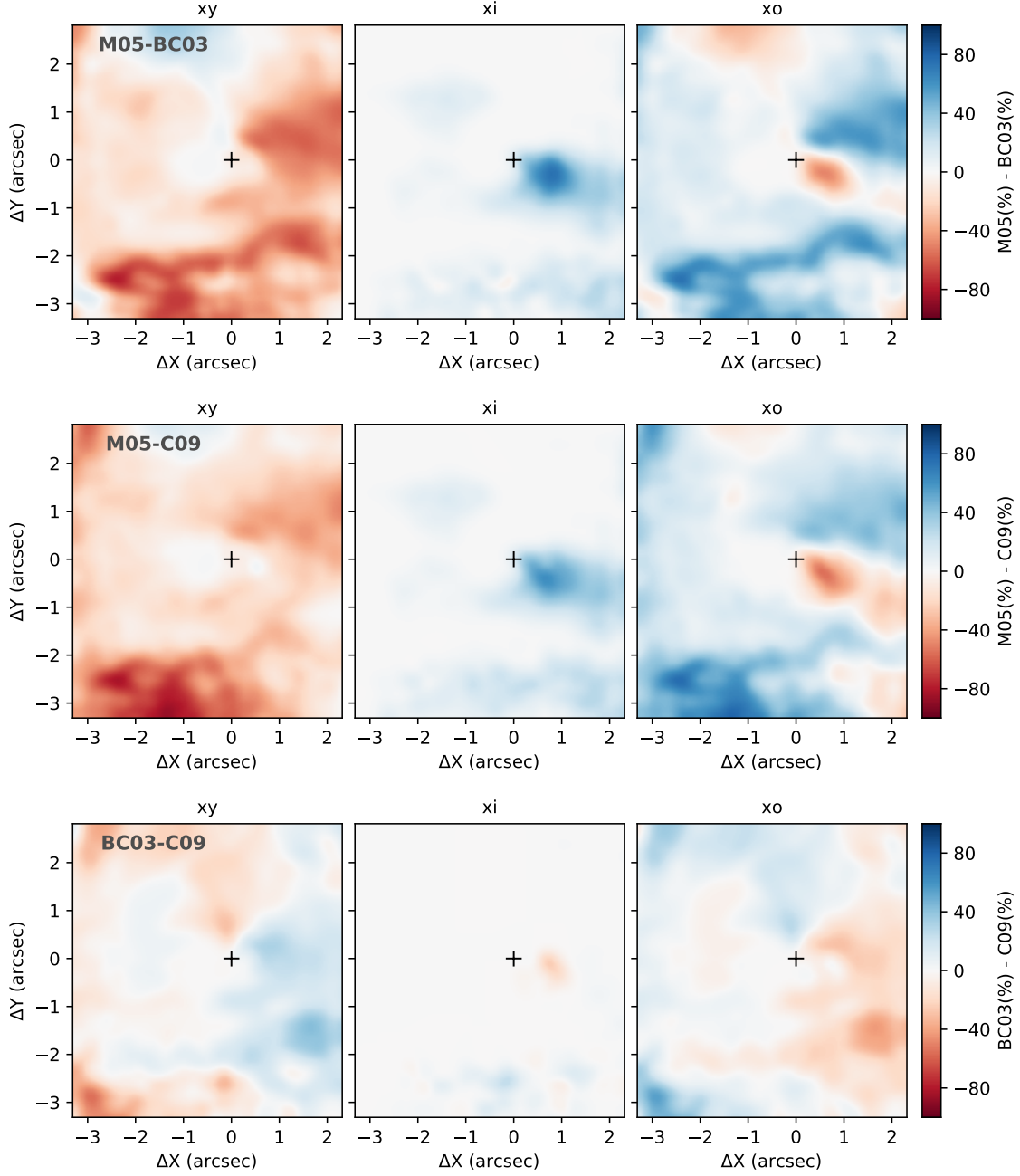
Figure 8. Comparison between the results produced with the different EPS models. Maps displaying the difference between the flux-weighted SPCs presented in Fig. 3, 6 and 7.

5 DISCUSSION

5.1 Distribution of the stellar populations: circumnuclear ring and spiral structures

Stellar population distribution in the inner ∼200 pc radius of NGC 4303 shows the presence of young and intermediate-age stars in a circumnuclear ring structure (see the mean age maps presented in Fig. 9), while the older components are distributed mainly along the more external parts of our FoV and we interpret them as the underlying bulge component. Previous 2D mapping studies of our AGNIFS group on Seyfert galaxies had shown a predominance of intermediate-age stars in the central kiloparsecs of these objects (Riffel et al. 2010, 2011c; Storchi-Bergmann et al. 2012; Schönell et al. 2017), while our results point out to a more conspicuous contribution of this SPC in the LLAGN NGC 4303: a blob southwest from the centre which extends to an internal spiral-arm like structure surrounding the central blob of young stars. These features suggest star formation is stratified along the inner regions of NGC 4303, with older knots shifted towards west of the centre, while the younger ones are to the east. C02 and R16 reported younger ages for the western knots, which are missed by our smaller FoV, it is important to highlight.

As discussed in R16, our results favor the interpretation of a circumnuclear ring with young/intermediate-age stars rather than a spiral-arm structure proposed by C02. We suggest the spiral structure traced by the UV emission is in fact tracing a region of low extinction inside the disk containing the circumnuclear ring. This interpretation is in agreement with previous results from C00. These authors presented a $V-H$ image of the central region of this source (see their figure 3), which reveled a rather complex gas/dust and stellar distribution with two-arm (star forming lane in the southwest and west regions, and dust lane at northeast) spiral structure.

In the aim of better visualizing these findings we constructed mean value maps. A more compressed but also useful way to represent the stellar population mixture in the galaxy is by computing the mean stellar age (flux and mass-weighted, respectively), as defined by Cid Fernandes et al. (2005a):

$$\langle \log t_\star \rangle_F = \sum_{j=1}^{N_\star} x_j log(t_j), \tag{3}$$

.

$$\langle \log t_\star \rangle_M = \sum_{j=1}^{N_\star} m_j log(t_j). \tag{4}$$

and mean stellar metallicity:

$$\langle Z_\star \rangle_F = \sum_{j=1}^{N^\star} x_j Z_j, \tag{5}$$

$$\langle Z_\star \rangle_M = \sum_{j=1}^{N^\star} m_j Z_j. \tag{6}$$

We present the maps for these parameters in Fig. 9. From the mean age maps we can see the younger stellar populations are co-spatial with the UV knots traced by the blue contours as well as the dustier regions at north-east probed by optical
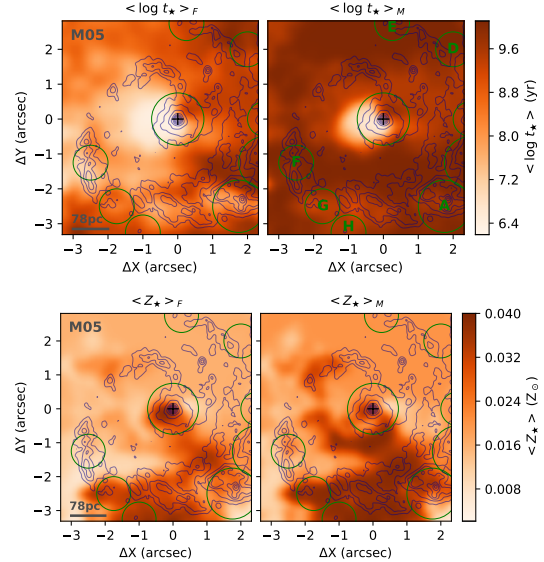
Figure 9. Logarithm of the mean age (top panels) and mean metallicity (bottom panels) weighted by flux (*left*) and weighted by mass (*right*). Black cross represents the centre, blue contours from UV image and green circles marking the CNSFRs (see Fig. 1 for more details).

imaging, as mentioned before. A comparison between the mean age and mean metallicity maps suggests the presence of a rather young metal rich SPC (∼2Z⊙) in the nuclear region of NGC 4303, as well as in the southern region, where the younger CNSFRs encompassed by our FoV are located. Moreover, higher metallicity values (up to 2 Z⊙) are tracing the inner spiral-arm structure of intermediate-age stars (see also Fig. 3). These results give further support to the age stratification scenario proposed for the SFH in this source.
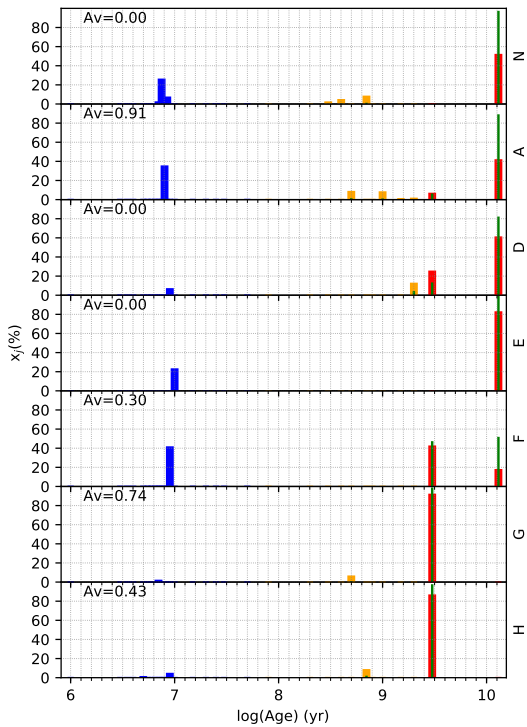
5.2 Stellar population in the CNSFRs

In R16 we present new maps of emission-line flux distributions and kinematics in both ionized and molecular gas in the inner 350 pc radius (a slightly wider FoV than the one we use in this work, see Sec. 4) of NGC 4303. The most prominent feature is a 200−250 pc ring of CNSFRs which is seen as a nuclear spiral in UV/HST images presented in C02. In order to better analyze and compare our results with those obtained from the study of the emission-lines in R16, we decided to extract the spectra of the CNSFRs encompassed by our FoV, matching the aperture defined in that work. The spectra were extracted as the summed flux inside each aperture (Regions: N/A, r=60 pc; D/E/F/G/H, r=39 pc).

In Fig. 10 we display a series of histograms with the stellar population synthesis results (also summarized in Tab. 1) for the CNSFRs: Each panel represents the results for the respective region marked in green circles in our maps. From these plots it is clear the presence of young stars (7−10 Myr) coexisting with an older SPC, which we attribute to the underlying bulge component (3/13 Gyr). A small contribution

14   *N. Z. Dametto et al.*

Table 1. Synthesis results for the CNSFRs shown in Fig. 10 (green circles in the maps).

Region	x_y (%)	x_i (%)	x_o (%)	m_y (%)	m_i (%)	m_o (%)	$<\log t_\star>_F$ (yr)	$<\log t_\star>_M$ (yr)	Z_F ($Z_\odot$)	Z_M ($Z_\odot$)	A_V (mag)	SFR ($M_\odot yr^{-1}$)	$\sum_{SFR}$ ($M_\odot yr^{-1} kpc^{-2}$)	Adev (%)
M05	*(1)*	*(2)*	*(3)*	*(4)*	*(5)*	*(6)*	*(7)*	*(8)*	*(9)*	*(10)*	*(11)*	*(12)*	*(13)*	*(14)*
(N)	35	14	51	0	2	97	6.17×10^8	1.74×10^{10}	1.81	1.98	0	0.426	39.62	1.04
(A)	35	18	47	1	4	96	5.50×10^8	1.00×10^{10}	1.20	1.83	0.91	0.144	13.39	1.65
(D)	6	12	82	0	4	96	4.68×10^9	9.77×10^9	1.00	1.00	0	0.005	1.0	2.90
(E)	22	0	78	0	0	100	2.75×10^9	1.29×10^9	1.00	1.00	0	0.018	3.66	3.35
(F)	41	0	59	1	0	99	3.63×10^8	6.17×10^9	1.33	1.21	0.30	0.046	9.71	1.98
(G)	2	6	92	0	1	99	2.45×10^9	2.95×10^9	1.88	1.98	0.74	0.002	0.46	1.87
(H)	5	8	87	0	2	98	1.95×10^9	2.88×10^9	1.85	1.96	0.43	0.005	1.09	1.53

Notes: (1), (2), (3): average contribution in flux of the young (y: ≤ 50 Myr), intermediate-age (i: $0.05-2$ Gyr) and old (o: > 2 Gyr) SP component, respectively; (4), (5), (6): average contribution of the SP components in mass; (7), (8): flux- and mass-weighted mean ages; (9), (10): flux- and mass-weighted mean metallicities; (11): visual extinction; (12): star formation rate; (13): star formation surface density; (14): percent mean deviation.

Figure 10. SP synthesis results for the CNSFRs in NGC 4303. Each panel displays the percent contribution in flux (color bars) and mass (green lines) at $\lambda = 2.067\mu$m of the stellar population vectors in each region. Blue, orange and red represent young (x_y), intermediate-age (x_i) and old (x_o) SPCs contributions respectively; The letters correspond to the regions identified by R16 and marked as green circles in our maps.

of up to 20% of intermediate-age stars with a large spread in age ($0.3-2.0$ Gyr) is seen in the CNSFRs, with exception of apertures E and F. Our results point out to a more complex nuclear ring SFH, with multiple starburst episodes, in agreement with recent results (Ma et al. 2018).

Previous studies have found an age dating for the star

clusters distributed along the circumnuclear ring-like structure in NGC 4303. C00 found the east UV knots (blue contours in our maps) are older ($\sim 10-25$ Myr) than the west knots ($\sim 5-7.5$ Myr), thus suggesting an age offset in the ring.

Even though emission-line measurements done by R16 show a trend suggesting an age sequence along the ring increasing from A to H (see Figures 4 and 9 from R16), the distribution of CNSFRs and their age differences indicate a rather episodic star formation along the ring, being equally consistent with regions to the east being older than regions to the west, in agreement with C00. For example, from $H_2/Br\gamma$ ratios, they found regions G and H to be older than regions $A-F$, in full agreement with our results, as can be seen in Fig. 10.

In Tab. 1 column (12) we present the SFRs derived for all the apertures. We can see *Region A* displays the highest SFR ($0.14 \, M_\odot yr^{-1}$) in the ring, co-spatial with high $H\alpha$ emission as presented by Colina & Arribas (1999). The range of the SFRs in the circumnuclear ring goes from $0.002-0.14 \, M_\odot yr^{-1}$, displaying ~ 1 order of magnitude higher than those presented in R16 using the $Br\gamma$ luminosity and assuming a constant rate. These discrepancies might be related to the fact that with the stellar population fitting we are probing different (older) starbursts than those which are effectively ionizing the gas. In fact, Ma et al. (2018) found evidence suggesting the SFH in nuclear rings are better described by models of multiple bursts of star-formation, rather than assuming a constant SFR. In this work, the authors derived the age of the circumnuclear ring of NGC 4303 through SED fitting and found it to be around 3 Gyr (using C09 and assuming $Z=Z_\odot$), in agreement with our results (see column (7) - Tab. 1).

In order to better compare our results with the literature, we divided the SFR by the area of the extractions, obtaining the star formation surface density ($\sum_{SFR}$, column (13) - Tab. 1). In the nucleus, $\sum_{SFR}$ reaches up to $\sim 40 \, M_\odot yr^{-1} kpc^{-2}$, while in the ring values are in the range of $0.5-13 \, M_\odot yr^{-1} kpc^{-2}$. Typical star formation surface density values range from $1-50 \, M_\odot yr^{-1} kpc^{-2}$ on hundreds of parsec scales, $50-500 M_\odot yr^{-1} kpc^{-2}$ on scales of tens of parsecs, while it increases up to $\sim 1000 \, M_\odot yr^{-1} kpc^{-2}$ on parsec scales (Valencia-S. et al. 2012, and references therein). Our $\sum_{SFR}$ values for the CNSFRs, including the nucleus (inner ~ 120 pc) are within the first $\sum_{SFR}$ ranges.

This is in agreement with previous results, such as those presented by Busch et al. (2017), which found $\sum_{SFR}$ of $\sim 28\,\mathrm{M_\odot yr^{-1} kpc^{-2}}$ in the nucleus and $5-13\,\mathrm{M_\odot yr^{-1} kpc^{-2}}$ in the ring of the nearby barred galaxy NGC 1808. Thus, confirming are results display typical star formation surface density values.

Based on the spatial distributions of CNSFRs in nuclear rings, for example, Böker et al. (2008) discussed two scenarios of star formation: the 'pop-corn' scenario in which the stellar clusters form at random positions producing no systematic age gradients and, the 'pearls-on-a-string' scenario in which the clusters are formed where the gas enters the ring and then age as they orbit the ring forming a string of aging clusters (see also Ryder et al. 2001; Díaz-Santos et al. 2007). R16 could not favor neither of the two scenarios from the emission-line study, suggesting stars formed quasi-simultaneously over a large sector of the ring, aging as they rotate with an orbital time of $\sim$10 Myr. (Seo & Kim 2013) performed simulations on how star formation proceed in nuclear rings of barred galaxies and found a critical SFR (SFR$_c$) of $\sim 1\,\mathrm{M_\odot yr^{-1}}$ which determines how star formation takes place in these rings. When the SFR in the ring is low ($<$SFR$_c$), star formation mostly takes place in the contact points of the ring with dust lanes leading to a age gradient ('pearls-on-a-string'). Otherwise, if the SFR is high ($>$SFR$_c$), then star formation is randomly distributed along the ring ('pop-corn'). Mazzuca et al. (2008) found similar results studying 22 nuclear rings (with SFRs in the range of $01-10\,\mathrm{M_\odot yr^{-1}}$), but for a higher SFR$_c$ of $\sim 3\,\mathrm{M_\odot yr^{-1}}$. Summing up the SFRs of the CNSFRs (excluding the nuclear aperture) we ended up with a SFR$\sim 0.2\,\mathrm{M_\odot yr^{-1}}$, a typical value for nuclear rings (Ma et al. 2018). Even if we add the mean SFR of the northeast section of the ring ($\lesssim 2.5 \times 10^{-3}\,\mathrm{M_\odot yr^{-1}}$, see Fig. 4), the SFR in the circumnuclear ring of NGC 4303 would still be lower that the SFR$_c$ proposed by these previous results. Thus, our SFR results favor the 'pearls-on-a-string' scenario, with a gradient of increasing age going from regions A to H.

When comparing the reddening values derived from the emission lines in R16 with those found with our stellar population fitting, the former present higher A$_V$ (reaching up to 2.5 mag in *Regions B* and *E*). This is expected and is related to the fact that the hot ionizing stars are associated to dustier regions with respect to the cold stellar population (Calzetti et al. 1994). The ring displays reddening values from $0-0.9$ mag, lower than typical values from previous studies ranging from $2-5$ mag (Krabbe et al. 1994; Kotilainen et al. 1996; Rosenberg et al. 2012; Busch et al. 2017), but consistent with UV and optical results from C00 for less obscured regions in the $V-H$ colors, as well as with Cluster G of C02 with A$_V$=0.6 mag (using R$_V$=4.05), which we call *Region A*.

In addition, the Adev values in Fig. 10, column (12) illustrate the good quality of the fits for the CNSFRs.

5.3 Stellar populations in the nuclear region: Is there any evidence of the LLAGN?

The presence of an AGN in the central region of NGC 4303 is still a matter of debate. Using NIR emission-line ratios, R16 constructed a NIR diagnostic diagram (proposed by Colina et al. 2015), which suggested the presence of an AGN at the

nucleus, confirming previous results that the nuclear emission of this galaxy has a composite nature (LLAGN plus a young massive stellar cluster - e.g., Colina et al. 2002; Jiménez-Bailón et al. 2003).

As already mentioned in Sec. 1, previous studies suggested a young (4 Myr) massive SSC dominates the UV emission, while an intermediate/old ($1-5$ Gyr) stellar population dominates the optical continuum (C00; C02). Our results in the nuclear region (inner 60 pc radius) of this source show the same trend, presenting a contribution of young stars with rather older ages ($7-8.5$ Myr) and a rather younger intermediate-age SPC ($0.3-0.7$ Gyr) plus a dominating ($\sim$50%) 13 Gyr old stellar population, which we attribute to the underlying bulge. Moreover, C00 suggested the H excess in the inner 8 pc could be related to the presence of luminous red supergiants, implying a second star formation episode with $\sim$10 Myr, which are close in age with the young stars we found. These authors also argued the large $V-H$ colors (3.2 mag) found in this inner region could not be fully accounted for by small amounts of dust extinction and suggested the presence of an extremely red source, such as a hidden AGN. Assuming a pure power law with ν=-1, representing the AGN featureless emission, they obtained values of V$-$H=2.3 mag, closer to the observed ones, but still not fully compatible.

From the stellar population synthesis we do not find contribution of the featureless continuum and/or hot emission component to the inner 60 pc radius. Although this result does not rule out the existence of a hidden AGN in the centre of NGC 4303, it supports the scenario of a LLAGN/LINER-like source rather than a Seyfert 2 nucleus (Colina & Arribas 1999). In a recent work, Burtscher et al. (2015) found no evidence of nuclear EW dilution of the CO feature by AGN light in this source (as can be seen in their figure 2.), in agreement with our stellar population analysis. It is important to call attention to the fact that the spectra of very young SSPs ($t \leq 5\,Myr$, Riffel et al. 2009b, and references therein) and the featureless continuum emission can be degenerate in the fits, meaning we cannot fully discriminate between these two components using our methodology. Nevertheless, we are favorable to believe the young SPC we are finding with stellar population synthesis is real, since there is more than sufficient evidence in the literature of the presence of young stars in the nuclear region of this source. Furthermore, our fits find SSPs in the range of $7-8.5$ Myr, which are not the younger SSPs ($t \lesssim 5$ Myr) which usually mimic the contribution of a featureless continuum (Cid Fernandes et al. 2004).

Additional support for the scenario of a LLAGN/LINER-like source rather than a Seyfert 2 nucleus comes from the fact that the inclusion of a featureless continuum (power law) and hot dust emission (blackbody functions) has been used to trace signatures of luminous AGNs by our AGNIFS group when performing stellar population synthesis in the NIR, and in the case of Seyfert sources these components are required to properly fit their spectral energy distribution.

5.3.1 Nuclear extinction

Typical nuclear reddening values (A$_V$) for Seyfert galaxies derived using NIR emission-lines are in the range of

1.3−5 mag for Type 1 nuclei and 1.8−9.0 mag for Type 2 (Valencia-S. et al. 2012, and references therein). These authors also derived a 2.5 mag reddening for the nuclear region of a starburst/Seyfert composite galaxy. In the same line, Dametto et al. (2014) found nuclear A_V ranging from 2.5−8.0 mag for the gas in four Starburst galaxies, while for the stars they found 1.0−3.2 mag. In addition, AGNIFS group derived nuclear reddening values using NIR data from Seyfert 2 galaxies and found values between 2−4 mag for the stars, while for the gas these values reach up to 7.0 mag in Mrk 573 (Riffel et al. 2010, 2011c; Diniz et al. 2017).

Previous reddening estimations were made for NGC 4303 in C02 using the emission lines as well as the UV shape of the spectrum for the nuclear region. These authors found A_V=0.2/0.4 mag using UV spectra (LMC/Calzetti extinction law), while using Hα/Hβ line ratio they fitted a dust free nuclear spectrum (r=0″.45∼35 pc) for this object. These low extinction values are in agreement with our results for the nuclear extraction (r=0″.75∼60 pc), as can be seen in the top panel of Fig. 10. However, when looking to the results spaxel-by-spaxel in Fig. 4 (left panel), we derived rather higher A_V values (∼2.3 mag) for the inner tens of parsecs in this source, which is within the typical reddening values. C00 had found large $V-H$ colors (3.2 mag) for the inner regions (<8 pc) of NGC 4303, as already mentioned, arguing this could possibly be related to a hidden AGN, which is consistent with our results (see Sec. 5.3).

5.3.2 Nuclear SFRs

In Tab. 1 we present SFR values for the nuclear region (0.43 M$_\odot$yr^{-1}), which are in the range of typical values found in the literature (see also Sec. 5.2). For example, using Brγ luminosity, Valencia-S. et al. (2012) and Busch et al. (2017) derived nuclear SFRs of 0.18 M$_\odot$yr^{-1} and < 0.35 M$_\odot$yr^{-1}, respectively, in the inner 57/50 pc radius in their sample. Jiménez-Bailón et al. (2003) and R16 also calculated the SFR in the inner hundreds of parsecs in NGC 4303 using emission line indicators in the optical and NIR, respectively, and both found 0.013 M$_\odot$yr^{-1}, a lower value than the one we are finding. As discussed in Sec. 5.2, this might be related to the different ages of the bursts we are probing with stellar populations synthesis, which considers a wide range of bursts up to 10 Myr. When using emission line indicators to derive SFRs, one is looking into a more instantaneous burst scenario, favoring the youngest components of the stellar population.

Assuming the SFR of 0.43 M$_\odot$yr^{-1} for the last 10 Myr, the inner 60 pc radius of this source would have formed ∼4×10^{6}M$_\odot$. Then, if we assume an efficiency of ∼0.1 to convert gas into stars, this region should comprise around 10^7 M$_\odot$ of cold molecular (H$_2$) gas (M$_{cold}$), which is in agreement with the values found by previous studies for the cold molecular gas in this region of NGC 4303, such as Schinnerer et al. (2002) and R16. The former derived M$_{cold}$=6.9×10^{7}M$_\odot$ directly from CO observations of the nuclear disc of this object, while the later estimated M$_{cold}$=6.25×10^{6}M$_\odot$ from converting hot to cold molecular gas masses (e.g. Mazzalay et al. 2013).

A alternative way to approach this would be to compare rates of star formation, mass-inflow and mass accre-

tion to the black hole. Mass-inflow rates are in the range of 10^{-2}−10 M$_\odot$yr^{-1}, which is consistent with our nuclear SFR (0.43 M$_\odot$yr^{-1}) plus a typical mass accretion rate to the black hole of 10^{-3} to 10^{-2} M$_\odot$yr^{-1} (Riffel 2013, and references therein). Thus, the values we are finding for the SFR in the central region of this source are feasible with the amount of gas available to form stars.

6 CONCLUSIONS

We present the first spatially resolved stellar population study of the inner ∼200 pc radius of NGC 4303 in the NIR. Using J-, H- and K-band SINFONI/VLT data, stellar population synthesis was performed with the STARLIGHT code and M05 SSP models. The main conclusions of this work go as follows:

(i) The dominant stellar population component presents a spatial variation in the inner ∼200 pc radius of this source, suggesting an age stratification. Younger stellar population components (t ≤ 2 Gyr) are distributed along a circumnuclear ring with 200−250 pc radius in agreement with previous studies (R16). Three main components stand out: two nuclear blobs, one composed by young stars (t ≤ 50 Myr) and shifted towards east from the centre (here defined as the peak of the Brγ emission line) and one composed by intermediate-age stars (50 Myr < t ≤ 2 Gyr) located southwest from the centre; and an internal spiral arm-like structure also composed by intermediate-age stars surrounding the blob of young stars. The old stellar population component which we attribute to an underlying bulge stellar population is distributed outside the two blob structures, with an enhanced contribution northwest from the centre. These results reveal a rather complex star formation history in NGC 4303, indicating star formation has occurred through multiple bursts in this source.

(ii) With our stellar population synthesis analysis we favor the interpretation of a circumnuclear ring of star formation in the inner ∼250 pc radius of NGC 4303 rather than a spiral arm structure as suggested by C02, in agreement with the analysis of the emission gas presented in R16. We suggest the spiral arm seen in UV images is tracing the less obscured star-forming regions of the circumnuclear ring.

(iii) Circumnuclear star-forming regions (CNSFRs) distributed along the ring present SFRs in the range of 0.002−0.14 M$_\odot$yr^{-1}. Our results favor the 'pearls-on-a-string' star formation scenario with an age gradient along the ring. This conclusion is based on the fact that we have found a value for the total SFR in the ring which is lower than the critical SFR (∼1 M$_\odot$yr^{-1}) to separate between the 'pearls-on-a-string' and the 'pop-corn' scenarios.

(iv) At the nuclear region (R≲ 60 pc) we find a series of star formation bursts: a first one occurring 13 Gyrs ago (x_o), accounting for 50% of the light at 2.067μm; a set of individual minor bursts with ages from 0.3−0.7 Gyr (x_i) corresponding to ∼15% of the light and a contribution of ∼35% of the x_y component with a major burst (∼ 30%) at 7.5 Myr. We derive a nuclear SFR of 0.43 M$_\odot$yr^{-1}, corresponding to a star formation surface density ($\sum_{SFR}$) of ∼40 M$_\odot$yr^{-1}kpc^{-2}.

(v) No signatures of non-thermal featureless continuum and hot dust (blackbody functions) components were nec-

essary to reproduce the nuclear (inner 60 pc) continuum of this source. This result supports the scenario in which a LLAGN/LINER-like source is hidden in the centre of NGC 4303, rather than a Seyfert 2 nucleus. In the case of Seyferts, such components are required to properly reproduce their spectral energy distribution.

(vi) A reddening free nuclear spectrum (R ≲ 60 pc) was fitted for this source, in agreement with UV and optical previous results. When looking to the most inner (unresolved) regions (<10 pc), we find a reddened solution consistent with the presence of a hidden AGN, as already proposed by C00 from the large $V-H$ colors (3.2 mag) in this region.

(vii) From our spatially resolved comparison of the results obtained using different SSP models, we concluded the use of M05 models, in general, yields a more consistent scenario for the distribution of the stellar populations. Results using BC03 and C09 models miss the contribution of intermediate-age stars, which were expected to be found in active star formation sources. We speculate the main reason for discrepancies found between the results using these three low-resolution EPS models sets is related to their prescription for implementing the TP-AGB phase to the models.

As LLAGNs are the most common type of nuclear activity in the Local Universe, the understanding of their nature and SFH is of utmost importance for the comprehension of galaxy formation and evolution. Our results on the spatially resolved stellar populations of the few hundreds of parsecs in the nearby LLAGN NGC 4303 show a complex star formation scenario, with different stellar population components coexisting with a low efficiency accreting black hole. Thus, this detailed study help to shed some light on the contemporary scenarios of galaxy formation and evolution.

REFERENCES

Asari N. V., Cid Fernandes R., Stasińska G., Torres-Papaqui J. P., Mateus A., Sodré L., Schoenell W., Gomes J. M., 2007, MNRAS, 381, 263
Baldwin C., McDermid R. M., Kuntschner H., Maraston C., Conroy C., 2018, MNRAS, 473, 4698
Belfiore F., et al., 2016, MNRAS, 461, 3111

Bessell M. S., Brett J. M., Wood P. R., Scholz M., 1989, A&AS, 77, 1
Bessell M. S., Brett J. M., Scholz M., Wood P. R., 1991, A&AS, 89, 335
Bica E., 1988, A&A, 195, 76
Bica E., Alloin D., 1986, A&A, 162, 21
Böker T., Falcón-Barroso J., Schinnerer E., Knapen J. H., Ryder S., 2008, AJ, 135, 479
Bolzonella M., Miralles J.-M., Pelló R., 2000, A&A, 363, 476
Bonnet H., et al., 2004, The Messenger, 117, 17
Bruzual G., Charlot S., 2003, MNRAS, 344, 1000
Burtscher L., et al., 2015, A&A, 578, A47
Busch G., Eckart A., Valencia-S. M., Fazeli N., Scharwächter J., Combes F., García-Burillo S., 2017, A&A, 598, A55
Calzetti D., Kinney A. L., Storchi-Bergmann T., 1994, ApJ, 429, 582
Calzetti D., Armus L., Bohlin R. C., Kinney A. L., Koornneef J., Storchi-Bergmann T., 2000, ApJ, 533, 682
Cassisi S., degl'Innocenti S., Salaris M., 1997a, MNRAS, 290, 515
Cassisi S., Castellani M., Castellani V., 1997b, A&A, 317, 108
Cid Fernandes R., Gu Q., Melnick J., Terlevich E., Terlevich R., Kunth D., Rodrigues Lacerda R., Joguet B., 2004, MNRAS, 355, 273
Cid Fernandes R., González Delgado R. M., Storchi-Bergmann T., Martins L. P., Schmitt H., 2005a, MNRAS, 356, 270
Cid Fernandes R., Mateus A., Sodré L., Stasińska G., Gomes J. M., 2005b, MNRAS, 358, 363
Colina L., Arribas S., 1999, ApJ, 514, 637
Colina L., Wada K., 2000, ApJ, 529, 845
Colina L., García Vargas M. L., Mas-Hesse J. M., Alberdi A., Krabbe A., 1997, ApJ, 484, L41
Colina L., Gonzalez Delgado R., Mas-Hesse J. M., Leitherer C., 2002, ApJ, 579, 545
Colina L., et al., 2015, A&A, 578, A48
Combes F., 2003, in Collin S., Combes F., Shlosman I., eds, Astronomical Society of the Pacific Conference Series Vol. 290, Active Galactic Nuclei: From Central Engine to Host Galaxy. p. 411 (arXiv:astro-ph/0210232)
Combes F., Prugniel P., Rampazzo R., Sulentic J. W., 1994, A&A, 281, 725
Conroy C., 2013, Annual Review of Astronomy and Astrophysics, 51, 393
Conroy C., Gunn J. E., White M., 2009, ApJ, 699, 486
Conroy C., Villaume A., van Dokkum P. G., Lind K., 2018, ApJ, 854, 139
Dahmer-Hahn L. G., Riffel R., Rodríguez-Ardila A., Martins L. P., Kehrig C., Heckman T. M., Pastoriza M. G., Dametto N. Z., 2018, MNRAS, 476, 4459
Dametto N. Z., Riffel R., Pastoriza M. G., Rodríguez-Ardila A., Hernandez-Jimenez J. A., Carvalho E. A., 2014, MNRAS, 443, 1754
Davies R. I., et al., 2006, ApJ, 646, 754
Davies R. I., Mueller Sánchez F., Genzel R., Tacconi L. J., Hicks E. K. S., Friedrich S., Sternberg A., 2007, ApJ, 671, 1388
Díaz-Santos T., Alonso-Herrero A., Colina L., Ryder S. D., Knapen J. H., 2007, ApJ, 661, 149
Diniz M. R., Riffel R. A., Riffel R., Crenshaw D. M., Storchi-Bergmann T., Fischer T. C., Schmitt H. R., Kraemer S. B., 2017, MNRAS, 469, 3286
Dors Jr. O. L., Storchi-Bergmann T., Riffel R. A., Schimdt A. A., 2008, A&A, 482, 59
Eisenhauer F., et al., 2003, in Iye M., Moorwood A. F. M., eds, Proc. SPIE Vol. 4841, Instrument Design and Performance for Optical/Infrared Ground-based Telescopes. pp 1548–1561 (arXiv:astro-ph/0306191), doi:10.1117/12.459468
Ferrarese L., Merritt D., 2000, ApJ, 539, L9
Ferrarese L., Livio M., Freedman W., Saha A., Stetson P. B., Ford H. C., Hill R. J., Madore B. F., 1996, ApJ, 468, L95

Filippenko A. V., 2003, 290, 369

Filippenko A. V., Sargent W. L. W., 1986, in Giuricin G., Mezzetti M., Ramella M., Mardirossian F., eds, Astrophysics and Space Science Library Vol. 121, Structure and Evolution of Active Galactic Nuclei. pp 21–42, doi:10.1007/978-90-277-2155-6_3

Fluks M. A., Plez B., The P. S., de Winter D., Westerlund B. E., Steenman H. C., 1994, A&AS, 105

Gebhardt K., et al., 2000, ApJ, 539, L13

Girardi L., Bressan A., Bertelli G., Chiosi C., 2000, A&AS, 141, 371

González Delgado R. M., Heckman T., Leitherer C., 2001, ApJ, 546, 845

Gu Q., Melnick J., Cid Fernandes R., Kunth D., Terlevich E., Terlevich R., 2006, MNRAS, 366, 480

Heckman T. M., González-Delgado R., Leitherer C., Meurer G. R., Krolik J., Wilson A. S., Koratkar A., Kinney A., 1997, ApJ, 482, 114

Ho L. C., Filippenko A. V., Sargent W. L. W., Peng C. Y., 1997, ApJS, 112, 391

Höfner S., Loidl R., Aringer B., Jørgensen U. G., Hron J., 2000, in ISO Beyond the Peaks: The 2nd ISO Workshop on Analytical Spectroscopy. p. 299

Hsieh B. C., et al., 2017, ApJ, 851, L24

Jiménez-Bailón E., Santos-Lleó M., Mas-Hesse J. M., Guainazzi M., Colina L., Cerviño M., González Delgado R. M., 2003, ApJ, 593, 127

Kennicutt Jr. R. C., 1988, ApJ, 334, 144

Kennicutt Jr. R. C., Keel W. C., Blaha C. A., 1989, AJ, 97, 1022

Kormendy J., Ho L. C., 2013, Annual Review of Astronomy and Astrophysics, 51, 511

Kotilainen J. K., Forbes D. A., Moorwood A. F. M., van der Werf P. P., Ward M. J., 1996, A&A, 313, 771

Krabbe A., Sternberg A., Genzel R., 1994, ApJ, 425, 72

Lançon A., Mouhcine M., 2002, A&A, 393, 167

Lançon A., Wood P. R., 2000, A&AS, 146, 217

Lejeune T., Cuisinier F., Buser R., 1997, A&AS, 125

Lejeune T., Cuisinier F., Buser R., 1998, A&AS, 130, 65

Ma C., de Grijs R., Ho L. C., 2018, ApJ, 857, 116

Maraston C., 2005, MNRAS, 362, 799

Maraston C., Strömbäck G., 2011, MNRAS, 418, 2785

Martins L. P., Riffel R., Rodríguez-Ardila A., Gruenwald R., de Souza R., 2010, MNRAS, 406, 2185

Martins L. P., Rodríguez-Ardila A., Diniz S., Gruenwald R., de Souza R., 2013a, MNRAS, 431, 1823

Martins L. P., Rodríguez-Ardila A., Diniz S., Riffel R., de Souza R., 2013b, MNRAS, 435, 2861

Mateus A., Sodré L., Cid Fernandes R., Stasińska G., Schoenell W., Gomes J. M., 2006, MNRAS, 370, 721

Mazzalay X., et al., 2013, MNRAS, 428, 2389

Mazzuca L. M., Knapen J. H., Veilleux S., Regan M. W., 2008, The Astrophysical Journal Supplement Series, 174, 337

Meneses-Goytia S., Peletier R. F., Trager S. C., Vazdekis A., 2015, A&A, 582, A97

Menezes R. B., Steiner J. E., Ricci T. V., 2014, MNRAS, 438, 2597

Menezes R. B., da Silva P., Ricci T. V., Steiner J. E., May D., Borges B. W., 2015, MNRAS, 450, 369

Mollá M., Hardy E., Beauchamp D., 1999, ApJ, 513, 695

Origlia L., Oliva E., 2000, New Astronomy Review, 44, 257

Pickles A. J., 1998, PASP, 110, 863

Ramos Almeida C., Pérez García A. M., Acosta-Pulido J. A., 2009, ApJ, 694, 1379

Riffel R. A., 2013, Boletin de la Asociacion Argentina de Astronomia La Plata Argentina, 56, 13

Riffel R., Pastoriza M. G., Rodríguez-Ardila A., Maraston C., 2007, ApJ, 659, L103

Riffel R. A., Storchi-Bergmann T., Dors O. L., Winge C., 2009a, MNRAS, 393, 783

Riffel R., Pastoriza M. G., Rodríguez-Ardila A., Bonatto C., 2009b, MNRAS, 400, 273

Riffel R. A., Storchi-Bergmann T., McGregor P. J., 2009c, ApJ, 698, 1767

Riffel R. A., Storchi-Bergmann T., Riffel R., Pastoriza M. G., 2010, ApJ, 713, 469

Riffel R., Ruschel-Dutra D., Pastoriza M. G., Rodríguez-Ardila A., Santos Jr. J. F. C., Bonatto C. J., Ducati J. R., 2011a, MNRAS, 410, 2714

Riffel R., Bonatto C., Cid Fernandes R., Pastoriza M. G., Balbinot E., 2011b, MNRAS, 411, 1897

Riffel R., Riffel R. A., Ferrari F., Storchi-Bergmann T., 2011c, MNRAS, 416, 493

Riffel R., et al., 2015, MNRAS, 450, 3069

Riffel R. A., et al., 2016, MNRAS, 461, 4192

Röck B., Vazdekis A., Ricciardelli E., Peletier R. F., Knapen J. H., Falcón-Barroso J., 2016, A&A, 589, A73

Rodríguez-Ardila A., Mazzalay X., 2006, MNRAS, 367, L57

Rodríguez-Ardila A., Contini M., Viegas S. M., 2005, MNRAS, 357, 220

Rosario D. J., et al., 2018, MNRAS, 473, 5658

Rosenberg M. J. F., van der Werf P. P., Israel F. P., 2012, A&A, 540, A116

Ryder S. D., Knapen J. H., Takamiya M., 2001, MNRAS, 323, 663

Schaller G., Schaerer D., Meynet G., Maeder A., 1992, A&AS, 96, 269

Schinnerer E., Maciejewski W., Scoville N., Moustakas L. A., 2002, ApJ, 575, 826

Schmidt A. A., Copetti M. V. F., Alloin D., Jablonka P., 1991, MNRAS, 249, 766

Schönell Astor J. J., Storchi-Bergmann T., Riffel R. A., Riffel R., 2017, MNRAS, 464, 1771

Seo W.-Y., Kim W.-T., 2013, ApJ, 769, 100

Shlosman I., Frank J., Begelman M. C., 1989, Nature, 338, 45

Shlosman I., Begelman M. C., Frank J., 1990, Nature, 345, 679

Singh R., et al., 2013, A&A, 558, A43

Storchi-Bergmann T., Raimann D., Bica E. L. D., Fraquelli H. A., 2000, ApJ, 544, 747

Storchi-Bergmann T., González Delgado R. M., Schmitt H. R., Cid Fernandes R., Heckman T., 2001, ApJ, 559, 147

Storchi-Bergmann T., Riffel R. A., Riffel R., Diniz M. R., Borges Vale T., McGregor P. J., 2012, ApJ, 755, 87

Valencia-S. M., Zuther J., Eckart A., García-Marín M., Iserlohe C., Wright G., 2012, A&A, 544, A129

Westera P., Lejeune T., Buser R., Cuisinier F., Bruzual G., 2002, A&A, 381, 524

Worthey G., Ottaviani D. L., 1997, ApJS, 111, 377

Zibetti S., Gallazzi A., Charlot S., Pierini D., Pasquali A., 2013, MNRAS, 428, 1479

de Vaucouleurs G., de Vaucouleurs A., Corwin Jr. H. G., Buta R. J., Paturel G., Fouque P., 1991, Third Reference Catalogue of Bright Galaxies

This paper has been typeset from a TeX/LaTeX file prepared by the author.

Capítulo 4

Considerações Finais

Na primeira parte deste trabalho, estudamos a variação espacial das SPs na região central de quatro galáxias *Starburst* do universo local: NGC 34, NGC 1614, NGC 3310 e NGC 7714, através de espectroscopia de fenda longa no NIR (0.8-2.4μm). O código usado nesse trabalho foi o STARLIGHT, atualizado com os modelos de SSPs calculados por Maraston (2005,M05). Nesses dados também fizemos um teste da metodologia a ser empregada em dados espacialmente resolvidos. Os principais resultados desses estudo são:

- A luz do NIR no entorno da região nuclear dessas galáxias é dominada por SPs de idade jovem ($t \leq 50 \times 10^6$ anos) à intermediária ($50 \times 10^6 < t \leq 2 \times 10^9$ anos), somando de 40% à 100% da contribuição em luz. O predomínio de SP de idade jovem à intermediária também é observado na região central das galáxias, com exceção de NGC 1614, para qual a contribuição da SP velha ($t \geq 2 \times 10^9$ anos) prevalece no núcleo.

- Encontramos evidências de uma estrutura em forma de anel circumnuclear de formação estelar e de um núcleo secundário em NGC 1614, em concordância com resultados da literatura. Também sugerimos que o processo de interação e/ou fusão em três das galáxias da amostra (NGC 1614, NGC 3310 e NGC 7714) pode explicar os baixos valores de metalicidade derivados para a componente jovem de SP dessas fontes. Nesse cenário, o gás não processado, pobre em metais, da galáxia companheira teria escoado para a região central das galáxias e diluído o gás já presente nessa região, antes de começar o último surto de formação estelar.

- Comparamos, também, os resultados obtidos com os modelos de melhor resolução de Maraston & Strömbäck (2011,- M11) e econtramos que os modelos

de M11 tendem a aumentar a contribuição das populações estelares de idade velha e intermediária com relação às idades mais jovens. Essa discrepância entre os resultados pode estar associada ao fato de que os modelos de SSPs para as idades mais jovens (abaixo de $\sim 100 \times 10^6$ anos) estão significativamente atenuados pela absorção da poeira no UV. Ainda, acima de $\sim 1 \mu$m, cerca de metade dos espectros não têm observações espectroscópicas. Dessa forma, os autores utilizaram fotometria de banda larga para construir uma distribuição de energia (suavizada), resultando em uma região sem linhas nos espectros de M11, o que pode implicar que algumas linhas de absorção do NIR não estejam bem resolvidas, mesmo nos modelos de mais alta resolução espectral. Devido às limitações dos modelos de M11, como discutido acima, não fica bem claro se o uso desses modelos de maior resolução espectral produzem resultados melhores e confiáveis o suficiente, para compensar o fato de que estão disponíveis somente para metalicidade solar no intervalo espectral do NIR. Assim, concluímos que os modelos de baixa resolução espectral de M05 ainda são a melhor opção para esse intervalo espectral.

O estudo da distribuição das populações estelares utilizando o intervalo espectral do NIR é uma ferramenta bastante útil para construir um cenário de formação estelar ao longo das galáxias, uma vez que com este intervalo penetramos mais fundo nas camadas de poeira, acessando informações que podem ser perdidas nos intervalos espectrais do óptico e do UV. Outro ponto importante está no fato de que os resultados para sistemas interagentes com intensa formação estelar no Universo Local podem oferecer apoio ao estudo de fontes a altos *redshifts*, as quais são de suma importância no entendimento do histórico de formação estelar do universo jovem.

Nesta segunda parte do trabalho, apresentamos os resultados obtidos no estudo das populações estelares espacialmente resolvidas na galáxia ativa NGC 4303, com dados de IFS na região do NIR obtidos com o instrumento SINFONI do telesópio VLT. Nosso principal objetivo é estudar a relação entre a formação estelar cicumnuclear e a atividade nuclear em galáxias ativas. Abaixo listamos nossas principais resultados para a galáxia protótipo estudada.

- A componente dominate da população estelar apresenta uma variação espacial no raio interno a ~ 200 pc nessa fonte, sugerindo uma estratificação em idade. As componentes mais jovens da população estelar ($t \leq 2 \times 10^9$ anos) estão distribuídas ao longo de um anel circumnuclear de formação estelar com

raio de $200-250\,\mathrm{pc}$, de acordo com estudos anteriores (Riffel et al., 2016, vide Apêndice A). Três principais estruturas se destacam: Dois *blobs*, um composto por estrelas jovens ($t \leq 50{\times}10^6$anos), deslocado a leste do centro (aqui definido como o pico da linha de emissão de Brγ) e outro composto por estrelas de idade intermediária ($50{\times}10^6$anos $< t \leq 2{\times}10^9$anos), localizado a sudoeste do centro; e uma estrutura do tipo braço-espiral interno com estrelas de idade intermediária, circundando o *blob* de estrelas jovens. A componente velha da população estelar ($t > 2{\times}10^9$anos), a qual atribuímos à população estelar do bojo, está distribuída fora dos dois *blobs* de idades mais jovens, com um aumento na contribuição a noroeste do centro. Esses resultados revelam um histórico de formação estelar complexo em NGC 4303, indicando que a formação estelar aconteceu através de múltiplos surtos de formação estelar nessa galáxia.

- Nossos resultados de síntese de população estelar favorecem a interpretação de um anel circumnuclear de formação estelar na região interna a um raio de $\sim$250 pc em NGC 4303, ao invés de uma estrutura de braço espiral, como sugerido por Colina et al. (2002), de acordo com nossa análise do gás em emissão apresentada em Riffel et al. (2016). Sugerimos que o braço espiral visto nas imagens do UV está traçando as regiões de formação estelar menos obscurecidas do anel circumnuclear.

- Regiões de formação estelar circumnuclear (CNSFRs) distribuídas ao longo do anel apresentam SFRs no intervalo de $0.002-0.14\,\mathrm{M_\odot ano^{-1}}$. Nossos resultados favorecem o cenário chamado *'pearls-on-a-string'* de formação estelar no anel, apresentando um gradiente de idades. Essa conclusão é baseada no fato de que encontramos um valor para o SFR total do anel, o qual está abaixo de um SFR crítico ($\sim$1 $\mathrm{M_\odot\,ano^{-1}}$), que separa entre os diferentees cenários para formação estelar em anéis circumnucleares.

- Na região nuclear (R$\lesssim$ 60 pc) encontramos uma série de surtos de formação estelar: o primeiro ocorrendo a $13{\times}10^9$anos (x_o) atrás, contribuindo com 50% da luz em 2.067μm; uma série de surtos menores individuais com idades entre $0.3-0.7{\times}10^9$anos (x_i), contribuindo com $\sim$15% da luz; e uma controbuição de $\sim$35% da componente jovem da população estelar (x_y), com um surto predominante a $7.5{\times}10^6$anos. Além disso, derivamos um SFR nuclear de $0.43\,\mathrm{M_\odot ano^{-1}}$, correspondendo a uma densidade superficial de formação estelar ($\sum_{SFR}$) de $\sim$40 $\mathrm{M_\odot ano^{-1}kpc^{-2}}$

- Não encontramos assinatura de contínuo não térmico ou emissão de poeira quente para a reprodução do contínuo nuclear (60 pc centrais) em NGC 4303. Esse resultado dá suporte ao cenário em que um LLAGN/LINER está obscurecido no centro dessa galáxia, em favor de um núcleo do tipo Seyfert 2. No caso de galáxias Seyferts, essas componentes são mais pronunciadas e, portanto, necessárias para reproduzir a distribuição espectral de energia nessas fontes.

- Um espectro nuclear (R$\lesssim$ 60 pc) livre de poeira foi ajustado para essa galáxia, em concordância com resultados anteriores do óptico e UV. Quando analisamos as regiões ainda mais internas (e não resolvidas, <10 pc), encontramos uma solução com avermelhamento considerável de ~2.5 amg, consistente com a presença de um AGN obscurecido, como proposto anteriormente por Colina & Wada (2000), devido ao alto valor para o excesso de cor de $V-H$ (3.2 mag) nessa região.

- Pela comparação espacialmente resolvida dos resultados utilizando diferentes modelos de SSP, concluímos que o uso dos models de Maraston (2005), em geral, proporcionam um cenário mais consistente para a distribuição das populações estelares. Os resultados utilizando os modelos de Bruzual & Charlot (2003) e Conroy et al. (2009) perdem a contribuição da estrelas de idade intermediária, as quais esperamos encontrar em fontes com formação estelar ativa, como é o caso de NGC 4303. Especulamos que a principal causa da discrepância entre os resultados utilizando esses três diferentes modelos EPS de baixa resolução está relacionada com a receita utilizada para a implementação da fase das TP-AGBs aos modelos.

Sendo LLAGNs o tipo de atividade nuclear mais comum no Universo Local, o entendimento de sua natureza e do histórico de formação estelar desse tipo de fonte é de suma importância para a compreensão da formação e evolução de galáxias. Nossos resultados das populações estelares espacialmente resolvidas nas centenas de parsecs internos da LLAGN próxima NGC 4303 mostram um cenário de formação estelar complexo, com diferentes componentes de população estelar coexistindo com um buraco negro de baixa eficiência de acreção. Dessa forma, esse estudo detalhado pode contribuir para a contrução de cenários contemporâneos de formação e evolução de galáxias.

Adicionalmente, nossos resultados apontam para o fato de que a LLAGN NGC 4303 tem uma taxa de formação estelar circumnuclear inferior aquela encontrada em galáxias *Starburst* clássicas, indicando que no caso de AGNs de baixa luminosidade

não parece haver uma correlação forte entre a formação estelar e a atividade nuclear, resultado esse que concorda com os de simulações (e.g. Zubovas & Bourne, 2017).

4.1 Perspectivas

Já com a metodologia consolidada, o próximo passo é aplicar os procedimentos para as outras galáxias da amostra (∼30 fontes) que compõe um projeto em desenvolvimento do nosso grupo: AGNIFS, no intuito de realizar o primeiro estudo espacialmente resolvido da relação entre a formação estelar circumnuclear e o AGN em uma amostra selecionada, contendo galáxias com diferentes tipos de atividade nuclear e em um grande intervalo de luminosidade. Essa amostra é completa em volume e estatisticamente significativa cobrindo uma grande faixa de luminosidades, incluindo luminosidades de AGNs que podem ser associadas com AGNs de mais alto *redshift* permitindo assim estudar indiretamente os efeitos dos processos de *feeding* e *feedback* na evolução de galáxias.

Apêndice A: Artigo

Riffel et al. (2016)

1. **A SINFONI view of the nuclear activity and circumnuclear star formation in NGC 4303**,
   R. A. Riffel, L. Colina, T. Storchi-Bergmann, J. Piqueras López, S. Arribas, R. Riffel, M. Pastoriza, D. A. Sales, **N.Z. Dametto**, A. Labiano and R. L. Davies
   Monthly Notices of the Royal Astronomical Society, v.461, p.4192-4205, July 2016.

Esse é o primeiro artigo da série sobre NGC 4303, no qual discutimos a dinâmica e cinemática do gás e das estrelas na região central dessa fonte. Os resultados aqui obtidos foram amplamente utilizados na discussão das populações estelares espacialmente resolvidas, apresentada neste trabalho.

A SINFONI view of the nuclear activity and circumnuclear star formation in NGC 4303

Rogemar A. Riffel,[1]★ L. Colina,[2,3] T. Storchi-Bergmann,[4] J. Piqueras López,[2]
S. Arribas,[2,3] R. Riffel,[4] M. Pastoriza,[4] Dinalva A. Sales,[4] N. Z. Dametto,[4]
A. Labiano[5] and R. I. Davies[6]

[1]*Departamento de Física, Centro de Ciências Naturais e Exatas, Universidade Federal de Santa Maria, Santa Maria, RS 97105-900, Brazil*
[2]*Centro de Astrobiología (CAB, CSIC-INTA), Carretera de Ajalvir, Torrejón de Ardoz, E-28850 Madrid, Spain*
[3]*ASTRO-UAM, Universidad Autónoma de Madrid (UAM), Unidad Asociada CSIC, E-28049 Madrid, Spain*
[4]*Departamento de Astronomia, Instituto de Física, Universidade Federal do Rio Grande do Sul, CP 15051, Porto Alegre, RS 91501-970, Brazil*
[5]*Institute for Astronomy, Department of Physics, ETH Zurich, CH-8093 Zurich, Switzerland*
[6]*Max-Planck-Institut für extraterrestrische Physik, Postfach 1312, D-85741 Garching, Germany*

ABSTRACT

We present new maps of emission-line flux distributions and kinematics in both ionized (traced by H I and [Fe II] lines) and molecular (H_2) gas of the inner $0.7 \times 0.7 \, kpc^2$ of the galaxy NGC 4303, with a spatial resolution 40–80 pc and velocity resolution 90–150 $km \, s^{-1}$ obtained from near-IR integral field spectroscopy using the Very Large Telescope instrument SINFONI. The most prominent feature is a 200–250 pc ring of circumnuclear star-forming regions. The emission from ionized and molecular gas shows distinct flux distributions: while the strongest H I and [Fe II] emission comes from regions in the west side of the ring (ages ~ 4 Myr), the H_2 emission is strongest at the nucleus and in the east side of the ring (ages > 10 Myr). We find that regions of enhanced hot H_2 emission are anti-correlated with those of enhanced [Fe II] and H I emission, which can be attributed to post-starburst regions that do not have ionizing photons anymore but still are hot enough (≈ 2000 K) to excite the H_2 molecule. The line ratios are consistent with the presence of an active galactic nucleus at the nucleus. The youngest regions have stellar masses in the range 0.3–1.5×10^5 $M_\odot$ and ionized and hot molecular gas masses of ~ 0.25–1.2×10^4 $M_\odot$ and ~ 2.5–$5 \, M_\odot$, respectively. The stellar and gas velocity fields show a rotation pattern, with the gas presenting larger velocity amplitudes than the stars, with a deviation observed for the H_2 along the nuclear bar, where increased velocity dispersion is also observed, possibly associated with non-circular motions along the bar. The stars in the ring show smaller velocity dispersion than the surroundings, which can be attributed to a cooler dynamics due to their recent formation from cool gas.

Key words: galaxies: active – galaxies: individual: NGC 4303 – galaxies: ISM – infrared: galaxies.

1 INTRODUCTION

Star formation (SF) in the circumnuclear regions of galaxies and its connection with the existence of nuclear young stellar clusters and/or active galactic nuclei (AGN) have been the subject of many studies over the past several decades since early models invoking dynamical resonances in a rotating bar potential (Combes & Gerin 1985), bars within bars (Shlosman, Frank & Begelman 1989) and the direct feeding of AGN due to stellar winds or cloud–cloud collisions in the vicinity of the nucleus (Norman & Scoville 1988;

Shlosman, Begelman & Frank 1990). Some models (e.g. Heller & Shlosman 1994; Knapen et al. 1995) suggest that gas could flow inwards from the ring, creating a disc of gas that, if massive enough, would become unstable. Under this scenario, a massive black hole in the nucleus could be fed triggering an AGN (Shlosman et al. 1989 1989; Fukuda, Wada & Habe 1998).

Regarding SF in nuclear rings, two scenarios have been proposed: the 'popcorn' (Elmegreen 1994) and the 'pearls on a string' (Böker et al. 2008). The 'popcorn' scenario assumes that the cold molecular gas is accumulated in a circumnuclear resonance ring. If massive enough, the ring becomes gravitational unstable, fragmenting in clumps and forming stellar clusters at random positions. On the other hand, in the 'pearls-on-a-string' scenario, new

★ E-mail: rogemar@ufsm.br

stars are exclusively formed in the regions where the gas enters the ring (i.e. the regions of maximum gas density). These young clusters evolve passively as they orbit along the ring, producing a string of ageing clusters. Independent of the formation mechanism of the stellar clusters, the role of these clusters as they move along the ring can be important. Stellar winds and subsequent supernova (SN) explosions can affect their surrounding interstellar medium, removing gas and halting subsequent SF, as well as generating shocks that will reduce the angular momentum of the gas, that could eventually fall towards the centre, feeding the AGN and/or forming a nuclear star cluster.

Detailed multi-wavelength two-dimensional spectroscopic studies in nearby galaxies with the adequate spatial resolution (∼10 pc, or less) are needed to further investigate the evolutionary scenarios mentioned above. CO interferometric maps [Plateau de Bure interferometer (PdBI)] have shown the presence of a wide range of molecular gas structures in the central kpc region of nearby galaxies with an AGN (García-Burillo et al. 2005). According to these studies, most of the molecular gas is concentrated in the form of a circumnuclear ring of several hundred pc to kpc size, while ≈33 per cent of the galaxies show the evidence for a direct gas fuelling into the AGN down to scales of ∼50 pc (García-Burillo & Combes 2012). Of particular importance, the near-infrared (near-IR) bands allow the study of the multi-phase gas, from molecular (H_2) to shocked partially ionized (Fe II) to highly ionized gas (e.g. Ca VIII), that can trace a number of different physical structures and mechanisms, from molecular gas reservoirs to AGN outflows.

In the near-IR, recent studies using integral field spectroscopy (IFS; Genzel et al. 1995) have been particularly useful to map the stellar and gas kinematics, as well the gas excitation and distribution of the different gas phases (e.g. Barbosa et al. 2014; Riffel et al. 2014). In nearby Seyfert galaxies, compact (scales of few tens of parsecs) molecular gas discs (Hicks et al. 2009; Riffel & Storchi-Bergmann 2011; Mazzalay et al. 2014), streaming motions towards the nucleus (e.g. Davies et al. 2014; Diniz et al. 2015), ionized gas outflows (e.g. Storchi-Bergmann et al. 2010; Iserlohe et al. 2013) and young stellar populations (e.g. Davies et al. 2007) have been mapped in the nuclear regions. In addition, studies of circumnuclear star-forming rings (CNSFRs) at hundred of pc from the nucleus in nearby spirals (Böker et al. 2008; van der Laan et al. 2013a, 2015; Falcón-Barroso et al. 2014) have focused on establishing the reality of the proposed evolutionary scenarios for the star-forming rings, such as the 'popcorn' scenario (Elmegreen 1994) and the 'pearls-on-a-string' scenario (Böker et al. 2008).

All these previous studies have been focused on either nearby luminous Seyfert galaxies where the output energy is dominated by the AGN or galaxies with luminous CNSFRs. Here we perform a similar study for NGC 4303, a nearby galaxy with both a (low-luminosity) AGN and a star-forming ring, and that has also a young massive cluster at the nucleus. In addition, multi-wavelength observations (Colina et al. 1997, 2002; Colina & Arribas 1999) reveal a spiral of CNSFRs that can be traced all the way into the inner few parsecs (e.g. Colina & Wada 2000; Jiménez-Bailón et al. 2003), suggesting that it could be the feeding channel to the AGN and nuclear star cluster. Finally, a high-velocity nuclear outflow extending up to ≈120 pc to the north-east of the nucleus has also been observed in optical line emission of [O III] (Colina & Arribas 1999).

NGC 4303 is at a distance of 16.1 Mpc (Colina & Arribas 1999), and is classified as an SB(rs)bc (de Vaucouleurs et al. 1991). It is abundant in cold molecular gas (Schinnerer et al. 2002) that shows the global distribution expected for the gas flow in a strong, large-scale bar, and the two-arm spiral structure in the inner kiloparsec

can be explained by a density wave activated by the potential of that bar.

In this paper, we present near-IR IFS of the inner 350 pc radius of NGC 4303, obtained with the integral field spectrograph SINFONI at the Very Large Telescope (VLT) in order to map the kinematics and excitation properties of the different phases of the interstellar medium in the circumnuclear region. It is the first time that such mapping is provided in the near-IR. This work is organized as follows: Section 2 presents the observations and data reduction procedure, while in Section 3, we present maps for emission-line flux distributions and ratios, as well as for the gas and stellar kinematics. The results are discussed in Section 4, and Section 5 presents the conclusions of this work.

2 OBSERVATIONS AND DATA REDUCTION

The observations were done using the near-IR spectrograph SINFONI of the VLT, during the period 82B (February 2009). The pointings were centred on the nucleus of the galaxy, covering a field of view (FoV) of ∼8 arcsec × 8 arcsec per exposure, enlarged by dithering up to ∼9.25 arcsec × 9.25 arcsec, with a plate scale of 0.125 × 0.220 arcsec pixel^{-1}. This corresponds to an average coverage of ∼0.7 × 0.7 kpc with a spatial sampling of ∼10 pc per spaxel.

The data were taken in the J (1.10–1.35 μm), H (1.45–1.80 μm) and K (1.97–2.44 μm) bands with a total integration time of 2400 s per band. In the same way, a set of photometric standard stars was observed to perform the telluric and flux calibration. We estimated the spatial resolution of our seeing-limited observations by fitting a 2D Gaussian profile to a collapsed image of the standard stars. The spatial resolution (full width at half-maximum) measured for each band is ∼1, ∼0.6 and ∼0.5 arcsec for the J, H and K band, respectively, that correspond to 78, 47 and 39 pc at the adopted distance of 16.1 Mpc.

The reduction and calibration processes were performed using the standard ESO pipeline ESOREX (version 3.8.3), and our own IDL routines. The usual corrections of dark, flat-fielding, detector linearity, geometrical distortion and wavelength calibration were applied to each object and sky frames, before subtracting the sky emission from each on-source frame. After each individual data cube was calibrated, we constructed a final data cube per band, taking the relative shifts in the dithering pattern into account.

The calibration of each individual data cube was performed in two steps. First, we removed the telluric absorption from the spectra. We extracted the integrated spectrum of the corresponding standard star within an aperture of 3σ of the best 2D Gaussian fit of a collapsed image. We normalized the spectrum by a blackbody profile at the T_{eff} from the Tycho-2 Spectral Type Catalog (Wright et al. 2003), after removing the strongest absorption features of the stars. The result is a *sensitivity function* that accounts for the telluric absorption.

Secondly, each data cube was flux calibrated. The spectrum of the standard star was converted from counts to physical units using the response curves of the 2MASS filters (Cohen, Wheaton & Megeath 2003), and the J, H and K magnitudes from the 2MASS catalogue (Skrutskie et al. 2006). We then obtained a conversion factor from counts to physical units. Each individual data cube was then divided by its corresponding *sensitivity function* and multiplied by this conversion factor to obtain a full-calibrated data cube. The estimated uncertainty for the conversion factor is ≤15 per cent for each band.

After the data reduction procedure, we performed a spatial filtering of the data cubes using a Butterworth bandpass filter (e.g. Gonzalez & Woods 2002; Menezes, Steiner & Ricci 2015) in order
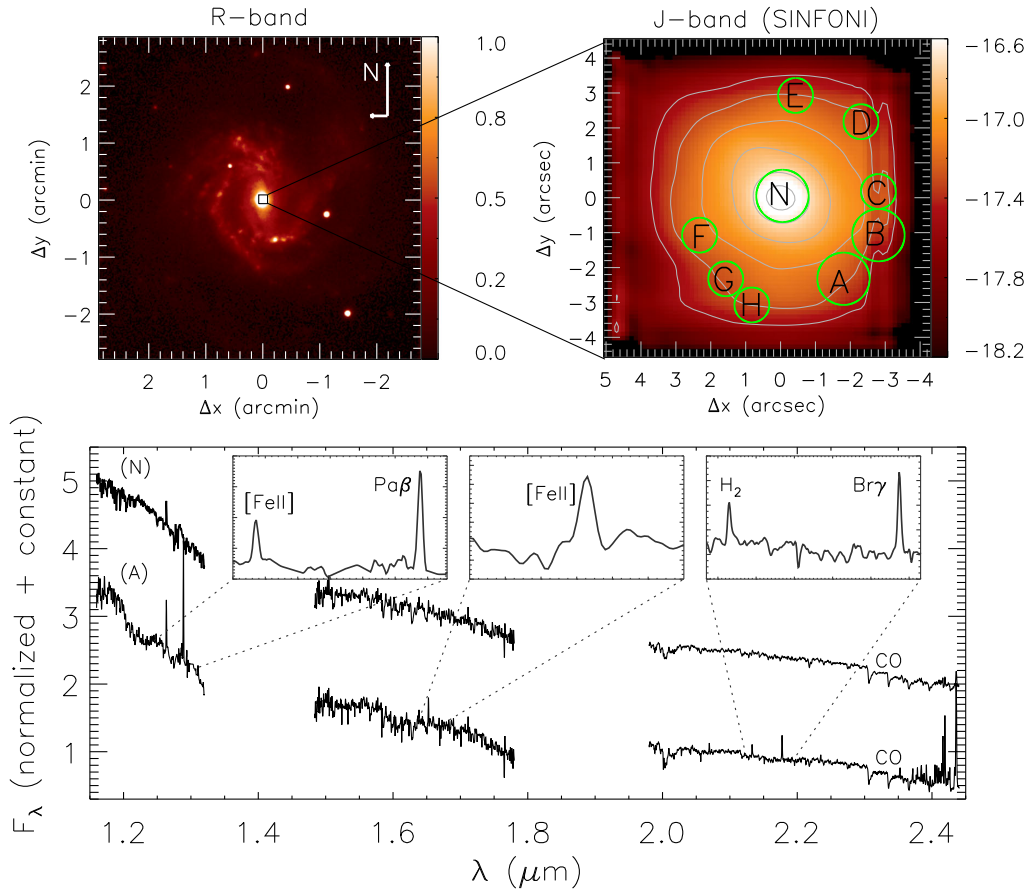
Figure 1. Large-scale image in the *R* band (top-left) from Koopmann, Kenney & Young (2001). *J*-band continuum, reconstructed from the SINFONI data cube as an average of the fluxes between 1.15 and 1.20 μm (top right). The circles mark the position of the CNSFRs and the bottom panel shows the near-IR spectra for the nucleus (top) and for position A (bottom), obtained for a circular aperture with radius 0.75 arcsec and normalized at 2.1 μm. The sub-panels present a zoom of the spectra from position A to better show the main emission lines. The *K*-band CO absorption band heads are clearly visible in both spectra. A constant (1.5) was added to the nuclear spectrum for visualization purpose. The colour bar for the large-scale image is in arbitrary units and for the *J* band it shows the fluxes in logarithmic units [log (erg s^{-1} cm^{-1} spaxel^{-1})].

to remove noise from the observed cubes. The final signal-to-noise ratio (snr) in the continuum is in the range 3–10 for the *J* band with the smallest values observed close to the borders of the FoV and the highest values at the nucleus, while for the *H* and *K* bands we get snr = 3–15. The improvement of the snr by the spatial filtering ranges from 30 to 5 per cent, from the borders of the FoV to the nucleus for all bands, as obtained by calculating the ratios between the snr of the filtered cubes and those of the original ones. By comparing the continuum images for the original and filtered cubes, we concluded that the filtering procedure does not change the angular resolution of the data.

3 RESULTS

The top-left panel of Fig. 1 shows a large-scale optical image of NGC 4303 in the *R* band from Koopmann et al. (2001).[1] In the

[1] This image is available at NASA/IPAC Extragalactic Database (http://ned.ipac.caltech.edu).

top-right panel, we show the *J*-band continuum image obtained from the SINFONI data cube for the inner 9 × 9 arcsec^2, where we label the nucleus 'N' as well as several star-forming regions, in particular region 'A' (a bright circumnuclear Brγ emitting clump), for which the spectra are shown in the bottom panels. The spectra were obtained by integrating the fluxes within a circular aperture of radius 0.75 arcsec and normalized to the flux at 2.1 μm. The two spectra show similar slopes, suggesting that the nuclear and extra-nuclear continuum emission have similar origins. On the other hand, the line emission is stronger in region 'A' than at the nucleus. In the bottom panel, we present also a zoom of spectrum from position A showing the main emission lines: [Fe ɪɪ] λ1.64 μm, [Fe ɪɪ] λ1.25 μm, Paβ, Brγ and H$_2$ λ2.12 μm.

3.1 Emission-line flux distributions and ratios

Different phases of the interstellar medium can be traced in the near-IR by distinct emission lines: ionized (traced by Brγ and Paβ lines),
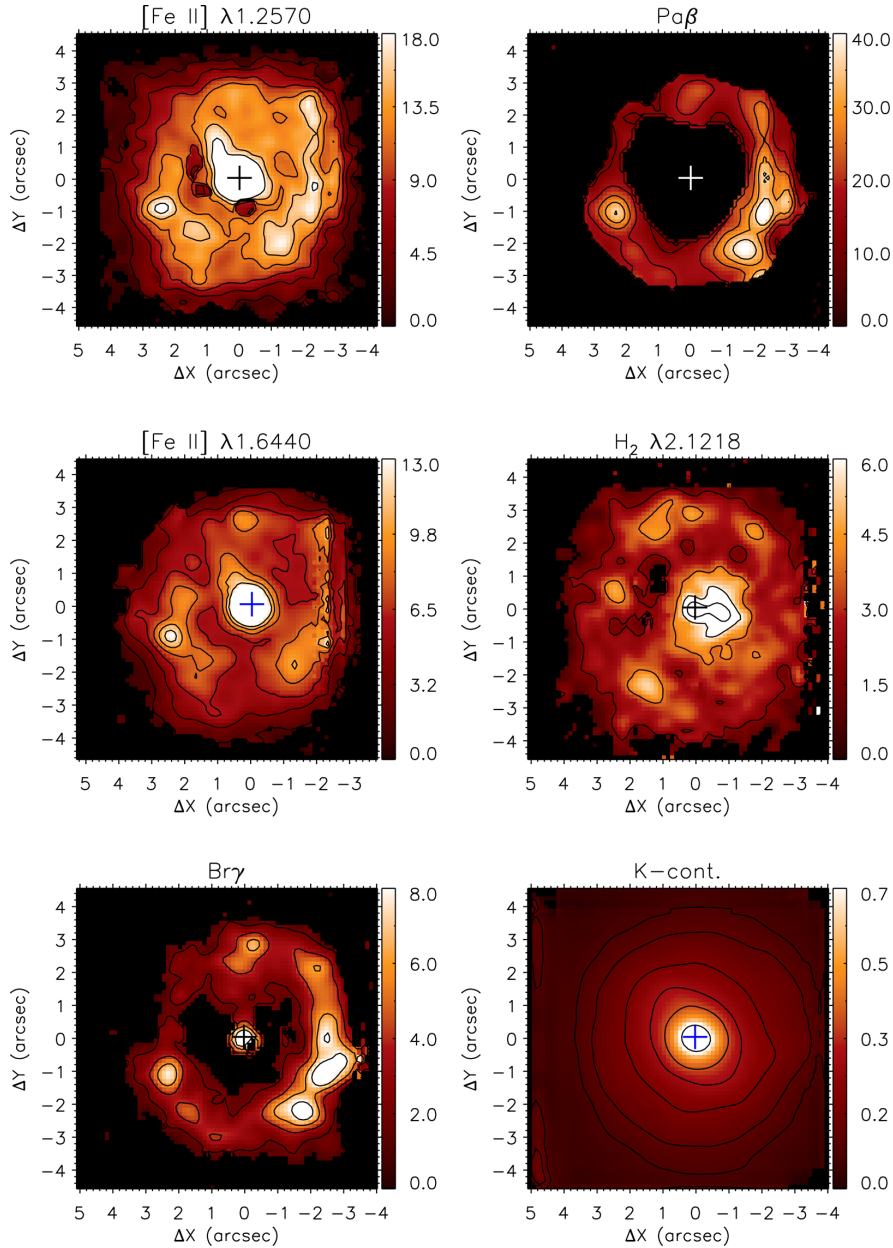
Figure 2. Emission-line flux distributions. The colour bars show the fluxes in units of $10^{-18}\,\mathrm{erg\,s^{-1}\,cm^{-2}}$ and the central cross marks the position of the nucleus. Black locations are masked regions due to the non-detection of the emission lines or due to bad fits of their profiles.

partially ionized/shocks ([Fe II] lines) and hot molecular gas (H$_2$ lines). We used the emission-line PROfile FITting (PROFIT) routine (Riffel 2010) to fit the line profiles with Gaussians and constructed maps for the flux distributions, centroid velocities and velocity dispersions for each emission line.

In Fig. 2, we show the flux distributions for the [Fe II] $\lambda1.25\,\mu$m, Paβ, [Fe II] $\lambda1.64\,\mu$m, H$_2$ $\lambda2.12\,\mu$m and Brγ emission lines. Black in these maps represent masked locations, where the snr of the lines

was not high enough to allow good fits, and regions where the lines were not detected. We masked regions with uncertainties in flux larger than 50 per cent, but, for most locations, the uncertainties are smaller than 20 per cent. The bottom-right panel shows the *K*-band continuum map. All emission lines present extended emission up to 4 arcsec ($\approx$300 pc), and the main feature of the flux distributions is a circumnuclear ring with clumps of enhanced line emission with radius in the range $\approx$2.5–3.2 arcsec (200–250 pc). Some differences

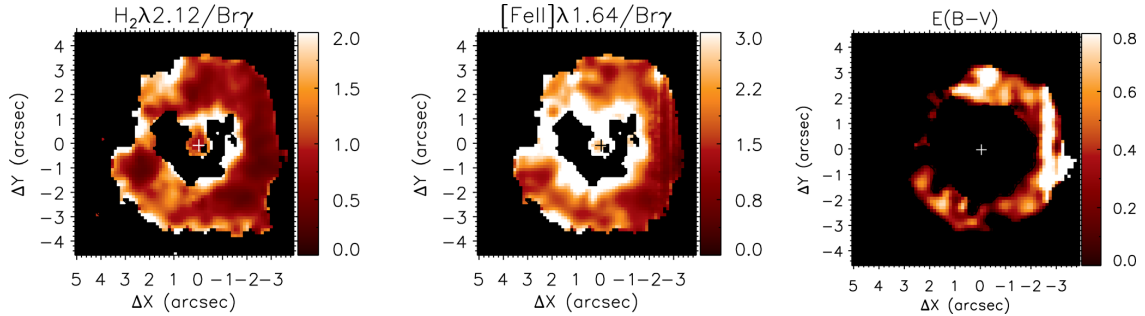**Figure 3.** H$_2$ λ2.12 μm/Brγ and [Fe II] λ1.64 μm/Brγ emission-line ratios and reddening map. The central cross marks the position of the nucleus and black locations are masked regions due to the non-detection of the emission lines or due to bad fits of their profiles.

Figure 4. Equivalent width maps in Å for the [Fe II] λ1.64 μm, H$_2$ λ2.12 μm and Brγ emission lines. The central cross marks the position of the nucleus and black locations are masked regions due to the non-detection o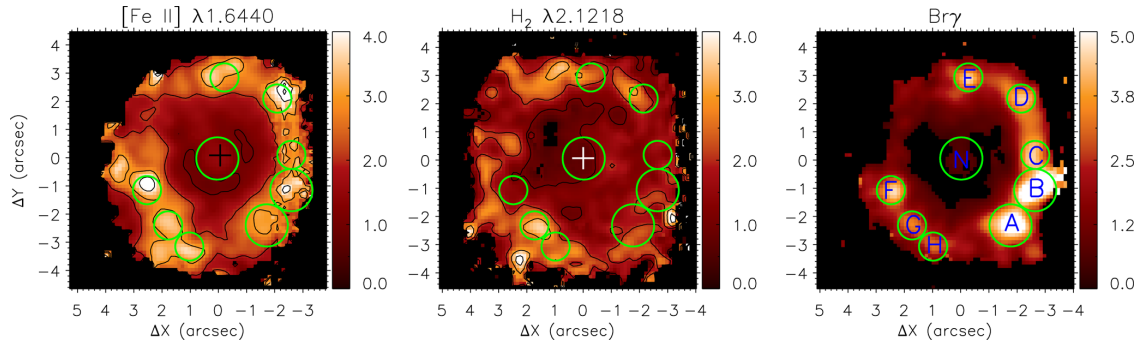f the emission lines or due to bad fits of their profiles. The circles in the Brγ map show the regions used to extract the spectra of the CNSFRs and obtain the quantities listed in Table 1.

are observed among the distinct emission lines: (i) while the [Fe II] and H$_2$ flux distributions present emission at the nucleus, Paβ is not detected there, while Brγ is marginally detected (snr ≈ 2); (ii) along the ring, the H I and [Fe II] emission is strongest to the west (including south-west), and at a region to the south-east, while the H$_2$ emission is strongest mostly to the east (including south-east and north-east).

In Fig. 3, we present the H$_2$ λ2.12 μm/Brγ and [Fe II] λ1.64 μm/Brγ emission-line ratio maps, useful to investigate the excitation mechanisms of the H$_2$ and [Fe II] emission lines (e.g. Reunanen, Kotilainen & Prieto 2002; Rodríguez-Ardila et al. 2004; Rodríguez-Ardila, Riffel & Pastoriza 2005; Dors et al. 2012; Riffel et al. 2013a; Colina et al. 2015). Both ratios present the smallest values at the locations of the star-forming clumps in the circumnuclear ring. Larger values are seen between the ring and the nucleus, but the uncertainties are high due to low Brγ emission. Typical values at the ring are H$_2$ λ2.12 μm/Brγ ∼ 0.3 and [Fe II] λ1.64 μm/Brγ ∼ 0.7, and, at the nucleus, ∼1.4 and ∼3, respectively. A reddening map obtained from Paβ/Brγ is shown in the right-hand panel of Fig. 3, with values ranging from 0 to 0.8, but most locations having values smaller than 0.4. As the extinction in the near-IR is thus small, the fluxes and flux ratios were not corrected for reddening.

Fig. 4 shows maps for the equivalent widths (EqWs) of the [Fe II]1.64, H$_2$ λ2.12 μm and Brγ emission lines. The highest values of EqW at the ring reach 5 Å for Brγ and 4 Å for the H$_2$ and [Fe II] emission lines. Several knots attributed to CNSFRs are clearly observed in the Brγ EqW map which we used to extract the spectrum

for each region. The EqW values we have measured are low when compared with those expected for young (<10 Myr) stellar populations, clearly indicating a large contribution of old stars to the near-IR continuum.

We have calculated the EqWs of the Brγ, Paβ, [Fe II] and H$_2$ λ2.12 μm emission lines for regions labelled from A to F along the ring as well as for the nucleus and show their values, together with those of the emission-line fluxes in Table 1. The spectra of these regions were extracted within apertures of 0.75 arcsec for the nucleus and CNSFR A and 0.50 arcsec for the remaining regions. The apertures were chosen to be larger than the seeing and to include most of the Brγ flux of each region.

3.2 Stellar and gas kinematics

We used the penalized pixel-fitting (pPXF) method of Cappellari & Emsellem (2004) to fit the CO absorption band heads at 2.3 μm and obtain the stellar velocity (V_*) field, velocity dispersion ($σ_*$) and higher order Gauss–Hermite moments (h_3 and h_4) as well as their uncertainties. We used the library of 60 stellar spectra of early-type stars from Winge, Riffel & Storchi-Bergmann (2009) as template spectra and fitted the galaxy spectra in the range from 2.29 to 2.41 μm. The spectral resolution of the stellar spectra is better than the resolution of the galaxy spectra; thus, we degraded the template spectra to the same resolution of the SINFONI observations by convolving the spectra with a Gaussian function to get reliable $σ_*$ measurements.

Table 1. Emission-line fluxes and equivalent widths for the CNSFRs in NGC 4303. Fluxes are shown in units of 10^{-16} erg s^{-1} cm^{-2} and the equivalent widths in Å.

Region	N	A	B	C	D	E	F	G	H
R	0.75 arcsec	0.75 arcsec	0.75 arcsec	0.50 arcsec	0.50 arcsec	0.50 arcsec	0.50 arcsec	0.50 arcsec	0.50 arcsec
$F_{Br\gamma}$	5.2 ± 3.7	7.1 ± 0.8	7.9 ± 1.0	3.3 ± 0.5	2.6 ± 0.5	2.4 ± 0.5	2.8 ± 0.5	1.9 ± 0.3	1.6 ± 0.4
EqW$_{Br\gamma}$	0.7 ± 0.5	4.4 ± 0.6	4.7 ± 0.7	4.0 ± 0.6	3.9 ± 0.8	3.5 ± 0.7	3.7 ± 0.7	2.9 ± 0.5	2.7 ± 0.7
$F_{Pa\beta}$	–	44.2 ± 8.9	42.6 ± 8.1	18.0 ± 3.8	15.7 ± 4.7	12.9 ± 4.7	17.7 ± 4.0	14.6 ± 4.1	14.5 ± 5.2
EqW$_{Pa\beta}$	–	12.3 ± 3.3	11.9 ± 3.3	9.5 ± 2.4	9.8 ± 3.3	8.2 ± 3.1	9.2 ± 2.4	9.8 ± 3.5	11.0 ± 4.8
$F_{[Fe\,II]1.64}$	18.9 ± 7.1	7.5 ± 1.7	7.1 ± 1.8	3.5 ± 1.2	4.3 ± 1.4	3.6 ± 1.3	4.7 ± 1.0	3.5 ± 0.8	2.9 ± 0.9
EqW$_{[Fe\,II]1.64}$	1.4 ± 0.5	3.0 ± 0.7	3.1 ± 0.9	3.0 ± 1.1	3.8 ± 1.4	3.2 ± 1.3	3.7 ± 1.0	3.3 ± 0.8	3.1 ± 1.1
$F_{[Fe\,II]1.25}$	34.3 ± 8.3	13.5 ± 2.2	12.6 ± 2.4	6.5 ± 1.4	7.2 ± 1.3	5.3 ± 1.4	7.7 ± 1.2	6.3 ± 0.9	5.6 ± 1.2
EqW$_{[Fe\,II]1.25}$	1.3 ± 0.3	3.0 ± 0.6	2.8 ± 0.7	2.8 ± 0.7	3.5 ± 0.9	2.7 ± 0.8	3.2 ± 0.7	3.3 ± 0.6	3.1 ± 0.8
$F_{H_2 2.12}$	7.5 ± 3.6	3.5 ± 0.8	3.4 ± 0.7	1.5 ± 0.5	1.9 ± 0.4	1.8 ± 0.3	1.3 ± 0.4	2.2 ± 0.3	1.8 ± 0.4
EqW$_{H_2 2.12}$	0.9 ± 0.4	2.1 ± 0.5	1.8 ± 0.4	1.8 ± 0.6	2.7 ± 0.6	2.4 ± 0.5	1.6 ± 0.5	3.1 ± 0.5	2.8 ± 0.6
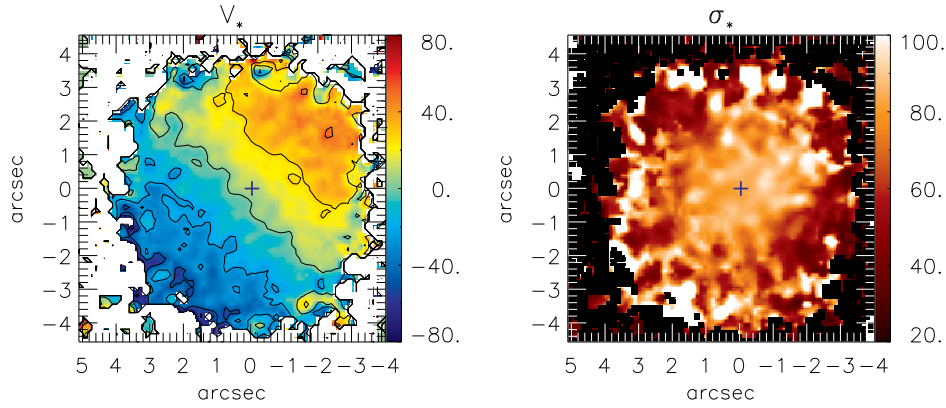
Figure 5. Stellar velocity (V_*) field (left) and velocity dispersion (σ_*) map (right) obtained from the fit of the CO absorption band heads at 2.3 μm using the pPXF routine. The central cross marks the position of the nucleus and white/black locations in V_*/σ_* maps are masked regions due to bad fits of their profiles. The colour coded maps are given in units of km s^{-1}.

In Fig. 5, we present the stellar velocity field in the left-hand panel and the σ_* map in the right-hand panel. Black regions in these maps correspond to locations where the uncertainties in V_* and/or σ_* are larger than 30 km s^{-1}. The systemic velocity of the galaxy, derived in Section 4.3, was subtracted from the measured velocities and the colour bars are shown in units of km s^{-1}. The stellar velocity field is consistent with rotation in a disc with the major axis oriented along the position angle PA $\sim 135°/315°$ and with a projected (along the line of sight) velocity amplitude of about 70 km s^{-1}. The σ_* map shows values ranging from $\sim$20 to $\sim$100 km s^{-1}, with the lowest values observed in a ring with radius of $\sim$2.5–3 arcsec surrounding the nucleus, corresponding to the location of the CNSFRs. The largest σ_* values are observed in patchy regions that appear just beyond or surrounding the star-forming clumps, which we attribute to the velocity dispersions of the stellar bulge.

Fig. 6 presents the velocity fields and velocity dispersion (σ) maps for the [Fe II]1.64, Brγ and H$_2$ λ2.12 μm emission lines. We do not show the maps for the [Fe II]1.25 and Paβ emission lines because they are very similar to those for the [Fe II]1.64 and Brγ lines, respectively, and have lower snr. All velocity fields present a similar rotation pattern as seen for the stars with the orientation of the line of nodes ($\sim$130°) and the projected velocity amplitude (70 km s^{-1}) in good agreement with the values previously derived from the Hβ emission line (Colina et al. 1997). The σ maps show small values over the whole FoV with the highest values reaching
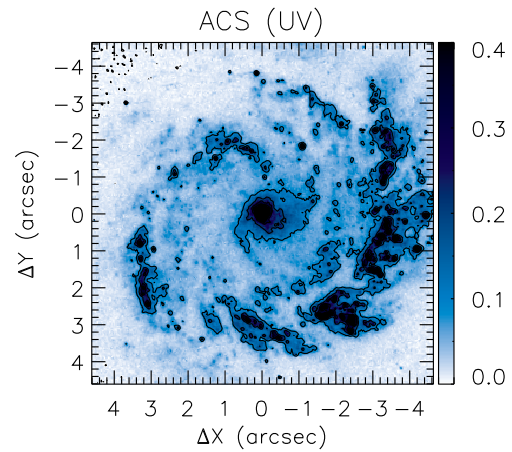
Figure 6. Velocity (V) fields (left) and velocity dispersion (σ) maps (right) for the [Fe II] λ1.64 μm (top), H$_2$ λ2.12 μm (middle) and Brγ emission lines. The central cross marks the position of the nucleus and white/black locations in V/σ maps are masked regions due to the non-detection of the emission lines or due to bad fits of their profiles. The colour bars are shown in units of km s^{-1}.
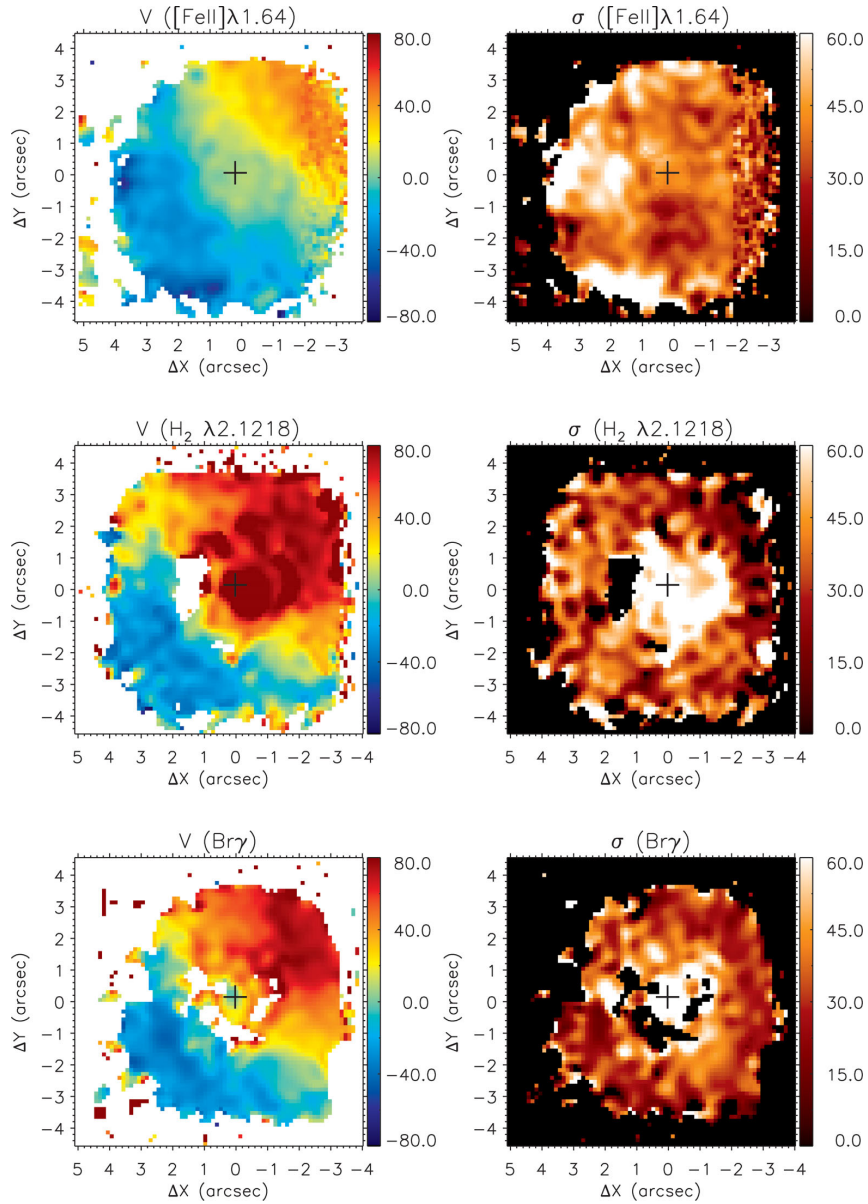
Figure 7. UV *HST* image of NGC 4303 previously discussed by Colina et al. (2002).

only 60 km s^{-1}. The [Fe II] map shows the highest values to the east and south-south-east of the nucleus and the H$_2$ and Brγ present the highest values at the nucleus. The uncertainties in σ and velocity are smaller than 15 km s^{-1} for all emission lines at most locations. For the nucleus, the uncertainties for the H$_2$ and Brγ are larger due to the low snr for these lines, with typical uncertainties of 25 km s^{-1}. Uncertainties of about 20 km s^{-1} are observed for the [Fe II] at locations between 2 and 3 arcsec west (right side of the FoV) due to a lower exposure time at these locations (effect of the spatial dithering).

4 DISCUSSION

4.1 (Circum)nuclear stellar and gas distribution: from spirals to ring structure?

UV and near-IR *Hubble Space Telescope* (*HST*) images of NGC 4303 show a nuclear spiral with several knots of star-forming clusters, as seen in Fig. 7, and a weak nuclear stellar bar (Colina & Wada 2000), respectively. The nuclear spiral is not evident in the near-IR emission-line flux distributions shown in Fig. 2, where the structure observed can be better described as a ring of CNSFRs with

radius of about 2.5–3.2 arcsec (200–250 pc). The CNSFRs seem to correspond to complexes of the strongest star-forming clusters observed in the UV *HST* image. This ring is coincident with the inner Lindblad resonance, as derived by Schinnerer et al. (2002) from the observations of the CO cold molecular gas, explaining why the gas has accumulated in the ring, giving origin to the star clusters.

The emission-line flux distributions presented in Fig. 2 show distinct structures for the different emission lines. The strongest emission for the [Fe II] and H_2 lines is from the nucleus, while the hydrogen recombination lines show emission predominantly from the CNSFRs. The [Fe II] shows an elongation to ≈1.5 arcsec (120 pc) north-east, where an outflow has been observed in [O III] line emission (Colina & Arribas 1999). No emission associated with this outflow is observed in the H_2 map, probably due to the dissociation of the H_2 molecule by the AGN emission, as commonly seen for Seyfert galaxies (e.g. Storchi-Bergmann et al. 2009; Riffel et al. 2014). The nuclear H_2 emission shows instead an elongation towards the west, the same orientation observed in the cold molecular gas emission, connecting the nucleus with the circumnuclear ring (Schinnerer et al. 2002).

In the ring, although the flux distribution in [Fe II] is similar to those of the hydrogen recombination lines, the brightest Paβ and Brγ regions (A and B) are located south-west of the nucleus, while for [Fe II] the brightest region is an unresolved knot (F) to the south-east. This difference is consistent with the scenario in which regions A and B are younger than region F, which has stronger [Fe II] emission due excitation by shocks from SNe, contributing more at a later age (see discussion below).

The hot H_2 emission is strongest in the east part of the ring, at locations that seem to be anti-correlated with the locations of strongest Paβ, Brγ and [Fe II] emission, that coincide also with the UV knots of recent SF. In previous studies by our group (e.g. Storchi-Bergmann et al. 2009), we concluded that the temperature of the region emitting hot H_2 is ≈2000 K, and that the excitation mechanism was thermal, as a result of heating by either X-rays from AGN or shocks from both AGN or SNe. In the ring, the eastern H_2 knots of emission probably originate in regions that are older than the eastern knot that emits [Fe II] and Brγ lines. These regions would still be hot enough to produce H_2 but not enough to produce Brγ and [Fe II] emission (that require 10 000–15 000 K).

Finally, the *K*-band image in Fig. 2 shows a small elongation to the north-east and south-west, visible in the second isocontour which is similar to that observed in the higher resolution *HST* image (Colina & Wada 2000) and attributed to a weak nuclear stellar bar.

4.1.1 The origin of the nuclear emission

The origin of the nuclear gas emission in NGC 4303 is still an open question, but previous works have suggested that the ionizing source is a combination of a low-luminosity AGN and a young massive stellar cluster (Colina et al. 1997, 2002; Colina & Arribas 1999).

The near-IR emission-line ratios can be used to further investigate this point. The line-ratio values from the nucleus can also be compared with those from the CNSFRs. For the nucleus, we obtain H_2/Brγ = 1.4 ± 1.2 and [Fe II]λ1.64/Brγ = 3.6 ± 2.8 using the values listed in Table 1. These values are typical of Seyfert nuclei, but also of excitation by shocks from SNe (Reunanen et al. 2002; Rodríguez-Ardila et al. 2004, 2005; Colina et al. 2015). They are also significantly higher than those observed in the ring, for example, from regions A and B (H_2/Brγ ∼ 0.4 and [Fe II]λ1.64/Brγ ∼ 1.0) where the presence of young (2.5–7.5 Myr)

clusters dominating the ionization is well established from UV spectroscopy (Colina et al. 2002). Thus, the near-IR diagnostics also suggest the presence of an AGN at the nucleus, confirming previous results that the nuclear emission has a composite nature. Alternatively, an SN-dominated 8–40 Myr star-forming cluster could produce such enhanced line ratios, but there is no evidence so far of a cluster with this age at the nucleus, only of a younger one (≈4 Myr old). Moreover, the fact that the [Fe II] emission at the nucleus is extended along the ionized [O III] outflow suggests that the nuclear emission of [Fe II] and the H_2 could be mainly due to X-rays emitted by the AGN (Jiménez-Bailón et al. 2003) and/or shocks in the outflow.

4.1.2 The circumnuclear star-forming regions

Colina et al. (1997) reported the presence of a circumnuclear spiral structure with several UV-bright knots identified as young (few Myr old) star-forming regions (Colina & Arribas 1999). The CNSFRs observed in the flux maps of Fig. 2 and EqW maps of Fig. 4 show a structure similar to that seen in the UV continuum and optical emission-line flux maps (Colina & Arribas 1999), but with a ring rather than a spiral structure. [We note that the region identified as A in Fig. 4 corresponds to regions G and F of Colina et al. (1997).] As discussed in Section 4.1, the location of the ring agrees with that of the inner Lindblad resonance and therefore it may be a stable structure.

Assuming that the CNSFR ring is circular and located in the plane of the galaxy, we can use the observed geometry to derive the inclination of the ring relative to the plane of the sky. In the Brγ EqW map (Fig. 4), the CNSFR shows an elliptical shape with major axis of $a \sim 6$ arcsec oriented along PA ≈ 135° and a minor axis of $b \sim 5$ arcsec. The resulting inclination of the ring is $i = \mathrm{acos}(b/a) \approx 33°$, which is similar to the inclination of large-scale disc of NGC 4303 ($i \approx 27°$).

The H_2/Brγ and [Fe II]/Brγ maps show small values in the CNSFR (see Fig. 3). [Fe II]/Brγ is smaller than 2 for all star-forming regions, being consistent with values expected for young stellar clusters (Colina et al. 2015). The H_2/Brγ ratio for most star-forming regions is smaller than 0.6, as expected for a young cluster, with exception of the regions G and H (identified in Fig. 4) with higher values (of ∼1), suggesting an additional mechanism for the excitation of the H_2 emission there, such as shocks from SN explosions or diffuse X-ray emission heating the gas and exciting the H_2 molecule.

The integrated emission-line fluxes given in Table 1 have been used to derive a number of physical properties of the star-forming clumps in the CNSFR that are listed in Table 2, as follows. The values of the rate of ionizing photons $Q[H^+]$ and star formation rate (SFR) were derived under the assumptions of continuous SF, and should be considered only a proxy of these parameters.

The emission rate of ionizing photons for each star-forming region was obtained following Riffel et al. (2009), using

$$\left(\frac{Q[H^+]}{s^{-1}}\right) = 7.47 \times 10^{13} \left(\frac{L_{Br\gamma}}{erg\,s^{-1}}\right) \quad (1)$$

and the star formation rate (SFR) using (Kennicutt 1998)

$$\left(\frac{SFR}{M_\odot\,yr^{-1}}\right) = 8.2 \times 10^{-40} \left(\frac{L_{Br\gamma}}{erg\,s^{-1}}\right), \quad (2)$$

where $L_{Br\gamma}$ is the Brγ luminosity, under the assumption of continuous rate.

In order to estimate the mass of stars of each CNSFR, we need to assume an age for the region. Detailed spectral energy distribution (SED) fitting of the *HST* UV spectra of the nucleus and of the

4200   *R. A. Riffel et al.*

Table 2. Physical parameters of the CNSFRs in NGC 4303. The location of each region is indicated in Fig. 4. $Q[H^+]$: ionizing photons rate, SFR: equivalent star formation rate under the assumption of continuous SF following Kennicutt (1998), M: mass of the cluster assuming a cluster instantaneously formed with age 4 Myr, M_{HII}: mass of ionized gas, M_{H_2}: mass of hot molecular gas, σ_l: velocity dispersion for the line l.

Region	N	A	B	C	D	E	F	G	H
$\log Q[H^+]$ (s^{-1})	51.1 ± 0.12	51.2 ± 0.02	51.3 ± 0.02	50.9 ± 0.02	50.8 ± 0.03	50.7 ± 0.03	50.8 ± 0.03	50.6 ± 0.03	50.6 ± 0.04
SFR (10^{-2} M$_\odot$ yr^{-1})	1.3 ± 0.31	1.8 ± 0.07	2.0 ± 0.09	0.8 ± 0.04	0.7 ± 0.04	0.6 ± 0.04	0.7 ± 0.04	0.5 ± 0.03	0.4 ± 0.03
$M(10^5$ M$_\odot$)	1.0 ± 0.30	1.3 ± 0.06	1.5 ± 0.06	0.6 ± 0.03	0.5 ± 0.03	0.4 ± 0.03	0.5 ± 0.04	0.4 ± 0.02	0.3 ± 0.02
M_{HII} (10^3 M$_\odot$)	8.2 ± 1.9	11.1 ± 0.4	12.4 ± 0.5	5.1 ± 0.3	4.0 ± 0.3	3.7 ± 0.2	4.4 ± 0.3	2.9 ± 0.2	2.5 ± 0.2
M_{H_2} (M$_\odot$)	9.8 ± 1.6	4.7 ± 0.3	4.4 ± 0.3	2.0 ± 0.2	2.5 ± 0.2	2.4 ± 0.1	1.7 ± 0.2	2.9 ± 0.1	2.4 ± 0.2
σ_{FeII} (km s^{-1})	44.6 ± 10.4	40.1 ± 6.1	37.9 ± 6.7	44.3 ± 9.2	45.5 ± 9.2	49.5 ± 10.3	52.9 ± 6.5	43.2 ± 6.1	58.9 ± 9.6
σ_{H_2} (km s^{-1})	80.2 ± 16.2	49.6 ± 5.5	39.1 ± 4.7	40.0 ± 7.3	36.7 ± 4.4	36.7 ± 3.6	43.8 ± 7.3	43.5 ± 3.1	39.3 ± 4.6
$\sigma_{Br\gamma}$ (km s^{-1})	81.8 ± 23.7	40.4 ± 2.6	32.3 ± 2.5	33.7 ± 3.0	32.8 ± 3.9	33.7 ± 3.9	30.9 ± 3.5	34.2 ± 3.6	29.3 ± 4.6

two brightest UV circumnuclear regions (Colina et al. 2002) led to the conclusion that they are best reproduced by instantaneous star-forming bursts of age about 4 Myr. This age was thus used to estimate the mass of each region under the assumption of instantaneous SF using the STARBURST 99 code (Leitherer et al. 1999, 2010, 2014; Vazquez & Leitherer 2005) and assuming the same initial mass function (IMF) parameters as in Colina et al. (2002) – i.e. a Salpeter IMF, with mass of the stars between 1 and 100 M$_\odot$ and solar metallicity. Considering these parameters, a 4 Myr old cluster with mass 1×10^5 M$_\odot$ will produce a rate of ionizing photons (<13.6 eV) of $\log Q_M \sim 51.1$ photons s^{-1}. Therefore, the mass of the young star-forming regions can be obtained from the observed $\log Q$ listed in Table 2 as $M = 1 \times 10^5$ M$_\odot$ Q/Q_M. The resulting masses for the clusters are shown in Table 2 and are in the range $0.30-1.45 \times 10^5$ M$_\odot$. For more evolved regions (e.g. with ages $\sim$ 10 Myr old instead of 4 Myr), the masses will increase by a factor of 100 as the ionizing radiation is a steep function of age for an instantaneous burst.

The mass of ionized (M_{HII}) gas can be derived as (e.g. Osterbrock & Ferland 2006; Storchi-Bergmann et al. 2009)

$$\left(\frac{M_{HII}}{M_\odot}\right) = 3 \times 10^{19} \left(\frac{F_{Br\gamma}}{erg\,cm^{-2}\,s^{-1}}\right) \left(\frac{D}{Mpc}\right)^2 \left(\frac{N_e}{cm^{-3}}\right)^{-1}, \quad (3)$$

where D is the distance to the galaxy, $F_{Br\gamma}$ is the Brγ flux and N_e is the electron density. We have assumed an electron temperature of 10^4 K and density of $N_e = 500$ cm^{-3}. The mass of hot molecular gas is estimated using (e.g. Scoville et al. 1982; Riffel et al. 2008, 2014)

$$\left(\frac{M_{H_2}}{M_\odot}\right) = 5.0776 \times 10^{13} \left(\frac{F_{H_2\lambda2.1218}}{erg\,s^{-1}\,cm^{-2}}\right) \left(\frac{D}{Mpc}\right)^2, \quad (4)$$

where $F_{H_2\lambda2.1218}$ is the H$_2$ (2.1218 μm) emission-line flux, and the assumptions of local thermal equilibrium and excitation temperature of 2000 K were used.

The resulting values of the ionized and hot molecular gas masses for the nucleus and for each CNSFR are also listed in Table 2. In summary, assuming a typical age of about 4 Myr for the star-forming clumps, the stellar masses in young stars are in the range $3-10 \times 10^4$ M$_\odot$, the ionized gas mass is about 10 times lower and the mass of hot molecular gas is in the range $3-4 \times 10^{-5}$ M$_\odot$. The ratios between the masses of ionized and hot molecular gas are between 1000 and 2800, with the lower ratios observed for the regions G and H. For the nucleus, $M_{HII}/M_{H_2} \approx 830$. These ratios are similar to those in the central region of Seyfert galaxies (e.g. Storchi-Bergmann et al. 2009; Riffel et al. 2014), although distinct scenarios are expected for the heating of the gas. In AGNs, the H$_2$

emission is usually due to thermal processes, i.e. heating of the gas by shocks or X-rays from the AGN, while for the CNSFRs, young stars play an important role in the excitation of the H$_2$. Finally, the $Q[H^+]$ and equivalent SFR derived for the CNSFR of NGC 4303 are in good agreement with those obtained for other CNSFRs in nearby galaxies characterized by a moderate star-forming regime (e.g. Shi, Gu & Peng 2006; Wold & Galliano 2006; Dors et al. 2008; Galliano & Alloin 2008; Falcón-Barroso et al. 2014).

4.1.3 The [Fe II]/Brγ versus H₂/Brγ diagnostic diagram

In order to better study the gas excitation, we constructed the [Fe II]/Brγ versus H$_2$/Brγ diagnostic diagram shown in Fig. 8. This diagram shows a big overlap of regions corresponding to SNe and AGN, as some excitation processes, like shocks and thermal heating, are common to both AGN and SN. The black dots correspond to all observed spaxels and are mostly located in the region of SNe and/or AGN, with some points covering part of the SF region. This behaviour is typical of luminous star-forming infrared galaxies and
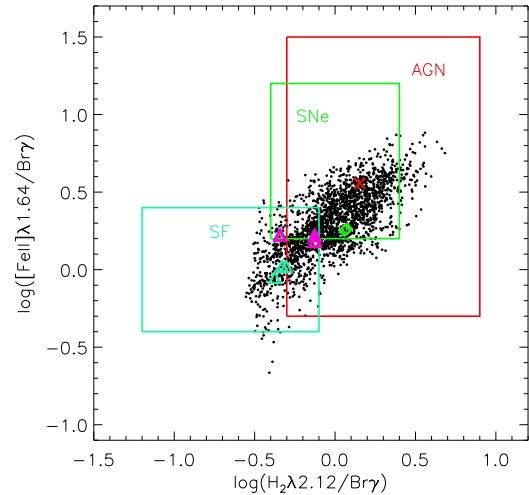

Figure 8. [Fe II] λ1.64 μm/Brγ versus H₂ λ2.12 μm/Brγ diagnostic diagram for the central region of NGC 4303. The black points correspond to all the spaxels for which we were able to measure both line ratios. The red cross represents the nucleus, the green diamonds are for regions G and H and the pink(blue) triangles represent the ratios for regions D to F (A to C), as labelled in Fig. 4. The limits corresponding to excitation by young stars (SF), SN remnants and AGN are from Colina et al. (2015).

interpreted as due to excitation by combined effects of the AGN and stellar ionizing radiation plus shocks in AGN outflows, stellar winds and SN explosions (Colina et al. 2015).

For the nucleus, the line ratios are high and typical of AGNs, while for the brightest regions in the UV (A to C) in the CNSFR, which are the youngest (see discussion below), the line ratios are typical of star-forming regions. The older star-forming regions in the CNSFR (D to H) are displaced towards the SN region, with regions G and H presenting the most extreme ratios, likely associated with SN explosions. The line ratios are thus compatible with an age difference between the east (older) and west (younger) side of the ring (see Section 4.1.4 for further discussion).

4.1.4 How does the SF proceed in the nucleus and CNSFRs ring?

The SF in the nuclear regions of early-type spirals frequently occurs in ring-like structures with radius of 1 kpc or less. Examples include galaxies with luminous AGNs in their centres as well as many others with a weak AGN or star-forming nucleus (Genzel et al. 1995; Storchi-Bergmann, Wilson & Baldwin 1996a; Storchi-Bergmann et al. 1996b; Böker et al. 2008; van der Laan et al. 2013a,b, 2015; Falcón-Barroso et al. 2014). It is well established that bars in galaxies can drive large quantities of gas to the inner regions, accumulating into inner resonances, generating and maintaining subsequent SF there (Combes & Gerin 1985; Buta & Combes 1996; Heller & Shlosman 1996). Two scenarios have been considered so far to explain the SF in circumnuclear rings: the 'popcorn' (Elmegreen 1994) and the 'pearls on a string' (Böker et al. 2008). As discussed in the introduction, in the 'popcorn' scenario the stellar clusters form at random positions with no age sequence, while in the 'pearls-on-a-string' scenario, the clusters are formed where the gas enters the rings and then age as they orbit the ring forming a string of ageing clusters.

Some previous studies favour the 'pearls-on-a-string' scenario (Böker et al. 2008; Falcón-Barroso et al. 2014), in galaxies with evidence of gas inflow into the ring (van der Laan et al. 2013a). However, there are also rings that appear to be a combination of the two scenarios (van der Laan et al. 2015). An Hα imaging survey of 22 galaxies with CNSFRs (Mazzuca et al. 2008) has shown that about half of the rings show azimuthal age gradients as expected in the 'pearls-on-a-string' scenario, while the other half show no age pattern, have a flat age distribution, or even a radial gradient. Thus, the SF in the (circum)nuclear regions of galaxies is far from clear.

In order to investigate the best scenario for the circumnuclear SF in NGC 4303, we show in Fig. 9 the sequence of values of the EqW and σ for the H_2, Brγ and [Fe II] emission lines, as well as the corresponding [Fe II]/Brγ and H_2/Brγ for each CNSFR, labelled from A to H. The top panel shows a small decrease in EqW values for Brγ, consistent with a small decrease in age from A to H. For the velocity dispersion (middle panel), no clear trend is observed for Brγ and H_2, while for the [Fe II], the σ values show a small increase from regions A to H. This variation is also consistent with a small increase in age from regions A to H, as the presence of SNs in older regions can increase the [Fe II] velocity dispersion. The bottom panel of Fig. 9 shows small positive gradients for both H_2/Brγ and [Fe II]/Brγ line ratios between regions A and H, and can also be understood as due to an increase in age as shocks from SNe contribute as an additional excitation source for the H_2 and [Fe II] as the regions age, while the evolution of massive stars away from the main sequence diminishes the amount of ionizing radiation, i.e. reducing the flux of Brγ. This relative age dating is in agreement
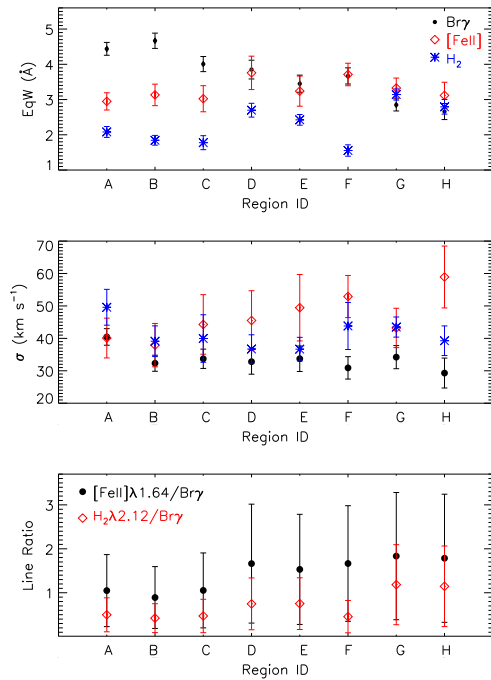

Figure 9. Plots for the EqW (top), σ (middle) and line ratios (bottom) versus region.

with previous conclusions (Colina & Wada 2000; Colina et al. 2002) that identified the east UV knots as older (∼10–25 Myr) than the west knots (∼2.5–7.5 Myr), therefore suggesting an age offset in the star-forming ring. Thus, relative age differences for the star-forming clumps are confirmed from independent tracers in the UV–optical and now the near-IR.

However, although our measurements show a trend suggesting an age sequence along the ring (increasing from A to H), the trend is small and present some ups and downs, being equally consistent just with regions to the east being older than regions to the west. For example, in the case of H_2/Brγ instead of a smooth gradient, the observed variation is more consistent with regions G and H being older than the regions A–F. We conclude that the data do not confirm the 'pearls-on-a-string' scenario neither the 'popcorn' scenario, as there is also no evidence for a random distribution of ages. We can only be sure of an age asymmetry, with the youngest regions to the west and oldest regions to the east.

One interesting new result that can be observed in Fig. 2 is that the regions of strongest H_2 emission in the ring are approximately anti-correlated with the regions of strongest Brγ and [Fe II] emission. While the latter coincide with the UV knots of recent SF, the H_2 knots are observed mostly in the east part of the ring, but not coincident with the bright Brγ and [Fe II] knot there. In previous results from our group (e.g. Storchi-Bergmann et al. 2009), we concluded that the temperature of the region where hot H_2 is observed is ≈2000 K, and that the mechanism producing the hot H_2 emission was thermal excitation as a result of heating either by X-rays from the AGN or shocks from SN. In the ring, the dominant mechanism should be shocks from SN; thus, the eastern knots of H_2 emission

would be hot (2000 K) regions associated with fading SN, being older than the eastern knot of [Fe II] and Brγ emission. These regions would be hot enough to produce H_2 but not to produce Brγ and [Fe II] emission (requiring 10 000–15 000 K).

Our results can be compared with those for the cold molecular gas (Schinnerer et al. 2002). The asymmetry in the SF along the ring appears to follow the distribution of cold molecular gas, dominated in mass and surface density by the western spiral and gas lane (Schinnerer et al. 2002). At the resolution of the CO observations (2 arcsec), the large concentration of molecular gas in the spiral seems to be located just outside the CNSFR, suggesting therefore not a direct correspondence between the regions were the SF is taking place now and the regions with the highest molecular gas densities (fig. 10 in Schinnerer et al. 2002). In addition, the east side of the ring appears to be forming very few stars now (as judged from the Brγ and UV emission), and is almost devoid of cold molecular gas, in particular the north-east region (Schinnerer et al. 2002). On the other hand, this is one of the regions where there is enhanced emission from hot molecular gas. Thus, molecular gas seems to exist there, but is heated by local SN, as discussed in the previous paragraph. In summary, regarding the cold molecular gas distribution, while there is a similar distribution with the youngest star-forming regions globally around the ring, this does not seem to occur on scales of a few pc.

The CNSFR is made up of small flocculent spirals or filament-like structures breaking into star-forming clumps extending along large sectors (≈300–400 pc) of the ring (see Fig. 7). This has been interpreted as fragmentation of a gas disc due to gravitational instabilities (Colina & Wada 2000). The fact that the range of estimated ages for the young star-forming regions in the south-west arc of the ring is very small suggests that the fragmentation is taking place quasi-simultaneously (i.e. in less than few Myr) over sectors extending by hundred of parsecs. In addition, the east side of the ring appears to have formed stars some 10–15 Myr before the west side. Again the lack of an obvious age gradient suggests that the SF was essentially simultaneous over a large sector of the ring. In addition, if the ring is rotating around the nucleus as indicated by our stellar and gas kinematic maps – which imply a rotational period of about 10 Myr – a possible scenario is that the oldest stellar clusters were formed in the west side of the ring, but, after 10 Myr, have already almost completed one turn and are now observed in the south-east part of the ring.

4.2 Mass of molecular and ionized gas in the ring

Equations (3) and (4) can be used to calculate the total mass of ionized and hot molecular gas in the inner 9 arcsec × 9 arcsec of NGC 4303 covered by our FoV. By integrating the spectra over the total FoV and fitting the H_2 and Brγ emission-line profiles from the resulting spectrum, we obtain $F_{H_2 \lambda 2.1218} \sim 1.2 \times 10^{-14}$ erg s^{-1} cm^{-2} and $F_{Br\gamma} \sim 8.5 \times 10^{-15}$ erg s^{-1} cm^{-2}. The corresponding masses are $M_{H_2} \sim 110\,M_\odot$ and $M_{HII} \sim 1.9 \times 10^5\,M_\odot$. Both values are about three times the sum of the masses for the individual star-forming regions, shown in Table 2 and are in good agreement with the values found for the central region of active galaxies (e.g. Riffel et al. 2014, 2015).

However, the M_{H_2} derived above may be just a small fraction of the total mass of molecular gas available in the central region of NGC 4303 as the ratio between cold and hot molecular gas is usually in the range 10^5–10^7 (Dale et al. 2005; Müller-Sánchez et al.

2006; Mazzalay et al. 2013). Following Mazzalay et al. (2013), the mass of cold molecular gas can be obtained by

$$\frac{M_{cold}}{M_\odot} \approx 1174 \times \left(\frac{L_{H_2\,\lambda2.1218}}{L_\odot} \right), \quad (5)$$

where $L_{H_2}\,\lambda2.1218$ is the luminosity of the H_2 line. We derive $M_{cold} \sim 10^8\,M_\odot$ and of $\sim$6.25 $\times$ $10^6\,M_\odot$ for the entire CNSFR and for the nucleus (60 pc radius), respectively. This large amount of molecular gas can be used to feed the AGN and/or to form stars. The estimated mass of cold H_2 gas for the entire CNSFR is in good agreement with the one obtained directly from CO observations of the nuclear disc of $6.9 \times 10^7\,M_\odot$, as derived by Schinnerer et al. (2002).

4.3 Stellar and gas kinematics

The stellar velocity field shown in the left-hand panel of Fig. 5 clearly presents a rotational component. In order to obtain relevant physical parameters, we fitted the stellar velocity field by a model of a thin disc, in which the stars have circular orbits in the plane of the galaxy, with velocities given by (Bertola et al. 1991)

$$V(R, \Psi) = V_s$$
$$+ \frac{AR\cos(\Psi - \Psi_0)\sin(i)\cos^p\theta}{R^2[\sin^2(\Psi - \Psi_0) + \cos^2(i)\cos^2(\Psi - \Psi_0)] + c_0^2\cos^2(i)]^{p/2}}, \quad (6)$$

where R and Ψ are the coordinates of each pixel in the plane of the sky, A is the amplitude of the rotation curve, Ψ_0 is the position angle of the line of nodes, V_s is the systemic velocity, i is the disc inclination relative to the plane of the sky, c_0 is a concentration parameter and p is a model fitting parameter.

During the fit, the kinematical centre was kept fixed at the location of the peak of the continuum emission, and the inclination of the disc was fixed to the inclination of the CNSFR $i = 33°$, obtained in Section 4.1.2. The difference between the observed and modelled velocities is smaller than 10 km s^{-1} at most locations and thus we conclude that the adopted rotating disc model is a good representation of the observed velocity field. The best-fitting model resulted in the following parameters: $V_s = 1567 \pm 17$ km s^{-1}, $\Psi_0 = 136° \pm 1°$, $A = 160 \pm 7$ km s^{-1} and $c_0 = 2.3 \pm 0.2$ arcsec. Based on optical IFS with a coarser angular resolution and lower spectral resolution, Colina & Arribas (1999) showed that the gas velocity field of NGC 4303 is consistent with a rotating disc with inclination of 45°, distinct from the inclination of the large-scale disc adopted here. Fixing the inclination of the disc to this value, we obtain similar physical parameters, except for the amplitude of the rotation curve that is smaller – $A = 132.1 \pm 5.2$ km s^{-1}, but the quality of the fit is worse and thus we decided to adopt the inclination of the large-scale disc.

The stellar velocity dispersion map shows a ring of small values co-spatial with the ring of CNSFRs, showing that the stars still have the 'cold' kinematics of the raw gas that formed the stars. These low-σ_* structures have been previously observed for Seyfert galaxies via similar near-IR IFS for which stellar population synthesis has confirmed that these structures are associated with intermediate-age (0.3–0.7 Gyr) stellar populations (e.g. Riffel et al. 2010). In Dametto et al. (in preparation), we will present a detailed study of the optical/near-IR SED and verify the validity of this interpretation. At locations just beyond the CNSFR, the higher σ_* values – ranging from 70 to 100 km s^{-1}, can be attributed to the bulge of the galaxy.

The velocity fields for all emission lines are similar to that presented by Colina & Arribas (1999) on the base of optical observations, presenting a rotation pattern similar to that of the stars. We
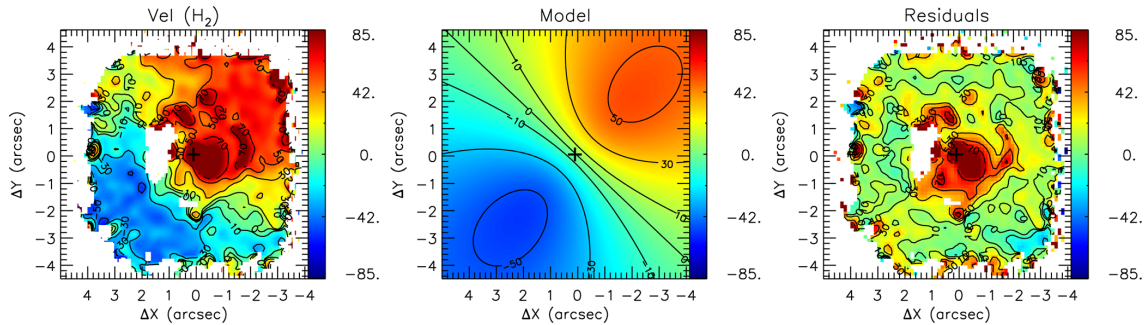
Figure 10. Left: H_2 velocity field; middle: rotating disc model and right: residual map, obtained as the difference of the observed velocities and the model. The colour bars show the velocity in units of $km\,s^{-1}$.

fitted the gas velocity field with the same model used to fit the stellar velocity field, keeping fixed all geometric parameters derived for the stars, allowing only the amplitude of the rotation curve to change. We confirm that this model reproduces well the various gas velocity fields, but with a larger velocity amplitude than that observed for the stars: $A = 236 \pm 32\,km\,s^{-1}$ for H_2, $A = 225 \pm 28\,km\,s^{-1}$ for $Br\gamma$ and $A = 151 \pm 25\,km\,s^{-1}$ for [Fe II] (corrected for the inclination of the disc). Distinct rotational velocity amplitudes for the ionized and molecular gas as well as for the stars are commonly observed for active galaxies (e.g. Riffel, Storchi-Bergmann & Winge 2013b; Barbosa et al. 2014), likely indicating a slightly different three-dimensional distribution.

The residuals between the measured and modelled gas velocities were usually smaller than $\approx$10–20 $km\,s^{-1}$, except for the H_2 velocity field shown in Fig. 10. Redshift residuals of $\approx$80–100 $km\,s^{-1}$ are observed in a region extending to $\approx$120 pc south-west of the nucleus, with similar orientation to that of the nuclear bar, revealing non-circular motions possibly associated with this bar. The velocity dispersion of H_2 is also larger there, suggesting that it may be due to the presence of more than one kinematic component (that our spectral resolution did not allow us to separate). It is interesting to note that a high velocity dispersion was observed also in CO (Schinnerer et al. 2002) in this region, that is identified with a possible molecular gas 'bridge' between the ring and the nucleus.

Regarding the ionized gas kinematics, Colina & Arribas (1999) have shown that the optical [O III] emission shows two components: one due to rotation in the disc and another due to a compact outflow along the minor axis of the galaxy. Although we do not see an outflow in the gas velocity residuals, our data show an increase in the [Fe II] velocity dispersion to the east-north-east, where the [Fe II] flux distribution shows an elongation at a similar orientation to that of the [O III] outflow.

Finally, although the stellar velocity dispersion shows lower velocity dispersion at the ring, the σ maps for the gas (Fig. 6) do not show a decrease or an increase associated with the star-forming regions in the ring. This suggests that the SF is not contributing significantly to the turbulence of the surrounding interstellar medium, as found also for a large sample of low-z Luminous Infrared Galaxies (LIRGs) and Ultra-luminous Infrared Galaxies (ULIRGs) (Arribas et al. 2014) and in high-z galaxies (Genzel et al. 2011). The average velocity dispersion for the ionized gas (traced by the $Br\gamma$ emission) of the CNSFR of NGC 4303 is $\sigma = 46 \pm 7\,km\,s^{-1}$, obtained by fitting the $Br\gamma$ line profile integrated within a ring with inner radius of 1.5 arcsec and outer radius of 4.0 arcsec, centred at the nucleus. This value is similar to that found for luminous

star-forming clumps ($\sigma = 43 \pm 3\,km\,s^{-1}$) of local (U)LIRGs (Arribas et al. 2014). If confirmed for larger samples of galaxies with CNSFR, it would indicate that the velocity dispersion is dominated by global dynamical processes and less affected by local processes like SF on scales of few parsecs.

5 CONCLUSIONS

We have presented new emission-line flux and velocity maps, as well stellar velocity maps of the inner 0.7 kpc $\times$ 0.7 kpc of the nearby spiral galaxy NGC 4303, at spatial resolutions of 78, 47 and 36 pc, for the *J*, *H* and *K* bands, respectively, using near-IR IFS with the VLT instrument SINFONI. The observations cover the nucleus and CNSFR with radius $\approx$200–250 pc. The main conclusions of this work are as follows.

(i) The near-IR emission-line flux distributions delineate the CNSFR, with emission-line knots in the flux distributions of the different gas phases observed at different locations along the ring. The H_2 and [Fe II] emission lines show emission peaks at the nucleus, while the H I recombination lines are dominated by emission from the CNSFR;

(ii) Along the ring, the strongest H I and [Fe II] emission are observed mostly in the west side of the ring and at a region to the south-east, while the strongest emission in H_2 seems to be anti-correlated with them, being observed mostly to the east.

(iii) The properties, [Fe II]/$Br\gamma$ and H_2/$Br\gamma$ line ratios, EqW and σ of the emission lines along the star-forming ring, support an age difference between the west and east sides of the CNSFR, with the former being younger (2.5–7.5 Myr) than the latter (10–25 Myr).

(iv) The distribution of the star-forming regions and their age differences do not support fully the 'popcorn' and the 'pearls-on-a-string' scenarios for SF in CNSFRs. The SF in the CNSFR of NGC 4303 appears to be instead episodic with stars forming quasi-simultaneously over a large sector of the ring (covering $\sim$ 300 pc along the ring), ageing as they rotate with an orbital time of several Myr.

(v) Assuming that the star-forming regions in the CNSFR are closer to instantaneous bursts with ages of about 4 Myr, we derive masses for the clusters in the range 0.3–1.5 $\times\,10^5$ $M_\odot$. The corresponding masses for the associated ionized and hot molecular gas are about $\sim$0.25–1.2 $\times\,10^4$ and $\sim$0.25–0.5 $\times\,10^1$ $M_\odot$, respectively. For stellar populations with older ages of up to 10 Myr, the corresponding stellar masses will increase by up to a factor of 100.

(vi) The [Fe II] emission shows an elongation to ≈ 120 pc north-east of the nucleus that could be associated with the previously known optical ([O III]) outflow.

(vii) The H_2 emission shows an elongation to ≈ 120 pc west of the nucleus that could be the hot counterpart of the already known cold molecular gas 'bridge' that connects the nucleus with the large circumnuclear molecular gas reservoir.

(viii) The near-IR emission-line ratios ([Fe II]/Brγ and H_2/Brγ) of the nucleus are consistent with the presence of an AGN and/or an SN-dominated star-forming region. Since there is no evidence for an aged stellar cluster in the nucleus, the line ratios are interpreted as due to the combined effect of X-ray radiation and shocks at the base of the ionization cone of the AGN. Higher angular resolution spectroscopy is required to further explore this scenario.

(ix) The stellar velocity field is well reproduced by a model of a rotating disc with an inclination $i = 33°$ relative to the plane of the sky, major axis oriented along PA $\sim 135°$, and with a velocity amplitude of about 160 km s^{-1}. The stars associated with the CNSFR show smaller velocity dispersion than the surroundings, revealing a cooler dynamical stellar population in the ring, consistent with their recent formation from cold gas.

(x) The gas velocity fields are also dominated by rotation, similar to that observed for the stars but with a larger amplitude. A significant deviation from rotation was observed for the H_2 emission in a region extending ≈ 120 pc to the south-west, along the orientation of the nuclear bar. A higher H_2 velocity dispersion is also observed at this location and is attributed to the presence of more than one kinematic component associated with non-circular motions along the nuclear bar.

All fits files for the emission-line flux distributions, velocity fields and velocity dispersion maps are available online as supplementary material.

ACKNOWLEDGEMENTS

REFERENCES

Arribas S., Colina L., Bellocchi E., Maiolino R., Villar-Martín M., 2014, A&A, 568, 14
Barbosa F. K. B., Storchi-Bergmann T., Vale T. B., McGregor P., Riffel R. A., 2014, MNRAS, 445, 2353
Bertola F., Bettoni D., Danziger J., Sadler E., Sparke L., de Zeeuw T., 1991, ApJ, 373, 369
Böker T., Falcón-Barroso J., Schinnerer E., Knapen J. H., Ryder S., 2008, AJ, 135, 479
Buta R., Combes F., 1996, Fundam. Cosm. Phys., 17, 95
Cappellari M., Emsellem E., 2004, PASP, 116, 138
Cohen M., Wheaton W. A., Megeath S. T., 2003, AJ, 126, 1090
Colina L., Arribas S., 1999, ApJ, 524, 637
Colina L., Wada K., 2000, ApJ, 529, 845
Colina L., García Vargas M. L., Mas-Hesse M., Alberdi A., Krabbe A., 1997, ApJ, 484, L41
Colina L., Gonzales Delgado R., Mas-Hesse J. M., Leitherer K., 2002, ApJ, 749, 545
Colina L. et al., 2015, A&A, 578, A48
Combes F., Gerin M., 1985, A&A, 150, 327
Dale D. A., Sheth K., Helou G., Regan M. W., Hüttemeister S., 2005, ApJ, 129, 2197
Davies R. I., Sánchez F. M., Genzel R., Tacconi L. J., Hicks E. K. S., Friedrich S., Sternberg A., 2007, ApJ, 671, 1388
Davies R. I. et al., 2014, ApJ, 792, 101
de Vaucouleurs G., de Vaucouleurs A., Corwin H. G., Jr, Buta R. J., Paturel G., Fouqué P., 1991, Third Reference Catalogue of Bright Galaxies. Springer-Verlag, New York
Diniz M. R., Riffel R. A., Storchi-Bergmann T., Winge C., 2015, MNRAS, 453, 1727
Dors O. L., Storchi-Bergmann T., Riffel R. A., Schmidt A. A., 2008, A&A, 482, 59
Dors O. L., Riffel R. A., Cardaci M. C., Hägele G. F., Krabbe A. C., Pérez-Montero E., Rodrigues I., 2012, MNRAS, 422, 252
Elmegreen B. G., 1994, ApJ, 425, L73
Falcón-Barroso J., Ramos Almeida C., Böker T., Schinnerer E., Knapen J. H., Lancon A., Ryder S., 2014, MNRAS, 438, 329
Fukuda H., Wada K., Habe A., 1998, MNRAS, 295, 463
Galliano E., Alloin D., 2008, A&A, 487, 519
García-Burillo S., Combes F., 2012, J. Phys.: Conf. Ser., 372, 012050
García-Burillo S., Combes F., Schinnerer E., Boone F., Hunt L. K., 2005, A&A, 441, 1011
Genzel R., Weitzel L., Tacconi-Garman L. E., Blietz M., Cameron M., Krabbe A., Lutz D., Sternberg A., 1995, ApJ, 444, 129
Genzel R. et al., 2011, ApJ, 733, 101
Gonzalez R. C., Woods R. E., 2002, Digital Image Processing, 2nd edn. Prentice-Hall, Englewood Cliffs, NJ
Heller C. H., Shlosman I., 1994, ApJ, 424, 84
Heller C. H., Shlosman I., 1996, ApJ, 471, 143
Hicks E. K. S., Davies R. I., Malkan M. A., Genzel R., Tacconi L. J., Sánchez F. M., Sternberg A., 2009, ApJ, 696, 448
Iserlohe C., Krabbe A., Larkin J. E., Barczys M., McElwain M. W., Quirrenbach A., Weiss J., Wright S. A., 2013, A&A, 556, 136
Jiménez-Bailón E., Santos-Lleó M., Mas-Hesse J. M., Guainazzi M., Colina L., Cerviño M., González Delgado R. M., 2003, ApJ, 593, 127
Kennicutt R. C., 1998, ARA&A, 36, 189
Knapen J. H., Beckman J. E., Heller C. H., Shlosman I., de Jong R. S., ApJ, 454, 623
Koopmann R. A., Kenney J. D. P., Young J., 2001, ApJS, 135, 125
Leitherer C. et al., 1999, ApJS, 123, 3
Leitherer C., Ortiz Otálvaro P. A., Bresolin F., Kudritzki R., Lo Faro B., Pauldrach A. W. A., Pettini M., Rix S. A., 2010, ApJS, 189, 309
Leitherer C., Ekström S., Meynet G., Schaerer D., Agienko K. B., Levesque E. M., 2014, ApJS, 212, 14
Leslie S. K., Kewley L. J., Sanders D. B., Lee N., 2016, MNRAS, 455, 82
Mazzalay X. et al., 2013, MNRAS, 428, 2389
Mazzalay X. et al., 2014, MNRAS, 438, 2036
Mazzuca L. M., Knapen J. H., Veilleux S., Regan M. W., 2008, ApJS, 174, 337
Menezes R. B., da Silva P., Ricci T. V., Steiner J. E., May D., Borges B. W., 2015, MNRAS, 450, 369
Müller-Sánchez F., Davies R. I., Eisenhauer F., Tacconi L. J., Genzel R., Sternberg A., 2006, A&A, 454, 492
Norman N., Scoville N., 1988, ApJ, 332, 124
Osterbrock D. E., Ferland G. J., 2006, Astrophysics of Gaseous Nebulae and Active Galactic Nuclei, 2nd edn. University Science Books, Mill Valley, CA
Reunanen J., Kotilainen J. K., Prieto M. A., 2002, MNRAS, 331, 154
Riffel R. A., 2010, Ap&SS, 327, 239
Riffel R. A., Storchi-Bergmann T., 2011, MNRAS, 411, 469
Riffel R. A., Storchi-Bergmann T., Winge C., McGregor P. J., Beck T., Schmitt H., 2008, MNRAS, 385, 1129
Riffel R. A., Storchi-Bergmann T., Dors O. L., Winge C., 2009, MNRAS, 393, 783

Riffel R. A., Storchi-Bergmann T., Riffel R., Pastoriza M. G., 2010, ApJ, 713, 469

Riffel R., Rodriguez-Ardila A., Aleman I., Brotherton M. S., Pastoriza M. G., Bonatto C., Dors O. L., 2013a, MNRAS, 430, 2002

Riffel R. A., Storchi-Bergmann T., Winge C., 2013b, 430, 2249

Riffel R. A., Storchi-Bergmann, Vale T. B., McGregor P., 2014, MNRAS, 442, 656

Riffel R. A., Storchi-Bergmann T., Riffel R., 2015, MNRAS, 451, 3587

Rodríguez-Ardila A., Pastoriza M. G., Viegas S., Sigut T. A. A., Pradhan A. K., 2004, A&A, 425, 457

Rodríguez-Ardila A., Riffel R., Pastoriza M. G., 2005, MNRAS, 364, 1041

Schinnerer E., Maciejewski W., Scoville N., Moustakas L. A., 2002, ApJ, 575, 826

Scoville N. Z., Hall D. N. B., Kleinmann S. G., Ridgway S. T., 1982, ApJ, 253, 136

Shi L., Gu Q. S., Peng Z. X., 2006, A&A, 450, 15

Shlosman I., Frank J., Begelman M. C., 1989, Nature, 338, 45

Shlosman I., Begelman M. C., Frank J., 1990, Nature, 345, 679

Skrutskie M. F. et al., 2006, AJ, 131, 1163

Storchi-Bergmann T., Wilson A. S., Baldwin J., 1996a, ApJ, 460, 252

Storchi-Bergmann T., Rodriguez-Ardila A., Schmitt H. R., Wilson A. S., Baldwin J., 1996b, ApJ, 472, 83

Storchi-Bergmann T., McGregor P. J., Riffel R. A., Simões Lopes R., Beck T., Dopita M., 2009, MNRAS, 394, 1148

Storchi-Bergmann T., Lopes R. D., McGregor P. J., Riffel R. A., Beck T., Martini P., 2010, MNRAS, 402, 819

van der Laan T. P. R. et al., 2015, A&A, 575, A83

van der Laan T. P. R., Schinnerer E., Emsellem E., Hunt L. K., McDermid R. M., Liu G., 2013a, A&A, 551, A81

van der Laan T. P. R. et al., 2013b, A&A, 556, A98

Vazquez G. A., Leitherer C., 2005, ApJ, 621, 695

Winge C., Riffel R. A., Storchi-Bergmann T., 2009, ApJS, 185, 186

Wold M., Galliano E., 2006, MNRAS, 369, 47

Wright C. O., Egan M. P., Kraemer K. E., Price S. D., 2003, AJ, 125, 359

SUPPORTING INFORMATION

Additional Supporting Information may be found in the online version of this article:

data_paper.tar

(http://www.mnras.oxfordjournals.org/lookup/suppl/doi:10.1093/mnras/stw1609/-/DC1).

Please note: Oxford University Press is not responsible for the content or functionality of any supporting materials supplied by the authors. Any queries (other than missing material) should be directed to the corresponding author for the article.

This paper has been typeset from a TeX/LaTeX file prepared by the author.

Referências Bibliográficas

[1] ALLOIN, D., BICA, E., BONATTO, C., PASTORIZA, M. Central Regions of Early-Type and Spiral Galaxies in the Uv: Nature of the UV Turnup and Probes of Starburst Activity. In: ULTRAVIOLET ASTROPHYSICS BEYOND THE IUE FINAL ARCHIVE, Wamsteker, W., Gonzalez Riestra, R., Harris, B., editores, v. 413 of **ESA Special Publication**, p. 545, 1998.

[2] ALONGI, M., BERTELLI, G., BRESSAN, A., CHIOSI, C., FAGOTTO, F., GREGGIO, L., NASI, E. Evolutionary sequences of stellar models with semiconvection and convective overshoot. I - Z = 0.008. **Astronomy and Astrophysics Supplement Series**, v. 97, p. 851–871, March 1993.

[3] ANTONUCCI, R. Unified models for active galactic nuclei and quasars. **Annual Review of Astronomy and Astrophysics**, v. 31, p. 473–521, 1993.

[4] ANTONUCCI, R. R. J., MILLER, J. S. Spectropolarimetry and the nature of NGC 1068. **Astrophysical Journal**, v. 297, p. 621–632, October 1985.

[5] ASARI, N. V., CID FERNANDES, R., STASIŃSKA, G., TORRES-PAPAQUI, J. P., MATEUS, A., SODRÉ, L., SCHOENELL, W., GOMES, J. M. The history of star-forming galaxies in the Sloan Digital Sky Survey. **Monthly Notices of the Royal Astronomical Society**, v. 381, p. 263–279, October 2007.

[6] BECKMANN, V., SHRADER, C. R. **Active Galactic Nuclei**: August 2012.

[7] BESSELL, M. S., BRETT, J. M., SCHOLZ, M., WOOD, P. R. Colors and stratifications of extended static model photospheres of M stars located on the FGB, AGB and supergiant branch. **Astronomy and Astrophysics Supplement Series**, v. 89, p. 335–366, August 1991.

[8] BESSELL, M. S., BRETT, J. M., WOOD, P. R., SCHOLZ, M. Colors of extended static model photospheres of M giants. **Astronomy and Astrophysics Supplement Series**, v. 77, p. 1–30, January 1989.

[9] BICA, E. Population synthesis in galactic nuclei using a library of star clusters. **Astronomy and Astrophysics**, v. 195, p. 76–92, April 1988.

[10] BICA, E., ALLOIN, D. A base of star clusters for stellar population synthesis. **Astronomy and Astrophysics**, v. 162, p. 21–31, July 1986.

[11] BÖKER, T., FALCÓN-BARROSO, J., SCHINNERER, E., KNAPEN, J. H., RYDER, S. A SINFONI View of Galaxy Centers: Morphology and Kinematics of Five Nuclear Star Formation-Rings. **Astronomical Journal**, v. 135, p. 479–495, February 2008.

[12] BOLZONELLA, M., MIRALLES, J.-M., PELLÓ, R. Photometric redshifts based on standard SED fitting procedures. **Astronomy and Astrophysics**, v. 363, p. 476–492, November 2000.

[13] BONATTO, C., BICA, E., PASTORIZA, M. G., ALLOIN, D. Ultraviolet spectral properties of magellanic and non-magellanic irregulars, H BT II and starburst galaxies. **Astronomy and Astrophysics**, v. 343, p. 100–110, March 1999.

[14] BONNET, H., ABUTER, R., BAKER, A., BORNEMANN, W., BROWN, A., CASTILLO, R., CONZELMANN, R., DAMSTER, R., DAVIES, R., DELABRE, B., DONALDSON, R., DUMAS, C., EISENHAUER, F., ELSWIJK, E., FEDRIGO, E., FINGER, G., GEMPERLEIN, H., GENZEL, R., GILBERT, A., GILLET, G., GOLDBRUNNER, A., HORROBIN, M., TER HORST, R., HUBER, S., HUBIN, N., ISERLOHE, C., KAUFER, A., KISSLER-PATIG, M., KRAGT, J., KROES, G., LEHNERT, M., LIEB, W., LISKE, J., LIZON, J.-L., LUTZ, D., MODIGLIANI, A., MONNET, G., NESVADBA, N., PATIG, J., PRAGT, J., REUNANEN, J., RÖHRLE, C., ROSSI, S., SCHMUTZER, R., SCHOENMAKER, T., SCHREIBER, J., STROEBELE, S., SZEIFERT, T., TACCONI, L., TECZA, M., THATTE, N., TORDO, S., VAN DER WERF, P., WEISZ, H. First light of SINFONI at the VLT. **The Messenger**, v. 117, p. 17–24, September 2004.

[15] BRESSAN, A., FAGOTTO, F., BERTELLI, G., CHIOSI, C. Evolutionary sequences of stellar models with new radiative opacities. II - Z = 0.02. **Astro-**

nomy and Astrophysics Supplement Series, v. 100, p. 647–664, September 1993.

[16] BRUZUAL, G., CHARLOT, S. Stellar population synthesis at the resolution of 2003. **Monthly Notices of the Royal Astronomical Society**, v. 344, p. 1000–1028, October 2003.

[17] BUNDY, KEVIN, BERSHADY, MATTHEW A., LAW, DAVID R., YAN, REN-BIN, DRORY, NIV, MACDONALD, NICHOLAS, WAKE, DAVID A., CHE-RINKA, BRIAN, SÁNCHEZ-GALLEGO, JOSÉ R., WEIJMANS, ANNE-MARIE, THOMAS, DANIEL, TREMONTI, CHRISTY, MASTERS, KA-REN, COCCATO, LODOVICO, DIAMOND-STANIC, ALEKSANDAR M., ARAGÓN-SALAMANCA, ALFONSO, AVILA-REESE, VLADIMIR, BADE-NES, CARLES, FALCÓN-BARROSO, JÉSUS, BELFIORE, FRANCESCO, BIZYAEV, DMITRY, BLANC, GUILLERMO A., BLAND- HAWTHORN, JOSS, BLANTON, MICHAEL R., BROWNSTEIN, JOEL R., BYLER, NELL, CAPPELLARI, MICHELE, CONROY, CHARLIE, DUTTON, AA-RON A., EMSELLEM, ERIC, ETHERINGTON, JAMES, FRINCHABOY, PETER M., FU, HAI, GUNN, JAMES E., HARDING, PAUL, JOHNS-TON, EVELYN J., KAUFFMANN, GUINEVERE, KINEMUCHI, KAREN, KLAENE, MARK A., KNAPEN, JOHAN H., LEAUTHAUD, ALEXIE, LI, CHENG, LIN, LIHWAI, MAIOLINO, ROBERTO, MALANUSHENKO, VIK-TOR, MALANUSHENKO, ELENA, MAO, SHUDE, MARASTON, CLAU-DIA, MCDERMID, RICHARD M., MERRIFIELD, MICHAEL R., NICHOL, ROBERT C., ORAVETZ, DANIEL, PAN, KAIKE, PAREJKO, JOHN K., SANCHEZ, SEBASTIAN F., SCHLEGEL, DAVID, SIMMONS, AUDREY, STEELE, OLIVER, STEINMETZ, MATTHIAS, THANJAVUR, KARUN, THOMPSON, BENJAMIN A., TINKER, JEREMY L., VAN DEN BOSCH, REMCO C. E., WESTFALL, KYLE B., WILKINSON, DAVID, WRIGHT, SHELLEY, XIAO, TING, ZHANG, KAI. Overview of the SDSS-IV MaNGA Survey: Mapping nearby Galaxies at Apache Point Observatory. **Astrophysical Journal**, v. 798, p. 7, January 2015.

[18] BURTSCHER, L., ORBAN DE XIVRY, G., DAVIES, R. I., JANSSEN, A., LUTZ, D., ROSARIO, D., CONTURSI, A., GENZEL, R., GRACIÁ-CARPIO, J., LIN, M.-Y., SCHNORR-MÜLLER, A., STERNBERG, A., STURM, E., TACCONI, L. Obscuration in active galactic nuclei: near-

infrared luminosity relations and dust colors. **Astronomy and Astrophysics**, v. 578, p. A47, June 2015.

[19] CALZETTI, D., ARMUS, L., BOHLIN, R. C., KINNEY, A. L., KOORNNEEF, J., STORCHI-BERGMANN, T. The Dust Content and Opacity of Actively Star-forming Galaxies. **Astrophysical Journal**, v. 533, p. 682–695, April 2000.

[20] CASSISI, S., CASTELLANI, M., CASTELLANI, V. Intermediate-age metal deficient stellar populations: the case of metallicity Z=0.00001. **Astronomy and Astrophysics**, v. 317, p. 108–113, January 1997a.

[21] CASSISI, S., DEGL'INNOCENTI, S., SALARIS, M. The effect of diffusion on the red giant luminosity function 'bump'. **Monthly Notices of the Royal Astronomical Society**, v. 290, p. 515–520, September 1997b.

[22] CHABRIER, G. Galactic Stellar and Substellar Initial Mass Function. **Publications of the Astronomical Society of the Pacific**, v. 115, p. 763–795, July 2003.

[23] CHANG, P., MURRAY-CLAY, R., CHIANG, E., QUATAERT, E. The Origin of the Young Stars in the Nucleus of M31. **Astrophysical Journal**, v. 668, p. 236–244, October 2007.

[24] CHARLOT, S., BRUZUAL, A. G. Stellar population synthesis revisited. **Astrophysical Journal**, v. 367, p. 126–140, January 1991.

[25] CHEN, X. Y., LIANG, Y. C., HAMMER, F., PRUGNIEL, P., ZHONG, G. H., RODRIGUES, M., ZHAO, Y. H., FLORES, H. Comparing six evolutionary population synthesis models by performing spectral synthesis for galaxies. **Astronomy and Astrophysics**, June 2010.

[26] CID FERNANDES, R., GONZÁLEZ DELGADO, R. M., STORCHI-BERGMANN, T., MARTINS, L. P., SCHMITT, H. The stellar populations of low-luminosity active galactic nuclei - III. Spatially resolved spectral properties. **Monthly Notices of the Royal Astronomical Society**, v. 356, p. 270–294, January 2005a.

[27] CID FERNANDES, R., GU, Q., MELNICK, J., TERLEVICH, E., TERLEVICH, R., KUNTH, D., RODRIGUES LACERDA, R., JOGUET, B. The star for-

mation history of Seyfert 2 nuclei. **Monthly Notices of the Royal Astronomical Society**, v. 355, p. 273–296, November 2004.

[28] CID FERNANDES, R., MATEUS, A., SODRÉ, L., STASIŃSKA, G., GOMES, J. M. Semi-empirical analysis of Sloan Digital Sky Survey galaxies - I. Spectral synthesis method. **Monthly Notices of the Royal Astronomical Society**, v. 358, p. 363–378, April 2005b.

[29] CID FERNANDES, R., PÉREZ, E., GARCíA BENITO, R., GONZÁLEZ DELGADO, R. M., DE AMORIM, A. L., SÁNCHEZ, S. F., HUSEMANN, B., FALCÓN BARROSO, J., SÁNCHEZ-BLÁZQUEZ, P., WALCHER, C. J., MAST, D. Resolving galaxies in time and space. I. Applying STARLIGHT to CALIFA datacubes. **Astronomy and Astrophysics**, v. 557, p. A86, September 2013.

[30] CID FERNANDES, R., SCHOENELL, W., GOMES, J. M., ASARI, N. V., SCHLICKMANN, M., MATEUS, A., STASINSKA, G., SODRÉ, L., JR., TORRES-PAPAQUI, J. P., SEAGAL COLLABORATION, . The Star Formation Histories of Galaxies: A tour through the STARLIGHT-SDSS database. In: REVISTA MEXICANA DE ASTRONOMIA Y ASTROFISICA CONFERENCE SERIES, v. 35 of **Revista Mexicana de Astronomia y Astrofisica, vol. 27**, p. 127–132, May 2009.

[31] CID FERNANDES, R., SODRÉ, L., SCHMITT, H. R., LEÃO, J. R. S. A probabilistic formulation for empirical population synthesis: sampling methods and tests. **Monthly Notices of the Royal Astronomical Society**, v. 325, p. 60–76, July 2001.

[32] CID FERNANDES, R., STASIŃSKA, G., MATEUS, A., VALE ASARI, N. A comprehensive classification of galaxies in the Sloan Digital Sky Survey: how to tell true from fake AGN? **Monthly Notices of the Royal Astronomical Society**, v. 413, p. 1687–1699, May 2011.

[33] CID FERNANDES, R., STASIŃSKA, G., SCHLICKMANN, M. S., MATEUS, A., VALE ASARI, N., SCHOENELL, W., SODRÉ, L. Alternative diagnostic diagrams and the 'forgotten' population of weak line galaxies in the SDSS. **Monthly Notices of the Royal Astronomical Society**, v. 403, p. 1036–1053, April 2010.

[34] COLINA, L., ARRIBAS, S. The Starburst-Active Galactic Nucleus Connection in Active Galaxies: The MassiveNuclear Star-Forming Disk in NGC 4303. **Astrophysical Journal**, v. 514, p. 637–647, April 1999.

[35] COLINA, L., GARCíA VARGAS, M. L., MAS-HESSE, J. M., ALBERDI, A., KRABBE, A. Nuclear Spiral and Ring Star-forming Structures and the Starburst–Active Galactic Nucleus Connection in Barred Spirals NGC 3351 and NGC 4303. **Astrophysical Journal Letters**, v. 484, p. L41–L45, July 1997.

[36] COLINA, L., GONZALEZ DELGADO, R., MAS-HESSE, J. M., LEITHERER, C. Detection of a Super-Star Cluster as the Ionizing Source in the Low-Luminosity Active Galactic Nucleus NGC 4303. **Astrophysical Journal**, v. 579, p. 545–553, November 2002.

[37] COLINA, L., PIQUERAS LÓPEZ, J., ARRIBAS, S., RIFFEL, R., RIFFEL, R. A., RODRIGUEZ-ARDILA, A., PASTORIZA, M., STORCHI-BERGMANN, T., ALONSO-HERRERO, A., SALES, D. Understanding the two-dimensional ionization structure in luminous infrared galaxies. A near-IR integral field spectroscopy perspective. **Astronomy and Astrophysics**, v. 578, p. A48, June 2015.

[38] COLINA, L., WADA, K. Nuclear Bar, Star Formation, and Gas Fueling in the Active Galaxy NGC 4303. **Astrophysical Journal**, v. 529, p. 845–852, February 2000.

[39] CONROY, C., GUNN, J. E., WHITE, M. The Propagation of Uncertainties in Stellar Population Synthesis Modeling. I. The Relevance of Uncertain Aspects of Stellar Evolution and the Initial Mass Function to the Derived Physical Properties of Galaxies. **Astrophysical Journal**, v. 699, p. 486–506, July 2009.

[40] CUADRA, J., NAYAKSHIN, S., SPRINGEL, V., DI MATTEO, T. Galactic Centre stellar winds and Sgr A* accretion. **Monthly Notices of the Royal Astronomical Society**, v. 366, p. 358–372, February 2006.

[41] DAMETTO, N. Z., RIFFEL, R., PASTORIZA, M. G., RODRíGUEZ-ARDILA, A., HERNANDEZ-JIMENEZ, J. A., CARVALHO, E. A. Probing the circum-nuclear stellar populations of starburst galaxies in the near-infrared. **Monthly**

Notices of the Royal Astronomical Society, v. 443, p. 1754–1778, September 2014.

[42] DAVIES, R. I., MUELLER SÁNCHEZ, F., GENZEL, R., TACCONI, L. J., HICKS, E. K. S., FRIEDRICH, S., STERNBERG, A. A Close Look at Star Formation around Active Galactic Nuclei. **Astrophysical Journal**, v. 671, p. 1388–1412, December 2007.

[43] DAVIES, R. I., THOMAS, J., GENZEL, R., MÜLLER SÁNCHEZ, F., TACCONI, L. J., STERNBERG, A., EISENHAUER, F., ABUTER, R., SAGLIA, R., BENDER, R. The Star-forming Torus and Stellar Dynamical Black Hole Mass in the Seyfert 1 Nucleus of NGC 3227. **Astrophysical Journal**, v. 646, p. 754–773, August 2006.

[44] DE VAUCOULEURS, G., DE VAUCOULEURS, A., CORWIN, H. G., JR., BUTA, R. J., PATUREL, G., FOUQUE, P. **Third Reference Catalogue of Bright Galaxies**: 1991.

[45] DIAMOND-STANIC, A. M., RIEKE, G. H. The Relationship between Black Hole Growth and Star Formation in Seyfert Galaxies. **Astrophysical Journal**, v. 746, p. 168, February 2012.

[46] DORS, O. L., AGARWAL, B., HÄGELE, G. F., CARDACI, M. V., RYDBERG, CLAES-ERIK, RIFFEL, R. A., OLIVEIRA, A. S., KRABBE, A. C. Nature and chemical abundances of a sample of Lyman-α emitter objects at high redshift. **Monthly Notices of the Royal Astronomical Society**, v. 479, p. 2294–2307, September 2018.

[47] DORS, O. L., JR., STORCHI-BERGMANN, T., RIFFEL, R. A., SCHIMDT, A. A. Ages and metallicities of circumnuclear star formation regions from Gemini IFU observations. **Astronomy and Astrophysics**, v. 482, p. 59–65, April 2008.

[48] EISENHAUER, F., ABUTER, R., BICKERT, K., BIANCAT-MARCHET, F., BONNET, H., BRYNNEL, J., CONZELMANN, R. D., DELABRE, B., DONALDSON, R., FARINATO, J., FEDRIGO, E., GENZEL, R., HUBIN, N. N., ISERLOHE, C., KASPER, M. E., KISSLER-PATIG, M., MONNET, G. J., ROEHRLE, C., SCHREIBER, J., STROEBELE, S., TECZA, M., THATTE, N. A., WEISZ, H. SINFONI - Integral field spectroscopy at 50 milli-arcsecond

resolution with the ESO VLT. In: INSTRUMENT DESIGN AND PERFOR-MANCE FOR OPTICAL/INFRARED GROUND-BASED TELESCOPES, Iye, M., Moorwood, A. F. M., editores, v. 4841 of **Proceedings of the International Society for Optical Engineering**, p. 1548–1561, March 2003.

[49] ELMEGREEN, B. G. Starbursts by gravitational collapse in the inner Lindblad resonance rings of galaxies. **Astrophysical Journal Letters**, v. 425, p. L73–L76, April 1994.

[50] FAGOTTO, F., BRESSAN, A., BERTELLI, G., CHIOSI, C. Evolutionary sequences of stellar models with new radiative opacities. III. Z=0.0004 and Z=0.05. **Astronomy and Astrophysics Supplement Series**, v. 104, April 1994a.

[51] FAGOTTO, F., BRESSAN, A., BERTELLI, G., CHIOSI, C. Evolutionary sequences of stellar models with new radiative opacities. IV. Z=0.004 and Z=0.008. **Astronomy and Astrophysics Supplement Series**, v. 105, May 1994b.

[52] FATHI, K., STORCHI-BERGMANN, T., RIFFEL-ROGEMAR, A., WINGE, C., AXON, D. J., ROBINSON, A., CAPETTI, A., MARCONI, A. Streaming Motions toward the Supermassive Black Hole in NGC 1097. **Astrophysical Journal Letters**, v. 641, p. L25–L28, April 2006.

[53] FERRARESE, L., MERRITT, D. A Fundamental Relation between Supermassive Black Holes and Their Host Galaxies. **Astrophysical Journal Letters**, v. 539, p. L9–L12, August 2000.

[54] FILIPPENKO, A. V., HO, L. C., SARGENT, W. L. W. HST observations of NGC 4395, the least luminous Seyfert 1 nucleus - Evidence against the starburst hypothesis for broad-lined active galactic nuclei. **Astrophysical Journal Letters**, v. 410, p. L75–L78, June 1993.

[55] FILIPPENKO, A. V., SARGENT, W. L. W. The properties of 'dwarf' Seyfert nuclei in nearby galaxies. In: STRUCTURE AND EVOLUTION OF ACTIVE GALACTIC NUCLEI, Giuricin, G., Mezzetti, M., Ramella, M., Mardirossian, F., editores, v. 121 of **Astrophysics and Space Science Library**, p. 21–42, 1986.

[56] FLUKS, M. A., PLEZ, B., THE, P. S., DE WINTER, D., WESTERLUND, B. E., STEENMAN, H. C. On the spectra and photometry of M-giant stars. **Astronomy and Astrophysics Supplement Series**, v. 105, June 1994.

[57] GIRARDI, L., BRESSAN, A., BERTELLI, G., CHIOSI, C. Evolutionary tracks and isochrones for low- and intermediate-mass stars: From 0.15 to 7 $M_{sun,}$ and from Z=0.0004 to 0.03. **Astronomy and Astrophysics Supplement Series**, v. 141, p. 371–383, February 2000.

[58] GIRARDI, L., BRESSAN, A., CHIOSI, C., BERTELLI, G., NASI, E. Evolutionary sequences of stellar models with new radiative opacities. VI. Z=0.0001. **Astronomy and Astrophysics Supplement Series**, v. 117, p. 113–125, May 1996.

[59] GODDARD, D., THOMAS, D., MARASTON, C., WESTFALL, K., ETHERINGTON, J., RIFFEL, R., MALLMANN, N. D., ZHENG, Z., ARGUDO-FERNÁNDEZ, M., BERSHADY, M., BUNDY, K., DRORY, N., LAW, D., YAN, R., WAKE, D., WEIJMANS, A., BIZYAEV, D., BROWNSTEIN, J., LANE, R. R., MAIOLINO, R., MASTERS, K., MERRIFIELD, M., NITSCHELM, C., PAN, K., ROMAN-LOPES, A., STORCHI-BERGMANN, T. SDSS-IV MaNGA: stellar population gradients as a function of galaxy environment. **Monthly Notices of the Royal Astronomical Society**, v. 465, p. 688–700, February 2017.

[60] GODDARD, D., THOMAS, D., MARASTON, C., WESTFALL, K., ETHERINGTON, J., RIFFEL, R., MALLMANN, N. D., ZHENG, Z., ARGUDO-FERNÁNDEZ, M., LIAN, J., BERSHADY, M., BUNDY, K., DRORY, N., LAW, D., YAN, R., WAKE, D., WEIJMANS, A., BIZYAEV, D., BROWNSTEIN, J., LANE, R. R., MAIOLINO, R., MASTERS, K., MERRIFIELD, M., NITSCHELM, C., PAN, K., ROMAN-LOPES, A., STORCHI-BERGMANN, T., SCHNEIDER, D. P. SDSS-IV MaNGA: Spatially resolved star formation histories in galaxies as a function of galaxy mass and type. **Monthly Notices of the Royal Astronomical Society**, December 2016.

[61] GONZÁLEZ DELGADO, R. M., HECKMAN, T., LEITHERER, C. The Nuclear and Circumnuclear Stellar Population in Seyfert 2 Galaxies: Implications for the Starburst-Active Galactic Nucleus Connection. **Astrophysical Journal**, v. 546, p. 845–865, January 2001.

[62] GONZÁLEZ DELGADO, R. M., HECKMAN, T., LEITHERER, C., MEURER, G., KROLIK, J., WILSON, A. S., KINNEY, A., KORATKAR, A. Ultraviolet-Optical Observations of the Seyfert 2 Galaxies NGC 7130, NGC 5135, and IC 3639: Implications for the Starburst-Active Galactic Nucleus Connection. **Astrophysical Journal**, v. 505, p. 174–198, September 1998.

[63] GU, Q., MELNICK, J., CID FERNANDES, R., KUNTH, D., TERLEVICH, E., TERLEVICH, R. Emission-line properties of Seyfert 2 nuclei. **Monthly Notices of the Royal Astronomical Society**, v. 366, p. 480–490, February 2006.

[64] GÜSTEN, R. Gas and Dust in the Inner Few Degrees of the Galaxy (review). In: THE CENTER OF THE GALAXY, Morris, M., editor, v. 136 of **IAU Symposium**, p. 89, 1989.

[65] HASTINGS, W. K. Monte Carlo Sampling Methods Using Markov Chains and Their Applications. **Biometrika Trust**, v. 57, p. 97–109, April 1970.

[66] HECKMAN, T. **Starburst Galaxies**. November 2000.

[67] HECKMAN, T. M. Star Formation in Active Galaxies: A Spectroscopic Perspective. **Coevolution of Black Holes and Galaxies**, p. 358, 2004.

[68] HECKMAN, T. M., GONZÁLEZ-DELGADO, R., LEITHERER, C., MEURER, G. R., KROLIK, J., WILSON, A. S., KORATKAR, A., KINNEY, A. A Powerful Nuclear Starburst in the Seyfert Galaxy Markarian 477: Implications for the Starburst-Active Galactic Nucleus Connection. **Astrophysical Journal**, v. 482, p. 114–132, June 1997.

[69] HERNQUIST, L., MIHOS, J. C. Excitation of Activity in Galaxies by Minor Mergers. **Astrophysical Journal**, v. 448, p. 41, July 1995.

[70] HO, L. C., FEIGELSON, E. D., TOWNSLEY, L. K., SAMBRUNA, R. M., GARMIRE, G. P., BRANDT, W. N., FILIPPENKO, A. V., GRIFFITHS, R. E., PTAK, A. F., SARGENT, W. L. W. Detection of Nuclear X-Ray Sources in Nearby Galaxies with Chandra. **Astrophysical Journal Letters**, v. 549, p. L51–L54, March 2001.

[71] HO, L. C., FILIPPENKO, A. V., SARGENT, W. L. W., PENG, C. Y. A Search for "Dwarf" Seyfert Nuclei. IV. Nuclei with Broad H alpha Emission.

Astrophysical Journal Supplement Series, v. 112, p. 391–+, October 1997.

[72] HOPKINS, P. F., QUATAERT, E. How do massive black holes get their gas? **Monthly Notices of the Royal Astronomical Society**, v. 407, p. 1529–1564, September 2010.

[73] HOYLE, F., FOWLER, W. A. On the nature of strong radio sources. **Monthly Notices of the Royal Astronomical Society**, v. 125, p. 169, 1963.

[74] IMANISHI, M. 3-4 Micron Spectroscopy of Seyfert 2 Nuclei to Quantitatively Assess the Energetic Importance of Compact Nuclear Starbursts. **Astrophysical Journal**, v. 569, p. 44–53, April 2002.

[75] IMANISHI, M., DUDLEY, C. C. Energy Diagnoses of Nine Infrared Luminous Galaxies Based on 3-4 Micron Spectra. **Astrophysical Journal**, v. 545, p. 701–711, December 2000.

[76] JIMÉNEZ-BAILÓN, E., SANTOS-LLEÓ, M., MAS-HESSE, J. M., GUAINAZZI, M., COLINA, L., CERVIÑO, M., GONZÁLEZ DELGADO, R. M. Nuclear Activity and Massive Star Formation in the Low-Luminosity Active Galactic Nucleus NGC 4303: Chandra X-Ray Observations. **Astrophysical Journal**, v. 593, p. 127–141, August 2003.

[77] KAUFFMANN, G., HECKMAN, T. M., TREMONTI, C., BRINCHMANN, J., CHARLOT, S., WHITE, S. D. M., RIDGWAY, S. E., BRINKMANN, J., FUKUGITA, M., HALL, P. B., IVEZIĆ, Ž., RICHARDS, G. T., SCHNEIDER, D. P. The host galaxies of active galactic nuclei. **Monthly Notices of the Royal Astronomical Society**, v. 346, p. 1055–1077, December 2003.

[78] KAWAKATU, N., WADA, K. Coevolution of Supermassive Black Holes and Circumnuclear Disks. **Astrophysical Journal**, v. 681, p. 73–83, July 2008.

[79] KENNICUTT, R. C., JR. Properties of H II region populations in galaxies. I - The first-ranked H II regions. **Astrophysical Journal**, v. 334, p. 144–158, November 1988.

[80] KENNICUTT, R. C., JR., KEEL, W. C., BLAHA, C. A. A comparison of the physical conditions in nuclear, hotspot, and disk H II regions. **Astronomical Journal**, v. 97, p. 1022–1035, April 1989.

[81] KIRKPATRICK, S., GELATT, C. D., VECCHI, M. P. Optimization by Simulated Annealing. **Science**, v. 220, p. 671–680, May 1983.

[82] KNAPEN, J. H., SHLOSMAN, I., PELETIER, R. F. A Subarcsecond Resolution Near-Infrared Study of Seyfert and "Normal" Galaxies. II. Morphology. **Astrophysical Journal**, v. 529, p. 93–100, January 2000.

[83] KOTULLA, R., FRITZE, U., WEILBACHER, P., ANDERS, P. GALEV evolutionary synthesis models - I. Code, input physics and web interface. **Monthly Notices of the Royal Astronomical Society**, v. 396, p. 462–484, June 2009.

[84] KROUPA, P. On the variation of the initial mass function. **Monthly Notices of the Royal Astronomical Society**, v. 322, p. 231–246, April 2001.

[85] LAMASSA, S. M., HECKMAN, T. M., PTAK, A., URRY, C. M. On the Star Formation-AGN Connection at z $<\sim$ 0.3. **Astrophysical Journal Letters**, v. 765, p. L33, March 2013.

[86] LANÇON, A., MOUHCINE, M. The modelling of intermediate-age stellar populations. II. Average spectra for upper AGB stars, and their use. **Astronomy and Astrophysics**, v. 393, p. 167–181, October 2002.

[87] LANÇON, A., WOOD, P. R. A library of 0.5 to 2.5 mu m spectra of luminous cool stars. **Astronomy and Astrophysics Supplement Series**, v. 146, p. 217–249, October 2000.

[88] LE BORGNE, J.-F., BRUZUAL, G., PELLÓ, R., LANÇON, A., ROCCA-VOLMERANGE, B., SANAHUJA, B., SCHAERER, D., SOUBIRAN, C., VíLCHEZ-GÓMEZ, R. STELIB: A library of stellar spectra at R ˜ 2000. **Astronomy and Astrophysics**, v. 402, p. 433–442, May 2003.

[89] LEJEUNE, T., CUISINIER, F., BUSER, R. Standard stellar library for evolutionary synthesis. I. Calibration of theoretical spectra. **Astronomy and Astrophysics Supplement Series**, v. 125, October 1997.

[90] LEJEUNE, T., CUISINIER, F., BUSER, R. A standard stellar library for evolutionary synthesis. II. The M dwarf extension. **Astronomy and Astrophysics Supplement Series**, v. 130, p. 65–75, May 1998.

[91] LÓPEZ FERNÁNDEZ, R., CID FERNANDES, R., GONZÁLEZ DELGADO, R. M., VALE ASARI, N., PÉREZ, E., GARCíA-BENITO, R., DE AMORIM, A. L., LACERDA, E. A. D., CORTIJO-FERRERO, C., SÁNCHEZ, S. F. Simultaneous spectroscopic and photometric analysis of galaxies with STARLIGHT: CALIFA+GALEX. **Monthly Notices of the Royal Astronomical Society**, v. 458, p. 184–199, May 2016.

[92] LYNDEN-BELL, D. Galactic Nuclei as Collapsed Old Quasars. **Nature**, v. 223, p. 690–694, August 1969.

[93] LYNDEN-BELL, D., KALNAJS, A. J. On the generating mechanism of spiral structure. **Monthly Notices of the Royal Astronomical Society**, v. 157, p. 1, 1972.

[94] LYNDEN-BELL, D., REES, M. J. On quasars, dust and the galactic centre. **Monthly Notices of the Royal Astronomical Society**, v. 152, p. 461, 1971.

[95] MAIOLINO, R., RUIZ, M., RIEKE, G. H., PAPADOPOULOS, P. Molecular Gas, Morphology, and Seyfert Galaxy Activity. **Astrophysical Journal**, v. 485, p. 552–569, August 1997.

[96] MALLMANN, NíCOLAS DULLIUS, RIFFEL, ROGÉRIO, STORCHI- BERGMANN, THAISA, REMBOLD, SANDRO BARBOZA, RIFFEL, ROGEMAR A., SCHIMOIA, JADERSON, DA COSTA, LUIZ NICOLACI, ÁVILA-REESE, VLADIMIR, SANCHEZ, SEBASTIAN F., MACHADO, ALICE D., CIROLINI, RAFAEL, ILHA, GABRIELE S., NASCIMENTO, JANAíNA C. DO. The first 62 AGN observed with SDSS-IV MaNGA - II. Resolvedstellar populations. **Monthly Notices of the Royal Astronomical Society**, v. 478, p. 5491–5504, August 2018.

[97] MARASTON, C. Evolutionary synthesis of stellar populations: a modular tool. **Monthly Notices of the Royal Astronomical Society**, v. 300, p. 872–892, November 1998.

[98] MARASTON, C. Evolutionary population synthesis: models, analysis of the ingredients and application to high-z galaxies. **Monthly Notices of the Royal Astronomical Society**, v. 362, p. 799–825, September 2005.

[99] MARASTON, C., STRÖMBÄCK, G. Stellar population models at high spectral resolution. **Monthly Notices of the Royal Astronomical Society**, v. 418, p. 2785–2811, December 2011.

[100] MARIGO, P., GIRARDI, L. Evolution of asymptotic giant branch stars. I. Updated synthetic TP-AGB models and their basic calibration. **Astronomy and Astrophysics**, v. 469, p. 239–263, July 2007.

[101] MARIGO, P., GIRARDI, L., BRESSAN, A., GROENEWEGEN, M. A. T., SILVA, L., GRANATO, G. L. Evolution of asymptotic giant branch stars. II. Optical to far-infrared isochrones with improved TP-AGB models. **Astronomy and Astrophysics**, v. 482, p. 883–905, May 2008.

[102] MARTINS, L. P., RIFFEL, R., RODRíGUEZ-ARDILA, A., GRUENWALD, R., DE SOUZA, R. Nuclear and extended spectra of NGC 1068 - II. Near-infrared stellar population synthesis. **Monthly Notices of the Royal Astronomical Society**, v. 406, p. 2185–2192, August 2010.

[103] MARTINS, L. P., RODRíGUEZ-ARDILA, A., DINIZ, S., GRUENWALD, R., DE SOUZA, R. A spectral atlas of H II galaxies in the near-infrared. **Monthly Notices of the Royal Astronomical Society**, v. 431, p. 1823–1839, May 2013a.

[104] MARTINS, L. P., RODRíGUEZ-ARDILA, A., DINIZ, S., RIFFEL, R., DE SOUZA, R. Spectral synthesis of star-forming galaxies in the near-infrared. **Monthly Notices of the Royal Astronomical Society**, v. 435, p. 2861–2877, November 2013b.

[105] MATEUS, A., SODRÉ, L., CID FERNANDES, R., STASIŃSKA, G., SCHOENELL, W., GOMES, J. M. Semi-empirical analysis of Sloan Digital Sky Survey galaxies - II. The bimodality of the galaxy population revisited. **Monthly Notices of the Royal Astronomical Society**, v. 370, p. 721–737, August 2006.

[106] MCGREGOR, P. J., HART, J., CONROY, P. G., PFITZNER, M. L., BLOXHAM, G. J., JONES, D. J., DOWNING, M. D., DAWSON, M., YOUNG, P., JARNYK, M., VAN HARMELEN, J. Gemini near-infrared integral field spectrograph (NIFS). In: INSTRUMENT DESIGN AND PERFORMANCE FOR OPTICAL/INFRARED GROUND-BASED TELESCOPES, Iye, M., Moorwood, A. F. M., editores, v. 4841 of **Proceedings of**

the **International Society for Optical Engineering**, p. 1581–1591, March 2003.

[107] MENESES-GOYTIA, S., PELETIER, R. F., TRAGER, S. C., VAZDEKIS, A. Single stellar populations in the near-infrared. II. Synthesis models. **Astronomy and Astrophysics**, v. 582, p. A97, October 2015.

[108] METROPOLIS, N., ROSENBLUTH, A., TELLER, A., TELLER, E. Equation of State Calculations by Fast Computing Machines. **Journal of Chemical Physics**, v. 21, p. 1087, 1953.

[109] MIZUTANI, K., SUTO, H., MAIHARA, T. 3.3 micron emission feature in infrared galaxies. **Astrophysical Journal**, v. 421, p. 475–480, February 1994.

[110] MORGAN, W. W. A Preliminary Classification of the Forms of Galaxies According to Their Stellar Population. **Publications of the Astronomical Society of the Pacific**, v. 70, p. 364–+, August 1958.

[111] NORMAN, C., SCOVILLE, N. The evolution of starburst galaxies to active galactic nuclei. **Astrophysical Journal**, v. 332, p. 124–134, September 1988.

[112] OLIVA, E., ORIGLIA, L., KOTILAINEN, J. K., MOORWOOD, A. F. M. Red supergiants as starburst tracers in galactic nuclei. **Astronomy and Astrophysics**, v. 301, p. 55, September 1995.

[113] ORIGLIA, L., OLIVA, E. Starbursts in the IR. **New Astronomy Review**, v. 44, p. 257–262, July 2000.

[114] OSMER, P. S., SMITH, M. G., WEEDMAN, D. W. The nuclei of peculiar emission-line galaxies. **Astrophysical Journal**, v. 192, p. 279–291, September 1974.

[115] PASTORIZA, M. G. Spectra of peculiar nuclei in galaxies. **The Observatory**, v. 87, p. 225–228, October 1967.

[116] PASTORIZA, M. G. Studies of galaxies with peculiar nuclei. **Astrophysics and Space Science**, v. 33, p. 173–188, March 1975.

[117] PETERSON, B. M. **An Introduction to Active Galactic Nuclei**: An introduction to active galactic nuclei, Publisher: Cambridge, New York Cambridge University Press, 1997 Physical description xvi, 238 p. ISBN 0521473489, February 1997.

[118] PICKLES, A. J. A Stellar Spectral Flux Library: 1150-25000 Å. **Publications of the Astronomical Society of the Pacific**, v. 110, p. 863–878, July 1998.

[119] POGGE, R. W. Ionized gas in the nuclear regions of nearby non-Seyfert spiral galaxies. **Astrophysical Journal Supplement Series**, v. 71, p. 433–453, November 1989.

[120] RAIMANN, D., BICA, E., STORCHI-BERGMANN, T., MELNICK, J., SCHMITT, H. Population synthesis of Hii galaxies. **Monthly Notices of the Royal Astronomical Society**, v. 314, p. 295–306, May 2000a.

[121] RAIMANN, D., STORCHI-BERGMANN, T., BICA, E., MELNICK, J., SCHMITT, H. Gas properties of Hii and starburst galaxies: relation with the stellar population. **Monthly Notices of the Royal Astronomical Society**, v. 316, p. 559–568, August 2000b.

[122] RAMOS ALMEIDA, C., PÉREZ GARCíA, A. M., ACOSTA-PULIDO, J. A. Near-Infrared Spectroscopy of Seyfert Galaxies. Nuclear Activity and Stellar Population. **Astrophysical Journal**, v. 694, p. 1379–1394, April 2009.

[123] REMBOLD, S. B., PASTORIZA, M. G. The cluster of galaxies LCDCS-S001: basic spectroscopic data and stellar population. **Monthly Notices of the Royal Astronomical Society**, v. 374, p. 1056–1066, January 2007.

[124] RENZINI, A. In: GALAXY FORMATION, Silk, J., Vittorio, J., editores, Amsterdam: North Holland, p. 303, 1981.

[125] RICKES, M. G., PASTORIZA, M. G., BONATTO, C. The elliptical galaxy NGC 5044: Stellar population and ionized gas. **Astronomy and Astrophysics**, v. 419, p. 449–458, May 2004.

[126] RIFFEL, R., BONATTO, C., CID FERNANDES, R., PASTORIZA, M. G., BALBINOT, E. Panchromatic averaged stellar populations. **Monthly Notices of the Royal Astronomical Society**, v. 411, p. 1897–1908, March 2011a.

[127] RIFFEL, R., MASON, R. E., MARTINS, L. P., RODRíGUEZ-ARDILA, A., HO, L. C., RIFFEL, R. A., LIRA, P., GONZALEZ MARTIN, O., RUSCHEL-DUTRA, D., ALONSO-HERRERO, A., FLOHIC, H., MCDERMID, R. M., RAMOS ALMEIDA, C., THANJAVUR, K., WINGE, C. The stellar spectral features of nearby galaxies in the near infrared: tracers of thermally pulsing

asymptotic giant branch stars? **Monthly Notices of the Royal Astronomical Society**, v. 450, p. 3069–3079, July 2015.

[128] RIFFEL, R., PASTORIZA, M. G., RODRíGUEZ-ARDILA, A., BONATTO, C. Probing the near-infrared stellar population of Seyfert galaxies. **Monthly Notices of the Royal Astronomical Society**, v. 400, p. 273–290, November 2009a.

[129] RIFFEL, R., PASTORIZA, M. G., RODRíGUEZ-ARDILA, A., MARASTON, C. The First Detection of Near-Infrared CN Bands in Active Galactic Nuclei: Signature of Star Formation. **Astrophysical Journal Letters**, v. 659, p. L103–L106, April 2007.

[130] RIFFEL, R., PASTORIZA, M. G., RODRíGUEZ-ARDILA, A., MARASTON, C. The stellar populations of starburst galaxies through near-infrared spectroscopy. **Monthly Notices of the Royal Astronomical Society**, v. 388, p. 803–814, August 2008a.

[131] RIFFEL, R., RIFFEL, R. A., FERRARI, F., STORCHI-BERGMANN, T. Intermediate-age stars as the origin of low stellar velocity dispersion nuclear rings: the case of Mrk 1157. **Monthly Notices of the Royal Astronomical Society**, v. 416, p. 493–500, September 2011b.

[132] RIFFEL, R., RUSCHEL-DUTRA, D., PASTORIZA, M. G., RODRíGUEZ-ARDILA, A., SANTOS, J. F. C., JR., BONATTO, C. J., DUCATI, J. R. Near-infrared integrated spectra of Galactic globular clusters: testing simple stellar population models. **Monthly Notices of the Royal Astronomical Society**, v. 410, p. 2714–2724, February 2011c.

[133] RIFFEL, R. A., COLINA, L., STORCHI-BERGMANN, T., PIQUERAS LÓPEZ, J., ARRIBAS, S., RIFFEL, R., PASTORIZA, M., SALES, D. A., DAMETTO, N. Z., LABIANO, A., DAVIES, R. I. A SINFONI view of the nuclear activity and circumnuclear star formation in NGC 4303. **Monthly Notices of the Royal Astronomical Society**, v. 461, p. 4192–4205, October 2016.

[134] RIFFEL, R. A., STORCHI-BERGMANN, T., DORS, O. L., WINGE, C. AGN-starburst connection in NGC7582: Gemini near-infrared spectrograph integral field unit observations. **Monthly Notices of the Royal Astronomical Society**, v. 393, p. 783–797, March 2009b.

[135] RIFFEL, R. A., STORCHI-BERGMANN, T., MCGREGOR, P. J. The Dusty Nuclear Torus in NGC 4151: Constraints from Gemini Near-Infrared Integral Field Spectrograph Observations. **Astrophysical Journal**, v. 698, p. 1767–1770, June 2009c.

[136] RIFFEL, R. A., STORCHI-BERGMANN, T., RIFFEL, R., PASTORIZA, M. G. Intermediate-age Stars as Origin of the Low-velocity Dispersion Nuclear Ring in Mrk 1066. **Astrophysical Journal**, v. 713, p. 469–474, April 2010.

[137] RIFFEL, R. A., STORCHI-BERGMANN, T., WINGE, C., MCGREGOR, P. J., BECK, T., SCHMITT, H. Mapping of molecular gas inflow towards the Seyfert nucleus of NGC4051 using Gemini NIFS. **Monthly Notices of the Royal Astronomical Society**, v. 385, p. 1129–1142, April 2008b.

[138] RÖCK, B., VAZDEKIS, A., RICCIARDELLI, E., PELETIER, R. F., KNAPEN, J. H., FALCÓN-BARROSO, J. MILES extended: Stellar population synthesis models from the optical to the infrared. **Astronomy and Astrophysics**, v. 589, p. A73, May 2016.

[139] RODRíGUEZ-ARDILA, A., CONTINI, M., VIEGAS, S. M. The continuum and narrow-line region of the narrow-line Seyfert 1 galaxy Mrk 766. **Monthly Notices of the Royal Astronomical Society**, v. 357, p. 220–234, February 2005.

[140] RODRíGUEZ-ARDILA, A., MAZZALAY, X. The near-infrared spectrum of Mrk 1239: direct evidence of the dusty torus? **Monthly Notices of the Royal Astronomical Society**, v. 367, p. L57–L61, March 2006.

[141] RODRíGUEZ-ARDILA, A., VIEGAS, S. M. Hidden starbursts in Seyfert 1 galaxies. **Monthly Notices of the Royal Astronomical Society**, v. 340, p. L33–L37, April 2003.

[142] SALPETER, E. E. The Luminosity Function and Stellar Evolution. **Astrophysical Journal**, v. 121, p. 161, January 1955.

[143] SALPETER, E. E. Accretion of Interstellar Matter by Massive Objects. **Astrophysical Journal**, v. 140, p. 796–800, August 1964.

[144] SÁNCHEZ-BLÁZQUEZ, P., ROSALES-ORTEGA, F. F., MÉNDEZ-ABREU, J., PÉREZ, I., SÁNCHEZ, S. F., ZIBETTI, S., AGUERRI, J. A. L., BLAND-HAWTHORN, J., CATALÁN-TORRECILLA, C., CID FERNANDES, R.,

DE AMORIM, A., DE LORENZO-CACERES, A., FALCÓN-BARROSO, J., GALAZZI, A., GARCíA BENITO, R., GIL DE PAZ, A., GONZÁLEZ DELGADO, R., HUSEMANN, B., IGLESIAS-PÁRAMO, J., JUNGWIERT, B., MARINO, R. A., MÁRQUEZ, I., MAST, D., MENDOZA, M. A., MOLLÁ, M., PAPADEROS, P., RUIZ-LARA, T., VAN DE VEN, G., WALCHER, C. J., WISOTZKI, L. Stellar population gradients in galaxy discs from the CALIFA survey. The influence of bars. **Astronomy and Astrophysics**, v. 570, p. A6, October 2014.

[145] SCHALLER, G., SCHAERER, D., MEYNET, G., MAEDER, A. New grids of stellar models from 0.8 to 120 solar masses at Z = 0.020 and Z = 0.001. **Astronomy and Astrophysics Supplement Series**, v. 96, p. 269–331, December 1992.

[146] SCHAWINSKI, K., KOSS, M., BERNEY, S., SARTORI, L. F. Active galactic nuclei flicker: an observational estimate of the duration of black hole growth phases of $\sim 10^5$ yr. **Monthly Notices of the Royal Astronomical Society**, v. 451, p. 2517–2523, August 2015.

[147] SCHIMOIA, J. S., STORCHI-BERGMANN, T., GRUPE, D., ERACLEOUS, M., PETERSON, B. M., BALDWIN, J. A., NEMMEN, R. S., WINGE, C. Short-timescale Monitoring of the X-Ray, UV, and Broad Double-peak Emission Line of the Nucleus of NGC 1097. **Astrophysical Journal**, v. 800, p. 63, February 2015.

[148] SCHINNERER, E., MACIEJEWSKI, W., SCOVILLE, N., MOUSTAKAS, L. A. Toward the Secondary Bar: Gas Morphology and Dynamics in NGC 4303. **Astrophysical Journal**, v. 575, p. 826–844, August 2002.

[149] SCHMIDT, A. A., COPETTI, M. V. F., ALLOIN, D., JABLONKA, P. Population synthesis methods - Discussion and tests on the solution uniqueness. **Monthly Notices of the Royal Astronomical Society**, v. 249, p. 766–778, April 1991.

[150] SCHMITT, H. R., BICA, E., PASTORIZA, M. G. Spectral analysis of the nuclear stellar population and gas emission in NGC 6240. **Monthly Notices of the Royal Astronomical Society**, v. 278, p. 965–974, February 1996.

[151] SCHÖNELL, A. J., STORCHI-BERGMANN, T., RIFFEL, R. A., RIFFEL, R. NGC 5548. **Monthly Notices of the Royal Astronomical Society**, 2016.

[152] SÉRSIC, J. L., PASTORIZA, M. Peculiar Nuclei of Galaxies. **Publications of the Astronomical Society of the Pacific**, v. 77, p. 287–+, August 1965.

[153] SEYFERT, C. K. Nuclear Emission in Spiral Nebulae. **Astrophysical Journal**, v. 97, p. 28–+, January 1943.

[154] SHLOSMAN, I., BEGELMAN, M. C., FRANK, J. The fuelling of active galactic nuclei. **Nature**, v. 345, p. 679–686, June 1990.

[155] SHLOSMAN, I., FRANK, J., BEGELMAN, M. C. Bars within bars - A mechanism for fuelling active galactic nuclei. **Nature**, v. 338, p. 45–47, March 1989.

[156] SILVERMAN, J. D., GREEN, P. J., BARKHOUSE, W. A., KIM, D.-W., KIM, M., WILKES, B. J., CAMERON, R. A., HASINGER, G., JANNUZI, B. T., SMITH, M. G., SMITH, P. S., TANANBAUM, H. The Luminosity Function of X-Ray-selected Active Galactic Nuclei: Evolution of Supermassive Black Holes at High Redshift. **Astrophysical Journal**, v. 679, p. 118–139, May 2008.

[157] STORCHI-BERGMANN, T., GONZÁLEZ DELGADO, R. M., SCHMITT, H. R., CID FERNANDES, R., HECKMAN, T. Circumnuclear Stellar Population, Morphology, and Environment of Seyfert 2 Galaxies: An Evolutionary Scenario. **Astrophysical Journal**, v. 559, p. 147–156, September 2001.

[158] STORCHI-BERGMANN, T., NEMMEN, R. S., SPINELLI, P. F., ERACLEOUS, M., WILSON, A. S., FILIPPENKO, A. V., LIVIO, M. Evidence of a Starburst within 9 Parsecs of the Active Nucleus of NGC 1097. **Astrophysical Journal Letters**, v. 624, p. L13–L16, May 2005.

[159] STORCHI-BERGMANN, T., RAIMANN, D., BICA, E. L. D., FRAQUELLI, H. A. The Frequency of Nuclear Star Formation in Seyfert 2 Galaxies. **Astrophysical Journal**, v. 544, p. 747–762, December 2000.

[160] STORCHI-BERGMANN, T., RIFFEL, R. A., RIFFEL, R., DINIZ, M. R., BORGES VALE, T., MCGREGOR, P. J. Two-dimensional Mapping of Young Stars in the Inner 180 pc of NGC 1068: Correlation with Molecular Gas Ring and Stellar Kinematics. **Astrophysical Journal**, v. 755, p. 87, August 2012.

[161] TERLEVICH, E., DIAZ, A. I., TERLEVICH, R. On the behaviour of the IR CA II triplet in normal and active galaxies. **Monthly Notices of the Royal Astronomical Society**, v. 242, p. 271–284, January 1990.

[162] TINSLEY, B. M. Galactic Evolution. **Astronomy and Astrophysics**, v. 20, p. 383, September 1972.

[163] TINSLEY, B. M., GUNN, J. E. Evolutionary synthesis of the stellar population in elliptical galaxies. I - Ingredients, broad-band colors, and infrared features. **Astrophysical Journal**, v. 203, p. 52–62, January 1976.

[164] VALE ASARI, N., STASIŃSKA, G., CID FERNANDES, R., GOMES, J. M., SCHLICKMANN, M., MATEUS, A., SCHOENELL, W. The evolution of the mass-metallicity relation in SDSS galaxies uncovered by astropaleontology. **Monthly Notices of the Royal Astronomical Society**, v. 396, p. L71–L75, June 2009.

[165] VOLLMER, B., BECKERT, T., DAVIES, R. I. Starbursts and torus evolution in AGN. **Astronomy and Astrophysics**, v. 491, p. 441–453, November 2008.

[166] VOLONTERI, M., CAPELO, P. R., NETZER, H., BELLOVARY, J., DOTTI, M., GOVERNATO, F. Growing black holes and galaxies: black hole accretion versus star formation rate. **Monthly Notices of the Royal Astronomical Society**, v. 449, p. 1470–1485, May 2015.

[167] WEEDMAN, D. W. Toward explaining Seyfert galaxies. **Astrophysical Journal**, v. 266, p. 479–484, March 1983.

[168] WESTERA, P., LEJEUNE, T., BUSER, R., CUISINIER, F., BRUZUAL, G. A standard stellar library for evolutionary synthesis. III. Metallicity calibration. **Astronomy and Astrophysics**, v. 381, p. 524–538, January 2002.

[169] WOLTJER, L. Emission Nuclei in Galaxies. **Astrophysical Journal**, v. 130, p. 38, July 1959.

[170] WORTHEY, G., OTTAVIANI, D. L. Hγ and Hδ Absorption Features in Stars and Stellar Populations. **Astrophysical Journal Supplement Series**, v. 111, p. 377–386, August 1997.

[171] WU, X.-B., WANG, F., FAN, X., YI, W., ZUO, W., BIAN, F., JIANG, L., MCGREER, I. D., WANG, R., YANG, J., YANG, Q., THOMPSON, D.,

BELETSKY, Y. An ultraluminous quasar with a twelve-billion-solar-mass black hole at redshift 6.30. **Nature**, v. 518, p. 512–515, February 2015.

[172] ZEL'DOVICH, Y. B., NOVIKOV, I. D. The Radiation of Gravity Waves by Bodies Moving in the Field of a Collapsing Star. **Soviet Physics Doklady**, v. 9, p. 246, October 1964.

[173] ZHENG, Z., WANG, H., GE, J., MAO, S., LI, C., LI, R., MO, H., GODDARD, D., BUNDY, K., LI, H., NAIR, P., LIN, L., LONG, R. J., RIFFEL, R., THOMAS, D., MASTERS, K., BIZYAEV, D., BROWNSTEIN, J. R., ZHANG, K., LAW, D. R., DRORY, N., ROMAN LOPES, A., MALANUSHENKO, O. SDSS-IV MaNGA: environmental dependence of stellar age and metallicity gradients in nearby galaxies. **Monthly Notices of the Royal Astronomical Society**, v. 465, p. 4572–4588, March 2017.

[174] ZIER, C., BIERMANN, P. L. Binary black holes and tori in AGN. II. Can stellar winds constitute a dusty torus? **Astronomy and Astrophysics**, v. 396, p. 91–108, December 2002.

[175] ZUBOVAS, KASTYTIS, BOURNE, MARTIN A. Do AGN outflows quench or enhance star formation? **Monthly Notices of the Royal Astronomical Society**, v. 468, p. 4956–4967, July 2017.